University of California
Santa Barbara

Ab initio property predictions of Wadsley-Roth phase chemistries as high power density lithium-ion electrode materials

A dissertation submitted in partial satisfaction
of the requirements for the degree

Doctor of Philosophy
in
Chemical Engineering

by

Muna Saber

Committee in charge:

Professor Anton Van der Ven, Co-chair
Professor M. Scott Shell, Co-chair
Professor Michael Gordon
Professor Phillip Christopher

September 2023

The Dissertation of Muna Saber is approved.

Professor Michael Gordon

Professor Phillip Christopher

Professor Anton Van der Ven, Committee Co-chair

Professor M. Scott Shell, Committee Co-chair

June 2023

Ab initio property predictions of Wadsley-Roth phase chemistries as high power density lithium-ion electrode materials

by

Muna Saber

I would like to dedicate this thesis to my mother, Aheda Amin Arafat.

Acknowledgements

I would like to thank my thesis advisor, Dr. Anton Van der Ven, for leading me on my path to being an independent researcher. I will forever be in debt to him for not giving up on me and giving me a chance to develop this field. His precise teaching approach and his patience in assisting me with my projects were instrumental to the completion of my degree. I would also like to thank my co-advisor, Dr. M. Scott Shell, for all his guidance and support throughout the years. His fantastic teaching style and the care he shows for his undergraduate and graduate students makes him not only a world-class professor, but a world-class person. I would also like to thank the remainder of my committee, Dr. Phillip Christopher and Dr. Michael Gordon, for their helpful advice and methodical insight. I am forever thankful to be surrounded and aided by these meticulous scientific minds.

My lab mates in the Van der Ven lab, both past and present, are very dear to my heart. Some of the most intelligent yet amicable and good-hearted people I have met, I have met through this lab. For past lab members, Dr. Jonas Kaufman, Dr. Sanjeev Kolli, Dr. Julija Vinckeviciute, Dr. Jonas Kaufman, Dr. N. S. Harsha Gunda, Dr. John Goiri, Dr. Daniil A. Kitchaev, Dr. Anirudh Raju Natarajan, and soon to be Drs. Flynn Walsh and Farnaz Kaboudvand, thank you for all of your support in both my research and in your friendship and kindness. For my current lab mates, thank you Colleen Reynolds, Sesha Sai Behara, Elizabeth Garcia Ponte, Derick Ober, Jonathan Li, Ray Hung, and Jeremiah Thomas for being great coworkers. I look forward to seeing your careers progress, and I hope to be able to refer to you all as doctor soon enough.

I would like to thank the friends in my graduate program from a wide variety of disciplines. There have been countless people who have made these last few years enjoyable, from my book club friends to my climbing friends to my biking friends. I would like to

thank Emily Foley, Rebecca Vincent, Victoria Christensen, Leah Mills, Carolina Frey, Lauren Fey, and Kira Pusch for their friendship and for a lot of fun these last few years. I am very thankful to have all of you in my life.

I would lastly like to thank the people in my life that gives this work meaning. First my mother, who herself attained her PhD in Chemistry in 1984. Without my mother's support and great advice, this process would have been almost insurmountable. I would also like to thank my sisters and brother, Suha, Rana, Maha, and Hysam who all gave me a helping hand during the rough points of my degree. Finally, I would like to thank my best friend Gavin Yancey for being my practice talk guinea pig, as well as my hiking and biking partner throughout my PhD.

Curriculum Vitæ

Muna Saber

Education

2023	Ph.D. in Chemical Engineering (Expected), University of California, Santa Barbara.
2016	B.S. in Chemical Engineering, University of Illinois at Chicago

Publications

Saber, M., Preefer, M.B., Kolli, S.K., Zhang, W., Laurita, G., Dunn, B., Seshadri, R. and Van der Ven, A., 2021. Role of Electronic Structure in Li Ordering and Chemical Strain in the Fast Charging Wadsley–Roth Phase PNb_9O_{25}. Chemistry of Materials, 33(19), pp.7755-7766.

Preefer, M.B., Saber, M., Wei, Q., Bashian, N.H., Bocarsly, J.D., Zhang, W., Lee, G., Milam-Guerrero, J., Howard, E.S., Vincent, R.C. and Melot, B.C., 2020. Multielectron redox and insulator-to-metal transition upon lithium insertion in the fast-charging, Wadsley-Roth phase PNb_9O_{25}. Chemistry of Materials, 32(11), pp.4553-4563.

Baek, S.W., Saber, M., Van der Ven, A. and Pilon, L., 2022. Thermodynamic Analysis and Interpretative Guide to Entropic Potential Measurements of Lithium-Ion Battery Electrodes. The Journal of Physical Chemistry C, 126(14), pp.6096-6110.

Baek, S.W., Preefer, M.B., Saber, M., Zhai, K., Frajnkovič, M., Zhou, Y., Dunn, B.S., Van der Ven, A., Seshadri, R. and Pilon, L., 2022. Potentiometric entropy and operando calorimetric measurements reveal fast charging mechanisms in PNb_9O_{25}. Journal of Power Sources, 520, p.230776.

Muna Saber, Anton Van der Ven. Redox mechanisms, structural changes, and electrochemistry of the Wadsley-Roth $Li_xTiNb_2O_7$ electrode material. Submitted. Chemistry of Materials.

Muna Saber, Colleen Reynolds, Jonathan Li, Anton Van der Ven. Chemical and structural factors affecting the stability of Wadsley-Roth block phases. Submitted. Inorganic Chemistry.

Abstract

Ab initio property predictions of Wadsley-Roth phase chemistries as high power density lithium-ion electrode materials

by

Muna Saber

High-throughput density functional theory calculations can provide a method for predicting material properties in alkali-ion electrode and electrolyte chemistries. Through these calculations, paired with cluster expansion models and uncertainty quantification methods, we have tools to understand the fundamental thermodynamic origins of crystallographic deformation and alkali-ion phase stabilities in these materials. In this analysis, we use these methods to understand phase stability and lithiation mechanisms in a family of high power density electrode chemistries called the Wadsley-Roth crystallographic shear phases. Due to the complexity and large cell sizes of Wadsley-Roth phase materials, this combination of methods is useful for tapping the origin of the high charge rates and power densities in these unique structures. The study begins with an examination of stability of compounds in the Ti-Nb-O ternary where we examine the effect of electrostatics and distortions on phase stability of the Wadsley-Roth phases. We then examine the effect of chemical strain in the lithium site-filling mechanism in the highly reversible Wadsley-Roth material, PNb_9O_{25}. We extend our analysis to the high-power density, commercialized Wadsley-Roth phase, $TiNb_2O_7$, where we examine the effect of metal-metal electronic interactions and pair distances on the complex lithium site filling mechanism present in this compound. We then do an in depth analysis of the effect of lithiation on octahedral distortions to acquire a complete understanding of structural changes upon lithiation. These analyses are paired with experimental results to exhibit

the validity of these calculations.

Contents

Curriculum Vitae **vii**

Abstract **viii**

1 Introduction **1**
1.1 An overview of high power density battery materials 1
1.2 Overview 4
1.3 Permissions and Attributions 5

2 Computational Methods and Theoretical Background **6**
2.1 Density functional theory overview 6
2.2 Cluster expansion formalism 25
2.3 Electrochemical derivations 27
2.4 Entropy derivations 30
2.5 Symmetry adapted collective displacement modes 34

3 Wadsley-Roth phases **45**
3.1 Introduction 46
3.2 Methods 48
3.3 Results 49
3.4 Discussion 77
3.5 Conclusion 85

4 Role of Electronic Structure in Li Ordering and Chemical Strain in the Fast Charging Wadsley–Roth Phase PNb_9O_{25} **87**
4.1 Introduction 88
4.2 Methods 90
4.3 Results 95
4.4 Discussion 126
4.5 Conclusion 130

5 Redox mechanisms and structural changes of the Wadsley-Roth phase, $Li_xTiNb_2O_7$ **132**
5.1 Introduction 133
5.2 Methods 135
5.3 Results 136
5.4 Discussion 165
5.5 Conclusion 171

6 Conclusion **172**

A Charge Density Evolution in Lithiated $TiNb_2O_7$ **177**
A.1 NbO_6 octahedra density of states 177
A.2 TiO_6 octahedra density of states 177

Bibliography **191**

Chapter 1

Introduction

1.1 An overview of high power density battery materials

Electrification of vehicles and aircraft requires batteries that can deliver the power densities needed for acceleration while allowing for fast charge times in a variety of environmental conditions. The appeal of electric vehicles lies within the lower total carbon footprint of this energy source and the mitigation of direct human exposure to small particulates as well as NO_x, SO_x, CO_2, and CO molecules that damage human health when emitted in the local environment of people [1].

Rechargeable alkali-ion batteries are electrochemical energy storage devices that can deliver power through the mobility of ions within an electrolyte solution from one electrode to the other [2]. During the charging process, ions flow from the cathode to the anode through an externally applied potential. During discharge, when the battery is in use, ions flow from the anode to the cathode due to the gradient in the chemical potentials between the cathode and the anode [3]. In most modern-day rechargeable batteries,

lithium-ions are the alkali-ions that are shuttled between the electrodes [4]. For emerging technologies, sodium and potassium ions are also being studied. There are also batteries that use other species than alkali-ions as the vehicle for storing and transporting charge, such as the alkaline-ion magnesium [5].

To ensure high power and energy densities, the selection of anode and cathode materials is of utmost importance. The first rechargeable intercalation battery system, constructed by Stanley Whittingham, used Li_xTiS_2 as the cathode [6]. Due to its low voltage (2.5V vs Li^+), alternative cathode chemistries were examined. Specifically, oxide chemistries were examined due to the theoretical voltage increase from this class of materials compared to sulfides. From this, Goodenough discovered that Li_xCoO_2 displayed higher voltages (4.0V vs Li^+) [7, 8]. For long after this discovery, Li_xCoO_2 was the standard cathode chemistry in industry. Due to its inadequate specific capacity, research was done on how to increase the specific capacity. The addition of nickel and manganese into these compounds greatly increased capacity, but further research is still performed to attain higher voltage profiles and longer capacities in cathode materials [9].

Lithium-ion battery anodes, on the other hand, were less studied. Graphite, the industry standard was quite cheap and had a reasonable capacity to be paired with the corresponding cathode materials. As the need for batteries that can deliver a large amount of power and fast charging times grew with the introduction of electric vehicles, it became apparent that graphite was not good enough. Despite it's reasonable capacity, graphite can not charge at high rates since its specific capacity quickly dies off with higher charge rates. Additionally, attempting to charge at high rates promotes the formation of dendrites [10]. Dendrites can pierce the membrane that separates the anode from the cathode, causing side reactions and then fires and explosions [11, 12].

As a result of these safety concerns and low charge rates, researchers sought to uncover an alternative to the graphite anode, and they did in the commercialized material

spinel-type $Li_4Ti_5O_{12}$ (LTO). Unfortunately, this material suffers from a low theoretical capacity, low electronic conductivity, and a charge rate that is still too low for electric vehicle applications [13, 14].

A new chemistry, initially chemically inserted with lithium in 1983 [15] and cycled in 2011 [16], showed significantly high reversible cycling. This material is called $TiNb_2O_7$. Onward from these studies, researchers began high charge rate studies and found that this material can reversibly cycle at rates of 20C, which corresponds to a 3 minute charge rate, or even higher rates [17, 18]. Studies of $TiNb_2O_7$ nanoparticles were able to achieve capacities as high as 341 mAh g^{-1} [19]. The discovery of this application for $TiNb_2O_7$, brought upon a new set of studies on other phases with similar crystal structure types that were also able to achieve high charge rates. These materials belong to a family of chemistries called Wadsley-Roth crystallographic shear phases.

Wadsley-Roth crystallographic shear phases are derived from the ReO_3 structure which is constructed from corner-sharing transition metal octahedra [15, 20, 21, 22]. The Wadsley-Roth phases differ from ReO_3 in that the blocks of corner-sharing octahedra are offset and share edges to other blocks of interconnected corner-sharing octahedra. These areas of octahedral edge-sharing at the periphery of the blocks of corner-sharing octahedra are called crystallographic shear planes. The construction of these structures types is chemically feasible due to the lower oxygen to metal ratio of Wadsley-Roth phase structures compared to ReO_3. The blocks of corner-sharing octahedra can be $n \times m$ in size, where n and m are the block dimensions, the number of corner-sharing octahedra in two dimensions. The limits on the block dimensions are based on the oxidation states available in the transition metal sublattice of the Wadsley-Roth phase. Phases with many transition metal ions with lower maximum oxidation states (like titanium or zirconium) form smaller blocks. On the other hand, phases that have transition metal ions with larger maximum oxidation states are able to host a larger number of oxygens and therefore form

structures with larger blocks. There is diversity in this family of chemistries in that phases with differing cation species, anion species, degrees of cation disorder, block sizes, and block shift types have been experimentally formed.

Computational methods can be used to understand phase stability in these structures. Atomistic simulations allow one to understand the electronic and crystallographic structure properties of a periodic phase. Density functional theory (DFT) in particular has been a useful tool in examining the atomic-scale properties of battery materials, as well as other periodic crystal structures. DFT is a method for modeling quantum mechanics in materials. At its theoretical core are the findings of Hohenberg and Kohn [23]. The ground state of a system can be uniquely determined through the electron density. Despite its simplicity, there is complexity in the details. The predominant challenge is that there is no known way to get the exact electron density functional. This is because the exact contribution from electron-electron interactions are unknown [24]. This contribution is often contained in a separate exchange-correlation functional [25, 26].

When paired with density functional theory, statistical mechanics methods can be a strong tool to aid in material design. Through models of the potential energy of lithium-vacancy orderings in a system, called cluster expansions, we can predict ground state orderings in these complex phases that can have eligible lithium-vacancy orderings on the order of 10^9. Moreover by constructing effective Hamiltonians parameterized by the cluster expansion models, we can attain finite temperature thermodynamic and electrochemical properties.

1.2 Overview

The following dissertation examines high power density battery material property predictions in the Wadsley-Roth phases. In Chapter 2, We begin with an overview

of the theoretical background behind ab initio calculations as well as methodological derivations of cluster expansions and displacement order parameters used to examine the first principles predictions. In Chapter 3, we examine phase stability in the titanium niobium oxygen ternary with a focus on Wadsley-Roth phase niobates and titanium niobates. In Chapter 4, we examine lithiation mechanisms in the 3×3 Wadsley-Roth phase structure PNb_9O_{25}. We use crytallographic strain calculations to understand the interplay between crystallographic strain and lithium site stability. We also examine the electronic structure evolution of the Wadsley-Roth phases to understand the electronic effects of these crystallographic changes. In chapter 5, we explore the effect of transition metal disorder on performance in the 3×3 Wadsley-Roth phase $TiNb_2O_7$. In particular, we examine the interplay between metal-metal bonding, strain, and octahedral distortions as the system undergoes lithiation. We use uncertainty quantification for a rigorous examination of electrochemical properties at zero-temperature and finite temperatures.

1.3 Permissions and Attributions

1. The contents of chapter 4 has previously appeared in Reference [27]: Saber, Muna, Molleigh B. Preefer, Sanjeev K. Kolli, William Zhang, Geneva Laurita, Bruce Dunn, Ram Seshadri, and Anton Van der Ven. "Role of Electronic Structure in Li Ordering and Chemical Strain in the Fast Charging Wadsley–Roth Phase PNb_9O_{25}." Chemistry of Materials 33, no. 19 (2021): 7755-7766.

2. The contents of chapter 4 has also previously appeared in Reference [28]: Preefer, Molleigh B., Muna Saber, Qiulong Wei, Nicholas H. Bashian, Joshua D. Bocarsly, William Zhang, Glenn Lee et al. "Multielectron redox and insulator-to-metal transition upon lithium insertion in the fast-charging, Wadsley-Roth phase PNb_9O_{25}." Chemistry of Materials 32, no. 11 (2020): 4553-4563..

Chapter 2

Computational Methods and Theoretical Background

2.1 Density functional theory overview

2.1.1 An introduction to the many-body problem

In order to begin our discussion on density functional theory, it is beneficial to have an understanding of the behavior of electrons in the many-body system. This can be done by first introducing the Hamiltonian that would need to be used to describe such a system, and the challenges that comes from solving the many-body Schrodinger equation. This is followed by simple mathematical approaches to approximating the solution to the many-body wavefunction through the Born-Oppenheimer, the Hartree, and the Hartree-Fock approximations. The former approximation relies on the size difference between electrons and neutrons to approximate a solution to the many-body system. Both of the latter methods use an approach where the many-body wavefunction is approximated through a product of single particle states. The main difference between these approxi-

mations is in their treatment in the Fermionic nature of electrons. Where these solutions are approximations by nature, another method for describing this problem comes from density functional theory, where it makes use of the principle that the total energy can be uniquely determined by a functional of the electron density [29].

2.1.2 The many-body Hamiltonian

The material properties of a system with multiple electrons and ions interacting through electrostatic forces can be described with the many-body wavefunction. The Hamiltonian for this system has the general form:

$$\widehat{H} = -\sum_{I=1}^{P} \frac{\hbar}{2M_I}\nabla_I^2 - \sum_{i=1}^{N} \frac{\hbar}{2m_i}\nabla_i^2 + \frac{e^2}{2}\sum_{I=1}^{P}\sum_{J\neq I}^{P} \frac{Z_I Z_J}{|R_I - R_J|} + \frac{e^2}{2}\sum_{i=1}^{N}\sum_{j\neq i}^{N} \frac{1}{|r_i - r_j|} - e^2 \sum_{I=1}^{P}\sum_{i=1}^{N} \frac{Z_I}{|R_I - r_i|}$$

where I indexes over the set of nuclear coordinates, i indexes over the set of electronic coordinates, Z_I are the nuclear charges, and M_I are the nuclear masses [30]. R are the nuclear coordinates while r are the electronic coordinates. The first two terms correspond to kinetic energy terms for the nuclei and electrons in the system. The next two terms correspond to coulombic interactions between nuclei and electrons separately. The last term describes the interactions between electrons and nuclei.

The eigenstates can be solved for with the Schrodinger equation

$$\widehat{H}\Psi_i(R, r) = E_i\Psi_i(R, r) \tag{2.1}$$

where Ψ_i are the wavefunctions for each particle. In performing this calculation, the full set of equations can not be decoupled into sets of independent equations. This leads to

sets of equations with $3P+3N$ coupled degrees of freedom. In all but the most simple of systems, this problem becomes analytically impossible to solve. In order to reasonably solve these equations for larger systems, approximations must be introduced.

2.1.3 The Born-Oppenheimer approximation

The Born-Oppenheimer approximation uses the large mass differences between electrons and ions to approximate a description for multi-electron systems [31, 32]. The theorem begins with the realization that the timescale associated with the motion of electrons and nuclei vary due to their large variation in mass. Therefore the electrons may be described as instantaneously following the motion of the nuclei. The stationary state would therefore vary in time, but as the nuclei follows its motion, the electrons will instantaneously adjust their wavefunction to the nuclear wavefunction. One may use this to separate out the time dependence of the wavefunction for only the nuclear wavefunction component, leading to the following factorization of the total wavefunction:

$$\Psi(R;r) = \Phi(R)\Psi_R(r) \tag{2.2}$$

where $\Phi(R)$ is the nuclear wavefunction and contains the ionic degrees of freedom. $\Psi_R(r)$ is the electronic wavefunction and depends on all the electronic degrees of freedom for a particular ionic configuration [30]. These wavefunctions can be solved for separately. The electronic wavefunction can be normalized for every R so that it does not explicitly depend on the electronic coordinates. The electronic wavefunction can be solved for through the Schrodinger equation

$$\widehat{H}_R^{ele}\Psi_R(r) = E_R^{ele}\Psi_R(r) \tag{2.3}$$

where H_R^{ele} and E^{ele} are the corresponding Hamiltonian and energy. A similar expression can be applied to solve for the total wavefunction [33]

$$\widehat{H}^{tot}(R;r)\Psi(R;r) = E^{tot}\Psi(R;r) \tag{2.4}$$

The separated electronic and nuclear wavefunctions can be used directly in the Schrodinger equation for the total wavefunction, and the conjugate of $\Psi_R(r)$ can be multiplied to the equations and integrated

$$\langle\Psi_R(r)|H^{tot}|\Psi_R(r)\rangle\Phi(R) = E^{tot}\Phi(R) \tag{2.5}$$

The notation above is written in bra-ket notation and is a commonly used notation in Quantum-mechanics. The right most side of the equation is called the "ket" and can be represented by $|v\rangle$ where v is an element of a complex vector space. It's adjoint is called the "bra" and is denoted generally by $\langle f|$ where f in this case is a vector in a different complex vector space.

More specifically, where the vector v is in the vector space V, both the ket, $|v\rangle$, and the label, v, are vectors. The "bra" object works differently in that it belongs to the $V*$ vector space which is a linear map from V to a complex vector space. This $\langle f|$ therefore is a linear function that belongs to $V*$ instead. Even though $\langle f|$ is a linear function, the label inside of it, f, is merely another vector. If we were to apply the bra, $\langle f|$, to the ket, $|v\rangle$, it would be similar to an inner product where the bra can be viewed as row vectors

where the elements are conjugate to its original elements and ket are column vectors:

$$\langle f|v\rangle = \begin{pmatrix} f_1^* & f_2^* & f_3^* & f_4^* & ... & f_N^* \end{pmatrix} \cdot \begin{pmatrix} v_1 \\ v_2 \\ v_3 \\ v_4 \\ \vdots \\ v_N \end{pmatrix} \tag{2.6}$$

for a vector with N elements, where $'*'$ indicates the conjugate of that element. Performing the multiplication gives the following:

$$\langle f|v\rangle = f_1^* v_1 + f_2^* v_2 + f_3^* v_3 + f_4^* v_4 + ... + f_N^* v_N \tag{2.7}$$

where the above derivation is for discrete values. If we extend the derivation to a an uncountably large number of vectors in Hilbert space, this summation can be seen as an integration.

If we know the wavefunction of a particle ($\Psi(x)$), we can describe that wavefunction through bra-ket notation with reference to its position dependence (x) by:

$$\Psi(x) \equiv \langle x|\Psi(x)\rangle \tag{2.8}$$

If two states were to overlap, it can be computed as

$$\langle \Psi_1(x)|\Psi_2(x)\rangle = \int \Psi_1^*(x)\Psi_2(x)dx \tag{2.9}$$

where again this would integrated since we are looking at an infinite number of values

for x possible.

If we return to our derivation, the potential and kinetic energy operators of the ions need to be determined, but these can be determined individually. Due to the normalization of the electronic wavefunction, the wavefunction does not depend on ionic coordinates. Thus, the potential energy for the ions can be determined from

$$\langle \Psi_R(r)|\frac{e^2}{2}\sum_{I=1}^{P}\sum_{J\neq I}^{P}\frac{Z_I Z_J}{|R_I - R_J|}|\Psi_R(r)\rangle = \frac{e^2}{2}\sum_{I=1}^{P}\sum_{J\neq I}^{P}\frac{Z_I Z_J}{|R_I - R_J|} \tag{2.10}$$

In order to determine the kinetic energy operator, one can apply the momentum operator to the total wavefunction

$$-i\hbar\nabla_{R_I}\Psi(R;r) = -i\hbar(\nabla_{R_I}\Phi(R))\Psi_R(r) - i\hbar\Phi(R)(\nabla_{R_I}\Psi_R(r)) \tag{2.11}$$

Again the conjugate of the electronic wavefunction can be multiplied to the left side of each equation, leaving a relation between the total wavefunction and the ionic wavefunction

$$\langle\Psi_R|(-i\hbar\nabla_{R_I})\Psi(R;r)\rangle = -i\hbar(\nabla_{R_I}\Phi(R)) - i\hbar\langle\Psi_R|\nabla_{R_I}|\Psi_R\rangle\Phi(R) \tag{2.12}$$

When the bra $\langle\Psi_R|$ is applied to the equation as well as the ket $|\Psi_R\rangle$, the result is merely unity due to the normalization applied to the wavefunctions.

Now that we have an expression for the momentum operator, we can use this equation directly into the definition of the kinetic energy. From this equation and the general definition of the kinetic energy operator, the kinetic energy expression for the motion of the ions can be written as

$$KE^{ion} = \sum_{I}\frac{(-i\hbar(\nabla_{R_I}\Phi(R)) - i\hbar\langle\Psi_R|\nabla_{R_I}|\Psi_R\rangle\Phi(R))^2}{2M_I} \tag{2.13}$$

where KE^{ion} is the kinetic energy of the ions. Specifically, the kinetic energy operator can be thought as the summation of all of the contributions to the kinetic energy from each ion. Using the original ionic wavefunction equation, the Schrodinger equation for the ionic wavefunction can be written as

$$(KE^{ion} + V^{ion} + E^{ele})\Phi(R) = E^{tot}\Phi(R) \tag{2.14}$$

where V^{ion} indicates the potential energy operator of the ion, and E^{ele} is the energy corresponding to the electronic wavefunction determined previously. Therefore one may write the equation as

$$(\sum_{I} \frac{-i\hbar((\nabla_{R_I}\Phi(R)) + \langle\Psi_R|\nabla_{R_I}\Psi_R\rangle\Phi(R))^2}{2M_I} + \frac{e^2}{2}\sum_{I=1}^{P}\sum_{J\neq I}^{P}\frac{Z_I Z_J}{|R_I - R_J|} + E^{ele})\Phi(R) = E^{tot}\Phi(R)$$

which can be used to find the total energy of the system [34].

2.1.4 The Hartree and Hartree-Fock approximations

The Hartree and Hartree-Fock approximations use single-particle wavefunctions as the basis to approximate the many-body wavefunction. From this wavefunction, one can determine the expectation value of the Hamiltonian which corresponds to the energy. The single particle state that forms the basis of the wavefunction can be varied such that the energy is minimized through these variations until a tolerance is reached.

The Hartree approximation effectively treats electrons as independent particles and disregards the Pauli exclusion principle and the fermionic nature of electrons that leads to this principle in the construction of each wavefunction. In other words, it does not

necessitate the asymmetry of the chosen wavefunctions. With this established, the total wavefunction can be approximated as

$$\Phi^H(r) = \phi_1(r_1)\phi_2(r_2)..\phi_N(r_N) \tag{2.15}$$

where $\Phi^H(r)$ is the total many-body wavefunction under the Hartree approximation, $\phi_i(r_i)$ are the single particle wavefunctions, and N indicates the number of particles. A set of the single particle states is chosen and is used to construct the total number density for the system which is itself used to determine the effective single-particle potential that describes the repulsive electrostatic interactions between a single electron and all other electrons. The Schrodinger equation can then be solved using this effective potential, allowing one to solve for a new set of single particle wavefunctions [35]. In other words one would be solving:

$$\left[\frac{-\hbar}{2m_e}\nabla_r^2 + V_i^{eff}(r, n^{(in)}(r)\right]\phi_i^{out} = \epsilon_i\phi_i^{out} \tag{2.16}$$

where V^{eff} is the effective single particle potential, $n^{(in)}$ is the number density calculated from the original wavefunctions chosen as the starting point of the calculation, and ϕ_i^{out} is the new wavefunction that is being solved for. The original single particle wavefunctions, ϕ_i^{in}, can be compared to the new single particle wavefunctions, ϕ_i^{out}. If the number densities that they construct are different within a tolerance, the values are set to the new single particle wavefunctions and the cycle is repeated. If the number densities for the two sets of wavefunctions are equal to each other within a tolerance window, then the cycle stops, and the energy and other properties can be described with the last set of wavefunctions.

The Hartree-Fock approximation takes into account the Fermionic nature of electrons,

and therefore requires the chosen wavefunction to be properly antisymmetrized. This can be done by describing the total wavefunction through the following determinant, which is called the Slater determinant [36, 37]

$$\Phi^{HF}(r) = \begin{vmatrix} \phi_1(r_1) & \phi_1(r_2) & ... & \phi_N(r_N) \\ \phi_2(r_1) & \phi_2(r_2) & ... & \phi_N(r_N) \\ \vdots & \vdots & \ddots & \vdots \\ \phi_N(r_1) & \phi_N(r_2) & ... & \phi_N(r_N) \end{vmatrix} \tag{2.17}$$

where $\Phi^{HF}(r)$ is the total wavefunctions as determined through the Hartree-Fock approximation method, and $\phi_i(r_i)$ are the single particle wave functions of different electrons, and N is the total number of electrons. Interchanging the positions of two electrons effectively changes their sign, which is what allows this to uphold the asymmetry of the wavefunctions.

The addition of the representation of the Fermionic nature of the electrons adds an electron-exchange interaction potential [38]. This exchange potential is described through a non-local integral operator dependent on both the position of the electron (r) and each other electron (r') [39, 40]. This term is analytically complex and therefore computationally expensive.

2.1.5 Formulation of DFT and the Kohn-Sham equations

Providing an approximate solution to the many-body wavefunction can be performed using another key aspect of the system, the electronic number density. Where the Hartree and Hartree-Fock approximations attempted to describe the behavior of the entire system from the start, one can alternatively describe the single particle equation exactly and then add additional approximations as needed. Seminal work from Hohenberg, Kohn

and Sham had derived that one can determine the ground state energy from a functional where the variable is the electron density, $n(r)$ [41].

The derivation of the electronic density begins with the assumption of a system comprised of a number of electrons with an applied potential. We can use the definition of the density operator to find an explicit expression for this. The electronic number density can be accessed from the expectation value of the density operator. $N(r)$, where

$$N(r) = \sum_{i=1}^{N} \delta(r - r_i) \tag{2.18}$$

and is dependent on the positions of the particles, r_i. Upon taking the expectation value of this operator, one finds that

$$n(r) = \langle \Psi | N(r) | \Psi \rangle \tag{2.19}$$

By putting this in integral form, we have a clearer definition of the electronic density. The electronic density for the ground state at a particular point, r, can thus be described as

$$n(r) = \sum_{i} \int \Psi^*(r_1 ... r_N) \delta(r - r_i) \Psi(r_1 ... r_N) dr_1 ... dr_N \tag{2.20}$$

where $n(r)$ is the electronic number density. In this case N is the number of electrons and i indexes over each electron in the system. Ψ is dependent on all of the positions of each electron as the density is dependent on all other electrons in the system. We can place the summation in the integral and apply it to the dirac-delta function directly to get N terms. This simplifies the equation to

$$n(r) = N \int \Psi^*(r, r_2, ... r_N) \Psi(r, r_2, ... r_N) dr_2 ... dr_N \tag{2.21}$$

so that $n(r)$ is directly related to the form of a wavefunction dependent on all other electrons in the system.

Furthermore the electronic density can be described as a functional with respect to an external potential ($v(r)$). One can prove that this potential $v(r)$ must be a unique functional of $n(r)$ by introducing another external potential, denoted by $v'(r)$. We assume that this $v'(r)$ and the corresponding ground state of Ψ' cause the same electronic density, $n(r)$, but Ψ' and Ψ can not be the same since they must be solved for by different forms of the Schrodinger equation, leading to a separate Hamiltonian and ground state energy. The variational principle, which states that the ground state energy is always higher than the expectation value of the Hamiltonian for a separate wavefunction, dictates that the expectation value of H with respect to Ψ' gives a bound for the energy where

$$E < \langle \Phi' | H | \Phi' \rangle \tag{2.22}$$

This relation can be written in terms of the expectation value of H'. If the expectation value of H is greater than E then the expectation value of H' combined with the difference between H' and H must also be greater than the energy calculated from H

$$E < \langle \Phi' | H' | \Phi' \rangle + \langle \Phi' | H - H' | \Phi' \rangle \tag{2.23}$$

Likewise, E' can be calculated from the first relation and the second equation can be written in terms of the external potentials. This is because H can be written in terms of the potential, making the relation

$$E < E' + \langle \Phi' | (v(r) - v(r)') | \Phi' \rangle \tag{2.24}$$

Using the definition for the electronic density above, one attains the equation

$$E < E' + \int [v(r) - v'(r)]n(r)dr \tag{2.25}$$

Through the same derivation of E', one would also find that

$$E' < E + \int [v'(r) - v(r)]n(r)dr \tag{2.26}$$

If one adds the two former equations for E and E' together (2.25 and 2.26) they find that the integral cancels. All that is left is the equality

$$E + E' < E' + E \tag{2.27}$$

This is an inconsistency. This inconsistency arises when multiple functions $v(r)$ can be attributed to an electronic number density, $n(r)$. Therefore, $v(r)$ must be unique for a specific $n(r)$. Since the Hamiltonian is dependent on the potential, the full ground state must be a unique functional of $n(r)$ as well [23]. This finding is the foundation for density functional theory.

Using this consideration, we know that the total energy of the system must directly be a functional of the electronic density [42, 43]. In general terms, this can be written as

$$E[n(r)] = F[n(r)] + \int V(r)n(r)dr \tag{2.28}$$

where $F[n(r)]$ is a universal functional of the density, and $V(r)$ is the potential.

While Hohenberg and Kohn proved the existence of the electronic functional, the theorem does not give the exact form of the functional. The form of $F[n(r)]$ in equation 2.28 must be approximated. The contributions of this equation can broken into the

following terms:

$$F[n(r)] = T_s[n(r)] + \frac{1}{2}\int \frac{n(r)n(r')}{|r-r'|}drdr' + E_{xc}[n(r)] \tag{2.29}$$

where the first term ($T_s[n(r)]$) corresponds to the kinetic energy contributions of the non-interacting particles with a density of $n(r)$, and the second term is merely a classical Coulombic interaction term. The final term ($E_{xc}[n(r)]$) takes into account the energy from exchange correlation interactions.

Along with the total wavefunction, the single particle wavefunctions must give the proper minimum energy for a certain electronic density for the system ground state. Therefore, we can begin examining this for the single particle case. The kinetic energy term for the single particle states can be written as,

$$T_s[n(r)] = \sum_i \langle\phi_i|\frac{-\hbar^2}{2m_e}|\phi_i\rangle \tag{2.30}$$

where ϕ_i are the single particle states. T_s itself is an approximation, where it accounts for the contribution of kinetic energy by a set of ficticious, non-interacting particles.

The exchange correlation term corresponds to the electrostatic interaction of the electrons at each position with the density of the exchange-correlation hole that surrounds them [44]. It is intrinsically connected to T_s as E_{xc} provides a correction to that approximation. Combining the terms together, one can get the exact form of the energy in the form of the total energy functional, often referred to as the Kohn-Sham functional:

$$E[n(r)] = T_s[n(r)] + \frac{1}{2}\int \frac{n(r)n(r')}{|r-r'|}drdr' + E_{xc}[n(r)] + \int V(r)n(r)dr \tag{2.31}$$

The exchange correlation term is approximated by different methods and is the source of differences between computationally determined groundstates and reality. Indeed one

would be able to determine the exact ground state energy and therefore properties, if the exact form of the exchange correlation energy functional were known. When performing density functional theory (DFT) calculations one may use different functionals that each treat the exchange correlation term in varying ways. This will be further discussed in section 2.1.9.

The Kohn-Sham functional can be minimized with respect to variations in the electronic density, which allows us to arrive at the Kohn-Sham equations

$$[-\frac{\hbar^2}{2m_e}\nabla_r^2 + V(r) + \int \frac{n(r')}{|r-r'|}dr' + \frac{\partial E^{xc}[n(r)]}{\partial n(r)}]\phi_i(r) = \epsilon_i\phi_i(r) \tag{2.32}$$

These equations allow for one to solve for the single particle orbitals that can in turn be used to solve for the electronic density.

2.1.6 The planewave expansion and the projector-augmented wave (PAW) formalism

For the Vienna ab initio software package (VASP), the basis set used for the expansion of electronic orbitals and charge densities is a plane wave-expansion. More specifically, VASP makes use of the projector-augmented-wave method which is used to describe the electron-ion interactions. In this method, one can determine the one-electron wavefunction from pseudo-orbitals which are functions calculated through a plane wave expansion,

$$\phi_{nk} = \frac{1}{\Omega^{\frac{1}{2}}}\sum_G C_{nGk}e^{i(G+k)r} \tag{2.33}$$

Where k indexes through all the k-points in the specified mesh, n indexes through the bands, Ω is the volume of the Wigner-Seitz cell, and G is the reciprocal lattice vector. The summation in the exponential requires a cutoff, which is dependent on G. This cutoff

is determined by including all planewaves that fall below a kinetic energy threshold. This kinetic energy threshold can be connected to the reciprocal lattice vectors by the definition of the kinetic energy

$$E_{cutoff} = \frac{\hbar^2}{2m} G_{cutoff} \tag{2.34}$$

where E_{cutoff} is the cutoff energy of the planewave expansion basis set. Likewise G_cutoff is the lattice vector cutoff. This can further be related to the planewave expansion by only including reciprocal lattice vectors where

$$|G + k| < G_{cutoff} \tag{2.35}$$

This may be a significant source of error if the energy cutoff is not chosen carefully. The error can be determined by performing static calculations with a particular energy cutoff off value and finding the difference between the energy for this calculation and a high cutoff energy calculation.

2.1.7 Pseudopotentials

The use of a plane wave expansion also introduces the need for an approximation of the ion-electron interactions, given in the form of pseudopotentials. This presents another form of error. In order to accurately, but efficiently describe the interaction between the core electrons and the valence electrons, approximations must be introduced. Pseudopotentials replace the contributions of the core electrons with an effective potential that acts on each the valence electrons. The exact error introduced by this method will be determined by the quality of the atomic pseudopotentials used in the calculation [45].

Pseudopotentials can be grouped into groups of 'soft' and 'hard' pseudopotentials

where the method for establishing the contributions of the core electrons differ significantly. For soft pseudopotentials, the all-electron wavefunction that would otherwise be used to describe the electrons in the system are replaced with a nodeless pseudo-wavefunction inside a core radius [46]. Generally, the main constraint is that the norm of the all electron wavefunction matches the norm of the pseudo-wavefunction. Hard pseudopotenials use atomic calculations to determine their wavefunctions and generally have a strongly repulsive core potential. Multiple studies have been used to quantify the error in these varying types of psuedopotentials. Work by Hamann et al.[47] determined that both hard and soft pseudopotenials agreed well when compared with both an empirical, non-local pseudopotential and an all-electron potential for semiconductors. When comparing the band energies at varying symmetry points of silicon for all four methods, the error between the potentials generally fell less than 10%, with the hard pseudopotentials showing a closer average energy to the all-electron potential than the soft pseudopotentials.

2.1.8 Sampling the Brillouin zone

Bloch vectors, also known as k-points, indicate points along which one is sampling the Brillouin zone. The Brillouin zone is a region that is enclosed by discrete sets of Bragg planes, the zone corresponding to the closest Bragg planes to the origin being the first Brillouin zone. Bragg planes will be discussed further in the next section. In calculations like charge density or density of states we require an integration over the Brillouin zone with respect to the wavevector. In doing these calculations, these integrals are replaced by a summation of discrete k-points to make these calculations faster. More specifically,

the integration is replaced with a weighted summation:

$$\frac{1}{\Omega}\int_{\Omega} \rightarrow \sum_{k} w_k \tag{2.36}$$

As a result of this, the accuracy of the calculation will be determined by the accuracy of the selection of the k-points, or more specifically, the ability of the chosen k-points to accurately be able to sample the cell. In order to sample the cell effectively, the VASP algorithm creates an equally spaced grid of k-points called a mesh. As proposed by Monkhorst and Pack, the method is used to find a set of "special k-points" that can be used to generate a periodic expansion in reciprocal space [48, 49].

Moreover, the type of material that is being simulated can also be a determination of the accuracy of the k-points chosen. For example, an insulating or semi-conducting material can be described by a step function, allowing the weighted summation above to be approximated by a dirac-delta function as the electrons are localized in space. On the other hand, metals have partially occupied bands and therefore any integrations that involve these states will need to account for these partially occupancies. This is done by replacing the delta function with a smoother function, that would require more k-points to correctly interpolate the function between each of the special points.

In determining the error associated with performing DFT calculations with a particular set of k-points, one can perform calculations at a discrete set of mesh point densities for an individual system; the energy of each set of calculated values can be compared to a calculation using a high mesh density.

2.1.9 Functionals

In application to computational DFT algorithms, multiple different functionals have been developed to take into account the unknown form of the exchange-correlation func-

tional. These methods can be grouped into two types of methods: empirical and semi-empirical. Empirical methods, like the generalized gradient approximation (GGA) proposed by Perdew, Burke, and Ernzerhof (PBE) [44, 50], satisfy exact constraints in their calculations and in the boundaries of the calculations [51]. Semi-empirical methods fit unknown coefficients to empirical reference values [52]. Inaccuracies between experiment and computation are therefore dependent on which functional is used, and more specifically, on the unknown nature of the exchange-correlation energy. Improvements on accuracy is dependent on providing a reasonable functional for the described system and accessing methods with additional considerations in the functional form of the exchange-correlation energy.

Hierarchies of functional forms are described in Jacob's ladder [53] as described by John Perdew and shown in Figure 2.1. The "base" of the ladder begins at the local density approximation (LDA) [54, 55] where the exchange-correlation functional is obtained through the electron charge density and the exchange-correlation of a homogeneous electron gas. The next rung up the ladder and in chemical accuracy is GGA. Here, the electron charge density of the homogeneous electron gas is both dependent on the electron density and a gradient of the electron density. In meta-GGA functionals, like the Strongly constrained and appropriately normed semi-local density functional (SCAN) [56] functional, the kinetic energy density of the electrons are also considered in the exchange-correlation function of the homogeneous electron gas. This adds a significant computational cost, but is made up in the accuracy of the calculation [57].

The hybrid Meta-GGA functional found on the next rung provides a mixture of density functional theory and Hartree-Fock theory. [58] The Hartree-Fock computation allows one to get an exact exchange energy functional. This functional can then be expressed as a function of the Kohn-Sham orbitals [59]. Different functionals, such as HSE and PBE0, differ in how the exchange functionals from Hartree-Fock and the the exchange

functionals from PBE and GGA are treated to form a hybrid exchange functional.

The class of methods with the highest degree of accuracy in use are those that provide a fully non-local solutions exchange correlation-functional. For example, in the random phase approximation (RPA) [60, 61], the correlation functional is dependent on the response function that can be determined from the kernels established from time-dependent density functional theory [62]. While providing accuracy in Van der Waal interactions and molecular disassociation energies at a far higher accuracy then the previous methods, non-local functional methods are highly computationally expensive [63].

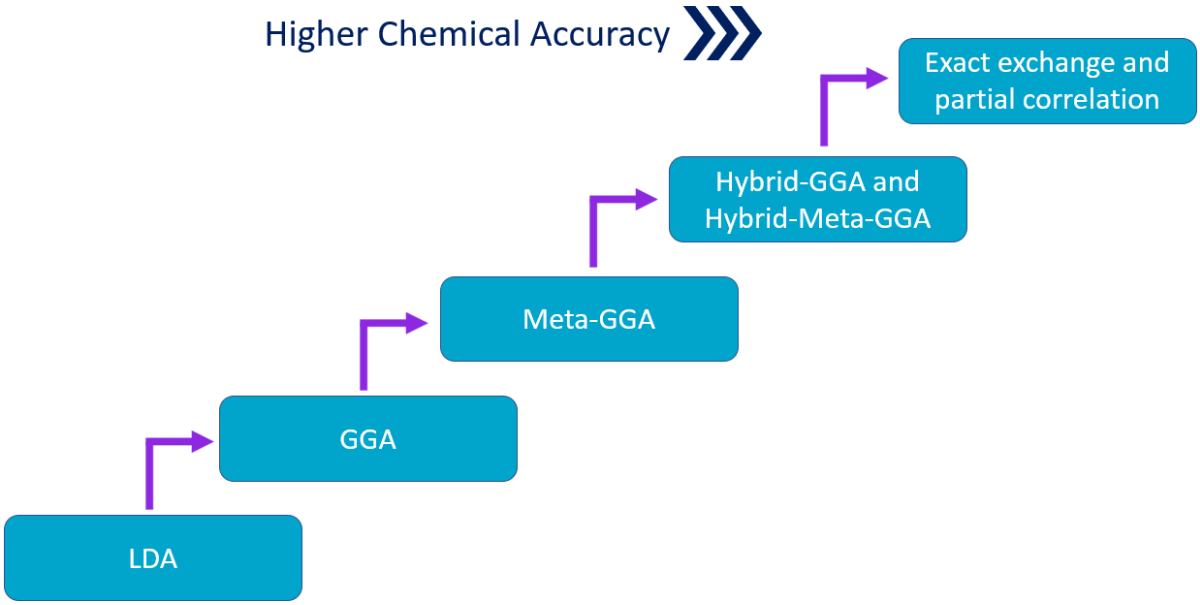

Figure 2.1: Jacob's ladder of DFT functionals where lower rungs correspond to lower accuracy yet computationally faster DFT functionals and higher rungs correspond to more computationally expensive methods.

There have been several assessments to quantify the error propagated by functional usage. For example, a study comparing PBE and LDA through a Bayesian approach found that when compared to an experimental database, LDA showed a mean atomization and cohesive energy error of 1.35 eV for periodic solids, while PBE showed an error of

0.16 eV [64].

In addition to determining error against experiment, the self-interaction error for varying functionals can also be compared theoretically. The method for determining the self-interaction error is dependent on comparing the electron density distribution garnered from these functionals with reference densities. When examining higher steps on Jacob's ladder, the functional PW91PW91, which contains both local and non-local terms, performed well compared to SVWN5, a local spin density approximation (LSDA) functional which is effectively an extension of LDA. When examining the Hydrogen molecule, PW91PW91 produced a self-interaction error of -0.13 eV while SVWN5 produced a self-interaction error of 1.26eV [65].

2.2 Cluster expansion formalism

The cluster expansion method is a linear expansion used to approximate the configurational energy of crystals from short range interactions [66, 67, 68] though the method could be extended to more general degrees of freedom [69]. We begin by assigning occupation variables σ_n to each site n of a crystal. When a site can be occupied by either a Li or a vacancy, the value of σ_n is 1 or -1, respectively. The collection of occupation variables can be assembled into a vector $\overrightarrow{\sigma}$=(σ_0,...,σ_n,...,σ_N), where N is the maximum number of sites in consideration.

The configurational energy of a binary solid can be written as an expansion in terms of crystal basis functions $\Phi_\alpha(\vec{\sigma})$ multiplied by expansion coefficients, referred to as effective cluster interactions, V_α, according to [66]

$$E(\vec{\sigma}) = V_0 + \sum_\alpha V_\alpha \Phi_\alpha(\vec{\sigma}) \tag{2.37}$$

For a binary system, the crystal basis functions are simply products of occupation variables belonging to sites of different clusters, labeled α, according to [66]

$$\Phi_\alpha(\vec{\sigma}) = \prod_{n\in\alpha} \sigma_n \tag{2.38}$$

The index α extends over all possible clusters of sites within the crystal.

The symmetry of the crystal can be used as a means to reduce the number of independent expansion coefficients. Specifically, the effective cluster interaction coefficients corresponding to clusters that map onto one another through application of a space group operation are equivalent. All clusters of a particular type that are equivalent by symmetry can be collected in an orbit labeled Ω_α, where α represents a prototype cluster. All effective cluster interaction coefficients within the same orbit have the same value. When symmetry is taken into account, the cluster expansion can be rewritten as

$$E(\vec{\sigma}) = V_0 + \sum_{\Omega_\alpha} V_\alpha \Big(\sum_{\beta\in\Omega_\alpha} \Phi_\beta(\vec{\sigma}) \Big) \tag{2.39}$$

where the outer sum extends over orbits of distinct cluster types and β of the inner sum indexes all clusters within a particular orbit, Ω_α. The energy can next be normalized by dividing by the number of unit cells, N_{unit}, yielding

$$e(\vec{\sigma}) = \frac{E(\vec{\sigma})}{N_{unit}} = \frac{V_0}{N_{unit}} + \sum_{\Omega_\alpha} m_\alpha V_\alpha \frac{\sum_{\beta\in\Omega_\alpha} \Phi_\beta(\vec{\sigma})}{m_\alpha N_{unit}} \tag{2.40}$$

where m_α is the multiplicity of symmetrically equivalent clusters per unit cell. By defining correlation functions $\xi_\alpha(\vec{\sigma})$ as the average over all crystal basis functions belonging to

the same orbit according to

$$\xi_\alpha(\vec{\sigma}) = \frac{1}{N_{unit} m_\alpha} \sum_{\beta \in \Omega_\alpha} \Phi_\beta(\vec{\sigma}) \tag{2.41}$$

Equation 2.40 can be rewritten as

$$e(\vec{\sigma}) = \frac{E(\vec{\sigma})}{N_{unit}} = \frac{V_0}{N_{unit}} + \sum_{\Omega_\alpha} m_\alpha V_\alpha \xi_\alpha(\vec{\sigma}) \tag{2.42}$$

In this form, the expansion coefficients of a truncated cluster expansion can be determined with conventional regression techniques given first-principles energies of $N_{orderings}$ ordered configurations.

2.3 Electrochemical derivations

The Gibbs free energy of a battery can be derived from the free energy of the phases in components of a battery through the relation [2]

$$G^{total} = G^e(N^e_{Li^+}) + G^a(N^a_{Li^+}, N^a_{e^-}) + G^c(N^c_{Li^+}, N^c_{e^-}) \tag{2.43}$$

where the Gibbs free energies of the cathode, $G^c(N^c_{Li^+}, N^c_{e^-})$, anode, $G^a(N^a_{Li^+}, N^a_{e^-})$ and electrolyte, $G^e(N^e_{Li^+})$ are dependent on the concentration of charged species, lithium ions and electrons. The Gibbs free energy of the electrodes involve both electrons and lithium ions since effective electrodes require both movement of ions and electrons. The Gibbs free energy of the electrolyte can be approximated to be dependent on only lithium since effective electrolytes will conduct only lithium ions and note electrons.

The electrochemical potential describes the dependence of the Gibbs free energy on the change in composition of the lithium ions and electrons. The electrochemical potential

of lithium in the cathode, for example, can be calculated through

$$\eta^c_{Li^+} = \frac{\partial G^c}{\partial N^c_{Li^+}} \tag{2.44}$$

while the electrochemical potential of the electron in the cathode can be calculated through

$$\eta^c_{e^-} = \frac{\partial G^c}{\partial N^c_{e^-}} \tag{2.45}$$

Likewise the electrochemical potential with respect to lithium and electrons in the anode can be determined through the same set of equations.

$$\eta^a_{Li^+} = \frac{\partial G^a}{\partial N^a_{Li^+}} \tag{2.46}$$

$$\eta^a_{e^-} = \frac{\partial G^a}{\partial N^a_{e^-}} \tag{2.47}$$

For the electrolyte, we only need to calculate the chemical potential with respect to lithium through

$$\eta^e_{Li^+} = \frac{\partial G^e}{\partial N^e_{Li^+}} \tag{2.48}$$

The open circuit voltage, the potential between the cathode and anode, when all cell components are at equilibrium. The voltage can be described with the above relations through the Nernst equation

$$V = \frac{\eta^a_{e^-} - \eta^c_{e^-}}{e} = -\frac{\eta^c_{e^-} - \eta^a_{e^-}}{e} \tag{2.49}$$

where e is the charge of one electron.

We can relate the chemical potential of lithium in the electrodes to the electrochemical potential of the individual lithium-ions and electrons involved in the redox process. The

chemical potential of a neutral ion in a phase β can also be determined by taking the derivative of the Gibbs free energy.

$$\mu_{Li}^{\beta} = \frac{\partial G^{\beta}}{\partial N_{Li}^{\beta}} \tag{2.50}$$

where μ_{Li}^{β} denotes the change in the Gibbs free energy of phase β with a change of neutral Li atoms in that electrode, N_{Li}^{β}. This relationship can be expanded through the chain rule as

$$\mu_{Li}^{\beta} = \frac{\partial G^{\beta}}{\partial N_{Li^+}^{\beta}} \frac{\partial N_{Li^+}^{\beta}}{\partial N_{Li}^{\beta}} + \frac{\partial G^{\beta}}{\partial N_{e^-}^{\beta}} \frac{\partial N_{e^-}^{\beta}}{\partial N_{Li}^{\beta}} \tag{2.51}$$

Since neutral Li atoms are produced by the reduction of one lithium-ion by one electron, this can be written as

$$\mu_{Li}^{\beta} = \eta_{Li^+}^{\beta} + \eta_{e^-}^{\beta} \tag{2.52}$$

since the change of the number of lithium ions is equivalent to the change in the number of lithium atoms. The change in the number of electrons would also be equivalent to the change in the number of lithium atoms.

This definition of the chemical potential can be used in the Nernst equation to define the relationship between the voltage and chemical potential. We begin with the definition of the voltage in an electrochemical cell [70]

$$V = -\frac{\eta_{e^-}^{c} - \eta_{e^-}^{a}}{e} = -\frac{\mu_{Li}^{c} - \eta_{Li^+}^{c} - \mu_{Li}^{a} + -\eta_{Li^+}^{a}}{e} \tag{2.53}$$

At equilibrium, the electrochemical potential of lithium ions in the anode, cathode, and electrolyte are equivalent, which gives us the Nernst relation

$$V = -\frac{\mu_{Li}^{c} - \mu_{Li}^{a}}{e} \tag{2.54}$$

Through this equation it can be inferred that the voltage at equilibrium can be calculated through the chemical potentials in the cathode and anode.

2.4 Entropy derivations

2.4.1 Relating voltage to entropy: an overview

The open-circuit voltage that is measured for an electrochemical system carries with it information of the chemical potential. They are related through the Nernst equation. In general terms, for a battery, the Nernst equation can be written as

$$V = -\frac{\eta_{e^-}^{cat} - \eta_{e^-}^{an}}{e} \tag{2.55}$$

where $\eta_{e^-}^{cat}$ and $\eta_{e^-}^{an}$ are the electrochemical potentials or electrons in the cathode and anode, respectively. At equilibrium conditions this voltage can instead be related to chemical potentials in the anode and the cathode through

$$V^{eq} = -\frac{\mu_{Li}^{cat} - \mu_{Li}^{an}}{e} \tag{2.56}$$

Where μ_{Li}^{cat} and μ_{Li}^{an} are the chemical potentials of lithium ions in the cathode and anode [70].

Information on the entropy of a system undergoing an intercalation reaction can be acquired by it's connection to the chemical potential. The Gibbs free energy is a thermodynamic potential that determines the maximum amount of reversible work that can be be accessed at constant temperature and pressure conditions [71]. The differential form of this function has temperature (T), pressure (P), and number of atoms or molecules

(N) as the independent variables

$$dG = -SdT + VdP + \sum_i \mu_i dN_i \tag{2.57}$$

where V is the volume and μ_i is the chemical potential of each particular atom or molecule. For an intercalation compound where the intercalant is lithium, this can be simplified to

$$dG = -SdT + VdP + \mu_{Li} dN_{Li} + \mu_{MA} dN_{MA} \tag{2.58}$$

where μ_{MA} refers to the chemical potential of the host material and dN_{MA} refers to the change in the number of atoms of the host material.

In an intercalation compound, the number of host atoms should not change, therefore the equation can be further simplified to

$$dG = -SdT + VdP + \mu_{Li} dN_{Li} \tag{2.59}$$

When two thermodynamic variables can be equated through a second derivative of a thermodynamic potential, these variables can be related through a Maxwell relation [72]. Starting with the Gibbs free energy as the thermodynamic potential, one can show that

$$\frac{\partial^2 G}{\partial N \partial T} = \frac{\partial}{\partial N}\left[\left(\frac{\partial G}{\partial T}\right)_{N,P}\right]_{T,P} = \frac{\partial}{\partial T}\left[\left(\frac{\partial G}{\partial N}\right)_{T,P}\right]_{N,P} \tag{2.60}$$

where G, N, T, P are the Gibbs free energy, number of atoms, temperature, and pressure for the system in question.

From the Gibbs free energy equation (Equation 2.59), we can determine the terms

inside the bracket. One may notice the equivalence of the first term to entropy

$$\left(\frac{\partial G}{\partial T}\right)_{N,P} = -S \tag{2.61}$$

and of the equivalence of the second term to the chemical potential of lithium-ions in the electrodes. This can thus be written as

$$\left(\frac{\partial G}{\partial N}\right)_{T,P} = \mu_{Li} \tag{2.62}$$

The molar entropy ($\overline{S_{Li}}$) can therefore be related to the chemical potential of lithium-ions in the electrodes through

$$-\overline{S_{Li}} = -\left[\frac{\partial S}{\partial N}\right]_{P,T} = \left[\frac{\partial \mu_{Li}}{\partial T}\right]_{P,N} \tag{2.63}$$

where the final term shows that the change in chemical potential with lithium with changing temperature gives information on the molar entropy of lithium in the system. Therefore thermodynamic information about the system is accessible through potentiostatic measurements, as long as a change in temperature can be induced in the system while holding pressure and number of ions fixed.

Our collaborators use this relation to provide accurate measurements of the entropy in the electrodes. In their experiments, a coin cell is placed on to a cold plate where the temperature can be varied. The chemical potential between the ends of the coin cells are then measured through the use of a potentiostat. By changing the temperature and measuring the change in voltage at constant compositions, our collaborators are able to acquire the difference in the partial molar entropy between the cathode and the anode. This is because, as shown previously, the voltage can be calculated from the chemical potentials in the electrodes.

2.4.2 Entropy measurements in battery materials

One can begin a full derivation for attaining entropic information for a battery through its voltage by beginning at the cathode

$$-\overline{S_{Li}} = -\left[\frac{\partial S^{cat}}{\partial N}\right]_{P,T} = \left[\frac{\partial \mu_{Li}^{cat}}{\partial T}\right]_{P,N} \tag{2.64}$$

where S^{cat} and μ_{Li}^{cat} is specifically the entropy and chemical potential of lithium at the cathode.

The chemical potential can be written as a function of the open circuit voltage and the chemical potential at the anode as

$$\mu_{Li}^{cat} = -(V^{eq}e - \mu_{Li}^{an}) \tag{2.65}$$

where μ_{Li}^{an} is the chemical potential of lithium at the anode. This equality can be added to Equation 2.64 to attain

$$-\overline{S_{Li}} = -\left[\frac{\partial S^{cat}}{\partial N}\right]_{P,T} = \left[\frac{\partial(-V^{eq}e - \mu_{Li}^{an})}{\partial T}\right]_{P,N} \tag{2.66}$$

One can put this in fractional coordinates by dividing by the total number of lithium. We attain

$$-\left[\frac{\partial S^{cat}}{M\partial x}\right]_{P,T} = \left[\frac{\partial(-V^{eq}e - \mu_{Li}^{an})}{\partial T}\right]_{P,x} \tag{2.67}$$

where M is the total number of lithium-ions.

If one is using a pure lithium counter-anode then the chemical potential at the anode should not change conceivably with temperature and we can simplify to

$$-\left[\frac{\partial S^{cat}}{M\partial x}\right]_{P,T} = \left[-e\frac{\partial(V^{eq})}{\partial T}\right]_{P,x} - \frac{\partial \mu_{Li}^{an}}{\partial T} \tag{2.68}$$

The last term in Equation 2.68 can be recognized as the entropy at the anode, therefore equation can be further simplified to

$$-\left[\frac{\partial S^{cat}}{M\partial x}\right]_{P,T} = \left[-e\frac{\partial(V^{eq})}{\partial T}\right]_{P,x} + s_{Li}^{an} \tag{2.69}$$

where s_{Li}^{an} is the entropy of the anode.

We can integrate to find the total entropy of the lithium in the cathode:

$$-\frac{S^{cat}}{M} = -e\int_0^x \left[\frac{\partial(V^{eq})}{\partial T}\right]_{P,x} dx + \int_0^x s_{Li}^{an} dx \tag{2.70}$$

Carrying out the integration gives the following simplified expression

$$-\frac{S^{cat}}{M} = -e\int_0^x \left[\frac{\partial(V^{eq})}{\partial T}\right]_{P,x} dx + x s_{Li}^{an} \tag{2.71}$$

where s_{Li}^{an} is a tabulated value acquired through NIST. At standard temperature and pressure (298.15K and 0.1MPa), the entropy for solid lithium is $29.085\frac{J}{molK}$ [73].

2.5 Symmetry adapted collective displacement modes

2.5.1 Analysis of octahedral deformations

Quantification of polyhedral distortions over different structures allows a cohesive understanding of which distortions lead to phase stability. Specifically, examining distortions within octahedra in the Wadsley-Roth phase crystal structures allows for an assessment of the extent distortions are affected by the topology of the crystal structure and whether these distortions play a role in determining which Wadsley-Roth structures are stable. In order to perform this examination, displacement modes specific to the sym-

metry of an ideal octahedron must be defined. These modes are vectors that describe collective displacements of the constituent atoms within the octahedron.

The transition metals ions that are components of the Wadsley-Roth phases are generally in their maximum oxidation state. Transition metal cations, such as W^{6+} and Nb^{5+}, have empty d-orbitals that make the cations susceptible to second-order Jahn-Teller distortions when octahedrally coordinated by oxygen [74, 75, 76, 77, 78]. The empty d-orbital can cause an energetically favorable interaction between the strong central charge of the d^0 cation and the surrounding anions that induces a perturbation away from the centrosymmetric state. This tendency can result in a displacement of the central cation as well as deformations of the octahedrally coordinated oxygen environments.

An MO_6 octahedron constitutes six oxygen ions coordinating a central ion, generally a transition metal cation, M [79]. The orientation, position, and deformation state of the octahedron can be described by $7 \times 3 = 21$ displacement degrees of freedom. Three degrees of freedom describe a rigid rotation of the octahedron. An additional three degrees of freedom describe a rigid translation of the octahedron. These six modes do not give information for how the octahedron distorts. The remaining $21 - 6 = 15$ degrees of freedom describe the extent of distortions of the octahedron relative to an ideal reference octahedron.

For complete definitions of distortion modes, distortions are quantified through symmetry adapted collective displacements of the atoms of an ideal octahedron. These symmetry adapted displacement modes are the decomposition of a distortion into a linear combination of different group and subgroup symmetry breaking collective distortions [80], specific to the point group of an octahedrally coordinated cluster of atoms. As an example, Figure 2.2 shows fifteen displacement modes of an octahedron divided into six irreducible subspaces according to the octahedral cubic point group. These modes can be further divided into one one-dimensional, one two-dimensional, and four three-

dimensional irreducible subspaces.

Before the distortions of a cluster of atoms can be quantified, it is first necessary to remove the rigid translations and rigid rotations of the distorted cluster relative to an ideal reference cluster. Any rigid translation can be removed by placing the geometric center of mass of the distorted and reference cluster at the origin of the Cartesian coordinate system.

The atomic coordinates of an N-site distorted cluster can be collected into a $3 \times N$ matrix $\mathbf{R} = [\vec{r}_1, \ldots, \vec{r}_N]$. Each $\vec{r}_i$ is a column vector of the Cartesian coordinates of the atom at site i. Similarly, the coordinates of the atoms of an ideal, high-symmetry N-site reference cluster can be described in the $3 \times N$ matrix $\mathbf{R_0} = [\vec{r}_1^{\,0}, \ldots, \vec{r}_N^{\,0}]$. Likewise, each $\vec{r}_i^{\,0}$ is a column vector in Cartesian space of the atom at site i. The coordinates of the distorted cluster can be related to those of the reference cluster according to

$$\mathbf{R} = \mathbf{U}(\mathbf{R}_0 + \mathbf{D}) \tag{2.72}$$

where $\mathbf{U}$ is a 3×3 rotation matrix. The $3 \times N$ matrix $\mathbf{D}$ describes the displacement of the atoms from the reference atomic positions. It can be written as $\mathbf{D}$=[$\vec{d}_1$, ..., $\vec{d}_N$] where $\vec{d}_i$ is a column vector that describes the displacement of each atom at each site, i. Equation 2.72 shows that the distorted cluster is obtained by first displacing each atom of the reference cluster at position $\vec{r}_i^{\,0}$ by the vector $\vec{d}_i$ and then rotating the distorted cluster with the rotation matrix $\mathbf{U}$ to generate the coordinate $\vec{r}_i$. The rotation matrix is unitary such that $\mathbf{U}^{-1} = \mathbf{U}^{\mathsf{T}}$, thus preserving lengths and angles.

The order of the atoms in the distorted cluster relative to the reference cluster described in the matrices $\mathbf{R}$ and $\mathbf{R_0}$ determines the rotation matrix, $\mathbf{U}$, and displacement matrix, $\mathbf{D}$. The Hungarian algorithm is a method used for optimally assigning atomic positions of the distorted polyhedron [81] relative to the reference polyhedron. Specif-

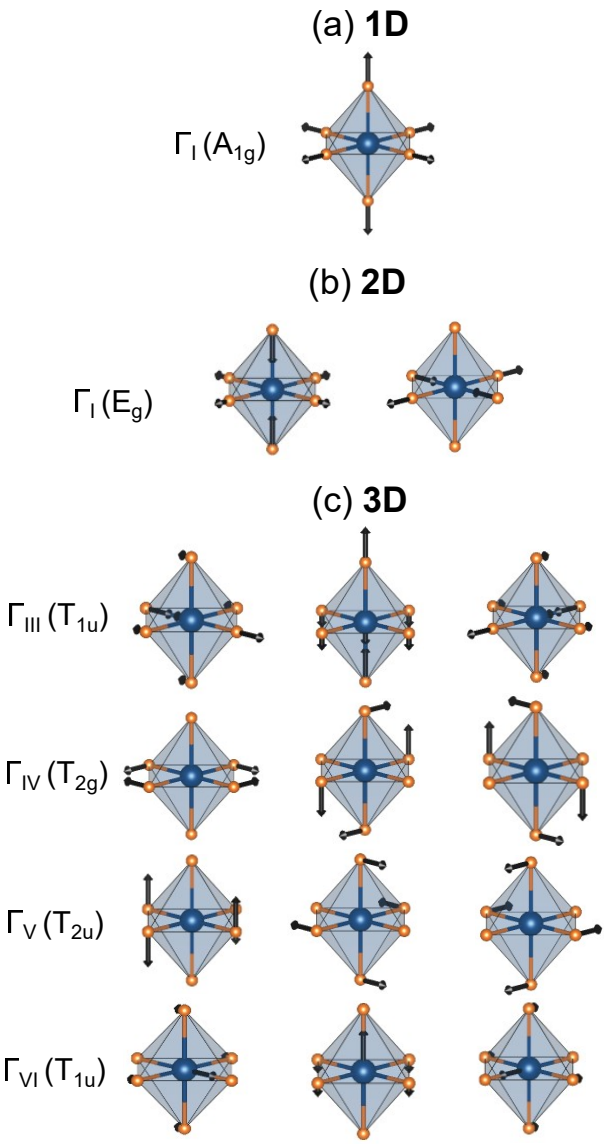

Figure 2.2: Symmetry adapted collective displacements for an octahedron with seven atoms, one central cation and six coordinating anions. These are grouped into (a) one one-dimensional irrep corresponding to volumetric distortions of point point group A_{1g}, (b) one two-dimensional irrep corresponding to tetragonal distortions of point group E_g, (c) four three-dimensional irreps corresponding to two T_{1u} distortions, one T_{2g} distortion and one T_{2u} distortion.

ically, an assignment of atoms from the distorted polyhedron to those of the reference polyhedron must be chosen to minimize the displacements at each site. The Hungarian algorithm is applied before the optimal rotation matrix, $\mathbf{U}$, can be calculated.

After the Hungarian algorithm is applied, the rotation matrix, $\mathbf{U}$, is chosen such that multiplying the matrix onto the distorted cluster minimizes the root mean square displacements between the distorted and the reference cluster according to

$$\sum_{i=1}^{N} |\vec{d}_i|^2 = \sum_{i=1}^{N} |\mathbf{U}^{\mathsf{T}} \vec{r}_i - \vec{r}_i^{\,0}|^2 \tag{2.73}$$

where the $\vec{d}_i$ are the columns of $\mathbf{D}$. $|\vec{d}_i|$ is the length of the vector $\vec{d}_i$. The Kabsch algorithm [82, 83, 84] can be used to find the rotation matrix $\mathbf{U}$ that minimizes Eq. 2.73. The derivation of the Kabsch algorithm can be found in Subsection 2.5.2. The displacements matrix, $\mathbf{D}$, as defined by Eq. 2.72, thus describes the deformation state of the distorted cluster relative to the reference high-symmetry cluster. These displacements can then be decomposed into a linear combination of symmetry adapted collective displacements.

To decompose the distorted state of a cluster of sites in terms of symmetry adapted collective displacements, it necessary to unroll the $3 \times N$ matrix of displacements $\mathbf{D}$ into a $3N$ vector, $\vec{D}^{\mathsf{T}}$. The symmetry adapted collective displacements can be described within the vectors $\vec{q}_j$ with a length of $3N$ where j indexes over the symmetry adapted collective displacements. There are a total of $3N - 6$ symmetry adapted collective displacements that describe deformations. These are orthogonal to the three collective displacements that describe a rigid translation of the cluster and the three collective displacements that describe infinitesimal rotations of the reference cluster. The displacements of the distorted cluster's atomic positions can therefore be expressed as a linear combination of

the $3N-6$ symmetry adapted collective modes according to

$$\vec{D} = \sum_{j=1}^{3N-6} \alpha_j \vec{q_j} \tag{2.74}$$

where the coefficients α_j are the amplitudes of each symmetry adapted collective displacement, $\vec{q_j}$. The symmetry adapted collective modes are constructed from group theoretical techniques [85]. Those shown in Figure 2.2 were generated algorithmically as described in Thomas and Van der Ven [86]. In our analysis of the octahedral distortions in Wadsley-Roth phases, we project the displacements as collected in the 21-dimensional column vector $\vec{D}$ onto the 15 symmetry adapted collective modes, $\vec{q}_1, \ldots, \vec{q}_{15}$, shown in Figure 2.2.

The symmetry adapted collective displacements, $\vec{q_j}$, fall into different irreducible subspaces, but all symmetrically equivalent distortions reside within the same irrep. This concept is illustrated in Figure 2.3 for the E_g irrep of the octahedron spanned by $\vec{q}_2$ and $\vec{q}_3$. In this figure, the coordinates are the amplitudes α_j appearing in Eq. 2.74. The points and lines having the same color represent symmetrically equivalent distortions of the octahedron according to the cubic point group of the reference octahedron.

The first irreducible subspace (irrep) for the octahedron ($\vec{q}_1$), shown in Figure 2.2(a), spans a one-dimensional subspace of the 15-dimensional space of displacement degrees of freedom. This mode describes the symmetry preserving volumetric distortions of an octahedron. The second irrep constructed from the reference octahedron ($\vec{q}_2$, $\vec{q}_3$), (Figure 2.2(b)), spans a two-dimensional subspace. These modes describe tetragonal and orthorhombic distortions of the cubic reference octahedron. More precisely, these symmetry adapted collective displacements correspond to the first-order Jahn-Teller distortions of the octahedron, a distortion induced by a system to relieve orbital degeneracy. There are an additional four irreps of symmetry adapted collective modes, each of dimension

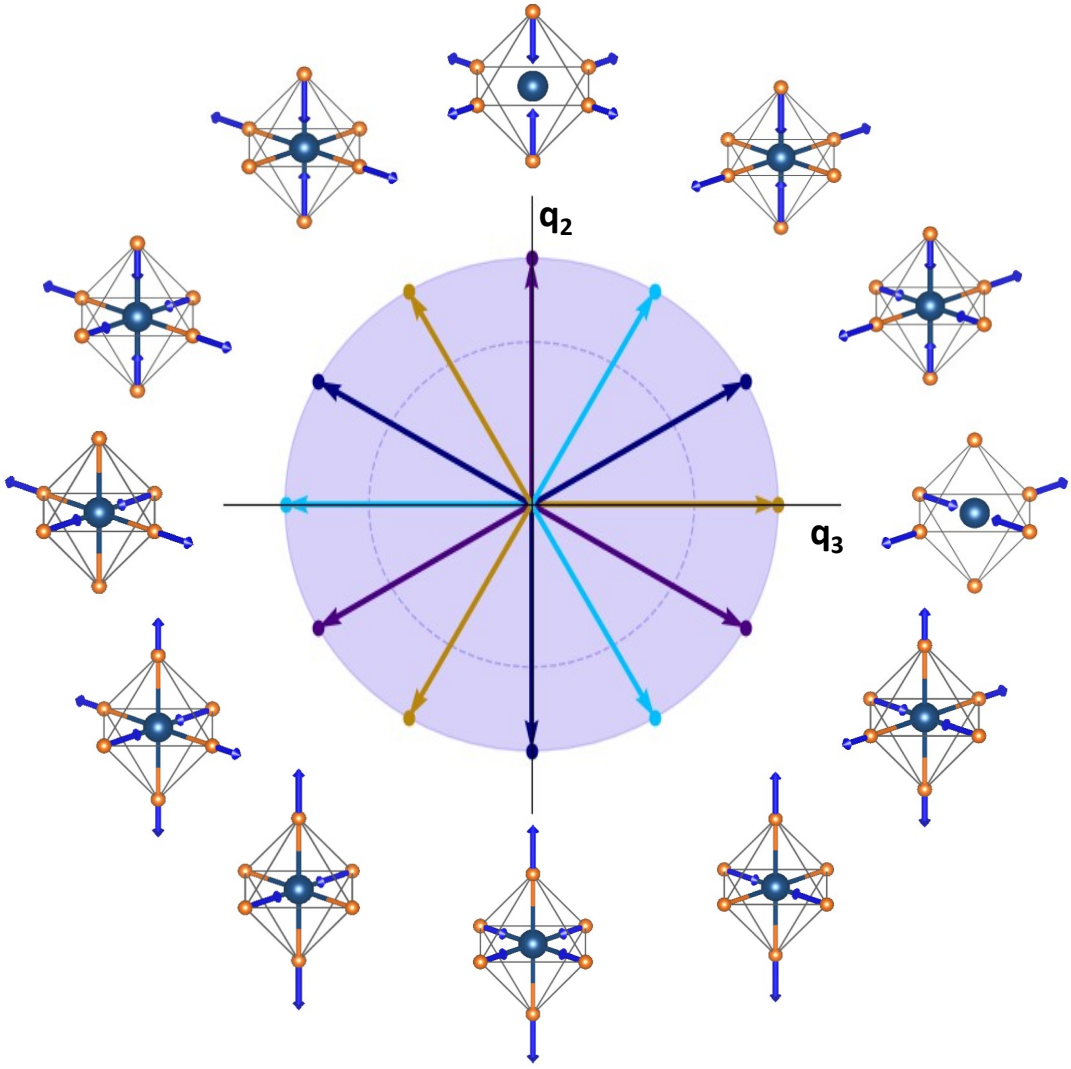

Figure 2.3: Representation of the norm of the two dimensional $\Gamma_{II}(E_g)$ irrep.

three, which are collected in Figure 2.2(c). These encompass modes $\vec{q}_4, \ldots, \vec{q}_{15}$.

The collection of amplitudes, α_j, of a distortion within a two or three-dimensional irreducible subspace forms a vector in that space. While the full vector of amplitudes within any given irrep is necessary to construct the precise symmetry breaking distortion allowed by that irrep, it is often sufficient to simply track whether a particular irrep is prominent in a distorted cluster. This can be assessed by calculating the length of the amplitude vector within each irrep. The Euclidean norm within each irrep takes the form

$$\gamma_i = \sqrt{\sum_{j \in \Gamma_i} \alpha_j^2} \tag{2.75}$$

where γ_i is the length of the amplitudes in irrep Γ_i and where the sum extends over all the amplitudes α_j within the irrep (i.e. $j \in \Gamma_i$). Through the calculation of the Euclidean norm, an accurate summation of all symmetrically equivalent contributions within a particular irrep on the distortions can be quantified. This magnitude can be compared between polyhedra in the same structure, to determine which irreps play a stronger role in distortions due to local chemical connectivity differences. Additionally, this magnitude can be used to compare the components of distortions in different structures with the same polyhedra type. As a result, this method allows for accurate quantification of distortion differences across distinct crystal structures and Wadsley-Roth phases with differing symmetries.

2.5.2 Kabsch Algorithm Derivation

We begin our determination of the 3×3 rotation matrix $\mathbf{U}$ with the defining equation, Eq. 2.73. The optimal rotation matrix is the one that gives the lowest root mean square displacement between the rotated cluster of atoms and the reference cluster [82, 84, 83]. To find the matrix $\mathbf{U}$ that minimizes Eq. 2.73, Eq. 2.73 can be rewritten according to

$\sum_{i=1}^{N} \mathbf{U}^T \vec{r}_i$ and $\sum_{i=1}^{N} \vec{r}_i^0$ as a trace of the corresponding $3 \times N$ matrix representations, $\mathbf{R}$ and $\mathbf{R_0}$. We first define a quantity $\mathbf{Q}$ where $\mathbf{Q} = \mathbf{U}^T$ This can be written as

$$\sum_{i=1}^{N} |\vec{d}_i|^2 = Tr[(\mathbf{QR} - \mathbf{R_0})^T(\mathbf{QR} - \mathbf{R_0})] \tag{2.76}$$

This equation can be further simplified through multiplication of the terms within the trace

$$\sum_{i=1}^{N} |\vec{d}_i|^2 = Tr[(\mathbf{R}^T\mathbf{Q}^T\mathbf{QR}) - (\mathbf{R_0}^T\mathbf{QR}) - (\mathbf{R}^T\mathbf{Q}^T\mathbf{R_0}) + (\mathbf{R_0}^T\mathbf{R_0})] \tag{2.77}$$

Since the trace of multiple components is a linear mapping, additivity is allowed. The trace can be rewritten as

$$\sum_{i=1}^{N} |\vec{d}_i|^2 = Tr[(\mathbf{R}^T\mathbf{Q}^T\mathbf{QR})] - Tr[(\mathbf{R_0}^T\mathbf{QR})] - Tr[(\mathbf{R}^T\mathbf{Q}^T\mathbf{R_0})] + Tr[(\mathbf{R_0}^T\mathbf{R_0})] \tag{2.78}$$

using the matrix relations $Tr[AB] = Tr[BA]$ and $Tr[A] = Tr[A^T]$, the relation can be further simplified to

$$\begin{aligned}\sum_{i=1}^{N} |\vec{d}_i|^2 &= Tr[(\mathbf{R}^T\mathbf{Q}^T\mathbf{QR})] - Tr[(\mathbf{R_0}^T\mathbf{QR})] - Tr[(\mathbf{R_0}^T\mathbf{QR})] + Tr[(\mathbf{R_0}^T\mathbf{R_0})] \\ &= Tr[(\mathbf{R}^T\mathbf{Q}^T\mathbf{QR})] + Tr[(\mathbf{R_0}^T\mathbf{R_0})] - 2Tr[(\mathbf{R_0}^T\mathbf{QR})]\end{aligned}$$

where the term $Tr[(\mathbf{R}^T\mathbf{Q}^T\mathbf{QR})]$ is equivalent to the length of the vectors of the positions of the rotated cluster of atoms, $\sum_{i=1}^{N} |\mathbf{Q}\vec{r}_i|^2$. It is important to note that $\mathbf{Q}^T\mathbf{Q} = I$ where I is a 3×3 identity matrix. Therefore $Tr[(\mathbf{R}^T\mathbf{Q}^T\mathbf{QR})] = Tr[\mathbf{R}^T\mathbf{R}]$ which in turn is independent of $\mathbf{Q}$. The term $Tr[(\mathbf{R_0}^T\mathbf{R_0})]$ gives the length of the positions of the

reference atomic positions, $\sum_{i=1}^{N} |\vec{r}_i^0|^2$. These terms are not dependent on the rotation matrix, $\mathbf{Q}$, and therefore are constants with respect to $\mathbf{Q}$. Minimization of the squared distance of the atomic displacements therefore requires maximization of $Tr[(\mathbf{R_0}^T\mathbf{QR})]$. We can decompose this term using singular value decomposition (SVD). To effectively perform the SVD, we must rearrange the matrices. Using the cyclic property of matrices, we can rewrite $Tr[(\mathbf{R_0}^T\mathbf{QR})]$ such that

$$Tr[(\mathbf{R_0}^T\mathbf{QR})] = Tr[\mathbf{RR_0}^T\mathbf{Q}] \tag{2.79}$$

The terms $\mathbf{RR_0}^T$ can be decomposed into three geometrical transformations: $\mathbf{V}$, $\mathbf{S}$, and $\mathbf{W}$. Specifically,$\mathbf{RR_0}^T$ can be decomposed into $\mathbf{VSW}^T$. The 3×3 matrix, $\mathbf{W}^T$, describes an initial rotation. $\mathbf{S}$, a 3×3 matrix that contains the singular values which scales the coordinates along these rotated vectors. $\mathbf{V}$ is a 3×3 matrix that describes a final rotation after the vectors have been scaled. The trace of the covariance matrix, $\mathbf{RR_0}^T$, can be written as

$$\begin{aligned} Tr[\mathbf{RR_0}^T\mathbf{Q}] &= Tr[\mathbf{VSW}^T\mathbf{Q}] \\ &= Tr[\mathbf{SW}^T\mathbf{QV}] \end{aligned}$$

where the columns of $\mathbf{W}^T$ and $\mathbf{V}$ are orthonormal basis vectors for the subspaces occupied by the atomic positions of the cluster of atoms and the atomic positions of the reference cluster of atoms. This can be rewritten as

$$Tr[\mathbf{SW}^T\mathbf{QV}] = Tr[\mathbf{S}\xi] \tag{2.80}$$

where ξ is an orthonormal matrix equivalent to $\mathbf{W}^T\mathbf{QV}$. Since ξ is orthonormal it may have a determinant of -1 or +1 and $Tr[\mathbf{S}\xi]$ is maximized when the determinant of ξ is

+1. Therefore we can set ξ equivalent to identity and we get the relation

$$\mathbf{W}^T\mathbf{Q}\mathbf{V} = \mathbf{I} \tag{2.81}$$

Therefore the optimal rotation matrix can then be written as

$$\mathbf{Q} = \mathbf{W}\mathbf{V}^T \tag{2.82}$$

This is the equation for the optimal rotation matrix of the chirality if the coordinate system is not to be considered. The last step is to ensure that the coordinate system is right-handed. To prevent improper rotations to be included as potential optimal rotation matrices, the determinant of $\mathbf{W}\mathbf{V}^T$ must be greater than 0.

Chapter 3

Wadsley-Roth phases

The Ti-Nb-O system is filled with a rich set of binary and ternary phases, many demonstrating promising properties for energy storage applications. In this section, we systematically determine the zero-K Ti-Nb-O ternary phase diagram from first principles and then study the driving forces for their stability. We focus on the Wadsley-Roth crystallographic shear phases, promising intercalation compounds for high power density battery electrodes. We find that Wadsley-Roth phases that minimize octahedral edge sharing are lower in energy. Also of importance is the ability of this structure to accommodate octahedral distortions. We quantify polyhedral distortion descriptors which show that while the distortions on TiO_6 and NbO_6 differ slightly, distortions are largely induced by the amount of octahedral edge sharing on a particular octahedron. We separate the effects of electrostatics and octahedral distortions on the phase stability of disordered orderings in the high power density lithium-ion battery anode material, $TiNb_2O_7$. Electrostatics cause TiO_6 octahedra to favor sites where they can share more edges; NbO_6 octahedra instead favor sites where they can share less edges. Despite this, the lowest energy ordering in $TiNb_2O_7$ is not the one that minimizes octahedral edge sharing on NbO_6 octahedra. Instead it is the ordering stabilized by distortions on the central nio-

bium induced by the broken symmetry of the neighboring metal cations. The balance between electrostatics and distortion on phase stability can likely be extended to other disordered Wadsley-Roth phases.

3.1 Introduction

The electrification of vehicles and high-power electronics requires the development of battery electrodes that can sustain fast charging rates and high power densities after many charging cycles. Early transition metal oxides have received much attention as candidates to replace the graphite anodes of current commercial batteries. The bronze-B polymorph of TiO_2 [87, 88, 89, 90, 91, 92] and spinel $Li_xTi_5O_{12}$,[93, 94, 95, 96] for example, can intercalate Li at voltages well above the Li plating potential, making them safer alternatives to graphite for high power applications. Several niobium oxides have also shown promising electrochemical properties that make them viable as anode materials of high power Li-ion batteries.[15, 97, 98] Multiple Nb_2O_5 polymorphs reversibly cycle lithium including TT-Nb_2O_5 [99, 100], T-Nb_2O_5 [101], monoclinic H-Nb_2O_5 [102, 103], and bronze Nb_2O_5 [104]. At an increased niobium composition, $Nb_{25}O_{62}$ shows high lithium intercalation capacity retention at rates of 10C [105]. With further increasing niobium composition, the monoclinic $Nb_{12}O_{29}$ structure demonstrates reversible cycling against lithium [106].

An especially promising class of materials to serve as high power anodes in Li-ion batteries are the Wadsley-Roth phases [107, 108]. Also referred to as crystallographic shear structures, the Wadsley-Roth phases are formed by early transition metal oxides and constitute a large family of open crystal structures that can intercalate Li at high rates. Their structures can accommodate Li over multiple redox couples and their crystallographic flexibility makes it possible to tune their structure through alloying. While

there are several Nb-oxides that form Wadsley-Roth phases [107, 108, 109, 110, 111, 112], many more have been synthesized by combining different early transition metals such as Nb, Ti, W and Mo [113, 20, 114, 115, 116, 21, 117, 22, 118, 119, 113, 120, 121]. For example, $TiNb_2O_7$, which has already been commercialized as an anode material, exhibits reversible capacities [93] up to 341mAh/g and high reversible charge rates [16, 19]. Other titanium-niobates such as $TiNb_{24}O_{62}$ [122] and $Ti_2Nb_{10}O_{29}$ [123] also exhibit high rate capabilities. Recent work by Griffith et al. [97], has demonstrated high rate capabilities in Wadsley-Roth phases containing different mixtures of Nb and W.

In this contribution, we investigate the structural diversity of Wadsley-Roth phases and identify chemical and crystallographic factors that determine phase stability among the many possible structural variants. We develop approaches to systematically enumerate Wadsley-Roth phases and extend the naming scheme proposed by Cava [15] to enable a more precise specification of each Wadsley-Roth crystal structure. We next explore the factors that make some Wadsley-Roth phases more preferable than others and find that the relative stability among different Wadsley-Roth crystal structures is to first order driven by a minimization of the number of edge-sharing octahedra. The varying flexibility of the metal-oxygen octahedra to undergo structural distortions in different Wadsley-Roth crystal structures is also found to play an important role in determining relative stability. To this end, we describe an approach to rigorously decompose octahedral distortions into a superposition of amplitudes of symmetry adapted collective displacement modes of an octahedron. This enables a rigorous analysis of the nature of octahedral distortions in structures with the crystallographic complexity of Wadsley-Roth phases. We also investigate the role of alloying over the cation sublattice of Wadsley-Roth phases with a particular focus on Ti and Nb. We find that cations with different oxidation states will arrange to reduce the fraction of high oxidation state cations that occupy edge-sharing octahedra. As a consequence, cations having low oxidation states

segregate to edge-sharing octahedra, while those with high oxidation states segregate to the corner sharing octahedra. Ordering tendencies among cations are also found to be affected by structural distortions of the octahedra.

3.2 Methods

3.2.1 First-principles electronic structure calculations

Density Functional Theory (DFT) calculations were performed with the Vienna ab initio simulation package (VASP) [124, 125, 126, 127]. The projector augmented wave (PAW) [128, 46] method was used to treat interactions between valence and core electrons. All calculations were performed within the generalized gradient approximation (GGA) as parameterized by Perdew, Burke, and Ernzerhof (PBE) [44]. Spin-polarized calculations were performed with a 575 eV plane wave energy cutoff and a Γ-centered k-point grid with a reciprocal space discretization of 45 K-points per Å^{-1} which were determined by performing an energy cutoff and k-point convergence to within 5 meV/atom. All structures were relaxed with respect to the lattice and atomic coordinates using a force convergence of 0.02 eV/Å and an energy convergence of 10^{-5} eV. Enumeration of symmetrically distinct configurations of titanium and niobium over the cation sites of different oxide Wadsley-Roth structures was performed using the Clusters Approach to Statistical Mechanics (CASM) [129, 130, 69, 131, 132] software package.

3.2.2 Analysis of octahedral deformations

The algorithm for obtaining octahedra from structures, octahedral rotations, and distortion amplitude analysis is given in Chapter 2.

3.3 Results

3.3.1 Wadsley-Roth Structural motifs

Wadsley-Roth block phases are transition metal oxide structures formed from transition metal octahedra. These octahedral units have anions, generally oxygen ions, at its vertices and metallic cations at their center. These octahedra are depicted in Figure 3.1(a). A multitude of differing block structures can be constructed. The most basic structure is one composed of $n \times m$ blocks repeating infinitely along the short axis. The octahedra at the edges of these blocks share edges with octahedra in its neighboring blocks such that the octahedra at the block's outer boundary. This creates an offset between the blocks that is one-half octahedra in length, in other words, the length between the central cation and the surrounding anion. This is shown parallel to the $\hat{x} - \hat{y}$ plane in Figure 3.1(b). This edge-sharing motif creates areas of crystallographic shear at the blocks out boundary that leads to consistent edge sharing along the short axis of the structure. The continuous connection of octahedral edge-sharing along the short axis (denoted the $\hat{z}$-axis) is shown in Figure 3.1(c).

Differences between Wadsley-Roth phases originate from the block sizes and the connectivity of the individual blocks. Figure 3.2(a) shows a Wadsley-Roth phase constructed from 4×4 blocks. To demonstrate a case where n and m differ, Figure 3.2(b) instead shows a 5×3. We can take the 5×3 structure and shift it either along the short edge of the block, in line with the $\hat{x}$-axis as shown in Figures 3.3(b) and 3.3(c) relative to the non shifted block (Figure 3.3(a)). The unit of the length from the oxygen on one side of an octahedron to the oxygen at the opposing side of the octahedron is called Δd. Alternatively, the blocks can be shifted relative to the long side of the block, which is in line with the $\hat{y}$-axis (Figures 3.3d-g).

To describe these phases, we extend the nomenclature that originates from Cava et

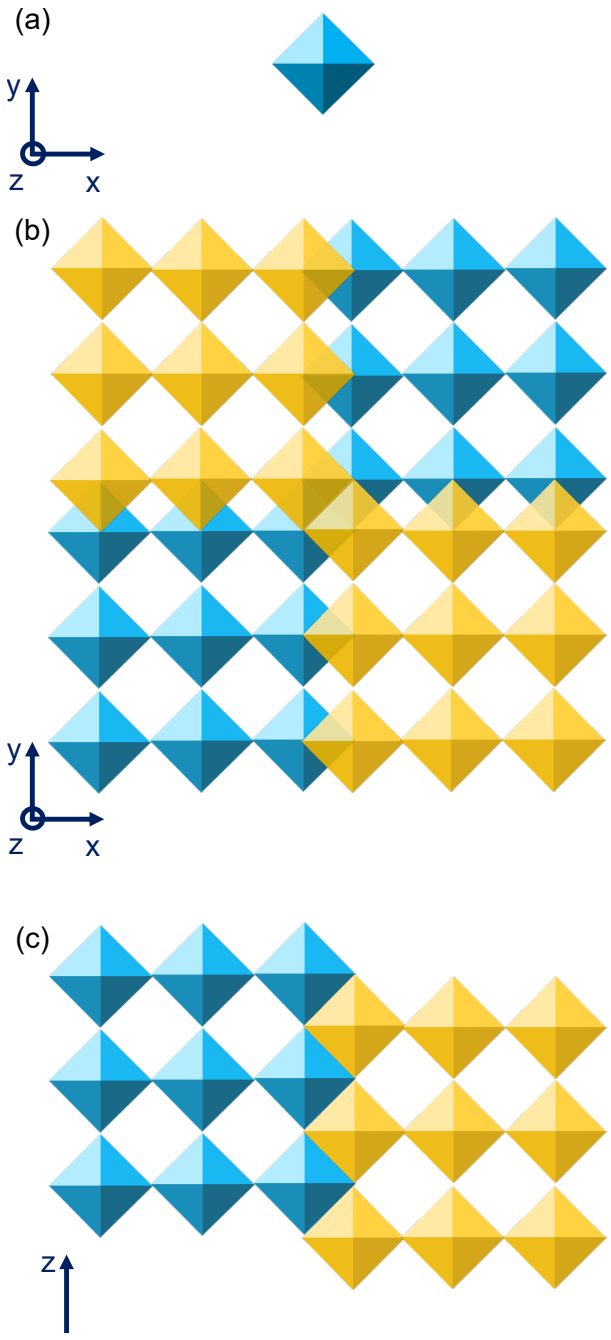

Figure 3.1: (a) Schematic of a transition metal octahedra. (b) An example 3×3 Wadsely-Roth structure as shown parallel to the $\hat{x} - \hat{y}$ plane. (c) An example of the 3×3 Wadsley-Roth phase parallel to the $\hat{x} - \hat{z}$ plane

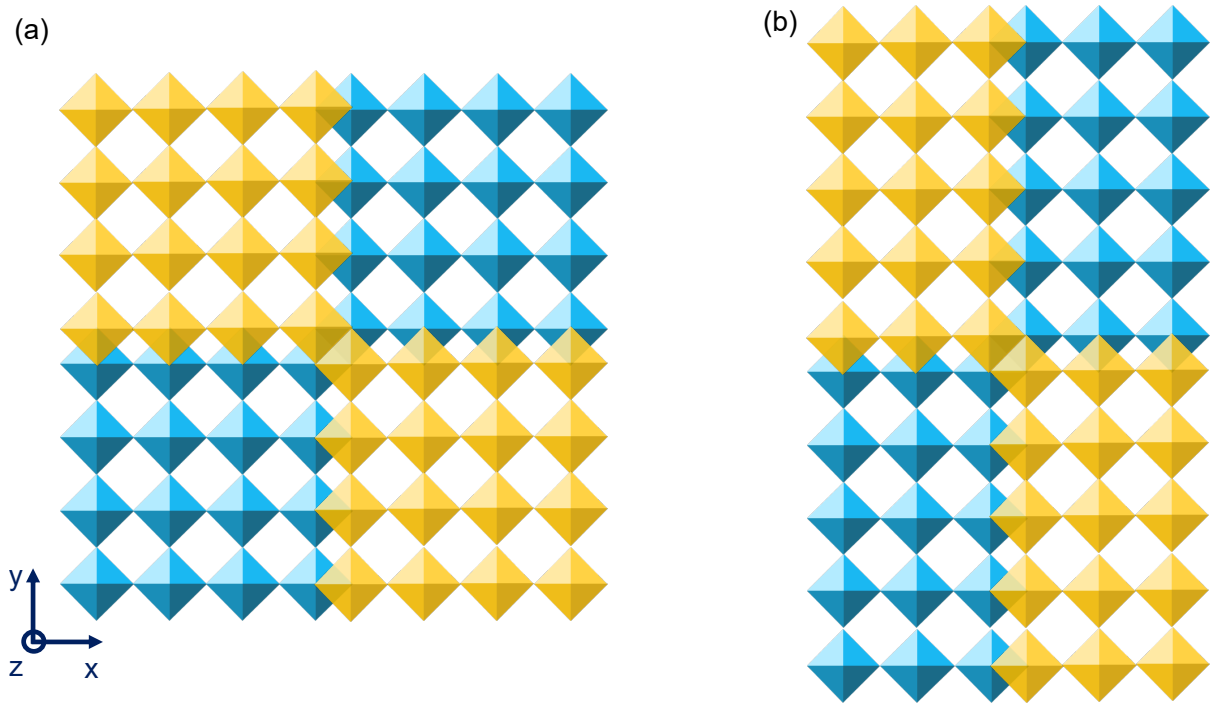

Figure 3.2: Wadsley-Roth phase constructed from 4×4 blocks (a) and 3×5 blocks (b).

al.[15] In Cava et al., phases are described by E, T, and M to denote Wadsley-Roth phases containing octahedral edge sharing alone, Wadsley-Roth phases containing tetrahedral sites, and extended Wadsley-Roth phases containing mixtures of these motifs.

We begin our expansion of this naming scheme with the type E Wadsley-Roth phases. The $n \times m$ blocks that make up Wadsley-Roth phases can be patterned such that the $n \times m$ block are in line with one another along both the $\hat{x}$ and the $\hat{y}$ directions. This phase (shown in Figure Figure 3.3(a)) is called an $E_0[3 \times 5]$. The blocks can be shifted along either the short direction (along $\hat{x}$) or the long axis (along $\hat{y}$). Phases shifted along either the $\hat{x}$ or the $\hat{y}$ direction can be described by $E_{ix,jy}[n \times m]$. The variable i is an integer value that dictates the number of octahedral lengths ($\Delta x = i * d$) that the blocks are shifted along the short axis. On the other hand, the j variable dictates the number of integer octahedral lengths that the blocks are shifted relative to one another along the long axis ($\Delta y = j * d$). Figure 3.3(a) shows an $E_0[3 \times 5]$ Wadsley-Roth phase.

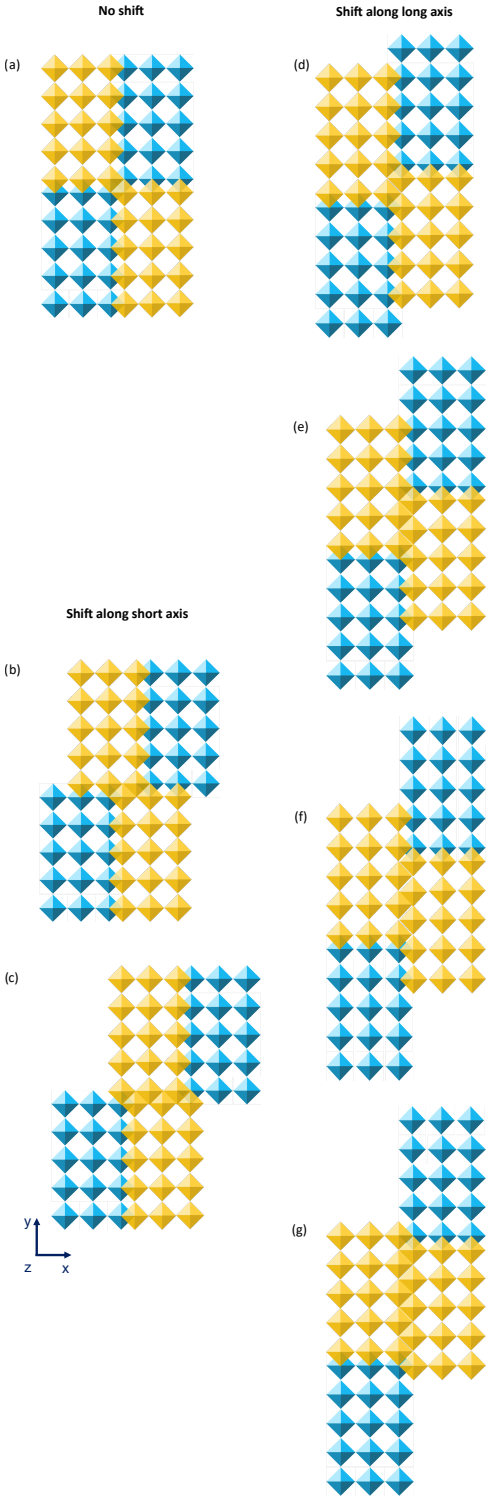

Figure 3.3: (a) A Wadsley-Roth phase constructed from no shift. Wadsley-Roth phases shifted along the short axis to shift a length of $\Delta x{=}d$ (b) and $\Delta x{=}2d$ (c) is shown. Additionally, Wadsley-Roth phases shifted along the long axis lengths of $\Delta y{=}d$ (d), $\Delta y{=}2d$ (e), $\Delta y{=}3d$ (f), and $\Delta y{=}4d$ (g).

Wadsley-Roth phases shifted along the short axis to produce $E_{1x}[3 \times 5]$ (Figure 3.3(b)) and $E_{2x}[3 \times 5]$ (Figure 3.3(c)) is shown. Additionally, Wadsley-Roth phases shifted along the long axis to produce $E_{1y}[3 \times 5]$ (Figure 3.3(d)), $E_{2y}[3 \times 5]$ (Figure 3.3(e)), $E_{3y}[3 \times 5]$ (Figure 3.3(f)), and $E_{4y}[3 \times 5]$ (Figure 3.3(g)) are shown.

For the E phases, only i or j can exhibit integer values, never both. If both variables are finite integer values, the phase is either a type T or M phase or it is not an experimentally known Wadsley-Roth phase. If i=1 and j=-1 (or alternatively if i=-1 and j=1), a vacancy opens up that can be filled with a tetrahedral site. Experimentally, this tetrahedral site has been filled with phosphorous, vanadium, tungsten, and a variety of other metal and non-metal species. This case is shown in Figure 3.4.

Experimentally, Wadsley-Roth phases with multiple shift types, block sizes, and block connectivities have been synthesized. Figures 3.5(a) and 3.5(b) are type "E" Wadsley Roth phases where one of the block lengths is infinite in length. This creates a crystallographic shear plane that is infinite along one axis (the $\hat{y}$ axis). An example of a type $E[3 \times \infty]$ structure as shown in Figure 3.5(a) is Nb_3O_7F.[133] The $E[2 \times \infty]$ structure is seen in a polymorph of Nb_2O_5 (R-Nb_2O_5[117]) and $W_3V_5O_{20}$[134]. The $E_1[3 \times 3]$ structure (Figure 3.5(c)) can be found in the high power density Wadsley-Roth phase, $TiNb_2O_7$[16]. $Nb_{12}O_{29}$ has a 3×4 shift type patterned in a $E_1[3 \times 4]$ structure (Figure 3.5(d)) while $E_1[4 \times 4]$ blocks can be found in M-Nb_2O_5 (Figure 3.5(e)).[106, 135] The type T phase can be found in many niobium tungsten oxides. The 4 by 4 type T phase is isostructural to $Nb_{14}W_3O_{44}$, a $T[4 \times 4]$ phase (Figure 3.5(f)).[136]

There are multitude of phases that also extend in complexity beyond the aforementioned shift types. Structures denoted M type phases cannot merely be constructed by shifting blocks in the x or y direction. Instead these are constructed from shifting larger subsets of these blocks, rather than individual blocks.Many of these structure have tetrahedra at their vertices as well as octahedral edge sharing motifs reminiscent of type E_1

phases, where some block are shifted by i=1. Experimentally, the H-Nb_2O_5 phase has a 3×5 block of NbO_6 octahedra edge sharing with a 3×4 block of NbO_6 octahedra. The combination of these blocks have tetrahedra at their vertices (Figure 3.5(g)).

In addition to phases with tetrahedral motifs, other structures where shifts occur relative to two blocks rather than one for structures without connecting tetrahedra. For example, the phase commonly referred to experimentally as the monoclinic phase M-$Ti_2Nb_{10}O_{29}$ is a type $E_1[3 \times 4]$ structure, as shown in Figure 3.6(a). This phase, as before, is constructed by shifting the 3×4 blocks by $i = 1$ relative to one another. Now if one where instead to take two blocks along y shifted by $i = 1$ and then shift that unit two-block unit by another $i = 1$ then the resulting structure would be the orthorhombic phase of $Ti_2Nb_{10}O_{29}$ (Figure 3.6(b)). Though these have the same block sizes and the same compositions with the same shift types present, these two structures differ due to the extended shift degree present in the orthorhombic phase.[113]

We constructed an equation for the Wadsley-Roth crystallographic shear phases, that allows one to construct, type E and type T Wadsley-Roth. The matrix equation, M_{WR}, can be written as

$$M_{WR} = \begin{bmatrix} nd - \frac{d}{2} & \delta x d & 0 \\ \delta y d & md - \frac{d}{2} & 0 \\ \frac{d}{2} & \frac{d}{2} & d \end{bmatrix} \tag{3.1}$$

where n is the first block dimension and m is the second block dimension. Conventionally, the $n < m$ when the block structure is described, e.g. E$[n \times m]$. As stated previously, d is the length of one MO_6 octahedra from one oxygen to the opposing oxygen. The exact value of d is thus dependent on the chemical structure of the Wadsley-Roth phase. As stated earlier in the section, δx corresponds to the shift along the n dimension of the block. δx is in values of octahedral lengths, d, and can take integer values. δy is the shift amount along the m dimension of the block For the construction of type M structures,

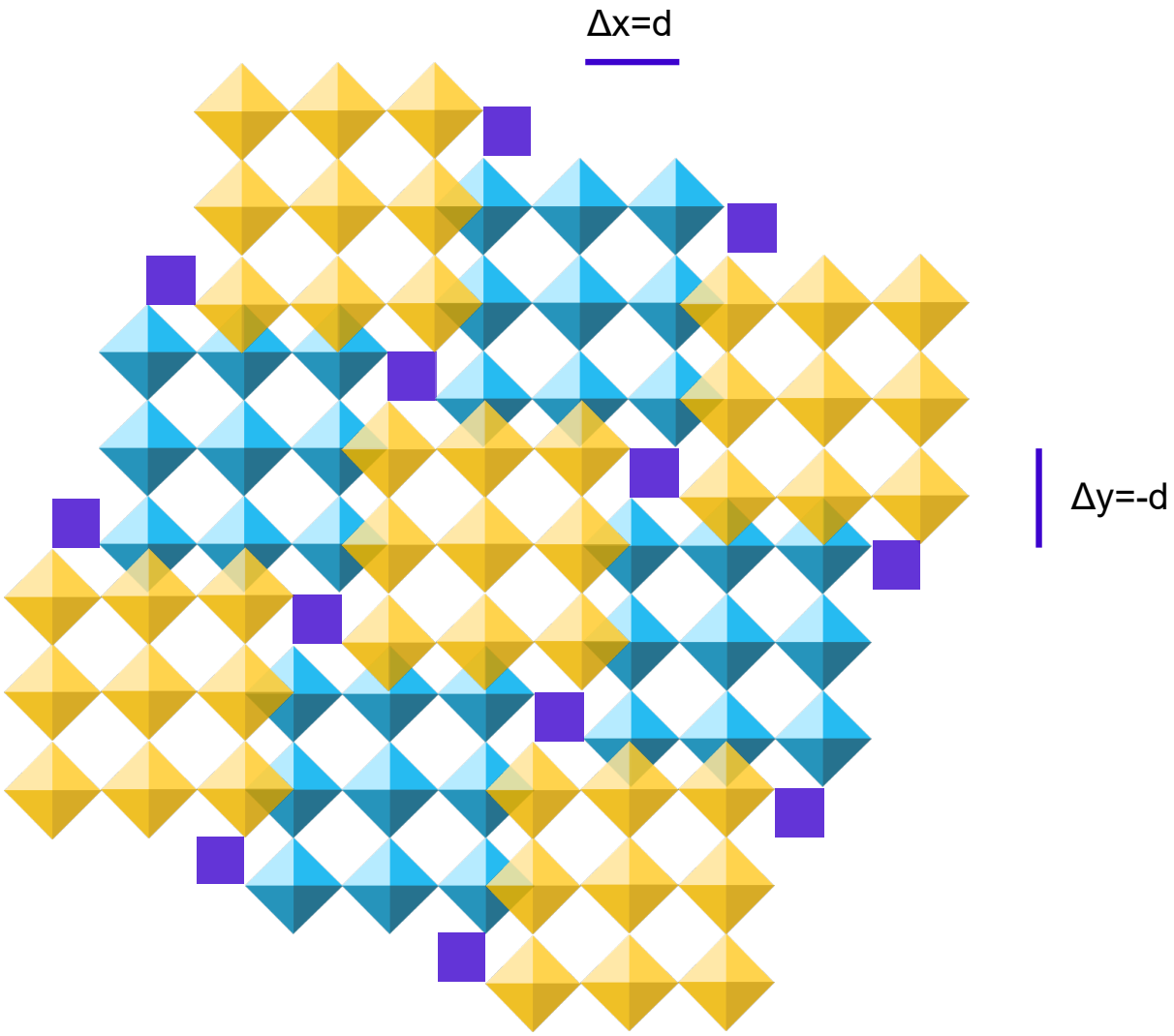

Figure 3.4: A type T[3 × 3] Wadsley-Roth phase.

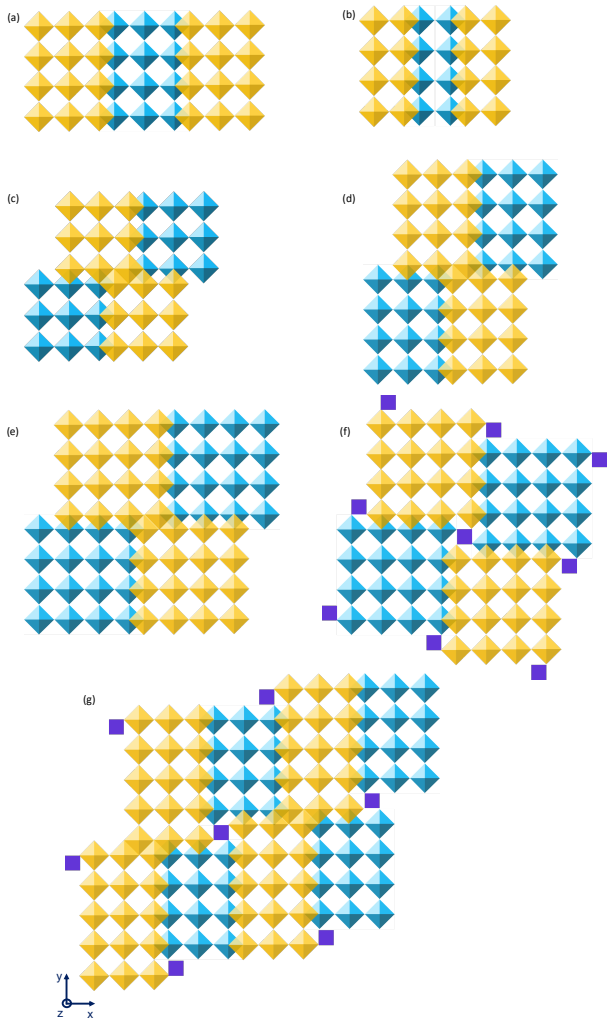

Figure 3.5: A subset of known experimentally synthesized Wadsley-Roth types including E$[3 \times \infty]$(a), E$[2 \times \infty]$ (b), E$_1[3 \times 3]$ (c), E$_1[3 \times 4]$ (d), E$_1[4 \times 4]$ (e), and T$[4 \times 4]$ (f). The type M phase M$[3 \times 4, 3 \times 5]$ is constructed by both subsets of 3×4 blocks and 3×5 blocks and contains motifs that can be found in both type T and type M phases.

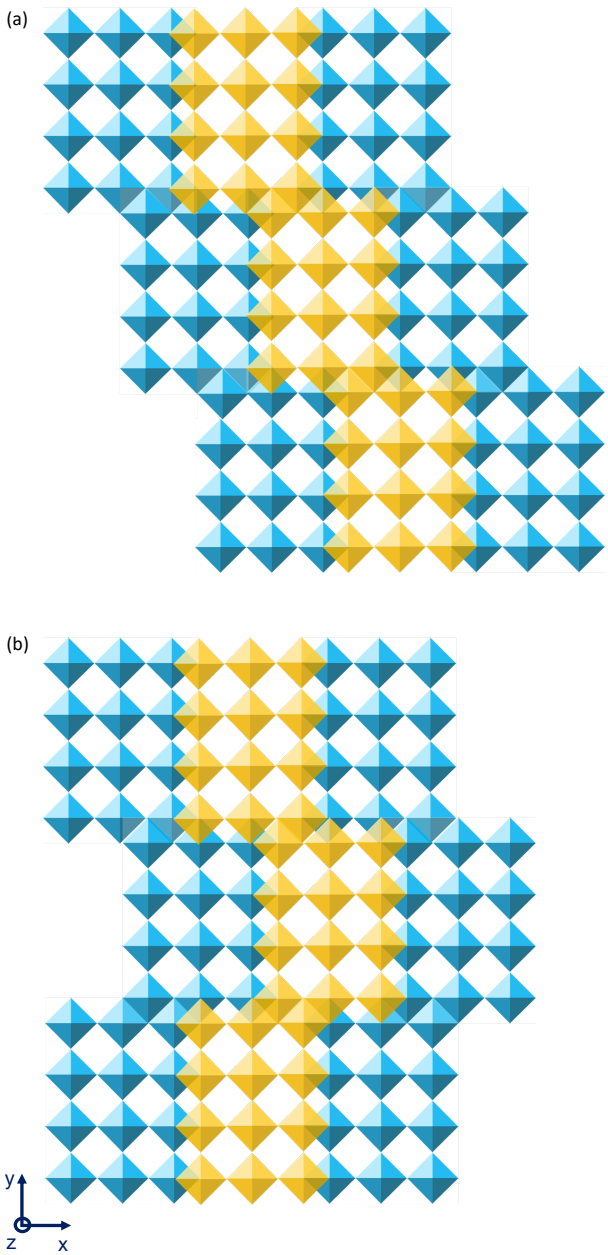

Figure 3.6: Two type E Wadsley-Roth phases constructed from blocks of the same size (3×4) but with differing repeat units in the primitive unit cell. The experimentally formed type M-$Ti_2Nb_{10}O_{29}$ basic structure is shown (a). The tetragonal phase, T-$Ti_2Nb_{10}O_{29}$ constructed by not only shifting the blocks but repeat subsets of two 3×4 blocks are sheared by a differing amount

a different matrix equation is required, and is still yet to be constructed.

3.3.2 Wadsley-Roth alloys: the $TiNb_2O_7$ compound

We next explore ordering preferences among different cations over the metal sites of Wadsley-Roth phases. Ordering tendencies within alloyed Wadsley-Roth phases are affected by chemical and structural factors. Electrostatic interactions will play a role when cations have different oxidation states. The results of the previous section, for example, have shown that edge-sharing between octahedrally coordinated cations with high oxidation states is unfavorable. In alloyed Wadsley-Roth phases, the cations with the higher oxidation states are, therefore, expected to avoid octahedral sites that share many edges with neighboring cation sites. Some cations of an alloyed Wadsley-Roth phase may tolerate or even favor octahedral distortions more readily than others, leading to competing ordering preferences that are dictated by the degree with which different sites are able to relax. To explore cation ordering tendencies in Wadsley-Roth phases, we focus on $TiNb_2O_7$, an important anode material for Li-ion batteries[137] that adopts the $E_1[3 \times 3]$ Wadsley-Roth crystal structure shown in Figure 3.7(a). The cation sites that can be alloyed with Ti and Nb are numbered as in Dreele et al. [138]. The Ti and Nb cations of this compound are in their maximum oxidation state (i.e. Nb^{5+} and Ti^{4+}) and both elements are susceptible to second order Jahn-Teller distortions in this oxidation state.

We calculated the energies of all symmetrically distinct Ti-Nb orderings (a total of 44) over the cation sites within the unit cell of the $E_1[3 \times 3]$ Wadsley-Roth structure at the $TiNb_2O_7$ composition. To separate the effects of relaxations from purely chemical and electrostatic interactions, we compare unrelaxed energies, in which all octahedra of the Wadsley-Roth phase are perfectly cubic, to fully relaxed energies. The energies are

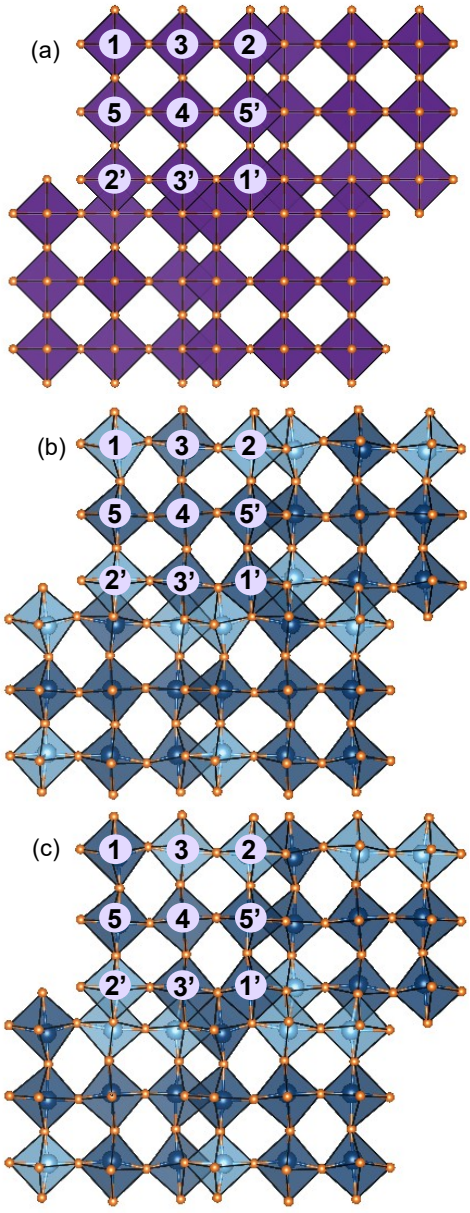

Figure 3.7: (a) Symmetrically inequivalent sites in the transition metal sublattice of $TiNb_2O_7$. Sites numbered with a prime are symmetrically equivalent to its corresponding site. (b) Crystallographic structure for the electrostatic ground state ordering in $TiNb_2O_7$ for volume 1 enumerated orderings. (c) Crystallographic structure for the ground state ordering $TiNb_2O_7$ for volume 1 enumerated orderings when structural optimization is performed.

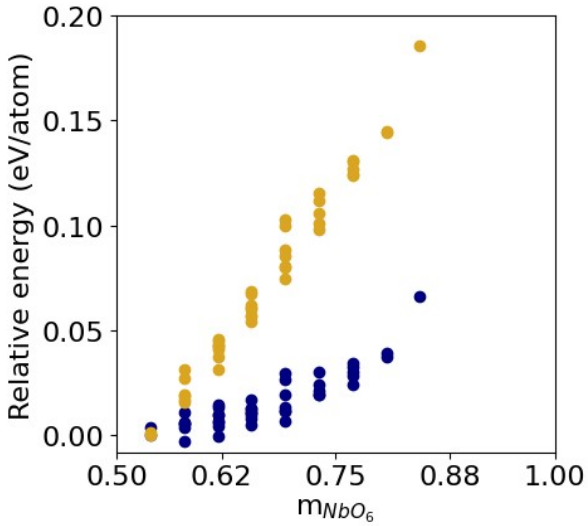

Figure 3.8: (a) Energies of $TiNb_2O_7$ orderings varied over the transition metal sublattice when atomic positions are held fixed (gold) and energies of $TiNb_2O_7$ orderings varied over the transition metal sublattice for relaxed orderings (blue).(b) Relaxation energies of all $TiNb_2O_7$ orderings.

shown in Figure 3.8(a), plotted as a function of the average number of edges shared by Nb, ξ_{Nb}, in each structure. As is clear in Figure 3.8(a), the unrelaxed energies, shown in yellow, exhibit a strong and almost linear correlation with this metric. The trend suggests that in the absence of relaxations, the Nb^{5+} cations seek to occupy sites that minimize the number of edge-sharing pairs. Figure 3.8(b) shows the Ti and Nb ordering over the cation sites of $E_1[3 \times 3]$ with the lowest unrelaxed energy. In this structure, the Nb occupy sites with the minimal number of edge-sharing pairs, which includes the central block site.

The correlation between the energy of the crystal and the average number of edge-sharing pairs per Nb^{5+} persists for the fully relaxed energies (blue points in Figure 3.8(a)). However, the spread in energy for a given value of ξ_{Nb} is increased. Furthermore, the lowest energy ordering without relaxations is no longer the lowest energy configuration after full relaxation. Instead, another configuration with a slightly higher value of ξ_{Nb} has the lowest fully relaxed energy. This configuration is shown in Figure 3.7(c) and

differs from the configuration of Figure 3.7(b) in that the occupants of sites 1 and 3 have been swapped.

While the energy of $TiNb_2O_7$ is highly correlated with the average number of edge-sharing pairs per Nb^{5+} cation, other factors also play a role. One among them is the ability of different octahedral sites within the $E_1[3 \times 3]$ Wadsley-Roth crystal of $TiNb_2O_7$ to distort as both the Ti^{4+} and Nb^{5+} cations are susceptible to second-order Jahn-Teller distortions. Furthermore, metal cations that share edges will relax in order to increase the length of the edge-sharing pair. Figure 3.8(b), which plots the reduction in energy during relaxation for each of the 44 different Ti-Nb orderings in $TiNb_2O_7$, shows a strong correlation of this relaxation energy with ξ_{Nb}, the average number of edge-sharing pairs of Nb in each structure. The more edge-sharing pairs per Nb, the more the crystal was able to lower its energy during relaxation.

It is clear from Figure 3.8(b) that all configurations are able to lower their energy as a result of relaxations more so than the ordering of Figure 3.7(b), the lowest-energy configuration when relaxations are neglected and the configuration that minimizes the number of edge-sharing octahedra simultaneously occupied by Nb^{5+}.

Relaxations within a Wadsley-Roth structure result in characteristic deformations of each metal-oxygen octahedron. The deformations of each MO_6 octahedron in the fully relaxed $TiNb_2O_7$ structures was analyzed by decomposing the octahedral displacements into a linear superposition of the symmetry adapted collective displacements of Figure 2.2 as described in Section 2.5.1. The length of the amplitudes within the different irreducible subspaces, γ_i, was calculated for each octahedron in each of the 44 different configurations of $TiNb_2O_7$ and binned into histograms.

Figures 3.9(a) and (b) show the histograms for the length of the amplitude vector in irrep Γ_V for the TiO_6 and NbO_6 octahedra, respectively. Distortions in irrep Γ_V correspond to a deformation of an equatorial square of oxygen, with opposite pairs of

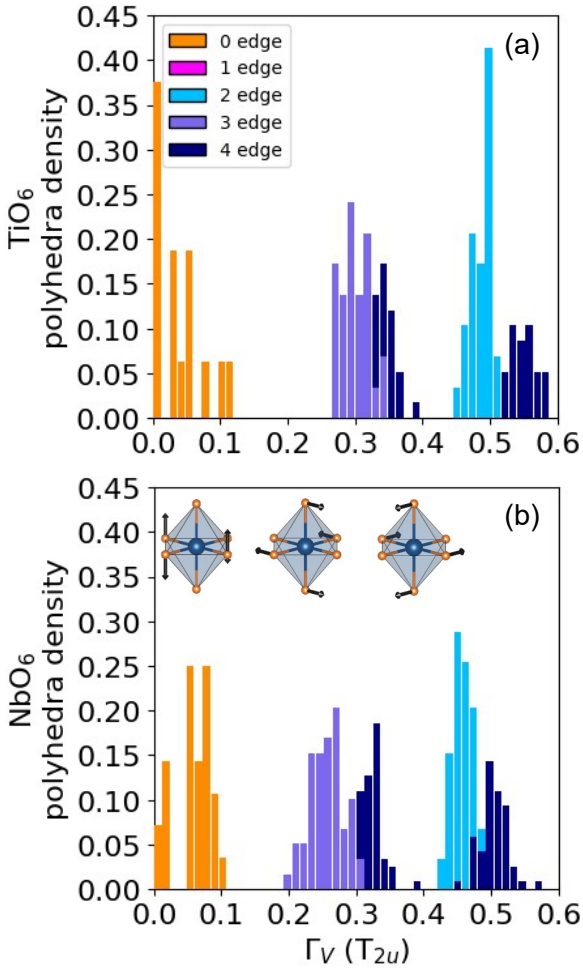

Figure 3.9: (a) Γ_V expression for all TiO_6 octahedra in all 44 symmetrically in-equivalent transition metal sublattice orderings of $TiNb_2O_7$. (b) Γ_V expression for all NbO_6 octahedra in all 44 symmetrically in-equivalent transition metal sublattice orderings in $TiNb_2O_7$.

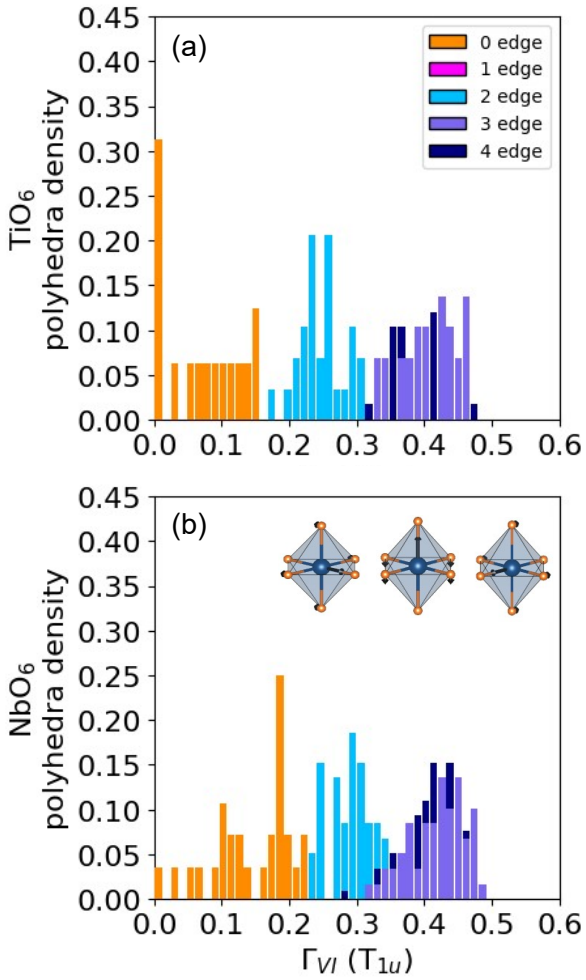

Figure 3.10: (a) Γ_{VI} expression for all TiO_6 octahedra in all 44 symmetrically in-equivalent transition metal sublattice orderings in $TiNb_2O_7$. (b) Γ_{VI} expression for all NbO_6 octahedra in all 44 symmetrically in-equivalent transition metal sublattice orderings in $TiNb_2O_7$.

oxygen moving perpendicular to the equatorial plane as illustrated in the inset in Figure 3.9. As is clear in Figure 3.9, the amplitude of the octahedral distortions corresponding to this mode is very sensitive to the number of edges that the octahedron shares with neighboring filled octahedra. The corner sharing octahedra at the center of the 3×3 blocks of the $TiNb_2O_7$ Wadsley-Roth structure, which share zero edges, undergo the smallest deformations according to the Γ_V mode. Somewhat surprisingly, the octahedra that share only two edges with neighboring filled octahedra undergo more severe deformations than many octahedra that share 3 or more edges. Overall, the deformations of the TiO_6 octahedra are very similar to those of the NbO_6 octahedra.

Figure 3.10 shows a similar histogram for the Γ_{VI} irrep. This irrep corresponds to off-centering displacements of the central metal cation as illustrated in the inset of Figure 3.10. Here again, the degree of distortion is very sensitive to the number of edges that the octahedron shares with neighboring filled octahedra. The degree with which the cation displaces from the center of the octahedron increases with the number of edges that the octahedron shares with neighboring occupied octahedra. A notable difference between Ti^{4+} and Nb^{5+} is that the latter displaces further from the center in the corner sharing octahedra of the center of the 3×3 block. The distortions in the other irreps, Γ_I, Γ_{II}, Γ_{III}, Γ_{IV}, are not as pronounced as those of Γ_V and Γ_{VI} for both the TiO_6 and NbO_6 octahedra as shown in Figure 3.11. The individual distortion amplitudes by amount of edge sharing are shown in Figures 3.12, 3.13, 3.14, and 3.15. An analysis of the distortion amplitudes as a function of energy are shown in Figure 3.16.

It is insightful to compare the octahedral distortions after relaxation of the configuration of Figure 3.7(b), which minimizes the number of edge-sharing pairs occupied by Nb^{5+}, to those of the configuration of Figure 3.7(c), which has the lowest energy after relaxation. Figure 3.17 compares the octahedral distortions for irrep Γ_{VI} for the equivalent octahedral sites in the two configurations. Similar comparisons for the other irreps

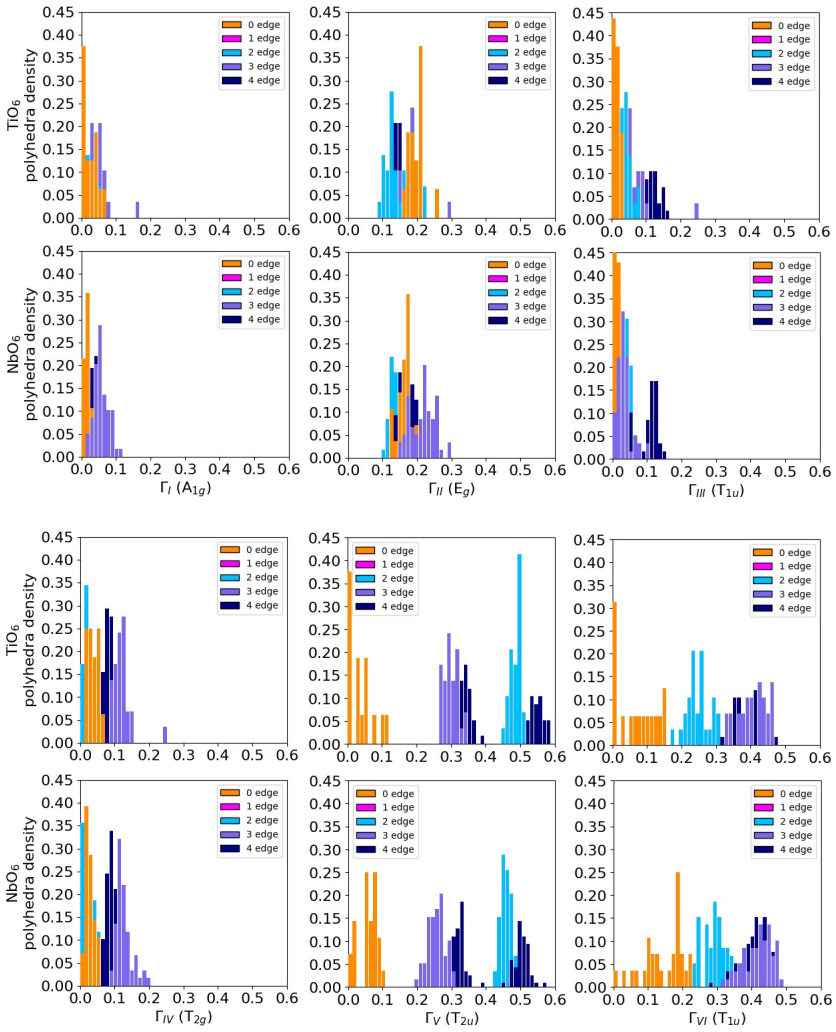

Figure 3.11: Histogram analysis of all symmetrically distinct orderings of $TiNb_2O_7$, where the only transition metal octahedra analysed are transition metal octahedra that share zero edges in the structure. Each ordering has one octahedra that shares no edges with neighboring transition metal octahedra, two octahedra that share two edges with neighboring transition metal octahedra, two octahedra that share three edges with neighboring transition metal octahedra, and four octahedra that share four edges with neighboring transition metal octahedra.

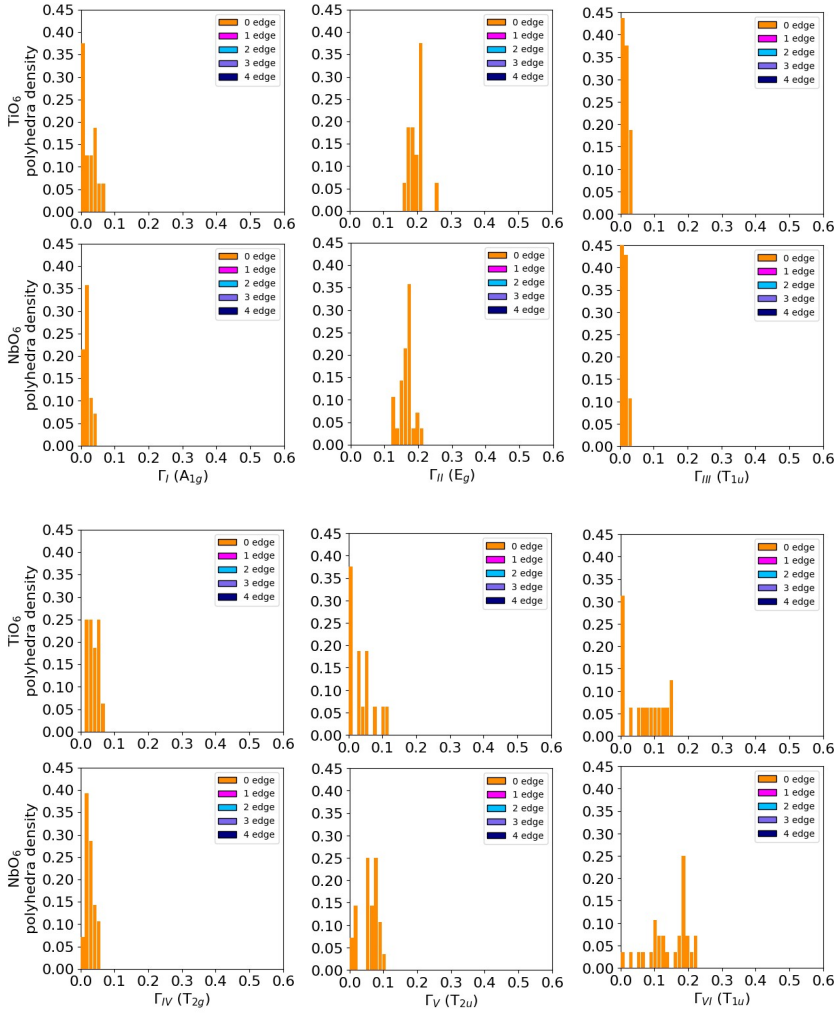

Figure 3.12: Histogram analysis of all symmetrically distinct orderings of $TiNb_2O_7$, where the only transition metal octahedra analysed are transition metal octahedra that share zero edges in the structure. Each ordering only has one octahedra that shares no edges with neighboring transition metal octahedra.

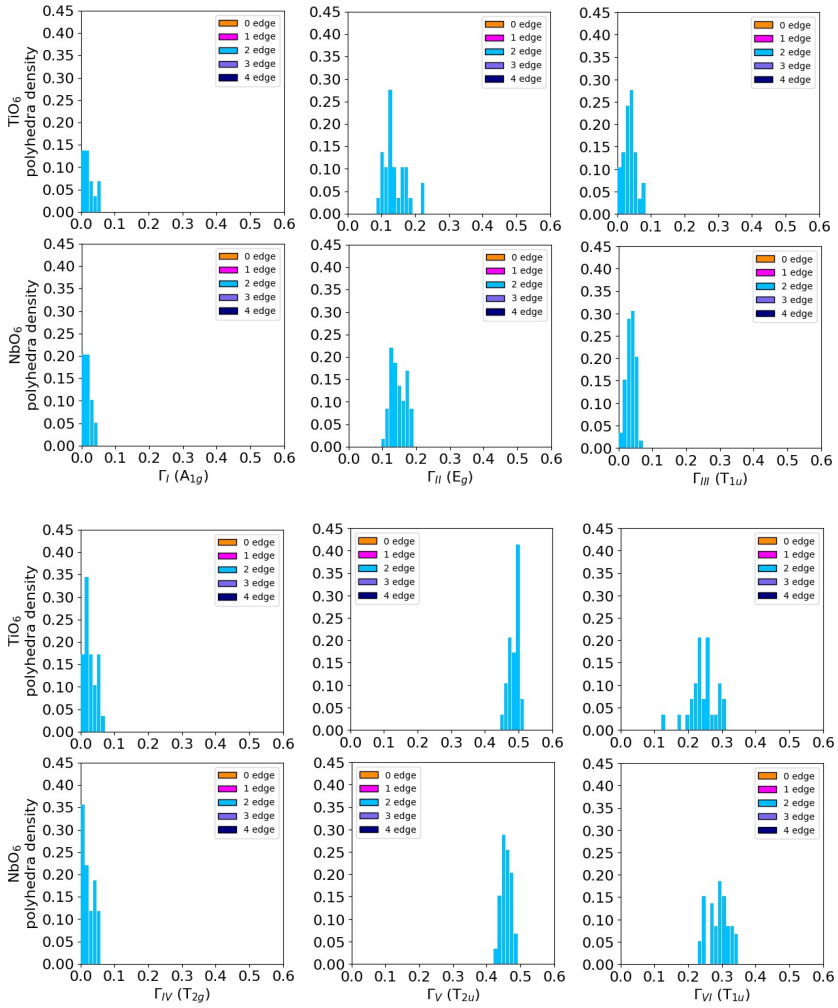

Figure 3.13: Histogram analysis of all symmetrically distinct orderings of $TiNb_2O_7$, where the only transition metal octahedra analysed are transition metal octahedra that share two edges in the structure. Each ordering only has two octahedra that share two edges with neighboring transition metal octahedra.

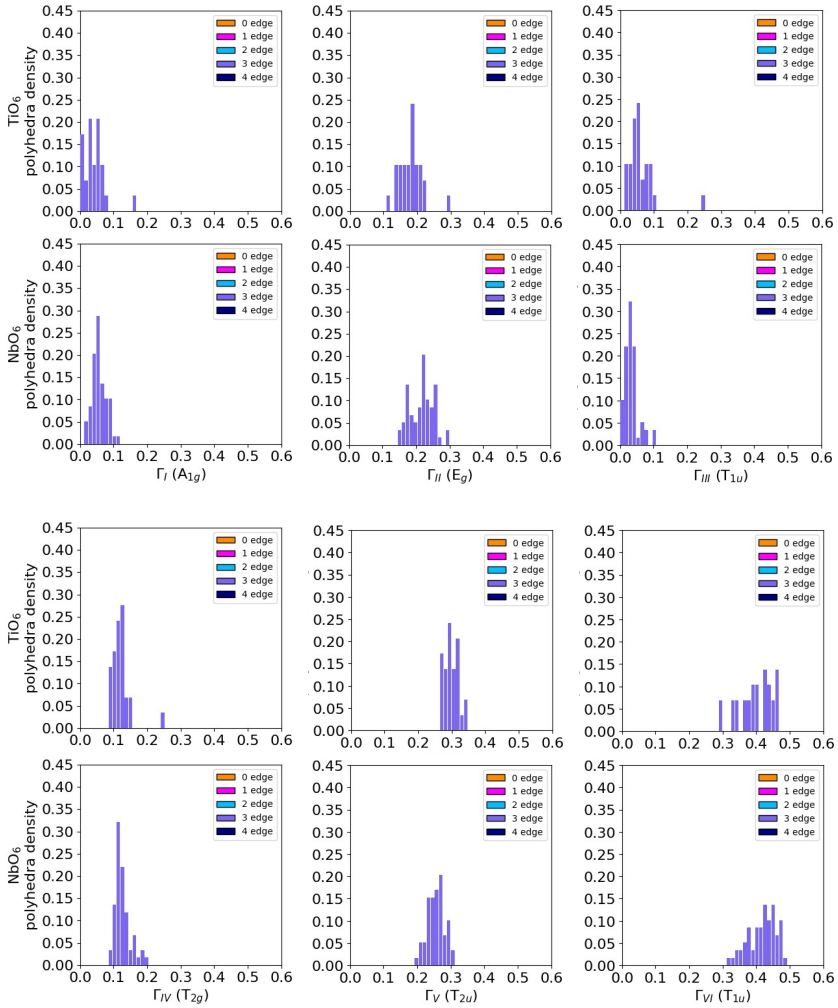

Figure 3.14: Histogram analysis of all symmetrically distinct orderings of $TiNb_2O_7$, where the only transition metal octahedra analysed are transition metal octahedra that share three edges in the structure. Each ordering only has two octahedra that shares three edges with neighboring transition metal octahedra.

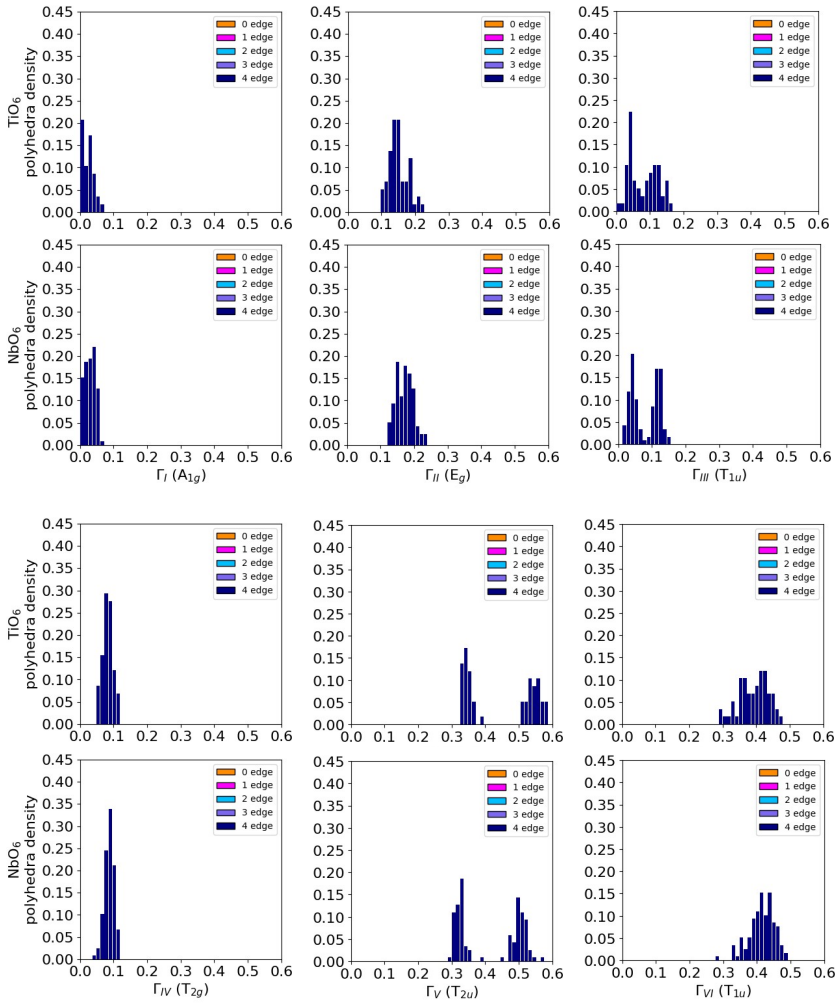

Figure 3.15: Histogram analysis of all symmetrically distinct orderings of $TiNb_2O_7$, where the only transition metal octahedra analysed are transition metal octahedra that share four edges in the structure. Each ordering has four octahedra that shares four edges with neighboring transition metal octahedra.

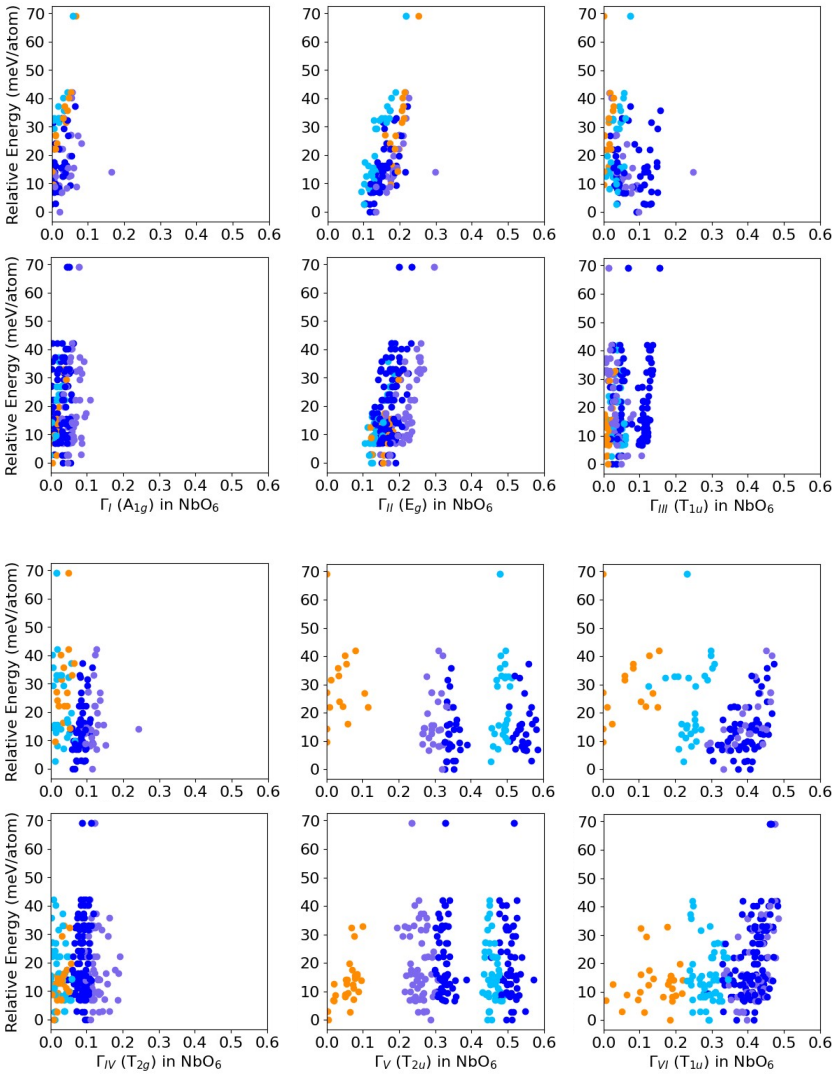

Figure 3.16: Distortion amplitudes for $TiNb_2O_7$ as a function of energy. Each point is an individual octahedra in the plot with the color dependent on the amount of octahedral edge sharing.

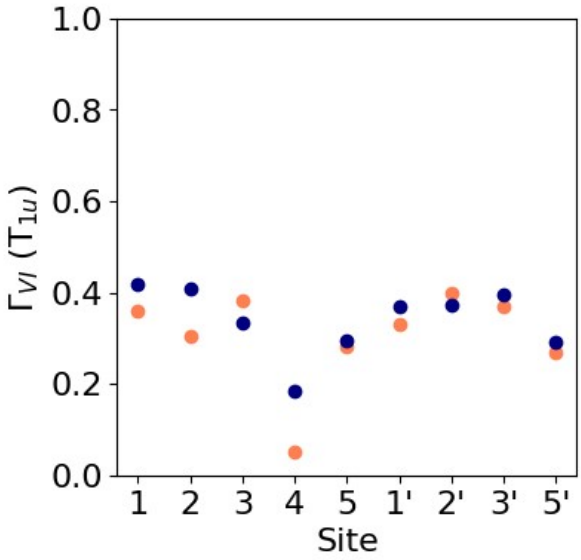

Figure 3.17: Distortion amplitudes over each numbered site where the light color data points are values for each octahedral site in the electrostatic $TiNb_2O_7$ ground state ordering while the dark color data points are values for the corresponding octahedral sites in the structurally optimized $TiNb_2O_7$ ground state ordering.

are shown in Figure 3.18.

While the only difference between the configurations in Figures 3.7(b) and (c) is the occupancy of sites 1 and 3, Figure 3.17 indicates that the distortions of the octahedra of sites 1 and 3 are narrowly affected by the swap. Instead, there is a marked difference in the off-centering of the Nb^{5+} cation in site 4, the corner sharing octahedron at the center of the 3×3 block of the $E_1[3\times3]$ structure. In configuration Figure 3.7(b), the Nb remains close to the center of the octahedron, while in the lower energy configuration of Figure 3.7(c), the Nb is more off centered. This is enabled by having a lower oxidation state Ti^{4+} cation as one of its corner sharing neighbors. The lower symmetry of configuration Figure 3.7(c) as compared to that of Figure 3.7(b) gives the central Nb more flexibility to off-center and thereby more fully express its tendency to undergo a second-order Jahn-Teller distortion.

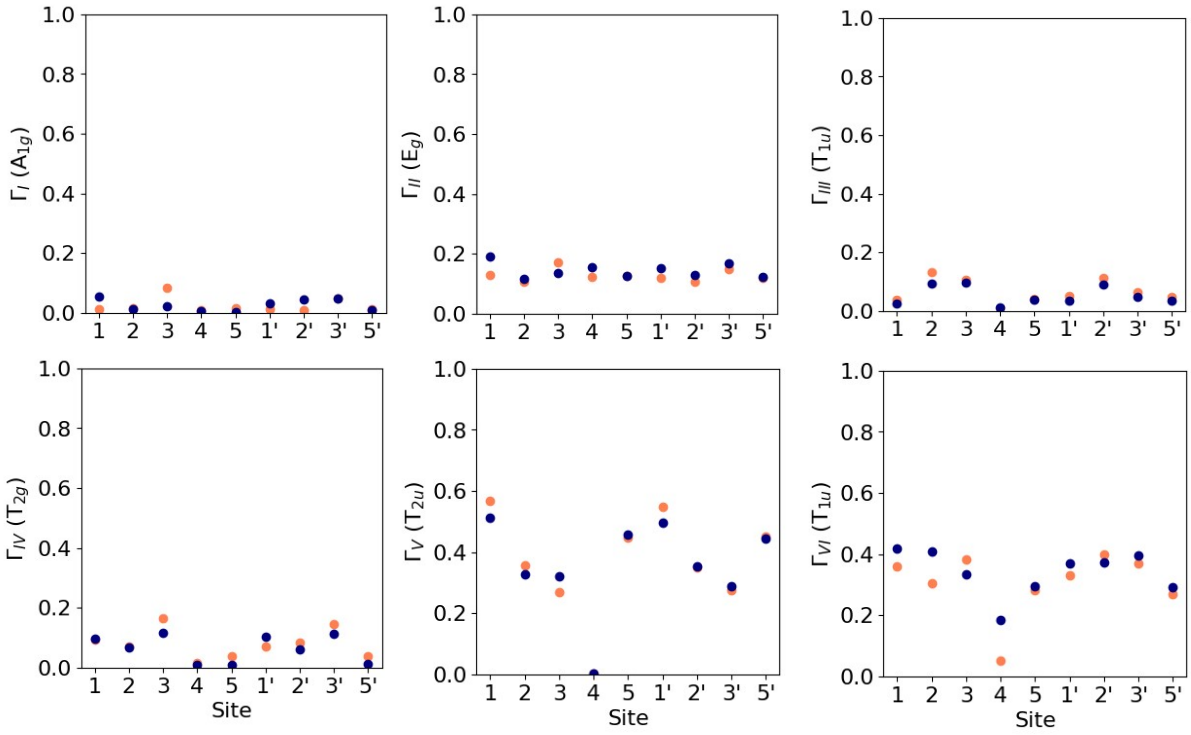

Figure 3.18: Distortion amplitudes on each octahedral site in the lowest energy unrelaxed ordering (orange) and the lowest energy relaxed ordering (blue).

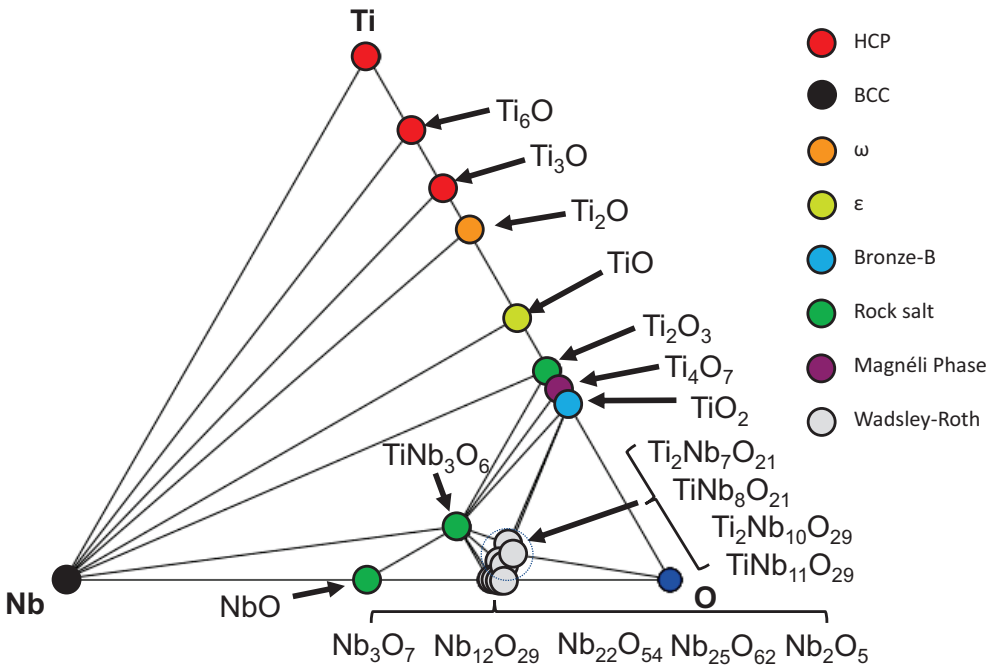

Figure 3.19: Zero-K Ti-Nb-O phase diagram calculated with PBE.

3.3.3 Wadsley-Roth phase stability in the Ti-Nb-O ternary

We next explore the thermodynamic stability of Wadsley-Roth phases relative to other polymorphs in the Ti-Nb-O ternary composition space. To this end, we generated alloyed Wadsley-Roth phases by decorating the cation sites of stable binary Nb_pO_q Wadsley-Roth phases with Ti and Nb cations. All symmetrically distinct Ti-Nb orderings within the unit cell of Nb_3O_7 in the $E_1[3 \times 3]$ structure at compositions $TiNb_8O_{21}$ and $Ti_2Nb_7O_{21}$ were calculated, as were all configurations over the sites of $Nb_{12}O_{29}$ in the $E_{1y}[3 \times 4]$ structure having the composition $TiNb_{11}O_{29}$. We also include the energies of the 44 different Ti-Nb orderings over the cation sites of $TiNb_2O_7$ in the $E_1[3 \times 3]$ structure in the list of candidate structures, discussed in the previous section. Additionally, all symmetrically distinct orderings of the type M $TiNb_{24}O_{62}$ phase were also enumerated and their energies are calculated.

Figure 3.19 shows the calculated zero-Kelvin phase diagram of the Ti-Nb-O compo-

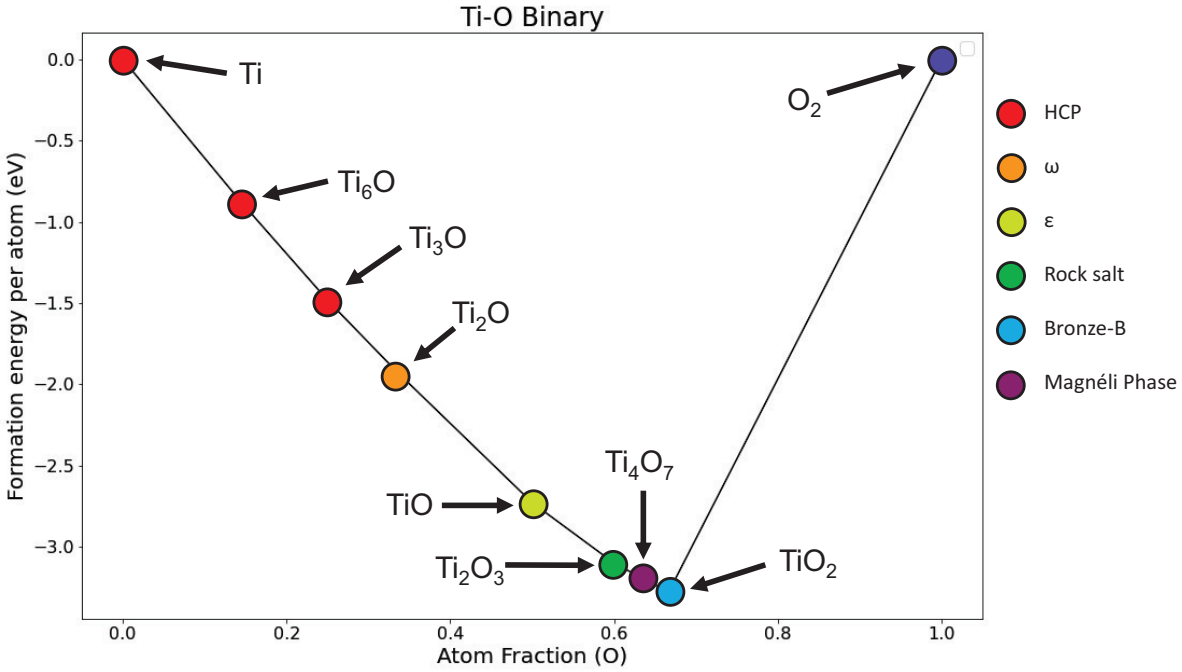

Figure 3.20: Titanium oxygen binary phase diagram, calculated in VASP using PAW_PBE potentials.

sition space. The ground states along the binary Ti-O composition axis were taken from Gunda et al. [139]. While the experimentally assessed Ti-O phase diagrams contain the corundum Ti_2O_3 structure as a stable oxide, DFT-PBE predicts instead a vacancy ordered rocksalt to be stable at that composition [139, 140]. As noted in Section 3.3.1, this vacancy ordered rocksalt can be viewed as a $E_1[1 \times 2]$ Wadsley-Roth phase. Also absent from the calculated phase diagram is the rutile-derived NbO_2 oxide along the Nb-O binary composition axis [141]. These disagreements with experiment are likely due to the PBE exchange-correlation functional. Nevertheless, the overall agreement with experiment is very good and the absence of NbO_2 and corundum Ti_2O_3 from the zero-Kelvin phase diagram can be attributed to errors in the calculated energy of only several meV per atom. The Nb-O and Ti-O binary formation energy plots are shown in Figures 3.20 and 3.21.

Figure 3.19 shows that a large number of Wadsley-Roth phases are predicted to be

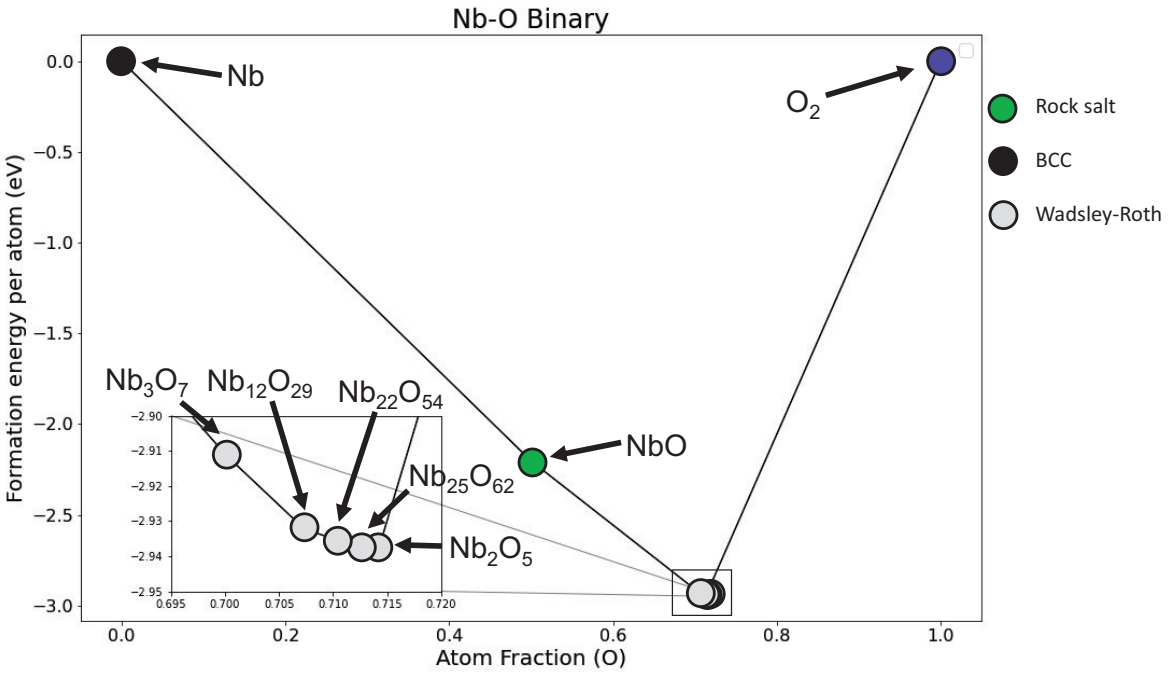

Figure 3.21: Niobium oxygen binary phase diagram, calculated in VASP using PAW_PBE potentials.

stable in the ternary composition space. The Wadsley-Roth compounds in the Ti-Nb-O composition space are all predicted as having negative formation energies relative to their binary counterparts on the Nb-O binary axis and the lowest energy polymorph of TiO_2.

Surprisingly, the $TiNb_2O_7$ compound, used as an anode in Li-ion batteries, is not a zero-Kelvin ground state when only considering Ti-Nb orderings in the primitive unit cell. This suggests that $TiNb_2O_7$ is stabilized at elevated temperature through configurational and/or vibrational entropy. While the list of candidate structures considered here is not exhaustive, and other Wadsley-Roth phases are also likely stable, these results conclusively show that DFT-PBE predicts Wadsley-Roth phases as being stable compounds in the Ti-Nb-O ternary. Voskanyan et al. [142], using calorimetry measurements, concluded that many Wadsley-Roth phases in the Ti-Nb-O ternary composition space have positive formation enthalpies and attributed their stability to entropic contributions to the free energy.

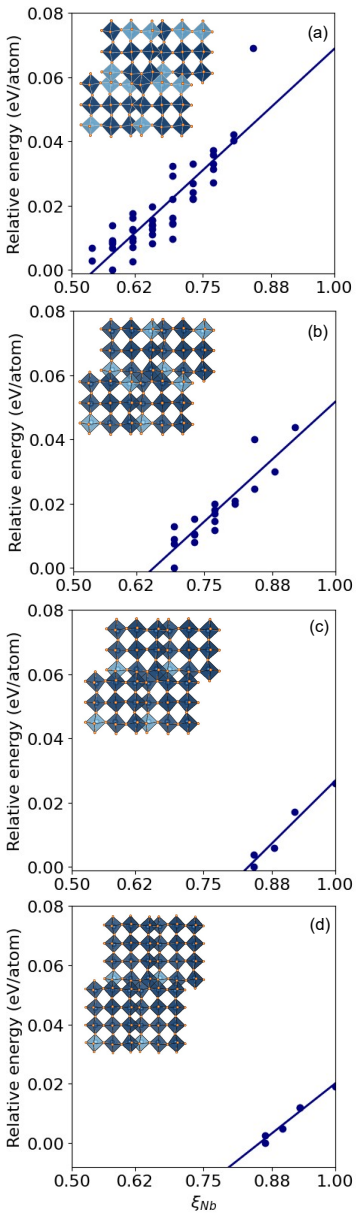

Figure 3.22: Relative energies and lowest energy states for full relaxations of all symmetrically distinct orderings for stoichiometries and block sizes of $TiNb_2O_7$ (a), $Ti_2Nb_7O_{21}$(b), $TiNb_8O_{21}$ (c), and $TiNb_{11}O_{29}$ (d).

As shown in the previous section, the Ti and Nb of $TiNb_2O_7$ prefer orderings that minimize the number of edge-sharing octahedra occupied by Nb cations. Similar correlations are predicted for the other alloyed Wadsley-Roth phases considered in this work. Figure 3.22(b), (c), and (d) shows the variation in the fully relaxed energies of different Ti-Nb orderings over the cation sites of $E_1[3 \times 3]$ at compositions $TiNb_8O_{21}$ and $Ti_2Nb_7O_{21}$ and of $E_{1y}[3 \times 4]$ at composition $TiNb_{11}O_{29}$ as a function of the average number of edge-sharing pairs per Nb cation. Again, as with $TiNb_2O_7$, the Ti cations, with their lower oxidation state, prefer to segregate to the crystallographic shear boundaries and fill the edge sharing octahedra, while the Nb segregate to the block interior and prefer the central corner-sharing octahedron.

The distortion amplitudes for the Ti-Nb-O ternary show that across the NbO_6 and TiO_6 octahedra exhibit similar distortions for each irrep type as shown in Figure 3.23. The Γ_V distortion is expressed to a slightly higher degree for TiO_6 octahedra than for NbO_6 octahedra. Conversely the Γ_{VI} distortion is expressed more in the NbO_6 octahedra than the TiO_6. Distortion amplitudes exclusively for maximum oxidation state compounds are shown in Figure 3.24. A sensitivity analysis of the distortion amplitudes for the ternary is shown in Figure 3.25.

3.4 Discussion

The Wadsley-Roth family of crystal structures are adopted by a wide variety of early transition metal oxides containing Ti, V, Nb, Ta, Cr, Mo and W. Many Wadsley-Roth phases are promising anode materials for Li-ion batteries due to their ability to intercalate Li ions at high rates and at low voltages [143, 98, 144, 16, 93, 28, 27, 145, 146, 142, 147, 148, 106, 149, 150, 151, 152, 103, 153, 154, 155, 156]. They are also important for structural applications as they are formed by many of the early transition metals of

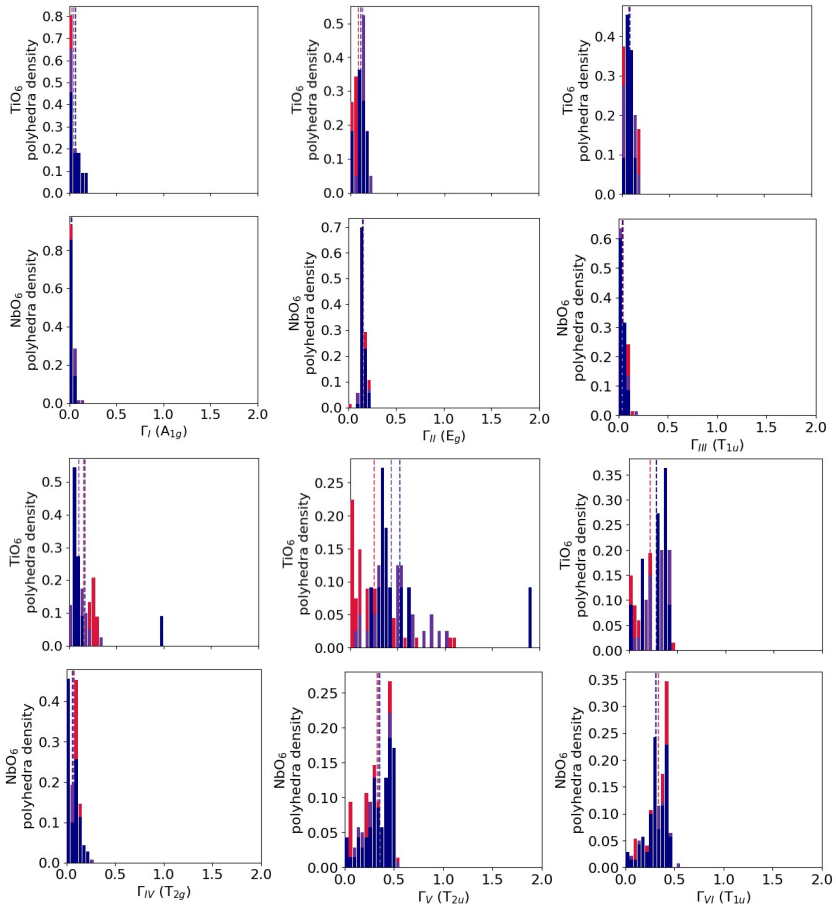

Figure 3.23: Histograms describing distortion amplitudes over all relevant irreducible representations for octahedra in all phases in the Ti-Nb-O ternary. The histograms are seperated between all available TiO_6 octahedra in structures within 25meV/atom of the hull and all available NbO_6 octahedra in structures within 25meV/atom above the hull. The histograms are colored based on the formation energies of the parent structure of each octahedra sampled. The blue histogram shows the distortion amplitudes for octahedra that are in ground state structures. The purple histogram shows the distortion amplitudes for octahedra in structures that are between 0meV/atom to 10meV/atom excluding ground states. The red histogram shows the distortion amplitudes for octahedra in the structures that are between 10meV/atom and 25meV/atom from the convex hull.

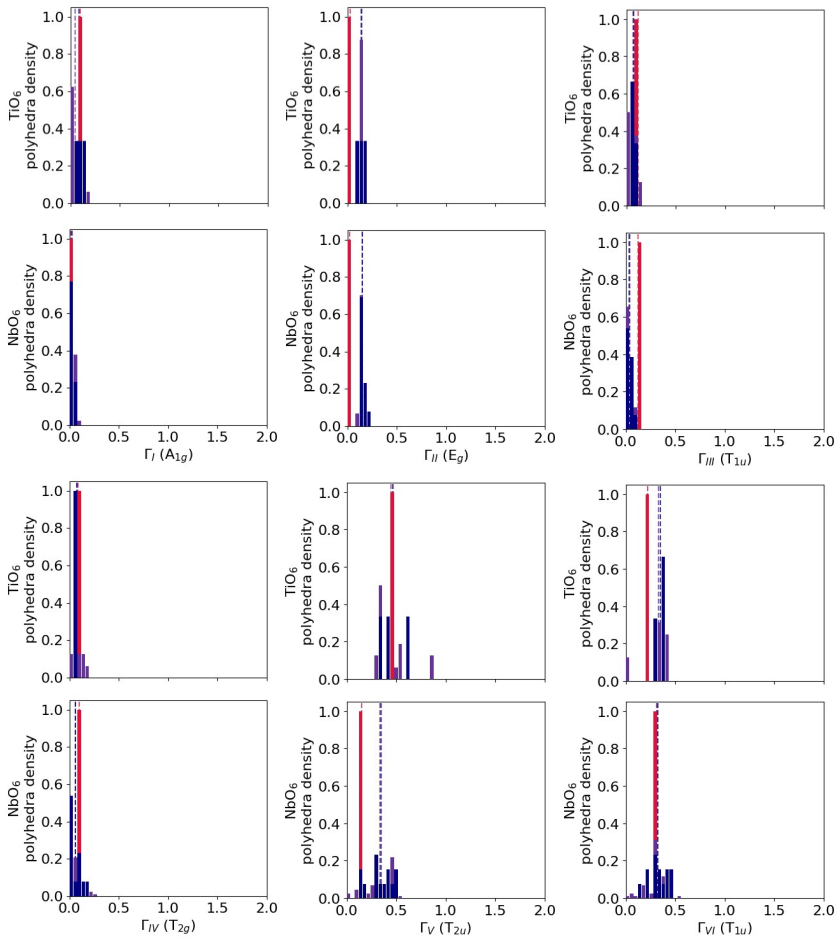

Figure 3.24: Histogram describing distortion amplitudes over all relevant irreducible representations for octahedra in phases where transition metals are at their maximum oxidation state in the Ti-Nb-O ternary. The histograms are separated between all available TiO_6 octahedra in structures within 25meV/atom of the hull and all available NbO_6 octahedra in structures within 25meV/atom above the hull. The histograms are colored based on the formation energies of the parent structure of each octahedra sampled. The blue histogram shows the distortion amplitudes for octahedra that are maximum-oxidation ground state structures. The purple histogram shows the distortion amplitudes for octahedra in maximum-oxidation state structures that are between 0meV/atom to 10meV/atom excluding ground states. The red histogram shows the distortion amplitudes for octahedra in the maximum-oxidation state structures that are between 10meV/atom and 25meV/atom from the convex hull.

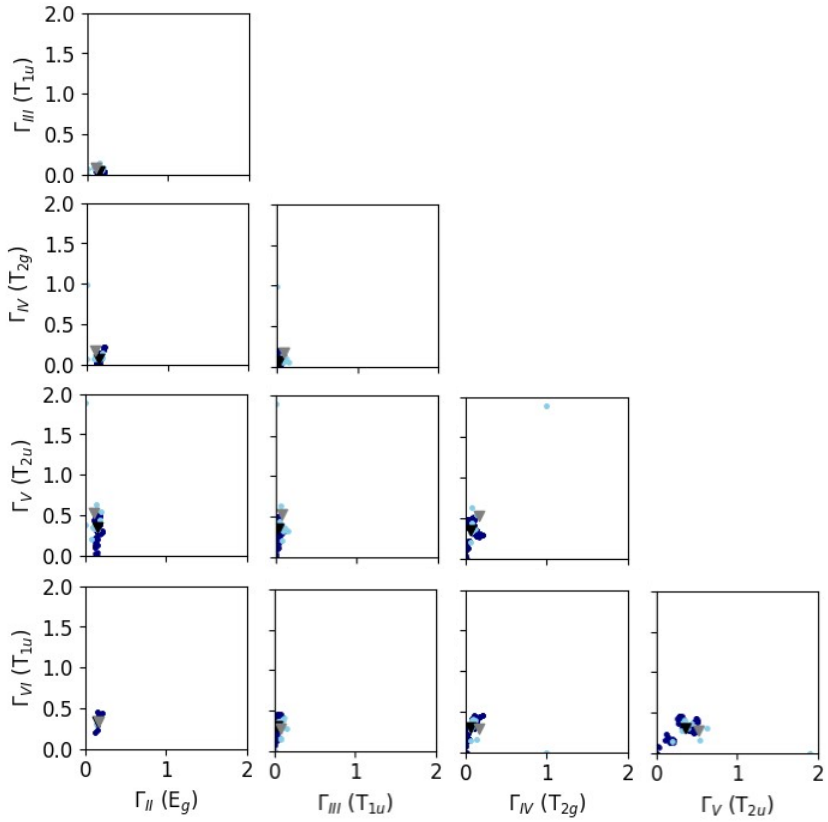

Figure 3.25: Sensitivity analysis for the distortion amplitudes for transition metal octahedra in stable structures in the Ti-Nb-O ternary. Data from TiO_6 octahedra are plotted in light blue. The mean distortion amplitudes for TiO_6 are shown as a light grey triangle. Data corresponding to NbO_6 octahedra are plotted in dark blue. The mean distortion amplitudes for NbO_6 is shown as a black triangle.

multi-principle element refractory alloys. Their open crystal structures, however, make them unsuited as protective oxide scales for corrosive or high temperature structural applications and strategies are desired to suppress their formation in favor of more dense and protective oxide scales.

In this work, we have analyzed and classified Wadsley-Roth phases and developed approaches to systematically enumerate an important subset of their crystal structures. We have extended Cava's naming scheme [15] to be more precise and descriptive by adding specifications for the block size and relative offset of neighboring blocks. By systematically enumerating the structures of two subclasses of Wadsley-Roth phases we have been able to identify relationships between important oxide crystal structures that were not previously evident. These are summarized in Figure 3.3.

A calculation of the energies of systematically enumerated Wadsley-Roth crystal structures in the Nb-O and Ti-Nb-O composition spaces has highlighted two predominant factors that determine phase stability among Wadsley-Roth structures. The first is the importance of the number of edge-sharing octahedra, which each contribute an energy cost due to the electrostatic repulsion between pairs of metal cations in high oxidation states. First-principles DFT calculations show that the Wadsley-Roth crystal structures that minimize the number of edge-sharing octahedra at a fixed oxygen to metal ratio are energetically preferred. Similar interactions involving edge-sharing octahedra also affect ordering preferences among cations with different oxidation states. Mixtures of Ti^{4+} and Nb^{5+} over the cation sites of Wadsley-Roth phases perfer orderings that minimize the average number of shared edges per Nb^{5+}. This leads to low energy orderings in which Ti^{4+} segregates to the block edges, where the edge-sharing octahedra reside, while Nb^{5+}, with its higher oxidation state, segregates to the corner sharing octahedra at the center of the blocks and to octahedra with the lowest number of shared edges.

A second factor affecting phase stability is related to structural features that restrict

the degree with which edge-sharing cations and individual octahedra can distort. The flexibility with which the cations and anions of the Wadsley-Roth phase are able to distort to lower their energy is negatively correlated with the number of shared octahedral edges that reside within the $\hat{x} - \hat{y}$ plane. Wadsley-Roth structures of type E with increasing relative block shifts accumulate a greater number of shared octahedra that lie within the $\hat{x} - \hat{y}$ plane, and as a result have less flexibility to relax and lower their energy.

An analysis of the octahedral distortions of the different Ti-Nb orderings within $TiNb_2O_7$ has shown that two types of octahedral distortions dominate. The first, as described by the Γ_V irrep octahedral distortion mode, involves a warping of equatorial oxygen as illustrated in the inset of Figure 3.9. This type of distortion is manifested most strongly by the edge-sharing octahedra and is a distortion that allows for an increase in the distance between edge-sharing transition metals (Figure 3.9). This type of distortion is especially large in the anatase form of TiO_2 as shown in Figure 3.26(a). It is also an important distortion mode of the edge-sharing octahedra in other polymorphs of Nb_2O_5 (Figure 3.26(a)). As is revealed in Figure 3.9 the octahedra of $TiNb_2O_7$ containing Ti tend to distort more strongly than those containing Nb, which is consistent with the trends exhibited in Figure 3.26(a) for other polymorphs of TiO_2 and Nb_2O_5. All distortion amplitudes for these Nb_2O_5 and TiO_2 phases can be found Figure 3.27.

Early transition metals in their maximum oxidation states, such as Ti^{4+} and Nb^{5+}, are susceptible to second order Jahn-Teller distortions when octahedrally coordinated by anions such as oxygen. The second-order Jahn-Teller distortion leads to an off-centering of the transition metal cation within the oxygen octahedron, a distortion that is described by the Γ_{VI} irrep . Both the Nb and the Ti cations exhibit a sizable off-centering when occupying the corner sharing octahedra at the center of the block, however, Nb exhibits slightly larger distortions. The off-centering becomes more pronounced in edge-sharing octahedra as a result of the electrostatic repulsion with neighboring cations.

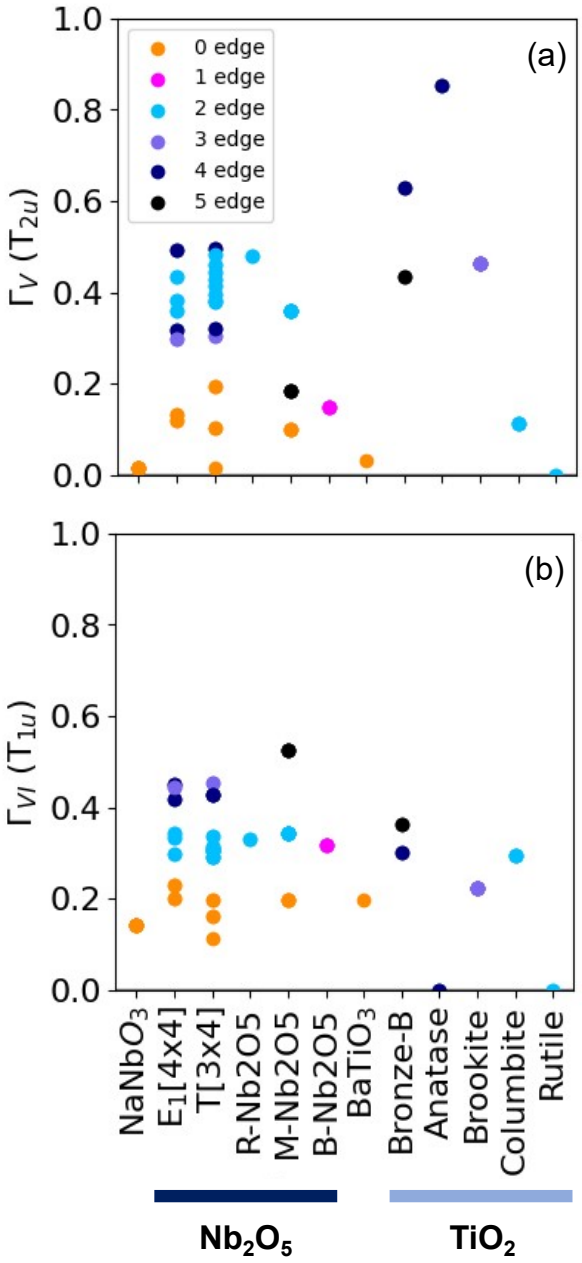

Figure 3.26: (a) Γ_V magnitudes for octahedra in experimentally synthesized Nb-O [157, 104, 117, 103] and Ti-O compounds [158, 159, 160, 161, 162] where the transition metal is at a maximum oxidation state. (b) Γ_{VI} magnitudes for octahedra in experimentally synthesized Nb-O and Ti-O compounds where the transition metal is at a maximum oxidation state.

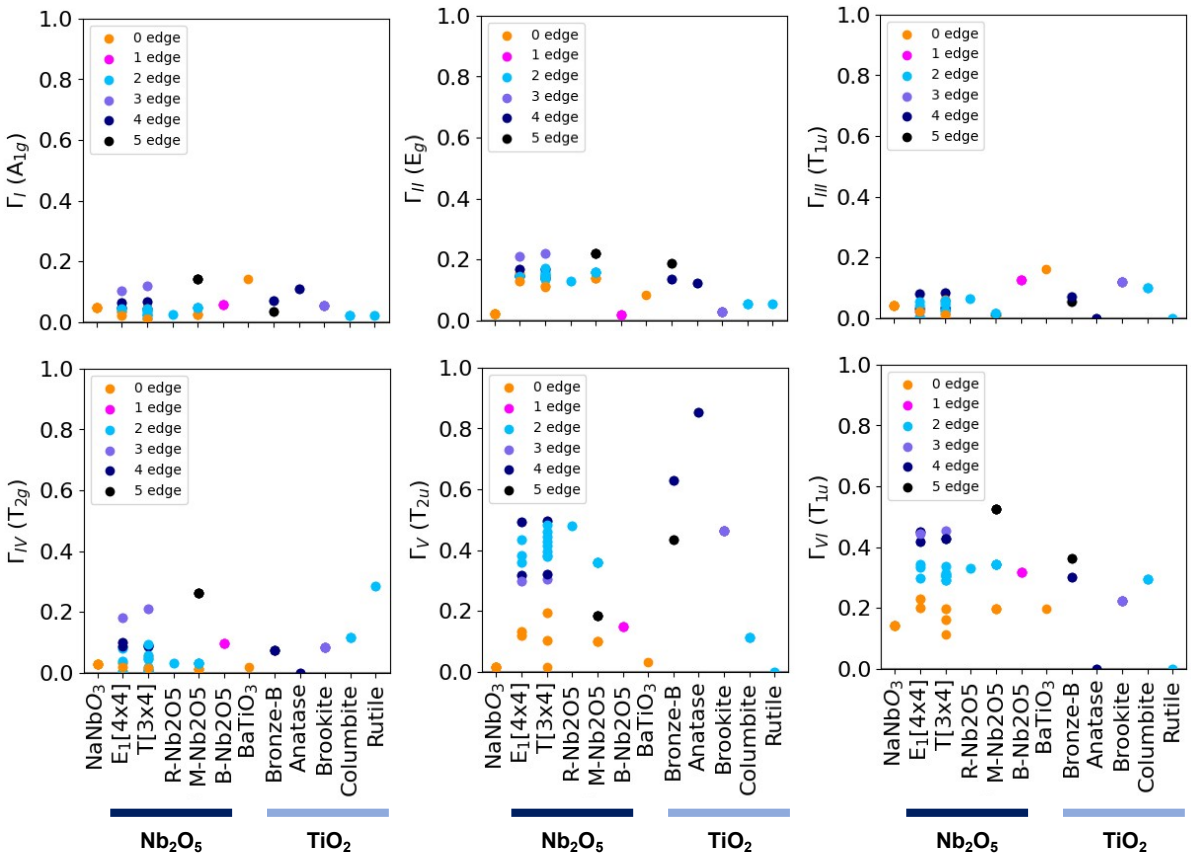

Figure 3.27: Distortion amplitudes for differing experimentally formed Nb-O compounds with Nb in its full oxidation state and Ti-O compounds with Ti in its full oxidation state.

3.5 Conclusion

We have presented a systematic way to generate an extensive subset of Wadsley-Roth block structures and link them to a wide range of experimentally observed and technologically important oxide crystal structures. This new perspective unifies a diverse range of structures from rocksalt to bronze TiO_2 to the perovskite framework of WO_3.

The study of structures with different relative block offsets revealed the two forces which drive phase stability: (1) minimizing electrostatic repulsion between the highly oxidized metal cations by reducing edge sharing interactions, and (2) maximizing the energy-reducing octahedral distortions by limiting the number of in-plane edge sharing interactions. These competing factors strongly favor the E_1 structures across all block geometries in the Nb-O system, and we predict that this trend would continue for structures composed of other metal cations.

Through a high throughput study of the Ti-Nb-O phase space, we examine the factors that affect stability in in the Nb-O and Ti-Nb-O Wadsley-Roth phases. Through these methods we find that electrostatics are the largest cause of phase stability in the Wadsley-Roth phases and that octahedral distortions are a secondary cause of phase stability of specific Wadsley-Roth shift types and orderings on the transition metal sublattice. Additionally we find that of that the relative energy of Ti-Nb-O Wadsley-Roth phases follows a linear trend with respect to the fraction of edge sharing on Nb containing octahedra. Characteristic distortions in Wadsley-Roth phase octahedra are quantified. These distortions show that Wadsley-Roth phases induce distortions that are linearly correlated to the amount of octahedral edge sharing. The results is a tendency for the Ti ions with the lower 4+ oxidation state to occupy edge sharing octahedral sites while the Nb^{5+} ions tends to prefer central corner-sharing octahedra. We expect this trend to be repeated in other alloyed Wadsley-Roth structures, where the cations with lower oxidation

states accumulate in edge sharing sites along the crystallographic shear boundary.

The Nb-O and Ti-Nb-O Wadsley-Roth structures as well as other structures discussed including the bronze TiO_2 phase and PNb_9O_{25} are of great interest for energy storage applications. The geometry of the Wadsley-Roth crystal structure and the ordering of the metal cations on their lattice can greatly impact the kinetics and thermodynamics of lithiation. This improved understanding of the factors which determine cation ordering in these complex phases will aide in the prediction and tuning of these characteristics for future energy storage materials.

Chapter 4

Role of Electronic Structure in Li Ordering and Chemical Strain in the Fast Charging Wadsley–Roth Phase PNb_9O_{25}

We continue this thesis with an examination of the thermodynamic and structural properties of a single Wadsley-Roth phase, PNb_9O_{25}. When used as anode material, PNb_9O_{25} has shown high cyclic reversibility at up to 60C charge rates. This section probes what thermodynamic and structural factors may be changing while the structure is lithiated and delithiated using ab initio calculations and semi-grand canonical Monte Carlo calculations.

4.1 Introduction

Secondary lithium-ion batteries have become a standard for portable electronics and electric vehicles due to their reliability, high cycle lives, and high efficiencies [163]. Despite their widespread use, Li-ion batteries continue to face challenges in high-power applications, where they have a propensity for thermal runaway reactions due to the formation of lithium dendrites on the anode during fast charging [164, 165, 166, 167]. The Li dendrites can pierce the separator and lead to direct contact between the anode and the cathode, thereby increasing explosion risks. These safety concerns put constraints on the charging times of Li-ion batteries, which limits their use in mobile applications, including electric and hybrid electric vehicles. There is, therefore, a tremendous interest to identify new anode chemistries that are able to rapidly intercalate large quantities of Li and at a slightly higher voltage than the voltage window of graphite based anodes.

The Wadsley-Roth crystallographic shear phases have received much attention in recent years due to their ability to intercalate Li at exceptionally high rates [97] and at voltages that make them viable anode materials. The early studies of lithium insertion into 14 different Wadsley-Roth chemistries by Cava *et al.* [15] demonstrated their ability to accommodate multielectron reduction and oxidation, thereby enabling higher energy densities when compared to intercalation compounds that exchange only one electron per redox center. More recent studies of the electrochemical properties of the Wadsley-Roth chemistries, including VNb_9O_{25} [148, 28], $TiNb_2O_7$ [168, 169, 137, 16], $Ti_2Nb_{10}O_{29}$ [170, 123], $Nb_{12}O_{29}$ [106, 105], $Nb_{12}WO_{33}$ [171, 172], $Nb_{14}W_3O_{44}$ [111, 173], $Nb_{16}W_5O_{55}$ [143], H-Nb_2O_5 [174, 103], and T-Nb_2O_5 [175, 176, 177], have further confirmed their high capacities and high rate capabilities.

Despite their favorable electrochemical properties, very little is known about the crystallographic changes, electronic structure, and lithium ordering tendencies of Wadsley-

Roth phases as a function of Li concentration. Here we report on a combined first-principles and experimental study of the structural and electrochemical properties of the PNb_9O_{25} Wadsley-Roth phase. First studied as an electrode material for Li-ion batteries by Patoux et al. [148], recent cycling data has shown that PNb_9O_{25} can reversibly cycle for over 500 cycles at a rate of 2C, which corresponds to a thirty minute charge or discharge when tested in a half-cell against lithium [28]. These half-cells were able to maintain a gravimetric capacity of 190 $mAhg^{-1}$. PNb_9O_{25} has also been shown to reversibly cycle up to rates of 60C, though with lower capacities and Coloumbic efficiencies. The insertion of Li into PNb_9O_{25} activates not only the $Nb^{5+/4+}$ redox couple, but also the $Nb^{4+/3+}$ couple [28, 148]. A Li:Nb ratio above 1 can, therefore, be achieved, which is greater than the Li to transition metal ratio of 1 that limits the capacity of most other transition metal oxide intercalation compounds. The open structure of PNb_9O_{25} allows for rapid lithium diffusion while operating in a potential window between 2V and 1V and accommodates approximately 11.5 Li when cycled at a C/20 rate against Li. The higher operating voltage window of PNb_9O_{25} makes it possible to discharge this electrode chemistry at higher current densities than graphite based anodes that operate at an average potential of 0.1V [178].

Our systematic study of the electrochemical properties of PNb_9O_{25} as a function of Li concentration reveals a complex site filling sequence that is strongly influenced by the chemical strain induced by changes in the electronic structure that accompany Li insertion. PNb_9O_{25} can host Li in three pyramidal sites and two window sites. The pyramidal sites are filled first, but are then slightly depopulated in favor of window sites. We identify a favorable Li ordering motif over the vertical window sites that forms a persistent backbone at intermediate to high Li concentrations, with the remaining sites accommodating Li through a solid solution. We find that the ordered motif becomes stable after the host undergoes a tetragonal strain due to the delocalization of donated

electrons over the d orbitals of edge-sharing Nb cations. Our results show a strong coupling between changes in electronic structure and variations in structural and chemical properties as a function of Li concentration.

4.2 Methods

4.2.1 First-principles statistical mechanics calculations

Density Functional Theory (DFT) calculations were performed with the Vienna Ab initio Simulation package (VASP) [124, 125, 126, 127] and were used to predict the energies of different lithium-vacancy orderings in $Li_xPNb_9O_{25}$. The generalized gradient approximation (GGA) as formulated by Perdew, Burke, and Ernzerhoff (PBE) [44] was used. The SCAN meta-GGA [56, 179] functional was also used to assess the sensitivity of the predictions to the exchange-correlation approximation. This analysis can be found in Figure 4.1. The interactions between the valence and core electrons was treated with the projector augmented wave (PAW) theory [128, 46] and a plane wave energy cutoff of 550eV was used. A fully automatic k-point mesh setting corresponding to a 2×2×7 Monkhorst-Pack grid was used for the primitive unit cell. Crystal structures and charge densities were visualized with VESTA [180]. A charge density isosurface of 0.004 $Å^{-3}$ were used for all calculations.

The electrochemical properties associated with Li insertion into PNb_9O_{25} were studied with a cluster expansion approach in combination with Monte Carlo simulations using the CASM code [131, 130, 69, 129]. The PNb_9O_{25} unit cell contains 20 stable lithium sites. Without taking symmetry into account, there are over 1 million different Li-vacancy orderings over the sites of the primitive unit cell of PNb_9O_{25}. This number of Li-vacancy orderings increases considerably within supercells of PNb_9O_{25}. To sample

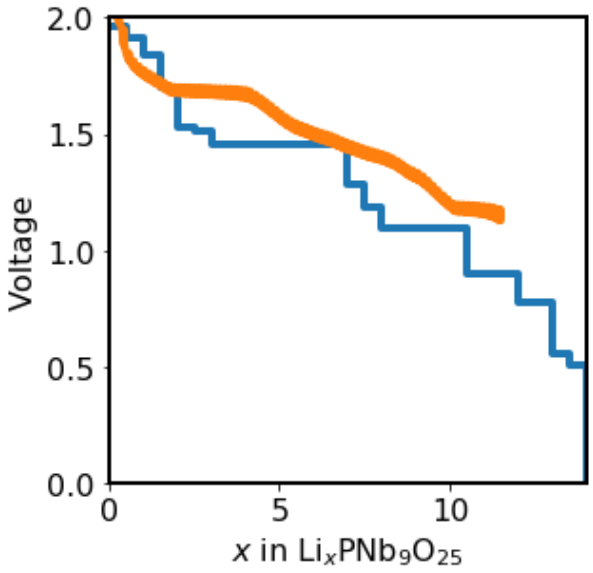

Figure 4.1: Voltage curve at 0 Kelvin (blue lines) as calculated with SCAN along with the experimental voltage curve at room temperature (orange curve). Energies were calculated for the ground states as determined with DFT-PBE. Vertical lines correspond to stable ground states and horizontal lines correspond to two-phase regions. SCAN predicted voltages are overall higher than those predicted with PBE.

important Li-vacancy configurations, we used an iterative approach whereby the energies of an initial sampling of Li-vacancy configurations were used to parameterize a cluster expansion, which was subsequently used to identify low-energy Li-vacancy configurations. The cluster expansion fit was iteratively improved with every batch of new low-energy orderings. Cluster expansion Hamiltonians were used in Monte Carlo simulations to predict finite temperature thermodynamic properties such as the voltage curve [69, 2, 181, 182, 183, 184, 185, 186, 187, 188, 189, 190].

4.2.2 Experimental Methods

Materials preparation

PNb_9O_{25} was prepared using traditional solid-state methods. Stoichiometric ratios of $(NH_4)_3PO_4$ (Sigma Aldrich, 98%) and Nb_2O_5 (Materion, 99.95%) were ground together

using an agate mortar and pestle for 20 minutes. The resulting powder mixture was pressed into a 13 mm pellet under 2.5 tons of force with a total mass of 1.5 g. The pellet was placed into an alumina crucible on a bed of the powder mixture and annealed at 623 K in air. After 20 hours, the furnace was adjusted to 1523 K, and the pellet annealed for another 18 hours. The pellet was slow-cooled in the atmosphere of the furnace and reground in a mortar and pestle for use. Additional descriptions can be found in previous work [28, 148].

Electrochemical characterization

The material was ball-milled in a 5 mL stainless steel grinding vial with SuperP (TIMCAL). A slurry was prepared by speedmixing a polyvinylidene fluoride binder (Kynar, Arkema) with N-methyl-2-pyrrolidone at 2000 rpm for 10 minutes until dissolved. Then the active material and SuperP mixture was added to the mixture and speedmixed at 2000 rpm for 10 minutes until a uniform suspension was formed. The resulting viscosity was equivalent to honey, and the ratio of active material:carbon:binder was 72:18:10 by weight. The mixture was cast onto Cu foil using a doctor blade set to 150 μm and dried under vacuum at 90 deg C. 10 mm diameter discs were punched, and a typical mass loading is 1.5 mg/cm ^{2}. 2032 coin cells were assembled in an Ar-filled glovebox (H_2O < 0.1 ppm, $O_2 < 0.1$ ppm) using a polypropylene separator (Celgard 2500) and flooded with 1 M $LiPF_6$ in ethylene carbonate/dimethyl carbonate (EC/DMC, Sigma Aldrich). Polished Li discs were used as a combined counter and reference electrode. Galvanostatic intermittent titration technique (GITT) was performed using a VMP3 potentiostat (Bio-logic) at a rate of C/40 with a 30-minute current step and 90-minute rest periods between a voltage window of 1 – 3V. To be consistent with prior work on $Li_xPNb_9O_{25}$, [28], we calculate the rate based on 12 Li ions inserted into the formula PNb_9O_{25}, such that C/40 = 12Q/40 = 254 mAh g^{-1} /40 h = 6.35 mA g^{-1}. We point out, however, that

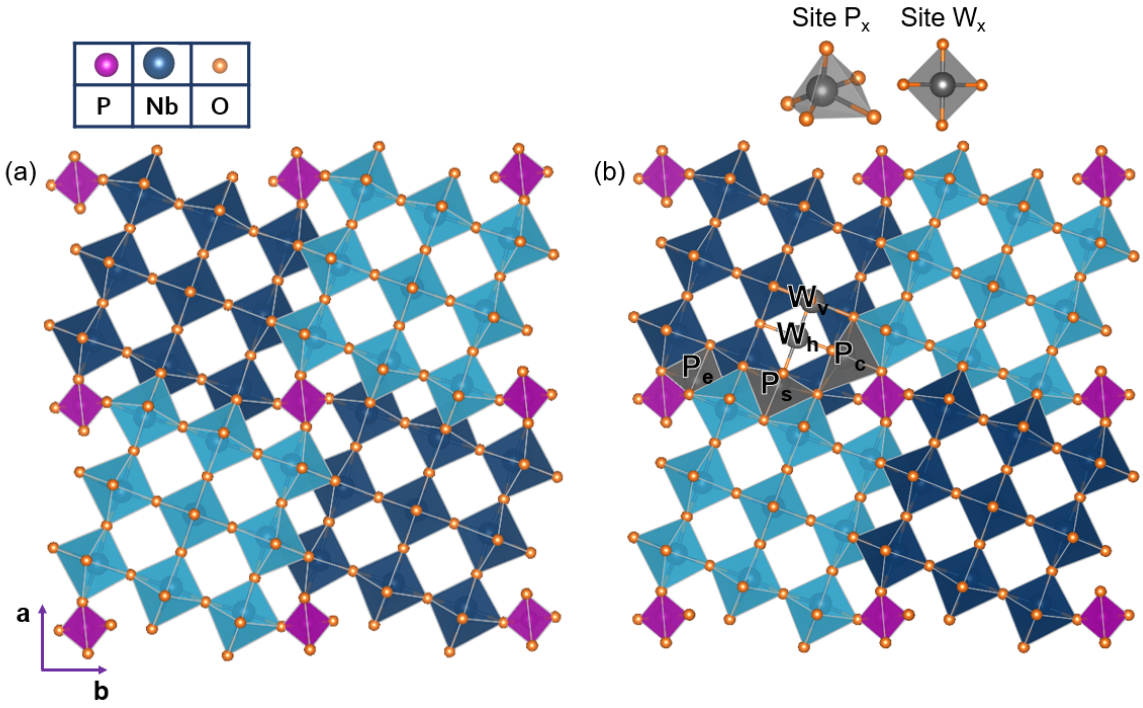

Figure 4.2: (a) The crystal structure of PNb_9O_{25} as viewed down the c axis. The octahedra correspond to the NbO_6, the tetrahedra correspond to PO_4. (b) The triangular and square polyhedra show one example of each symmetrically distinct lithium site.

the maximum theoretical capacity based on crystallographically available Li sites is 20 per PNb_9O_{25} formula unit.

Neutron scattering and refinements

In order to produce ex-situ material at differing states of lithiation, PNb_9O_{25} was electrochemically cycled as loose powder that was mechanically ball milled with SuperP (TIMCAL) in a 5 mL stainless steel can for 30 minutes (80% active material by weight). Approximately 200 mg of the mixture was carefully loaded onto a stainless steel plunger of a swagelok cell with a 1.5 inch diameter. The powder was compacted with two glass fiber separators (Whatman GF/D) cut to size and compressed with another plunger. The cells were assembled in an Ar-filled glovebox ($H_2O < 0.1$ ppm, $O_2 < 0.1$ ppm) us-

ing enriched ^{7}Li as the counter electrode (Sigma Aldrich) and enriched $^{7}LiPF_6$ (Sigma Aldrich) made into a 1 M electrolyte solution in 1:1 v/v EC/DMC (Sigma Aldrich). The cells were cycled at a rate of C/80 to ensure expected lithiation in the bulk, loose powder format. The first cell was cycled to 1.695 V (OCV = 3.1 V, 1.5 Li inserted), and the second cell was cycled to 1.635 V (OCV = 3.2 V, 4.3 Li inserted). The Galvanostatic discharge profiles are provided in Figure 4.3. The cells were deconstructed in the Ar-filled glovebox, and the cycled materials were scraped off of the stainless steel plunger. The powders were washed three times in dimethyl carbonate and dried under vacuum. Once dry, they were loaded into glass capillaries as provided by the mail-in program at NOMAD (BL-1B, Spallation Neutron Source, Oak Ridge National Laboratory), where the time-of-flight data was collected at room temperature (Figure 4.4). Rietveld refinements on the diffraction data were done using GSAS-II using both banks 4 and 5 [191]. The non-lithiated structure was refined using the previously-reported structure solution for PNb_9O_{25} (space group I4/m, 87) [192]. Both atomic positions and atomic displacement parameters were allowed to refine. The lithiated structures were refined by placing Li onto the expected Wyckoff positions within the parent structure based on the predicted structures from the DFT calculations. The structure was first refined against the original PNb_9O_{25} structure without Li. Then, Li was systematically placed onto each of the 5 identified sites, separately. Position (except special positions), isotropic atomic displacement parameters, and lattice parameters were allowed to refine. All occupancies, including Li, were fixed to the nominal stoichiometry as derived from the electrochemical experiments. The unphysical results were separated from the physical results to identify the plausible experimental structures. For all patterns, backgrounds were initially fit graphically with a 36-term polynomial to account for the amorphous nature of the carbon additive and left fixed for the remainder of the refinements. Visualizations of the crystal structures from the resulting cif files were done using VESTA [180]. Partial pair

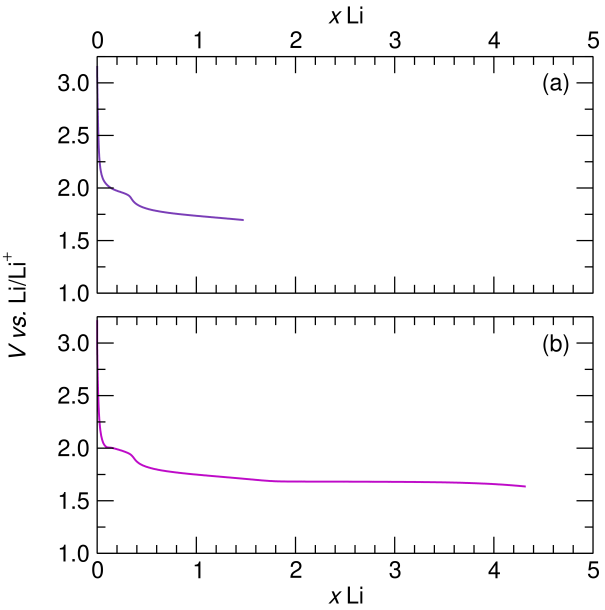

Figure 4.3: Galvanostatic discharge of PNb_9O_{25} in large format, loose powder Swagelok cells. Each cell contained an average of 200 mg of the electrode mixture (160 mg of active material). The cells were discharged at a rate of C/80 with a lower voltage cutoff of (a) 1.695 V and (b) 1.635 in order to capture the structural changes before and after the main plateau at 1.65 V. The electrochemistry seen here directly corresponds to the samples used for all of the refinements.

distribution functions can be found in Figure 4.5 and were calculated using the PDFgui program [193].

4.3 Results

4.3.1 Lithium site preferences and lithium ordering

The PNb_9O_{25} compound is a member of the Wadsley-Roth family of crystallographic shear phases [22, 194, 171, 195]. The PNb_9O_{25} unit cell, shown in Figure 4.2(a), consists of $3 \times 3 \times \infty$ blocks of corner-sharing NbO_6 octahedra that are connected to each other by edge sharing NbO_6 octahedra along each block periphery. The blocks are offset along the a and b lattice vectors, allowing for a tetrahedral PO_4 site at the block corners. There are

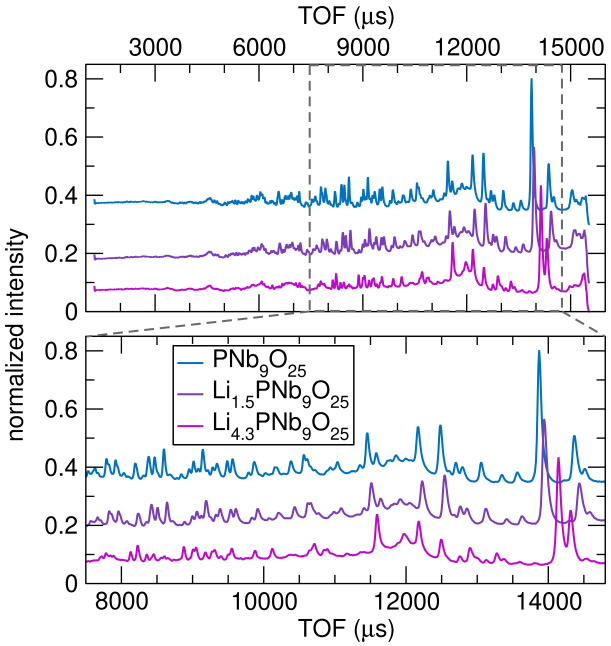

Figure 4.4: Time-of-flight data for PNb_9O_{25}, $Li_{1.5}PNb_9O_{25}$, and $Li_{4.3}Nb_9O_{25}$ collected at the Spallation Neutron Source at Oak Ridge National Lab (NOMAD, wavelength = 1.4 Angstroms) (a) in the full range of data collection for bank 5, and (b) the selected range used for refinements. The range was chosen to capture a consistent range of complete, well-defined peaks between all samples.

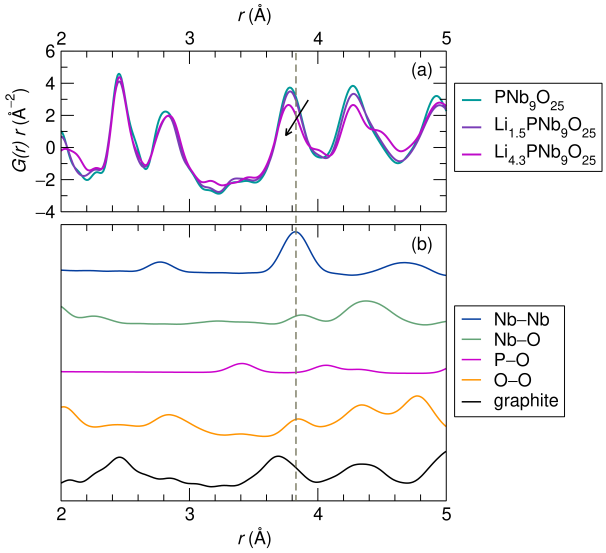

Figure 4.5: (a) Neutron pair distribution function data of PNb_9O_{25}, $Li_{1.5}PNb_9O_{25}$, and $Li_{4.3}PNb_9O_{25}$ from 2-5 Å. The arrow points to the shifting of the peak at 3.8 Å to shorter distances. (b) Calculated atomic distances for all of the atom pairs from the known crystallographic structure of PNb_9O_{25} (space group I 4/m, 87) showing the deconvolution of each peak. The peak centered at 3.81 Å corresponds to the Nb-Nb atomic distance, marked with a grey dashed line. The shift in the peak at 3.8 Å in $Li_{4.3}PNb_9O_{25}$ to shorter distances supports the result from DFT that Nb-Nb distances become shorter with lithiation.

two symmetrically equivalent tetrahedral sites per unit cell, one above the other along the c axis, that can be occupied by P. In experimentally prepared samples, P fills these sites with equal probability, leading to a partial occupancy of 0.5. In all our calculations, we picked one of the two sites, and thereby work with a model that has an increased degree of order and hence a lower symmetry. Furthermore, the experimentally refined structure of PNb_9O_{25} has the Nb at the center of the block distributed over two off-centered positions with partial occupancies of 0.5. These off-centered positions cannot be simultaneously occupied by two Nb. In all our calculations, the position of the Nb at the center of the block was initialized at the geometric average of the off-centered positions.

We have identified five symmetrically distinct candidate lithium sites in PNb_9O_{25}. An example of each type of site is shown in Figure 4.2(b). The P_e, P_c and P_s sites are pyramidally coordinated by oxygen and reside along the block periphery. Each P_e site shares an edge with a PO_4 tetrahedron while each P_c site shares a corner with a PO_4 tetrahedron. The P_s sites are located in the middle of the block periphery and are coordinated by six NbO_6 octahedra. Li can also reside in two symmetrically distinct window sites: the vertical W_v sites and the horizontal W_h sites. These sites reside in the interior of the $3 \times 3 \times \infty$ blocks of corner-sharing NbO_6 octahedra and are each coordinated by a planar square of oxygen ions. Each of the five symmetrically distinct Li sites have a multiplicity of four per unit cell. The stability of pyramidal and window sites in PNb_9O_{25} is consistent with past neutron diffraction and first-principles studies by Catti et al. [196, 197, 198] and Morris et al. [143, 98] of other Wadsley-Roth phases.

We first investigated Li site preferences at very dilute Li concentrations. All symmetrically distinct arrangements of a single Li within a super cell containing two units of PNb_9O_{25} stacked along the c-axis were enumerated. This corresponds to a Li concentration of x=0.5 in $Li_xPNb_9O_{25}$. Figure 4.6(a) shows their energies as calculated with DFT-PBE. At this very dilute concentration, Li prefers the pyramidal P_s sites. The

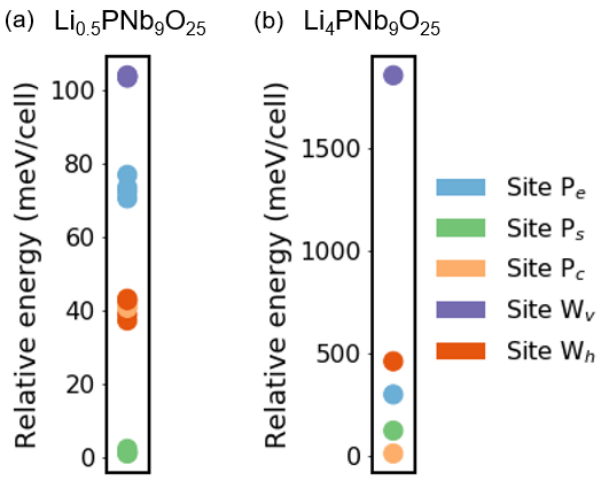

Figure 4.6: (a) Energies per unit cell of different Li-vacancy orderings in $Li_xPNb_9O_{25}$ at x=0.5. The energies were calculated with DFT-PBE in a super cell containing 2 unit cells stacked along the c-axis. The lowest energy configuration was chosen as the reference (i.e. the zero of the energy scale). P_e, P_s, and P_c refer to different pyramidally coordinated Li sites (b) Energies per unit cell of $Li_xPNb_9O_{25}$ at x=4, in which all symmetrically equivalent sites of a particular Li site are completely filled.

least favored site is the vertical window site W_v. The Li site preference changes upon the addition of more Li. This is evident in Figure 4.6(b), which shows the energy at x=4 in which all four symmetrically equivalent sites of each type of Li site are filled. At this concentration, the P_c sites are preferred over the P_s sites. Note the large change in energy scale in Figure 4.6(b) compared to that in Figure 4.6(a).

We further explored Li site preferences and ordering tendencies over the whole composition range $0 < x < 20$ in $Li_xPNb_9O_{25}$ by calculating the formation energies of 4298 Li-vacancy orderings over all five candidate Li-sites within differently sized super cells with DFT-PBE. The calculated formation energies are shown in Figure 4.7. The majority of these orderings were enumerated with CASM [129, 130, 199, 131] using the cluster expansion in an iterative approach to identify low-energy Li-vacancy orderings within $Li_xPNb_9O_{25}$. To highlight changes in site preference as a function of Li concentration, we have color-coded configurations based on their site occupancies. The three formation

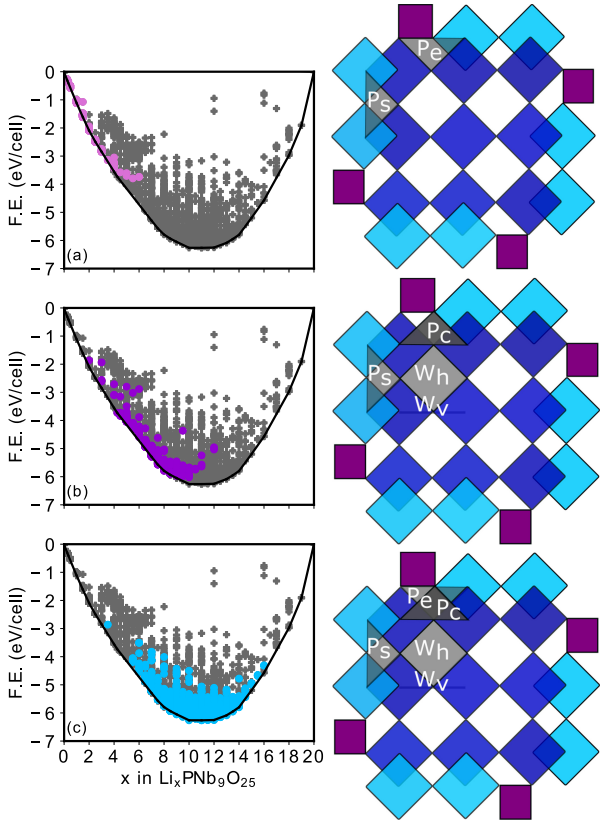

Figure 4.7: Calculated formation energies of 4298 Li-vacancy orderings within $Li_xPNb_9O_{25}$. (a) Configurations in which Li only occupies the P_s and/or P_e sites are highlighted. (b) Configurations with some degree of Li occupancy of the P_c sites as well as W_h and/or W_v sites are highlighted. (c) Configurations with all P_c sites filled by Li and a partial filling of P_s, W_h and/or W_v sites by Li are highlighted.

energy plots and the accompanying schematics show which site types are filled in the lowest energy orderings in three separate composition intervals.

At low compositions ($0 < x < 3$), the low energy Li-vacancy orderings have Li occupying the P_s and/or P_e sites. The energies of these configurations are shown in pink in Figure 4.7(a). A site preference inversion occurs at x=4 where the lowest energy Li-vacancy ordering has three Li per unit cell occupying the P_c site and one Li per unit cell occupying the P_e site. Beyond x=4, the P_s and P_e sites are no longer preferred and all ground states and low energy orderings have completely filled P_c sites. Furthermore, both the horizontal and vertical window sites, W_h and W_v, which are not favored at

dilute Li concentrations, start filling as more Li is added. The energies of orderings with P_c, W_h and W_v partially or fully filled are shown in purple in Figure 4.7(b). As the Li concentration increases further, the P_s sites start filling again in the low energy orderings. The energies of configurations in which all the P_c sites are filled and where the W_h, W_v and P_s sites are fully or partially occupied are shown in light blue in Figure 4.7(c).

An intriguing feature about the ground states and a large number of low energy orderings in the interval $7 < x < 14$ is that almost all share a common Li-vacancy ordering over the W_v vertical window sites. This ordering leads to a doubling of the unit cell along the c-axis and can be described as an interweaved pattern with pairs of occupied W_v sites alternating their orientation by 90^o upon moving along the c-axis as shown in Figure 4.8. The composition at which this ordering can set in is x=6, with all four P_c sites and two of the four W_v sites filled per unit cell. Additional Li is then accommodated by the gradual filling of the horizontal W_h sites followed by the P_s sites. Schematics of the ground state orderings can be found Figures 4.3.1, 4.3.1, 4.3.1, 4.3.1, and 4.3.1.

The convex hull connecting the formation energies of the ground state orderings can be used to calculate the voltage profile of $Li_xPNb_9O_{25}$ relative to a pure Li anode at zero kelvin. The slopes along the convex hull are linearly related to the Li chemical potential μ_{Li}, which in turn determines the voltage according to the Nernst equation [2]. Figure 4.14 shows the zero kelvin voltage curve of $Li_xPNb_9O_{25}$. Each step corresponds to a stable Li-vacancy ordering over the sites of $Li_xPNb_9O_{25}$, while the plateaus represent equilibrium voltages at which one stable Li-vacancy ordering transitions to another through a two-phase reaction. The plot also summarizes the site preference in the ground state orderings as a function of Li concentration, clearly showing a dramatic shift in site preference between x=3 and $x \approx 4$ through a two-phase reaction. The interweaved ordering of Figure 4.8 sets in around x=7 and is present in most subsequent ground states

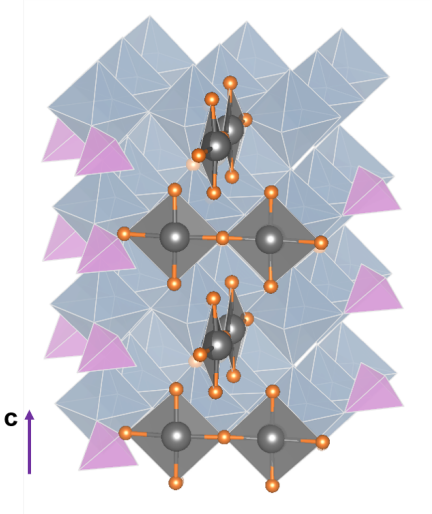

Figure 4.8: The interweaved Li-vacancy ordering over the W_v sites that forms the backbone of all ground states as predicted with DFT-PBE between x=7 and x=14. The ordering consists of pairs of occupied W_v sites that alter their orientation by 90^o upon moving along the c axis.

up to x=14.

4.3.2 Electrochemical properties at Finite Temperatures

We next explored the effect of temperature and thermal excitations on the electrochemical properties of $Li_xPNb_9O_{25}$ using statistical mechanics approaches that rely on the cluster expansion method and Monte Carlo simulations. The inclusion of the effects of temperature facilitates comparisons to experimentally measured electrochemical properties. We only considered configurational degrees of freedom associated with the many possible ways of arranging Li and vacancies over the sites of $Li_xPNb_9O_{25}$. The cluster expansion approach was used to extrapolate the DFT-PBE formation energies of Figure 4.7 within Monte Carlo simulations. More details about this approach can be found elsewhere [69, 2].

Two separate cluster expansions were trained using the formation energies calculated with DFT-PBE. The first cluster expansion was restricted to the P_s and P_e sites and

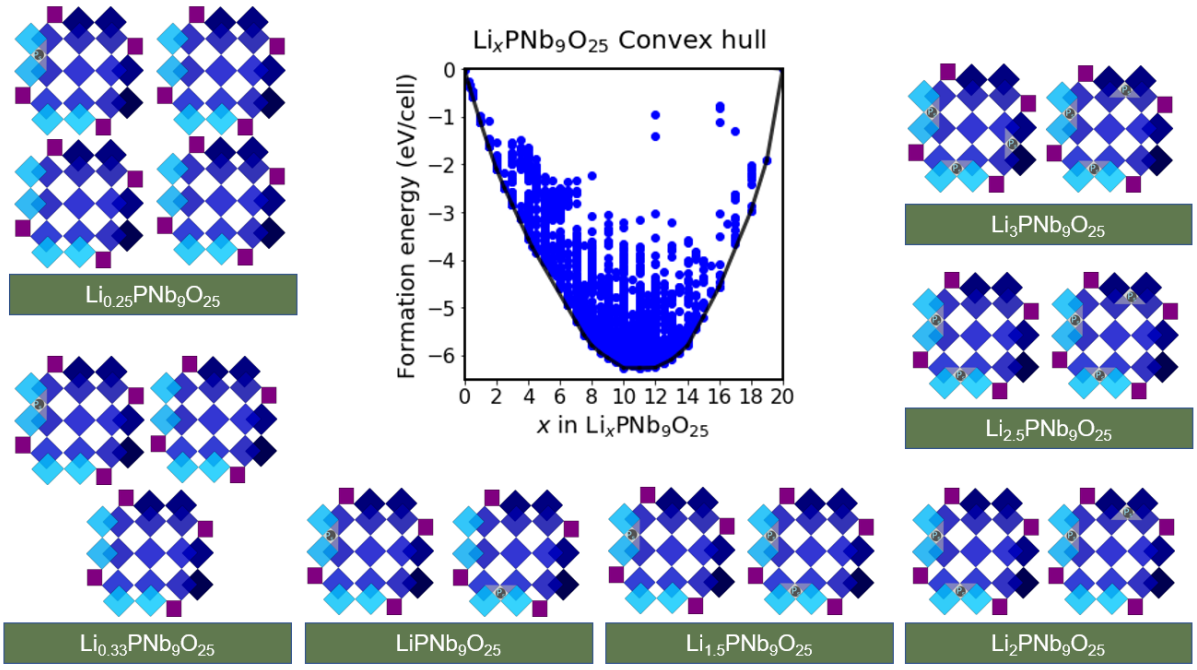

Figure 4.9: Formation energies and schematics of ground state orderings of $Li_xPNb_9O_{25}$ at low compositions as determined with DFT-PBE calculations. The Li ions of the ground states at low compositions exclusively fill P_s sites. Many ground states are Li-vacancy orderings in super cells of the primitive cell obtained by doubling (or quadrupling in the case of $Li_{4.25}PNb_9O_{25}$) the primitive cell c axis. Orderings in each layer are shown side by side.

was used to calculate electrochemical properties at low Li concentrations, where these sites are preferred. A second cluster expansion was constructed that explicitly treated Li occupancy on the W_h, W_v and P_s sites while keeping the P_c sites filled. This cluster expansion was used to predict finite temperature properties between x=4 and x=16, where as predicted by the DFT formation energies of the previous section, all low energy configurations (with the exception of the ground state at x=4) have completely filled P_c sites and varying degrees of Li occupancy over the W_h, W_v and P_s sites. Details about the cluster expansion fits can be found in Figures 4.15 and 4.16.

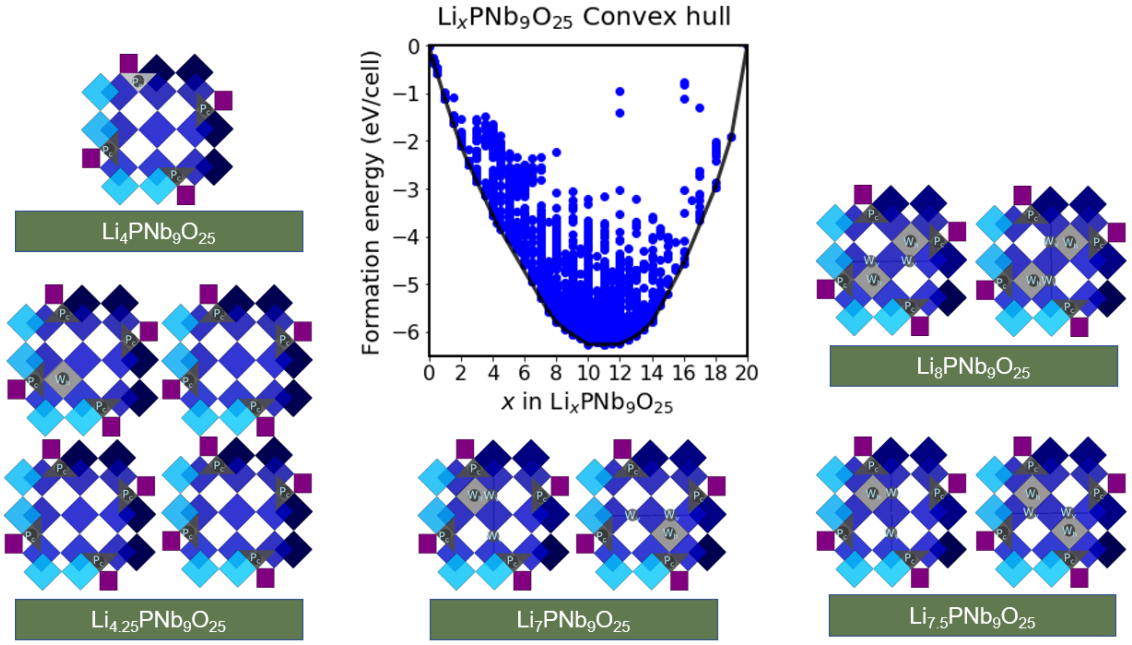

Figure 4.10: Formation Energies and schematics of ground state orderings of $Li_xPNb_9O_{25}$ at intermediate compositions as determined with DFT-PBE calculations. Between compositions of x=4 and x=8, Li no longer fills P_s sites, but instead fills P_c sites. The interweaved ordering over the W_v sites is stable at compositions greater than x=7.

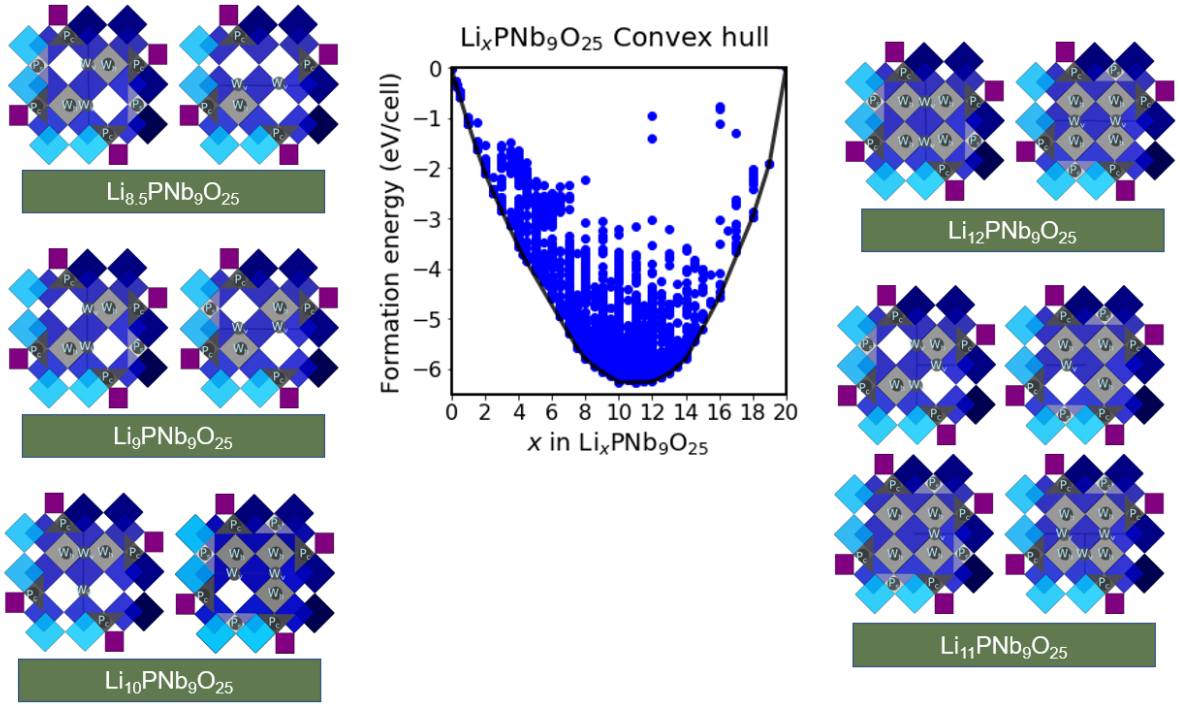

Figure 4.11: Formation energies and schematics of ground state orderings of $Li_xPNb_9O_{25}$ at intermediate compositions as determined with DFT-PBE calculations. Between compositions of x=8.5 and x=12, Li fills P_s sites in addition to the P_c sites and the window sites. The interweaved ordering over the W_v sites is stable in most ground states in this composition range.

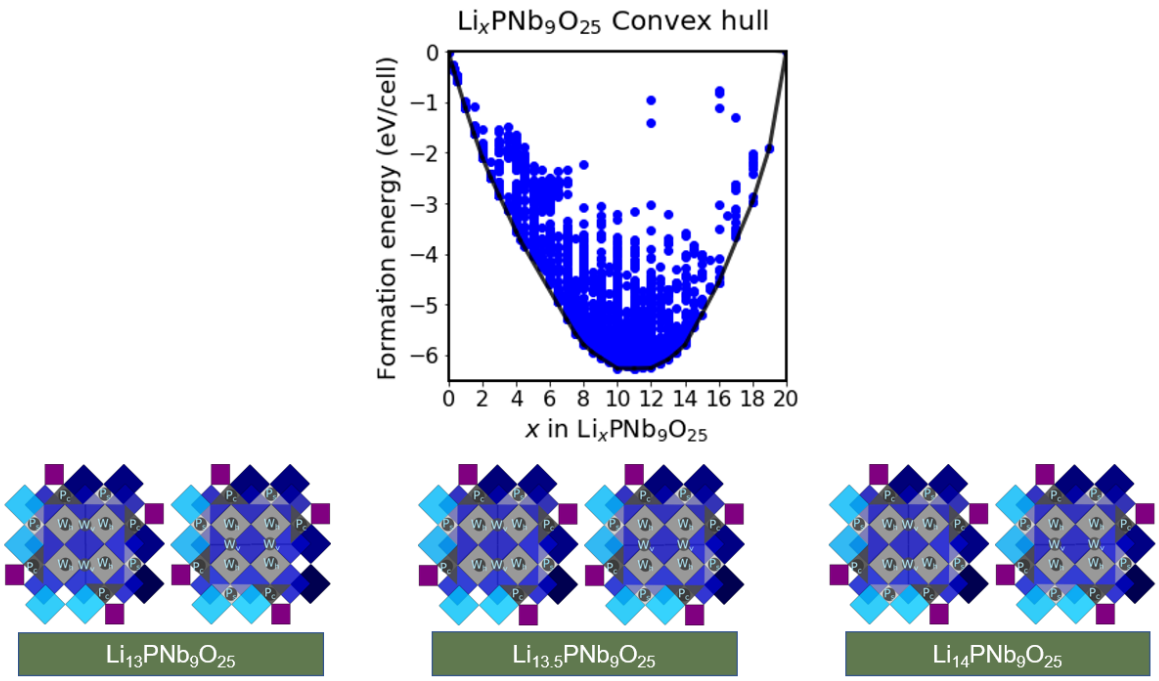

Figure 4.12: Formation energies and schematics of ground state orderings of $Li_xPNb_9O_{25}$ between x=13 and x=14 as determined with DFT-PBE calculations.

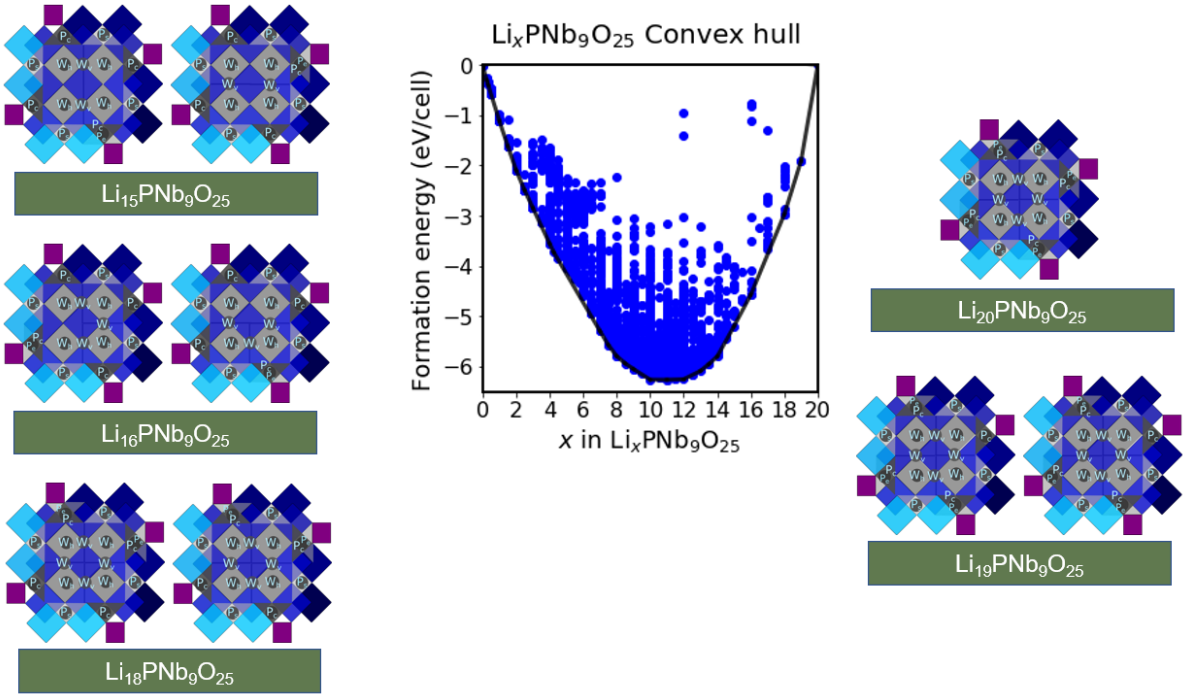

Figure 4.13: Formation energies and schematics of ground state orderings of LixPNb$_9$O$_{25}$ beyond x=15 as determined with DFT-PBE calculations.

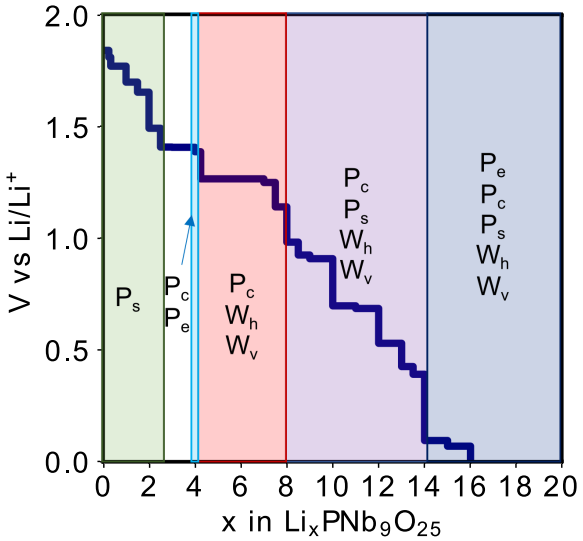

Figure 4.14: Calculated voltage curve of Li$_x$PNb$_9$O$_{25}$ at zero kelvin. Each step corresponds to a ground state Li-vacancy ordering and each plateau corresponds to the voltage of a two-phase reaction. Also shown are the occupied sites in the ground states as a function of Li concentration x.

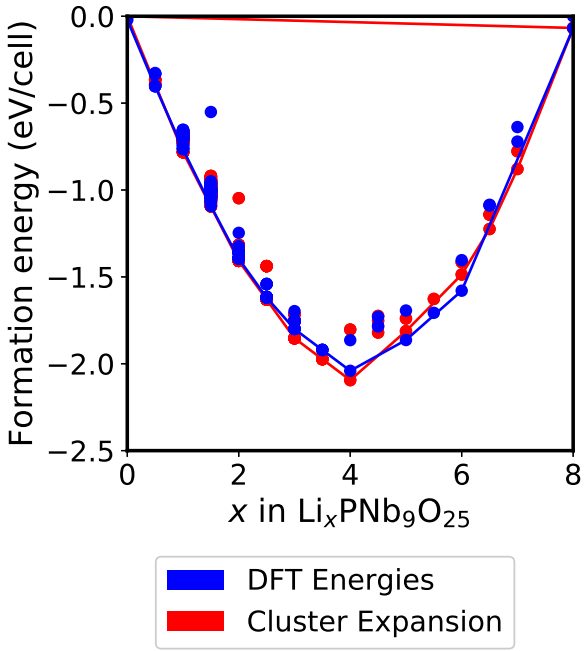

Figure 4.15: Comparison of formation energies as calculated with DFT-PBE and the cluster expansion at low Li concentrations. At low Li concentrations Li preferentially fills the P_e and P_s sites. The cluster expansion model for low concentrations explicitly treated the P_e and P_s sites.

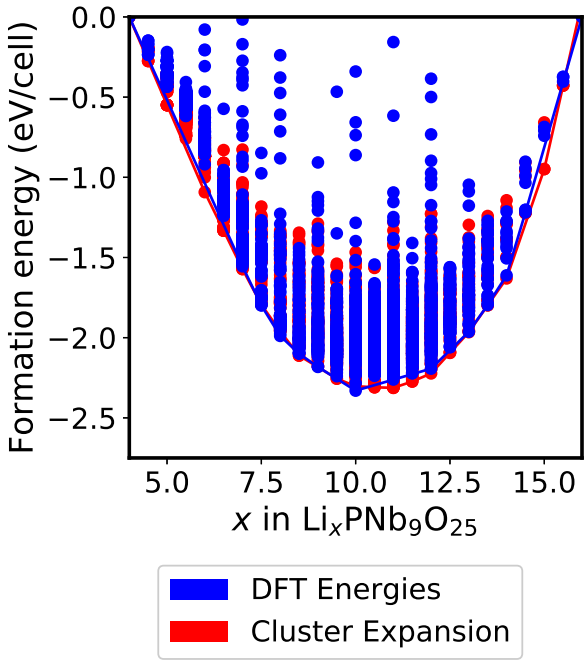

Figure 4.16: Comparison of formation energies as calculated with DFT-PBE and the cluster expansion at intermediate to high Li concentrations. Between x=4 and x=16 Li fills P_s, P_c, W_h and W_v sites. The cluster expansion model treats configurational degrees of freedom over the P_s, W_h and W_v sites, with the P_c sites fully filled by Li.

Figure 4.17(a) shows the voltage curve (dark blue) of $Li_xPNb_9O_{25}$ as calculated with Monte Carlo simulations at 300 K. The Monte Carlo simulations were applied to the cluster expansions to calculate the concentration dependence of the Li chemical potential, which was in turn substituted into the Nernst equation [2] to obtain the voltage curve. A 10×10×20 super cell of the PNb_9O_{25} primitive cell was used. Most of the steps and plateaus that are present in the zero kelvin voltage curve of Figure 4.14 have been smoothed out due to contributions from configurational entropy at 300 K. A sloping voltage profile is generally a sign of a disordered solid solution. Also shown is an experimental voltage curve (purple) of $Li_xPNb_9O_{25}$ measured with GITT. While the calculated voltage curve has a similar shape, it is lower than the experimental curve. It is common that approximations to density functional theory, such as the PBE approximation used in this work, systematically under predicts voltages [2].

Both the calculated and experimental voltage curves exhibit a plateau signifying a two-phase reaction between x=2 and x=4. The existence of a two-phase reaction between x=2 and x=4 was first reported by Patoux et al. [148] and was recently confirmed by others [28, 200] using in-situ diffraction. The Monte Carlo simulations indicate that the two-phase reaction arises from a change in site preference. This is evident in Figure 4.17(b), which plots the average concentrations of each type of Li site as calculated with the Monte Carlo simulations. Below x=2, the Li predominantly occupies the P_s sites (green), with some occupancy on the P_e sites (blue). Upon crossing the two-phase region between x=2 and x=4, the site preference switches abruptly, with four Li per unit cell occupying the P_c sites (light orange) and none occupying P_s and P_e. The abrupt increase in the number of occupied P_c sites at x=4 is an artefact of our cluster expansion model. Our zero kelvin DFT-PBE calculations predict that the ground state at x=4 has only 3 Li in P_c and a fourth in P_e and we therefore expect some P_e occupancy at finite temperature.

A second plateau is evident in the calculated voltage curve that is not present in the experimental voltage curve between x=5 and x=7. It is possible that there is more structural disorder in the experimental samples (e.g. due to partial occupancy of the two equivalent P sites) such that the predicted two-phase region between x=5 and 7 gives way to a solid solution. The average site occupancies as calculated with Monte Carlo simulations in Figure 4.17(b) indicates that passage through the second two-phase region leads to an abrupt increase in the concentration of occupied vertical window sites W_v. This is due to the onset of the interweaved Li-vacancy ordering over half the W_v sites shown in Figure 4.8. The interweaved ordering remains locked in place until x=14, with additional Li filling the W_h horizontal window sites and then the P_s sites in a continuous and disordered manner. This is a unique example of an intercalation process where Li ions adopt a stable ordered arrangement over a subset of sublattices and a solid solution over the other sublattice sites. While some Li are locked into a well ordered arrangement over the P_c and W_v sites, their disordered arrangement over the W_h and P_s sites leads to a smooth and sloping voltage curve. It is likely that this partial ordering tendency that is restricted to one sublattice will have significant implications for the kinetics of Li diffusion and reversibility of the compound.

4.3.3 Neutron Diffraction

Our systematic investigation of Li-vacancy orderings in $Li_xPNb_9O_{25}$ with DFT-PBE calculations predicts a change in Li site preference between x=2 and x=4. At dilute concentrations, Li ions prefer the P_s and P_e sites, but they switch their preference to the P_c sites, albeit with a small fraction of Li still in the P_e sites, when the Li concentration x is in the vicinity of 4. The calculations also clearly predict the absence of Li in window sites below x=6. To validate these predictions, we used neutron diffraction to determine

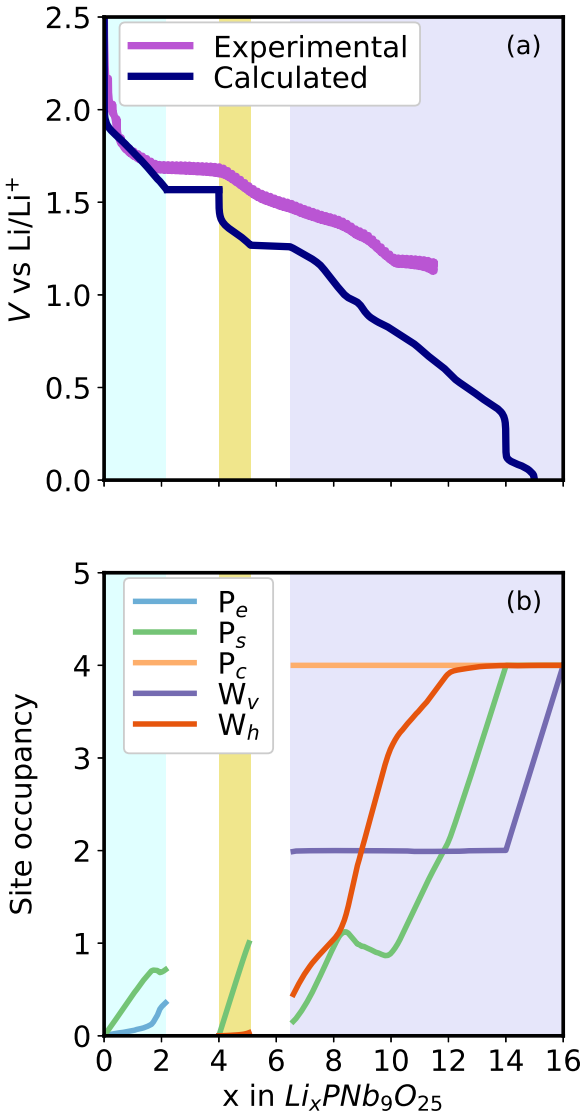

Figure 4.17: (a) Equilibrium voltage curve at 300K as calculated with grand canonical Monte Carlo simulations applied to cluster expansions of the Li-vacancy energy in PNb_9O_{25}. (b) Calculated site occupancy as a function of Li concentration.

site occupancy in $Li_{1.5}PNb_9O_{25}$, a composition before the plateau, and in $Li_{4.3}PNb_9O_{25}$, a composition immediately after the plateau (Figures 4.18(b-g)).

Extreme care was taken to measure lithiated samples that are representative of the galvanostatic discharge of cast electrodes. Typical open circuit voltages for PNb_9O_{25} as cycled in coin cells range between 3.0 – 3.2 V. The cell that resulted in the insertion of an average of 1.5 Li into PNb_9O_{25} (as determined by the galvanostatic discharge) started with an OCV of 3.1 V. Similarly, the cell that resulted in the insertion of 4.3 Li into PNb_9O_{25} started with an OCV of 3.2 V. The galvanostatic discharge profile of both cells cycled at a rate of C/80, with an average of 200 mg of loose powder (160 mg active material) per cell, mirrored that of the GITT experiment (Figure 4.18(a)). The large mass loadings are necessary to acquire neutron scattering data, and one giant cell was used to minimize the possibility of combining material across multiple cells that may have lithiated inhomogeneously. The characteristic initial plateau observed at 2 V, corresponding to the insertion of roughly 0.4 Li per formula unit, can be clearly seen in both traces. Therefore, we are confident that the collected Neutron scattering data is an accurate representation of the structures of previous studies [28, 148] at the selected states of discharge.

Rietveld refinements were performed on the $Li_{1.5}PNb_9O_{25}$ and $Li_{4.3}PNb_9O_{25}$ samples by considering each of the five Li sites, P_c, P_e, P_s, W_h, W_v. All structures retained the symmetry of the parent compound and could be fit to the I4/m space group. For both $Li_{1.5}PNb_9O_{25}$ and $Li_{4.3}PNb_9O_{25}$, the results from fitting the structure with the two window sites, W_h and W_v, led to unphysical bond lengths (highly distorted Li–O polyhedra and in some cases Nb–O polyhedra). Therefore, the window sites are deemed as unlikely candidates for Li insertion at these compositions from the experimental data. Among the fits that gave physical results for $Li_{1.5}PNb_9O_{25}$, the refinement for Li in the P_e site yielded the lowest refined Li thermal parameter and lowest R_{wp} (weighted profile

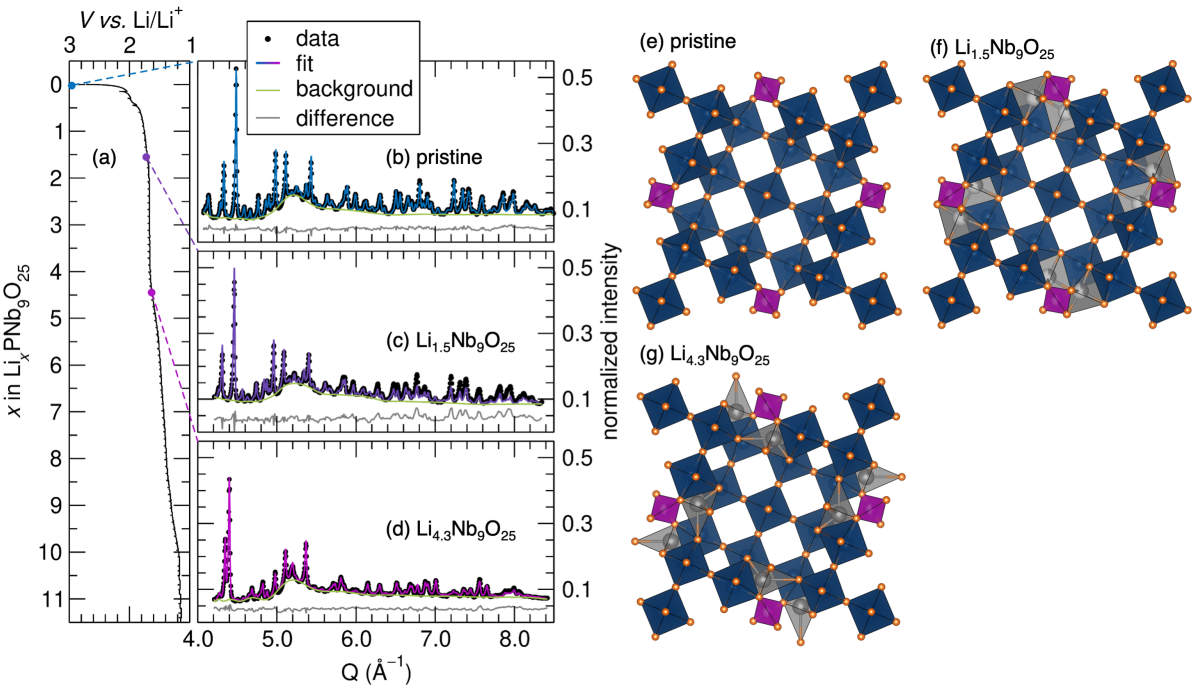

Figure 4.18: (a) GITT of PNb_9O_{25} between 3 and 1 V (first discharge). Neutron diffraction from NOMAD at the Spallation Neutron Source at Oak Ridge National Lab (bank 5 represented) of (b) pristine PNb_9O_{25} mixed with SuperP, (c) $Li_{1.5}PNb_9O_{25}$ lithiated as loose powder mixed with SuperP, and (d) $Li_{4.3}PNb_9O_{25}$ lithiated as a loose powder mixed with SuperP. The fit and difference curves are a result of Rietveld refinements, and all structures were fit with the I 4/m space group (87). Representations of the crystal structures as determined by the shown Rietveld refinements for (e) the pristine material, (f) $Li_{1.5}PNb_9O_{25}$, and (g) $Li_{4.3}PNb_9O_{25}$. $Li_{1.5}PNb_9O_{25}$ is best described by the configuration with Li in the P_e site, though P_s is also a candidate site. $Li_{4.3}PNb_9O_{25}$ is best described by the configuration with Li in the P_c site, though P_e and P_s are very statistically similar.

residual) values for both banks 4 and 5. Li occupancy in P_s is also a candidate structure, as Li–O bond lengths, thermal parameters, and R_{wp} values are all reasonable, as well. Li in the P_c site yields highly distorted Li–O tetrahedra, pointing to an unlikely solution. Both window sites yielded unphysical values. It is worth noting that while peak position and peak shape are being fit well in the candidate structures, peak intensities, particularly at high Q, are not. This points to some disorder that is not being captured adequately in the structure, together with the already relatively high thermal parameters. This is not surprising given that the fits only take into account one Li site at a time, which are already partially occupied. The structure at x=1.5 likely has combined Li occupancy in the P_e and P_s sites, and possibly in the P_c site. Similarly, the refinements for the P_c, P_s, and P_e sites yielded reasonable fits for $Li_{4.3}PNb_9O_{25}$, suggesting any of these sites are candidates at this composition. Among these three, Li in the P_c site gave the lowest thermal parameters and lowest R_{wp} values for banks 4 and 5. However, all three refinements are statistically similar. Likely all three Li environments can be found in the structure at this composition.

4.3.4 Effect of Lithium Insertion on Strain and Volume

The insertion of Li into an intercalation compound usually results in a change of its volume and unit cell shape, which can lead to electrode fragmentation and fracture, and thereby capacity fade [201, 202]. Dimensional changes of an intercalation compound can be measured with symmetry adapted strain order parameters[86, 69, 203]. A convenient set of symmetry adapted strain order parameters for a tetragonal crystal such as PNb_9O_{25}

takes the form[86]

$$\begin{pmatrix} e_1 \\ e_2 \\ e_3 \\ e_4 \\ e_5 \\ e_6 \end{pmatrix} = \begin{pmatrix} \frac{(E_{xx}+E_{yy}+E_{zz})}{\sqrt{3}} \\ \frac{(E_{xx}-E_{yy})}{\sqrt{2}} \\ \frac{(2E_{zz}-E_{xx}-E_{yy})}{\sqrt{6}} \\ \sqrt{2}E_{yz} \\ \sqrt{2}E_{xz} \\ \sqrt{2}E_{xy} \end{pmatrix} \tag{4.1}$$

where E_{xx}, etc. are conventional strains of the $Li_xPNb_9O_{25}$ unit cell relative to the fully relaxed PNb_9O_{25} reference state having tetragonal symmetry with its c axis aligned parallel to the Cartesian $\hat{z}$ axis.

The first strain order parameter, e_1, measures dimensional changes of the unit cell that are symmetry invariant. When using Hencky strains, e_1 becomes equal to the change in the volume of $Li_xPNb_9O_{25}$ relative to that of the PNb_9O_{25} reference volume [86]. Figure 4.19(a), shows the e_1 strain order parameter for each of the 4298 fully relaxed Li-vacancy orderings of $Li_xPNb_9O_{25}$ considered in this work. Figure 4.19 clearly shows an overall increase in the volume of the cell upon the insertion of Li. The volume of the lowest energy configurations (darker points) increase monotonically up to x=4, decrease slightly between x=4 and 7, but then increase again beyond x=7. The overall increase in volume is consistent with the in-situ diffraction study of Patoux et al. [148]. For example, the calculated volume change at x=10.25 is approximately 7%. This value is in quantitative agreement with the value extracted from in situ XRD [148], where the volume changed by 7.4% upon the insertion of 10.25 Li. The slight reduction in volume between x=4 and 7, however, is not observed experimentally, with the study of Patoux et al. [148] showing instead a slight expansion.

One that varies appreciably with Li concentration is e_3, which is also shown in Figure 4.19(b). The e_3 strain order parameter filters out tetragonal distortions of the crystal. For

$Li_xPNb_9O_{25}$, a positive value of e_3 measures an elongation along the c axis, which is parallel to the block length, and a uniform contraction perpendicular to the c axis as shown in Figure 4.20(a). It is a measure of the change in the c/a ratio of a conventional tetragonal unit cell. Figure 4.19(b) shows that e_3 remains close to zero up to $x \approx 4$, increases over a narrow concentration interval to a value of approximately 7%, and subsequently remains relatively unchanged beyond x=7. While there is a large scatter in e_3 values between x=4 and x=7, outside of this interval the e_3 values are relatively insensitive to the Li-vacancy ordering and are instead largely determined by the average concentration. This implies that the dimensional changes with Li concentration as measured by e_3 are affected by a global property, such as a shift in the Fermi-level, that is more sensitive to the average concentration than to any particular Li-vacancy ordering. It should be noted that the abrupt increase of e_3 around x=7 for the ground state structures (connected by the blue line in Figure 4.19(b)) coincides with the onset of the interweaved ordering over the W_v vertical window sites (Figure 4.8). A similar elongation of the blocks coupled with an in-plane constriction perpendicular to the blocks was observed by Patoux et al. [148] for $Li_xPNb_9O_{25}$ and by Kocer et al. [143, 144] in other Wadsley-Roth phases. The other strain order parameters are plotted in Figure 4.21.

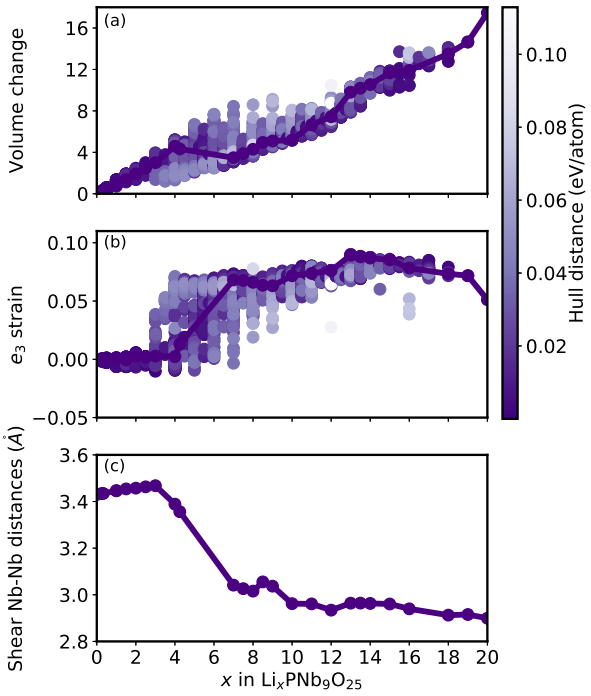

Figure 4.19: (a) The volume change of $Li_xPNb_9O_{25}$ relative to that of fully relaxed PNb_9O_{25} for each of the 4298 Li-vacancy orderings studied with DFT-PBE. Darker colors, tending towards purple, correspond to orderings with a lower energy, while lighter colors signify orderings with a high energy (measured as the distance from the convex hull). The ground states are connected with a black line. (b) The e_3 strain order parameter for the same 4298 Li-vacancy orderings, which measures an elongation along the c axis (parallel to the block length) and a contraction in the plane perpendicular to the c axis. (c) Bond distances between niobium ions in the edge-sharing octahedra at the perifery of the blocks of the ground state structures.

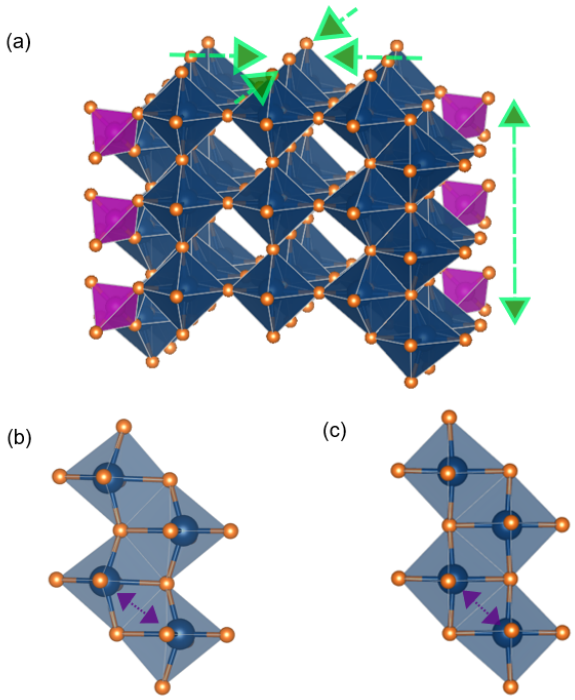

Figure 4.20: (a) Schematic of the strain measured with the e_3 strain order parameter. An increase in e_3 corresponds to an expansion along the c axis and a constriction in the plane perpendicular to the c axis. (b) Visualization of the edge-sharing niobium octahedra at a low composition, $Li_{0.5}PNb_9O_{25}$. At low Li compositions, Nb^{5+} of the edge-sharing NbO_6 octahedra undergo a second-order Jahn-Teller distortion. (c) At high Li concentrations, the distortions go away and the distance between edge-sharing Nb decreases.

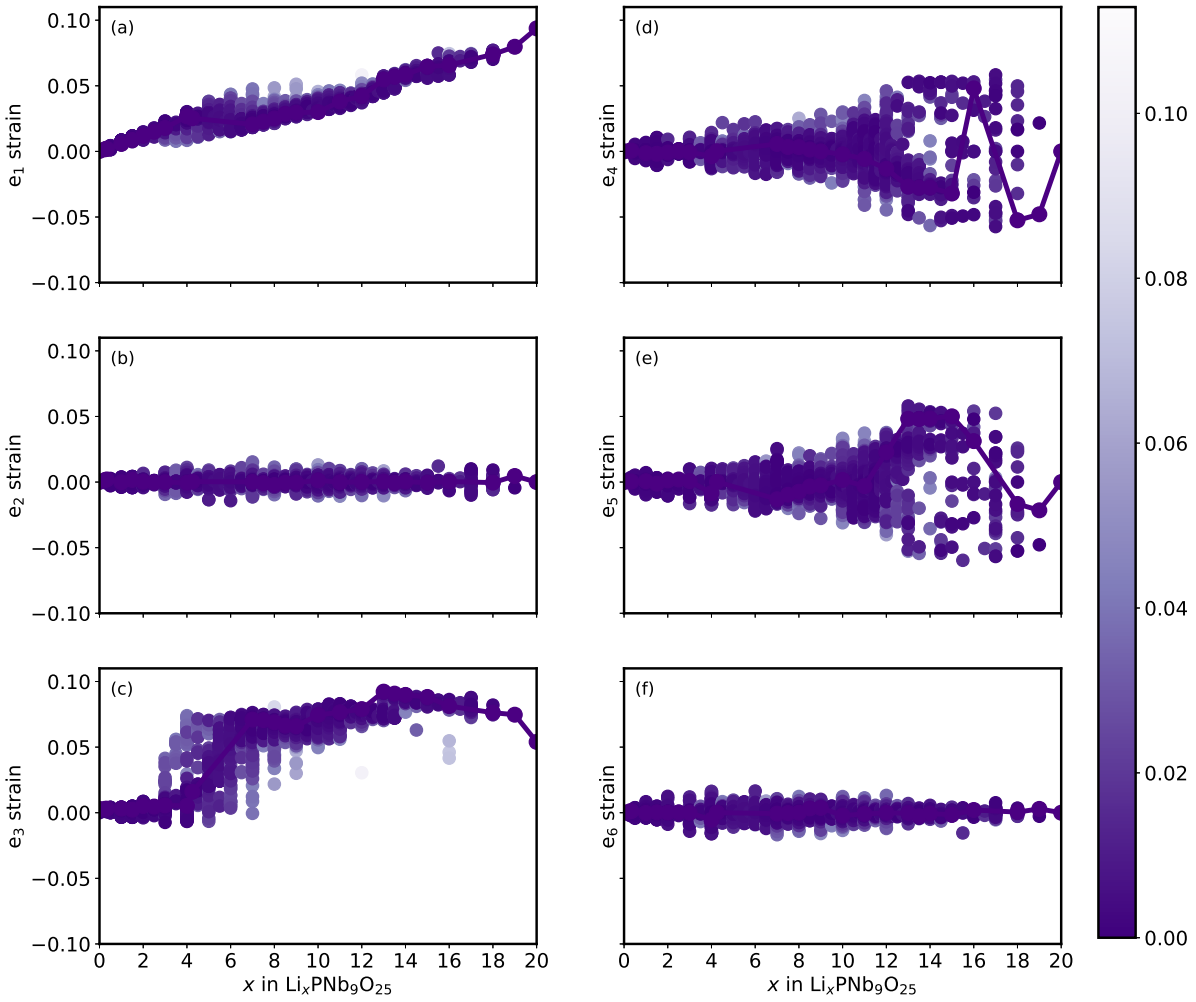

Figure 4.21: Distortions of the $Li_xPNb_9O_{25}$ unit cell (relative to that of PNb_9O_{25}) upon lithiation as measured with symmetry adapted strain order parameters. The formulation of the strain order parameters can be found in the text.

The variation of e_3 with Li concentration in the ground states is strongly correlated with changes in the Nb-Nb pair distances of edge sharing NbO_6 octahedra at the periphery of the blocks. Figure 4.19(c) shows that the average Nb-Nb distances decrease from values that range between 3.4 and 3.5 Å for $x < 4$ to values that average around 3.0 Å above x=7. Below x=4, the edge sharing NbO_6 octahedra of the block peripheries are highly distorted due to the off-centering of the Nb cations that arises from a second-order Jahn-Teller distortion as shown in Figure 4.20(b). The four coordinating oxygen ions of the vertical window sites form a highly distorted square for $x < 4$, with two sets of oxygen pairs having a larger bond length than the remaining two. The distortions of the edge-sharing NbO_6 octahedra and the vertical window sites are largely absent above x=7 as shown in Figure 4.20(c). A shortening of the Nb-Nb distance for the edge-sharing NbO_6 octahedra leads to an elongation along the block length (i.e. c axis) and a simultaneous contraction in a plane perpendicular to the block length. These dimensional changes have their origin in modifications to the electronic structure that occurs upon Li insertion, as is described in the next section.

4.3.5 Electronic Structure

The Nb cations of PNb_9O_{25} have a formal oxidation state of 5+. The Nb d levels, when octahedrally coordinated by oxygen, split into three degenerate t_{2g} (d_{xy}, d_{xz}, d_{yz}) levels with lobes that point between oxygen ions and two e_g levels (d_{z^2} and $d_{x^2-y^2}$) with lobes that point towards the oxygen as shown in Figure 4.22. The degeneracy of the t_{2g} and e_g levels are lifted further when the symmetry of the NbO_6 octahedra are lowered by the surrounding crystal and/or distortions of the octahedra themselves. In PNb_9O_{25}, all the t_{2g} and e_g levels are empty and the compound is an insulator. The e_g levels, which are anti-bonding states that arise from a hybridization between Nb d_{z^2} and $d_{x^2-y^2}$

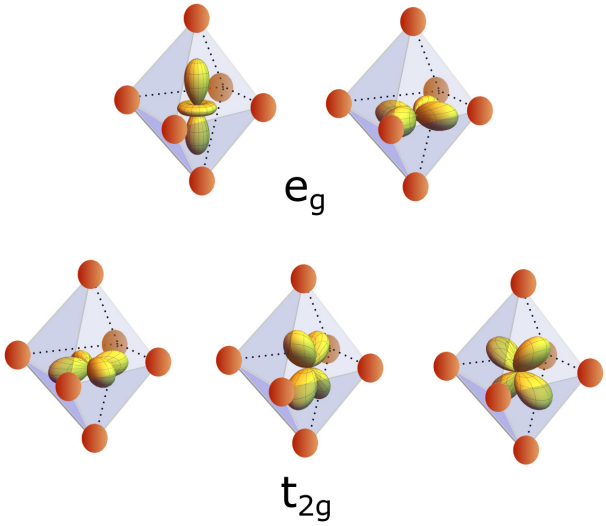

Figure 4.22: Illustration of the e_g and t_{2g} states on Nb of a NbO_6 octahedron.

orbitals and the surrounding oxygen p orbitals, have a higher energy than the t_{2g} levels. When Li atoms are added to PNb_9O_{25}, they will, therefore, donate their electrons to the t_{2g} levels.

Figure 4.23 shows the charge density of the occupied t_{2g} levels upon the addition of a very dilute concentration of Li. The calculation was performed on a supercell consisting of four PNb_9O_{25} unit cells and one Li ion, constituting a Li concentration of x=0.25. As is evident in Figure 4.23, the electron donated by the Li atom fills a t_{2g} orbital on a Nb that resides in a corner sharing NbO_6 octahedron at the center of the $3\times3\times\infty$ block. The t_{2g} orbitals in these octahedra are non-bonding and, therefore, highly localized, as is evident in Figure 4.23.

It is only after the non-bonding t_{2g} orbitals at the centers of the blocks are filled that a further addition of Li leads to a gradual filling of t_{2g} levels on the Nb cations that reside in the edge-sharing NbO_6 octahedra at the periphery of the blocks. This is evident in Figure 4.24. The charge density of the filled t_{2g} states of $Li_5PNb_9O_{25}$ shown in Figure 4.24 reveals not only electron density on all the non-bonding t_{2g} levels at the center of

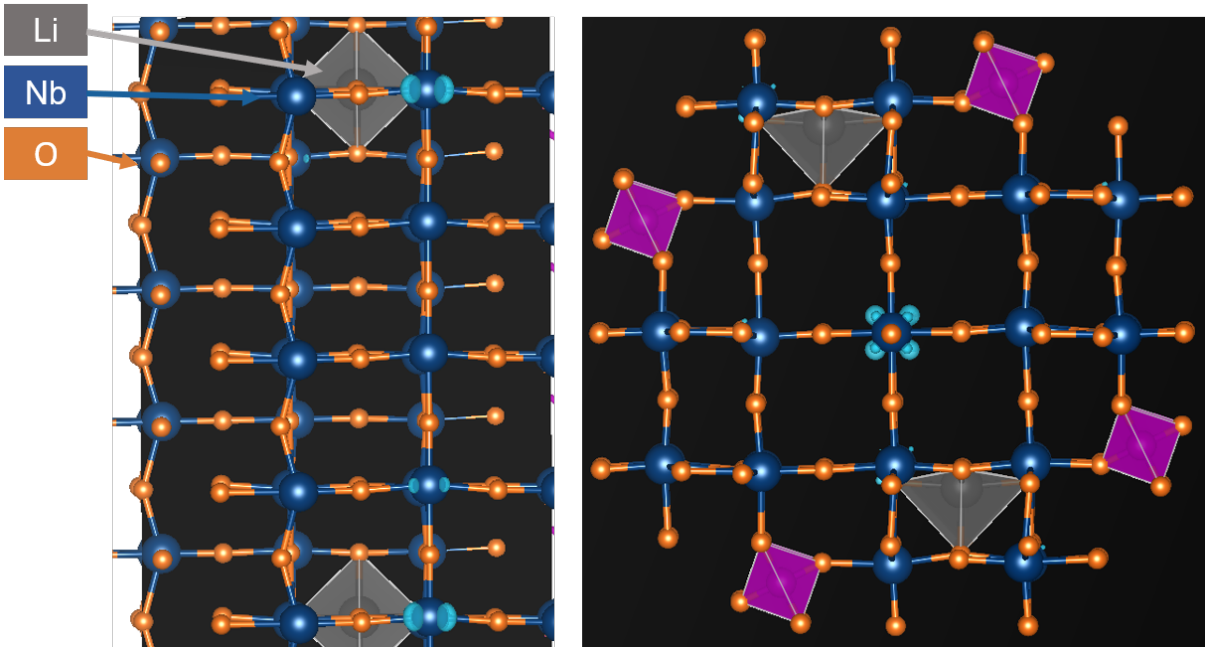

Figure 4.23: Charge density of the electron denoted by Li in $Li_{0.25}PNb_9O_{25}$ having a 1×1×4 super cell of the PNb_9O_{25} primitive cell. The donated electrons localize on a Nb of a corner sharing octahedron at the center of the 3×3×∞ perovskite block. (Left panel is a side view of the crystal, with the c axis pointing up while the right panel is a view down the c axis.)

the blocks, but also an appreciable density on the Nb in the edge-sharing octahedra. An increase of the Li concentration to x=7 results in a further accumulation of charge on the t_{2g} states of the edge-sharing NbO_6 octahedra as is evident in $Li_7PNb_9O_{25}$. In fact the charge density of $Li_7PNb_9O_{25}$ in Figure 4.24 suggests the onset of Nb-Nb bond formation, which is made possible by the overlap of t_{2g}-like orbitals between the metals of edge-sharing octahedra. The charge density plots also suggest an increase in the degree of electron delocalization, which is expected to enhance electronic conductivity [28].

A similar progression of orbital filling was predicted by Kocer et al. [143] in their study of Wadsley-Roth phases containing Nb and W. They pointed out that the electrons donated by Li first accumulate on localized, non-bonding t_{2g} orbitals at the center of the blocks before they start filling t_{2g} levels on the edge-sharing transition metals. This order of orbital filling has also been used to explain the origin of the insulator-metal transition at low Li concentrations in $Li_xPNb_9O_{25}$ [28].

Filling of the t_{2g} orbitals of the edge-sharing NbO_6 octahedra plays an important role in effecting the structural changes that occur as the Li concentration of the host increases, including the shortening of the Nb-Nb bond lengths between edge-sharing NbO_6 octahedra and an increase in the e_3 strain order parameter. The Nb of the edge-sharing blocks are distorted away from the centers of the octahedra in PNb_9O_{25}. The off-centering is likely a result of a combination of factors [143]. The Nb^{5+} oxidation state makes the cation susceptible to a second-order Jahn-Teller distortion, which leads to cation off-centering in octahedral environments. The off-centering may also arise from an electrostatic repulsion between edge-sharing Nb^{5+} cations, biasing the off-centering in directions that increase the Nb-Nb distance. As electrons fill the edge sharing t_{2g} levels, the effective valence of the Nb is no longer 5^+ but progressively becomes closer to 4^+ and then 3^+. This should lead to a reduction in electrostatic repulsion between edge-sharing Nb and eliminate the susceptibility for second order Jahn-Teller distortions. Furthermore,

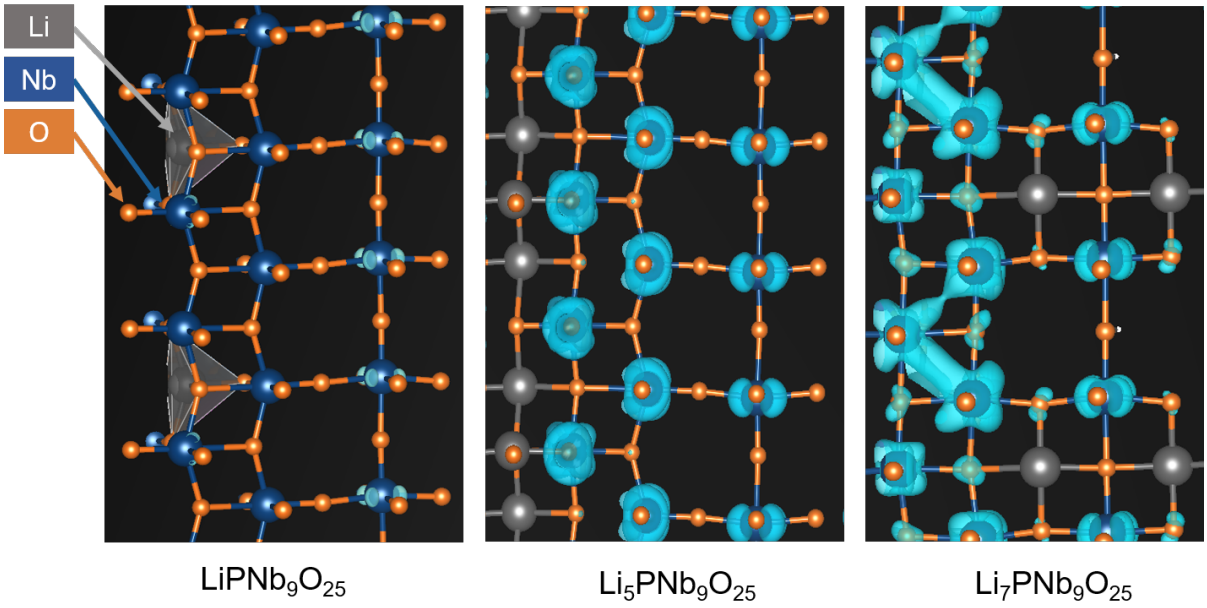

Figure 4.24: Charge density along the edge-sharing niobium octahedral sites with increasing composition. The charge density is viewed perpendicular to the c lattice vector. At low compositions, electrons localize on the central, corner-sharing niobium in the middle of the perovskite blocks. As more electrons are added at higher Li concentrations, electrons begin filling d orbitals in the edge-sharing NbO_6 octahedra and delocalize. Increasing electron delocalization occurs in conjunction with decreasing edge-sharing niobium-niobium distances and increasing values of the e_3 strain order parameter.

the t_{2g} orbitals of the edge-sharing NbO_6 octahedra appear to form metal-metal bonds beyond x=7 (Figure 4.24), which should also tend to shorten Nb-Nb distances. The shortening of the Nb-Nb distances along the block peripheries relieve the distortions of the NbO_6 octahedra. As a consequence, the W_v vertical window sites become less distorted making them more amenable for Li occupancy. It is likely that these structural changes in response to electron filling are responsible for the stability of the interweaved ordering that forms a backbone of the majority of low energy structures between x=7 and x=14. Density of states and charge densities for low energy structures between x=4 and x=7 are shown in Figure 4.25. Metal-metal bonding begins to form after the lithium ordering inversion.

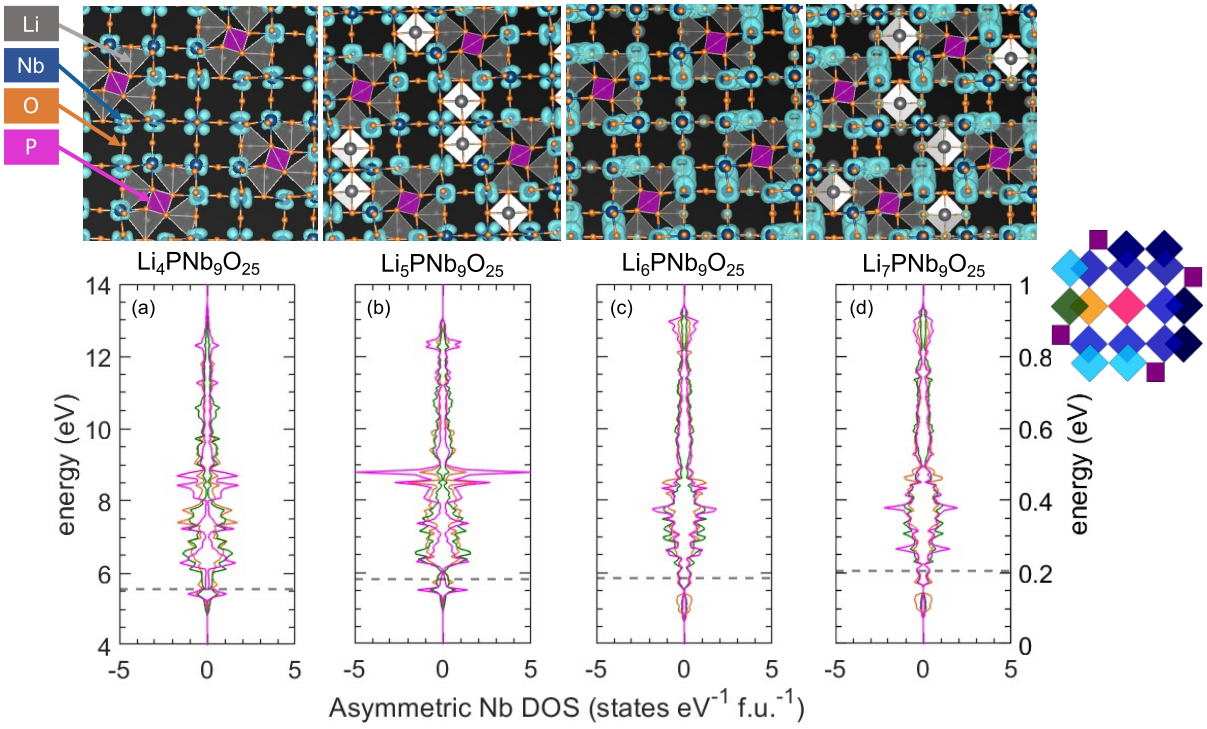

Figure 4.25: (a-d) Calculated charge density and density of states at x=4, 5, 6, and 7 in $Li_xPNb_9O_{25}$. Metal-metal bonding increases as lithiation occurs.

4.4 Discussion

The Wadsley-Roth phases are a promising class of anode materials for high power Li-ion batteries. They exhibit a rich variety of open crystal structures that can host Li ions over multiple types of interstitial sites. A common structural feature among all Wadsley-Roth phases are their blocks of corner sharing octahedra that are held together by edge-sharing octahedra. While they have impressive electrochemical properties and can accommodate more than one Li per transition metal, very little is known about the mechanisms of Li insertion into Wadsley-Roth phases.

The results of our study on $Li_xPNb_9O_{25}$ show that the electronic and thermodynamic properties associated with Li insertion into Wadsley-Roth phases is more complex than those of most other common intercalation compounds [204, 70]. PNb_9O_{25} can host Li in

five symmetrically distinct sites, three of which have pyramidal coordination by oxygen (P_s, P_e and P_c) and two that are coordinated by four coplanar oxygen ions (W_v and W_h) also known as window sites [196, 143]. An important prediction of this work is the occurrence of a site preference inversion upon Li insertion into PNb_9O_{25}. Using an iterative approach that relies on the cluster expansion method to extrapolate computationally expensive DFT calculations, we predict that Li initially fills the P_s and P_e pyramidal sites, but that these sites fall out of favor at higher Li concentrations where Li first fills the P_c sites (with some residual occupancy on the P_e sites) and then gradually fills the two window sites, W_v and W_h. Only at much higher Li concentrations ($x \approx 8$) does Li return to the P_s sites. The site inversion from P_s and P_e at x=2 to predominantly P_c at x=4 is responsible for a plateau in the voltage curve at low Li concentrations. The plateau is present in both the experimental voltage curve [148, 28] as well as the calculated voltage curve and appears to be a common feature of many other similar Wadsley-Roth phases. Our neutron diffraction refinements, while somewhat ambiguous in its assignments of site occupancy over the pyramidal sites, P_s, P_e and P_c, do not contradict our DFT predictions. Furthermore, the neutron diffraction refinements unequivocally confirm that Li does not fill window sites during the early stages of Li insertion (i.e. $x < 4.3$).

A second important prediction of this study is the stability of the interweaved backbone ordering over the W_v vertical window sites that sets in between $7 < x < 14$ and is present in almost all ground states and low energy Li-vacancy orderings in that concentration interval. The interweaved ordering leads to a doubling of the unit cell along the c-axis. While the ordering on average remains locked in place over a wide concentration interval, the remaining W_h and P_s sites accommodate Li in a disordered manner. This leads to a unique intercalation process in which Li orders over one sublattice (i.e. W_v) but forms a solid solution over other sublattices (W_h and P_s). The result is a sloping voltage profile that is characteristic of a solid solution, with occasional kinks due to

secondary ordering tendencies over the W_h and P_s sites. The influence of this partial ordering on kinetic properties is likely to be significant and will be the focus of future studies. Our DFT calculations predict that the interweaved backbone ordering can easily tolerate defects whereby pairs of Li in W_v sites in a given layer rearrange and occupy W_v sites that form a 90^o angle with each other (as opposed to pairs of W_v sites that form a 180^o angle with each other in the interweaved ordering). The preference for window sites at higher Li concentrations is consistent with neutron diffraction studies of other Wadsley-Roth phases by Catti et al. [196, 197, 198].

Our calculations have also shown that changes in electronic structure due to the filling of the t_{2g} levels upon Li insertion results in structural distortions that in turn affect Li-site preferences. The Nb of the edge-sharing octahedra distort off-center in the pristine PNb_9O_{25} compound, likely due to a combination of factors that includes a second-order Jahn-Teller distortion of the Nb^{5+} cations within their octahedra and electrostatic interactions between edge-sharing Nb^{5+} cations [143]. This leads to highly distorted NbO_6 octahedra that then distort the neighboring W_v vertical window sites, making them unfavorable for Li occupancy. The addition of electrons to the host upon Li insertion reduces the Nb^{5+} to lower oxidation states, thereby eliminating the susceptibility for second-order Jahn-Teller distortions and promoting the formation of metal-metal bonds between edge-sharing Nb. The combination of these factors results in a shortening of Nb-Nb distances between edge-sharing octahedra and a reduction in the degree with which the octahedra are distorted. As a result, the W_v sites become more square planar and therefore more favorable. Our calculations clearly show that it is only after the structural distortions of the edge-sharing octahedra are eliminated beyond x=7 that the filling of the W_v vertical window sites sets in. Similar behavior has been observed in other Wadsley-Roth phases by Griffith et al. [97, 137] and Kocer et al. [143, 98, 144], who found an increased stability of the window sites due to the disappearance of the distortions

of the edge-sharing transition metal-oxygen octahedra at high Li concentrations. The phenomenon has also been noted in other intercalation compounds such as anatase TiO_2, where the elimination of structural distortions due to the reduction of Ti was shown to deleteriously affect Li diffusion kinetics [205]. Our results taken together with the earlier work of Kocer et al. [143, 98, 144] suggests that the coupling between electronic structure and crystallographic distortions is a common phenomenon of Wadsley-Roth phases.

The ability to predict stable Li-site preferences and ordering tendencies in Wadsley-Roth phases is made especially challenging by the combinatorial explosion of all the possible ways of distributing Li ions and vacancies over the many sites of these phases. The number of Li-vacancy orderings within the primitive cell of PNb_9O_{25}, for example, is already 2^{20} or 1,048,576 due to the fact that the primitive cell contains 20 candidate Li sites. Often stable orderings form in super cells of the primitive cell. The doubling of the PNb_9O_{25} unit cell along the c-axis, for instance, increases the number of candidate Li-vacancy orderings to 2^{40} or over 10^{12}. Overcoming these combinatorial challenges requires tools such as the cluster expansion, as they allow for a rapid search over configuration space with Monte Carlo techniques to identify low energy Li-vacancy orderings. It should be noted, however, that while cluster expansions are generally superior to other approaches that screen candidate orderings based on electrostatic energy, for example, they are not necessarily exhaustive. The approach is iterative, whereby cluster expansions are trained to an ever increasing database of first-principles energies to increase their predictive accuracy. As with any method that relies on extrapolation, however, there is no guarantee that it accurately predicts the true ground state Li-vacancy orderings.

While the calculated and measured voltage curves of Figure 4.17 show reasonable qualitative agreement, there is a systematic under prediction above x=2. This is not unexpected as DFT-PBE is known to systematically under predict voltages [2, 206]. Below x=2, the quantitative agreement is better, however, the shape of the calculated volt-

age profile differs from the experimental one (Figure 4.17). The experimental voltage curve exhibits a small plateau followed by a step around x=0.5 that is not present in the calculated voltage curve. The discrepancy may arise from the neglect of additional degrees of freedom in the statistical mechanics calculation of the room temperature voltage curve. $Li_xPNb_9O_{25}$ undergoes an insulator to metal transition at low Li concentrations that may require more accurate electronic structure methods to describe correctly. Our DFT-PBE calculations already indicate a high degree of electron localization at very dilute concentrations. It is possible that these localized states may have a high degree of degeneracy with respect to their placement within the crystal, leading to an additional source of configurational entropy that was not accounted for in this study. A similar phenomenon was proposed to explain the role of the metal-insulator transition in causing a two-phase reaction in Li_xCoO_2 between x=0.93 and x=0.75 [207]. It is suggested that the electronic properties of $Li_xPNb_9O_{25}$ at dilute Li concentrations receive further attention both experimentally and theoretically.

4.5 Conclusion

We have performed a first-principles statistical mechanics study of the electrochemical properties of PNb_9O_{25} as a function of Li concentration. PNb_9O_{25}, which is a Wadsley-Roth phase made of $3\times3\times\infty$ perovskite-like blocks, can host Li in three symmetrically distinct types of pyramidal sites at the block edges and two types of window sites within the blocks. Our first-principles DFT-PBE calculations predict that Li initially prefers pyramidal sites, only filling the window sites at intermediate to high Li concentrations. Neutron diffraction is consistent with DFT predictions of pyramidal site occupancy at low Li concentrations. The window sites only become favorable after the host undergoes a tetragonal distortion due to a chemical strain that accompanies Li insertion. The

tetragonal distortion of the host is found to correlate with the filling of Nb d orbitals in the edge-sharing NbO_6 octahedra, which relieves second-order Jahn-Teller distortions and leads to metal-metal bonding. The lowest energy configurations above x=7 are found to share a common Li-vacancy ordering motif over the vertical window sites, with the other sites accommodating Li as a solid solution. Our predictions of the sequence of site filling and the nature of Li-vacancy ordering in PNb_9O_{25} set the stage for studies of Li diffusion mechanisms within this complex host. Due to the vast structural similarities among different Wadsley-Roth phases, many of our findings for PNb_9O_{25} should also apply to other Wadsley-Roth phase chemistries.

Chapter 5

Redox mechanisms and structural changes of the Wadsley-Roth phase, $Li_xTiNb_2O_7$

In this chapter, we seek to understand what factors influence $TiNb_2O_7$, a Wadsley-Roth phase that can be used as a lithium-ion electrode chemistry with one of the highest reversible power densities, as a material that has a very high rate performance. This section begins with an overview of the Bayesian probabilistic methods used to accurately quantify the robustness of our calculations, to ensure the fidelity of our predictions in this complex system. It then examines the relationship between metal-metal bonding, octahedral distortions and crystallographic strain upon lithiation. In its pristine state, $TiNb_2O_7$ is predicted to be insulating, a finding that can be corroborated by both experiments and other computational analysis in literature. Upon lithiation, metal-metal bonds begin to form, beginning with some of the highest edge sharing octahedra. As more electrons are added to the system at increasing lithium concentrations, NbO_6 octahedra that share fewer edges and TiO_6 octahedra begin to metal-metal bond as well.

This change in metal-metal bonding causes a decrease in the transition metal bond distance which causes a significant relaxation of octahedral distortions at the compositions where metal-metal bonding occurs. This occurs in conjunction with a dramatic increase in the e_3 crystallographic strain mode which is a mode that dictates how the length of the octahedra along the short axis and a decrease parallel with the block plane. Crsytallographic findings and lithiation mechanisms are compared to experiment, and we find high accuracy with experiment. Through the findings of this analysis, we hypothesize that if we combine our knowledge of transition metals that tend toward the edges of the Wadsley-Roth phases (the less electrostatically active transition metal species), and the sites that tend to undergo transition metal-bonding (the highly edge sharing octahedra), we can tune which transition metal sites undergo metal-metal bonding. This can have significant impacts of the crystallographic strain expressed in a disordered Wadsley-Roth phase.

5.1 Introduction

Lithium-ion batteries continue to dominate the secondary energy storage space. A large fraction of energy storage demand originates in the automotive sector, where electric motors show an efficiency of over 90% [208] and enable the elimination of CO_2, CO, NO_x, and SO_x exhaust emitted by internal combustion engines. Despite their benefits and widespread usage, current lithium ion battery technologies that rely on graphite anodes possess lower charge rates, power densities, and operating temperature ranges than needed for future generations of electric vehicles [209, 210].

Wadsley-Roth phases are a family of complex inorganic chemistries that exhibit high power densities when used as electrode materials. $TiNb_2O_7$ is a commercialized Wadsley-Roth phase that can reversibly cycle while achieving capacities of 341 mAh g^{-1} [93, 19].

This compound is also capable of cycling at rates of 20 C with little gravimetric capacity losses [211, 17, 212]. The ability of $TiNb_2O_7$ to intercalate lithium was first demonstrated by Cava in 1983 [15] and was first cycled against lithium in 2011 [156]. $TiNb_2O_7$ has since displayed the capability to supply high power densities at high charge rates [213, 214, 215, 216, 217, 218, 219, 220].

Despite an increased interest in Wadsley-Roth phases as anodes in Li-ion batteries [106, 221, 97, 137, 93, 28], there is still a limited understanding about their thermodynamic and structural properties as a function of the degree of Li insertion. This section examines the full lithiation profile of $TiNb_2O_7$ using first-principles statistical mechanics to understand redoc mechanisms and their effect on Li site preference and structural properties. We use distortion amplitude analysis to examine how octahedra distort as a function of lithium concentration for octahedra of different degrees of octahedral edge sharing. We pair this analysis with density of states calculations, transition metal bond distance analysis, and strain calculations to determine the cause of structural distortions. We find that upon lithiation, $Li_xTiNb_2O_7$ undergoes metal-metal bonding, decreasing the distance between transition metals at the edges of the Wadsley-Roth phase. This arises from hybridization between t_{2g} orbitals for edge-sharing transition metal cations.The filling of these bond states leads to shortened metal-metal distances which has structural consequences including a modification of Li-ion site preferences upon lithiation. Since the metal-metal redox mechanism specifically occurs on edge-sharing transition metal octahedra, a subset of motifs present in all Wadsley-Roth phases, the findings of this section are likely relevant to a host of other Wadsley-Roth phases as well.

5.2 Methods

5.2.1 First-principles electronic structure calculations

Energies of titanium-niobium orderings are calculated using density functional theory (DFT) as parameterized by Perdew, Burke, and Ernzerhof (PBE) [44]. DFT calculations are performed using the Vienna ab initio simulation package (VASP) [126, 127]. Core electron effects are approximated using the projector augmented wave (PAW) method [128, 46]. Titanium-niobium orderings are enumerated with the Clusters Approach to Statistical Mechanics (CASM) [69, 131, 130, 132, 222] simulation package. A plane-wave energy cutoff of 550 eV is used for PBE-DFT calculation of titanium-niobium orderings in addition to a reciprocal space discretization of 25 K-points per Å^{-1}.

Lithium-vacancy ordering calculations are enumerated with CASM. Due to the large number of symmetrically distinct orderings possible in this phase, limited volume one, volume 2, and volume 4 lithium vacancy orderings are enumerated, and of the enumerated phases those predicted to be low in energy or those used to begin training the cluster expansion model are calculated using DFT. Lithium-vacancy DFT-PBE calculations are performed with a 650eV energy cutoff.

A standard deviation of 1 meV/atom on the calculated formation energies was used in the Gaussian likelihood distribution and a standard deviation of 49 meV was assumed for the Gaussian prior distribution of each effective cluster interaction (ECI), the coefficients of the cluster expansion. The mean of the prior distribution of the ECI was chosen to ensure that the predicted ground states and low energy structures are consistent with the DFT predictions as described by Ober et al.[223]

5.3 Results

5.3.1 The $TiNb_2O_7$ Wadsley-Roth host structure

Wadsley-Roth phases are a family of chemistries with crystal structures derived from the ReO_3 phase. Their structures consist of infinitely long blocks of corner sharing transition metal oxygen octahedra. The dimensions of each block is designated $n \times m$, where n and m count the number of octahedra along two orthogonal axes that are both perpendicular to the infinitely long axis of the block. The blocks can tile space in different patterns, with the octahedra at the peripheries of each block sharing edges with octahedra of neighboring blocks. Figure 5.1 shows the Wadsley-Roth structure adopted by $TiNb_2O_7$, which consists of 3×3 blocks that are shifted relative to each other in one direction by the width of an octahedron as they tile space.

The unit cell of the $TiNb_2O_7$ Wadsley-Roth structure of Figure 5.1 has nine transition metal sites. There are a total of 44 symmetrically distinct ways of arranging Ti and Nb over the cation sites of the primitive unit cell of $TiNb_2O_7$. The arrangement with the lowest energy as predicted with DFT-PBE is shown in Figure 5.1.[137]

$TiNb_2O_7$ is a disordered Wadsley-Roth phase and Ti and Nb can host multiple different arrangements on the transition metal sublattice. These arrangements differ by the octahedral edge sharing and local octahedral connectivity for each transition metal site. There are five symmetrically distinct transition metal sites (Figure 5.2). Site M1 and M2 (and their symmetric equivalents, M1' and M2') are located in octahedra that share four edges with neighboring octahedra. Site M3 (and it's symmetric equivalent, M3') is located in an octahedra that shares three edges. Site M4 is the central transition metal site and is symmetrically distinct from all other sites in the 3 by 3 block. This is entirely corner-sharing with neighboring octahedra. Site M5 (and M5') shares two edges.

The higher oxidation state Nb^{5+} cations prefer to occupy the corner-sharing octahedra

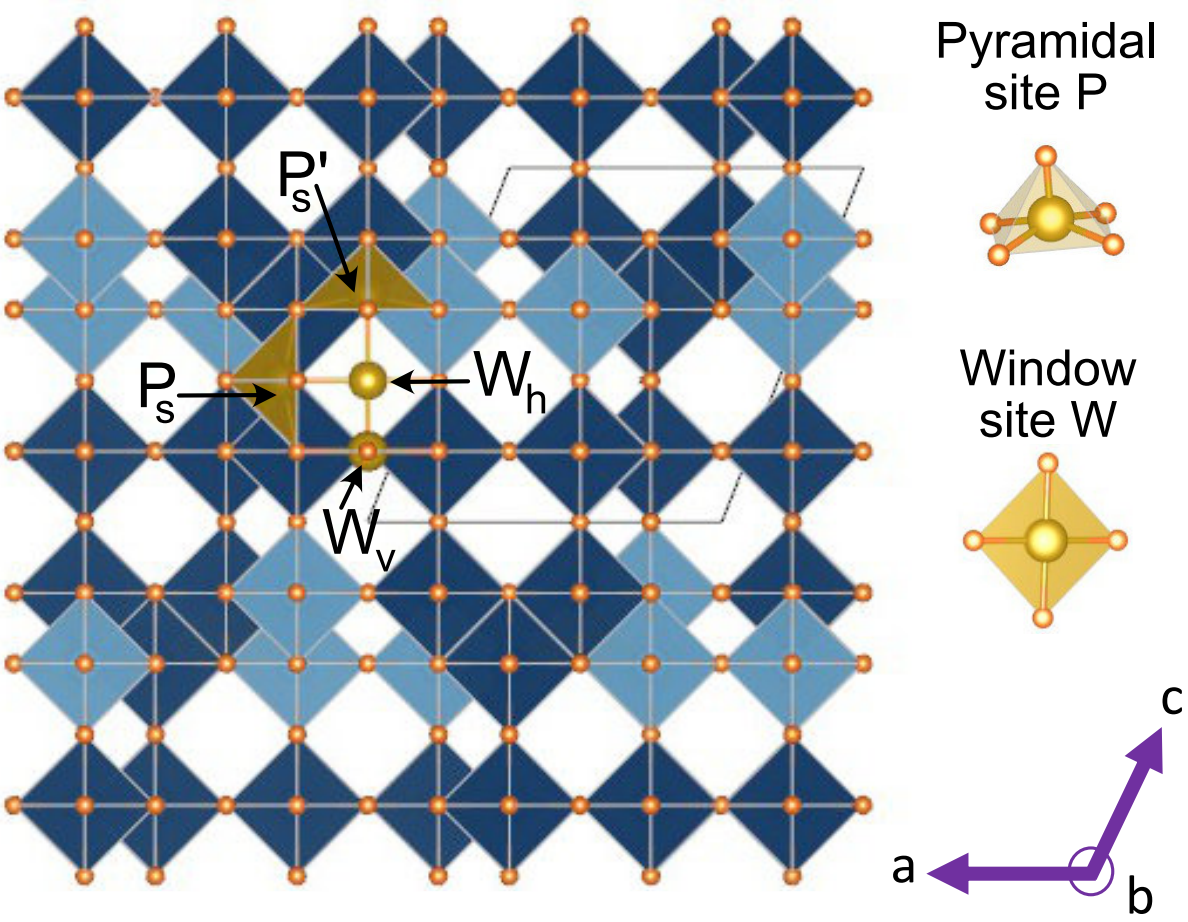

Figure 5.1: The idealized Wadsley-Roth crystal structure of $TiNb_2O_7$ consisting of corner-sharing and edge-sharing TiO_6 (light blue) and NbO_6 (dark blue) octahedra. The Ti and Nb of this model adopt their lowest energy arrangement over the octahedrally coordinated cation sites. The TiO_6 and NbO_6 octahedra are highly distorted in the fully relaxed $TiNb_2O_7$ structure (not shown). Intercalated Li ions can occupy pyramidal and window sites.

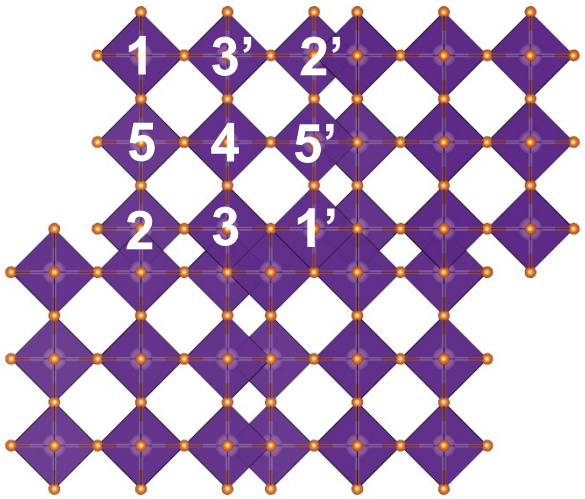

Figure 5.2: Symmetrically distinct transition metal sites in the transition metal sublattice of $TiNb_2O_7$

at the center of the block, while lower oxidation state cations such as Ti^{4+} tend to segregate to the edge-sharing octahedra at the peripheries of each block. Previous neutron diffraction studies show that the titanium concentration in M2 is the highest at 64.5% [138]. Similarly, the lowest energy set of $TiNb_2O_7$ orderings as predicted through DFT-PBE are ones where Ti is in the M2 site as shown in Figure 5.3. The next highest concentration of titanium is in the M1 sites (33.8% titanium concentration), followed by the M3 sites (26% titanium concentration). Likewise, as predicted through DFT-PBE, orderings that have M1 sites filled with Ti are the next lowest energy orderings, followed by orderings with M3 sites filled with Ti.

The $TiNb_2O_7$ Wadsley-Roth crystal can host Li ions in four types of interstitial sites coordinated by oxygen. These are shown in Figure 5.1. Two groups of interstitial sites are pyramidally coordinated by five oxygen ions. These are referred to as P_s and P_s'. They differ by the number of transition metal cations that share edges with the sites; the P_s sites share six edges with neighboring transition metals while the P_s' sites share seven. There are six P_s sites and two P_s' sites within each unit cell of $TiNb_2O_7$. The $TiNb_2O_7$

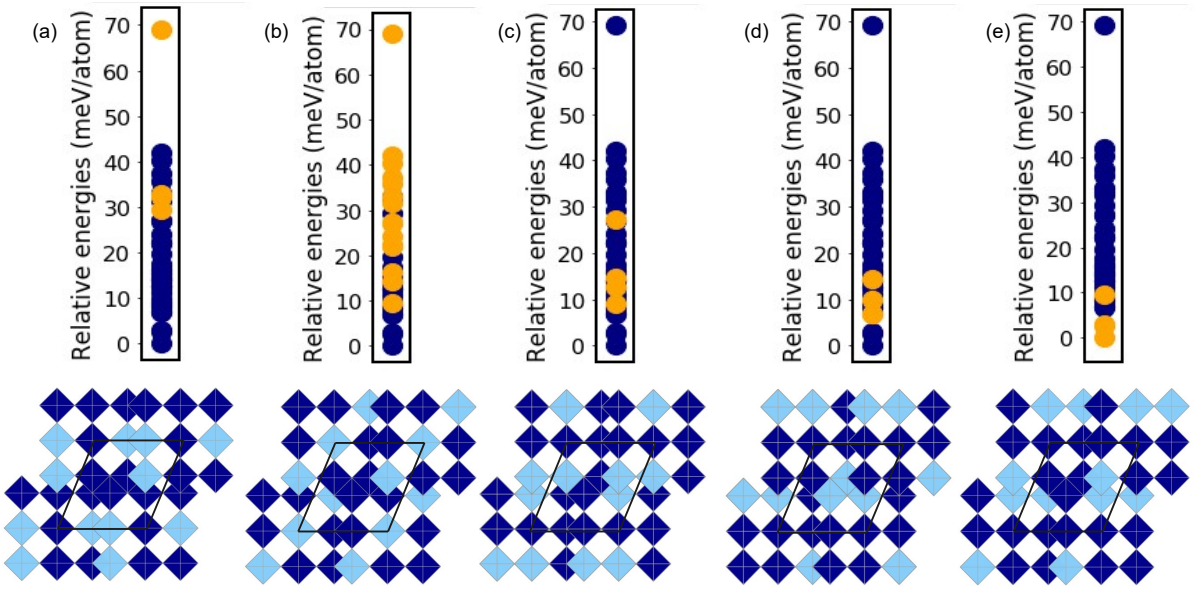

Figure 5.3: The relative formation energies of $TiNb_2O_7$ orderings that have all M5 sites filled (a), all M4 sites filled (b), all M3 sites filled (c), all M1 sites filled(d), and all M2 sites (e) filled are shown in gold, overlayed over the formation energies of all points as show in blue.

can also host Li in horizontal and vertical window sites, labeled W_h and W_v, respectively. Both sites are coordinated by four oxygen ions in a square planar configuration. There are four W_h and four W_v sites per unit cell of $TiNb_2O_7$, residing in the blocks as illustrated in Figure 5.1.

5.3.2 Li insertion into $TiNb_2O_7$ at zero Kelvin

The energies of 937 symmetrically distinct orderings of Li and vacancies over the interstitial sites of $TiNb_2O_7$ (i.e. P_s, P'_s, W_v and W_h) were calculated with DFT-PBE. In each of these structures, the $TiNb_2O_7$ host is the lowest energy Ti-Nb ordering shown in Figure 5.1. The different Li-vacancy configurations were enumerated with CASM[132] and include different orderings within the primitive unit cell and in super cells in which the b axis along the block lengths are doubled or quadrupled. Figure 5.4(a) shows the calculated formation energies as a function of Li concentration. Many Li-vacancy ar-

rangements reside on the convex hull. However, with the exception of three ordered phases at $x = 0.66$, $x = 2.833$, and $x = 3.5$, most are weakly stable and very close in energy to other structures that have similar Li-vacancy arrangements and compositions.

At dilute lithium concentrations up to $Li_{0.33}TiNb_2O_7$, P_s sites are stable. At $Li_{0.66}TiNb_2O_7$ vertical window sites begin to stabilize. By $Li_{2.83}TiNb_2O_7$ we see complete filling of all P_s sites. Additionally at this ordering, all pyramidal sites (P_s and P'_s) that are coordinated by Ti ions are filled. Window sites begin to fill as concentration increases, and at $Li_{3.5}TiNb_2O_7$, half filling of vertical window sites occurs with the vertical window sites parallel throughout the block. Filling of half of available vertical window sites is experimentally supported through neutron diffraction studies at intermediate lithium concentrations [198].

The voltage at zero Kelvin is linearly related to the slope of the convex hull as a function of lithium concentration.[2] The zero Kelvin voltage profile is shown in Figure 5.4(b). Each ordered phase with an energy on the convex hull appears as a step in the zero Kelvin voltage curve. Each plateau corresponds to a two-phase reaction from one ordered phase to another ordered phase. The large steps at x=0.66, x=2.833, and x=3.5 correspond to strong ground state orderings. The voltage curve, which starts at 2 V upon insertion of a dilute concentration of Li, shows that $TiNb_2O_7$ can intercalate more than 5 Li per formula unit while maintaining a positive voltage.

The voltage at zero Kelvin is linearly related to the slope of the convex hull as a function of lithium concentration.[2] The zero Kelvin voltage profile is shown in Figure 5.4(b). Each ordered phase with an energy on the convex hull appears as a step in the zero Kelvin voltage curve, while each plateau corresponds to a two-phase coexistence between a pair of ordered phases.[224, 70, 2] The voltage curve, which starts at 2 V upon insertion of a dilute concentration of Li, shows that $TiNb_2O_7$ can intercalate more than 5 Li per formula unit while maintaining a positive voltage.

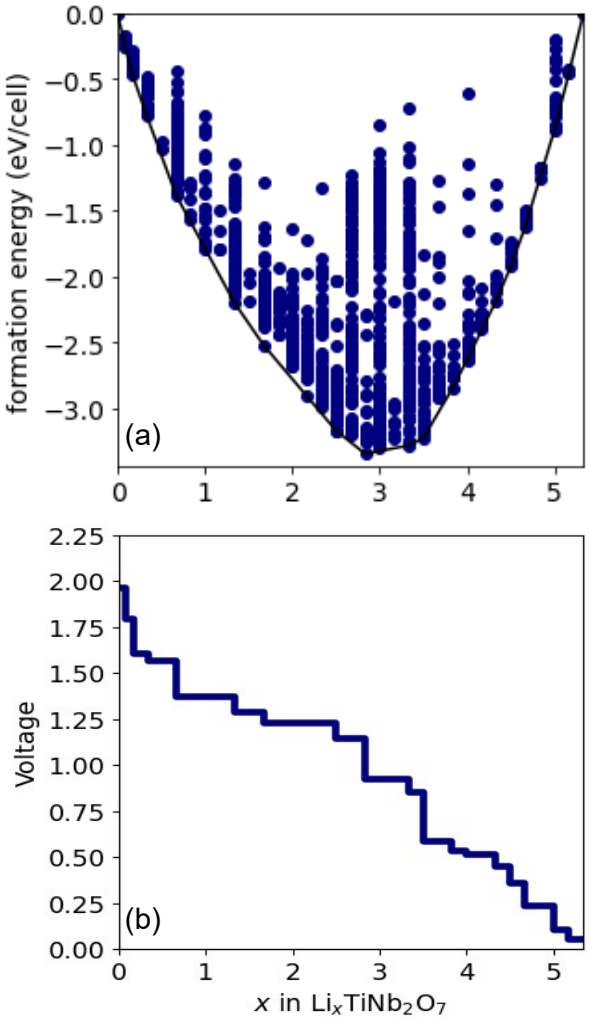

Figure 5.4: (a) Convex hull and formation energies as a function of composition for $Li_xTiNb_2O_7$. (b) 0K Voltage as a function of composition for $TiNb_2O_7$.

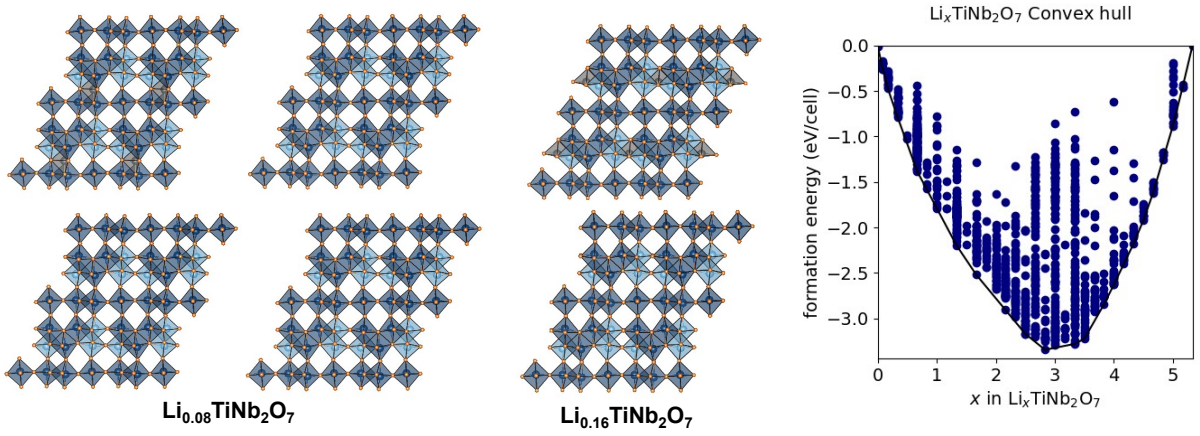

Figure 5.5: Ground state lithium-vacancy orderings at x=0.008 and x=0.16.

An important property affecting Li diffusion is the Li site preference as a function of Li concentration.[137, 225, 182, 226] Figure 5.4(c) plots the number of each type of Li site that is occupied in each ground state ordering. The pyramidal P_s sites fill initially and have the highest occupancy at all Li concentrations. For the Ti and Nb ordering shown in Figure 5.1, vertical window sites begin to fill at $x = 0.66$. Both the vertical and horizontal window sites, W_v and W_h, fill steadily beyond $x = 0.66$, but the largest fraction of Li continue to fill the pyramidal P_s sites until they are close to saturated at around $x = 3.5$. Close to half the vertical window sites are filled beyond $x = 2.5$, which is consistent with neutron diffraction studies.[198] The pyramidal P'_s sites, which share seven edges with neighboring transition metal cations, only start to fill gradually past $x = 2$. Li-vacancy ground states are shown in Figure 5.5 for dilute limit orderings. Higher composition Li-vacancy orderings are shown in Figures 5.6, 5.7, 5.8, 5.9, and 5.10.

5.3.3 Redox mechanisms: formation of metal-metal bonds

The pristine $TiNb_2O_7$ Wadsley-Roth phase is an insulator. At this composition, the d^0 Ti^{4+} and Nb^{5+} cations are in their maximum oxidation states. Figure 5.11(a), shows that DFT-PBE predicts a large band gap in the electronic density of states (DOS) of

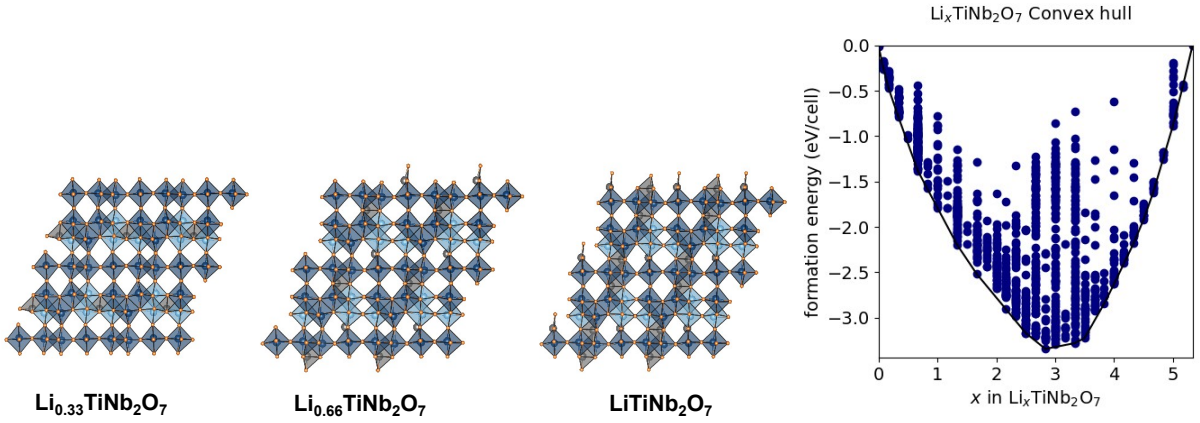

Figure 5.6: Ground state lithium-vacancy orderings at x=0.33, x=0.66, and x=1.

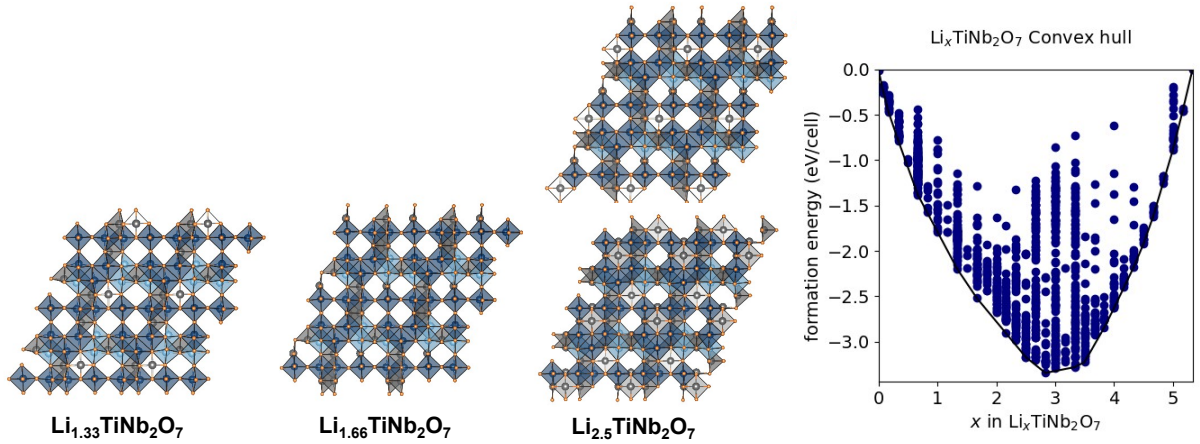

Figure 5.7: Ground state lithium-vacancy orderings at x=1.33, x=1.66, and x=2.5.

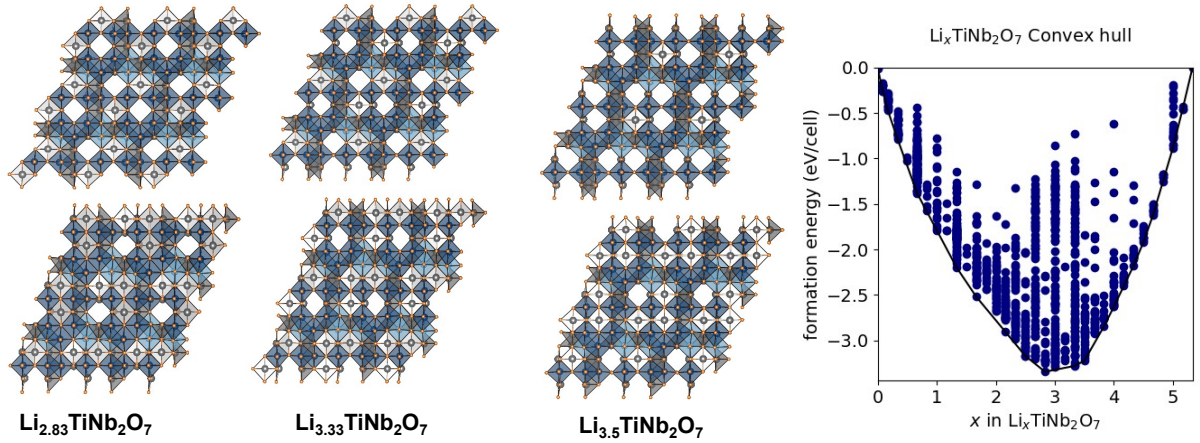

Figure 5.8: Ground state lithium-vacancy orderings at x=2.83, x=3.33, and x=3.5.

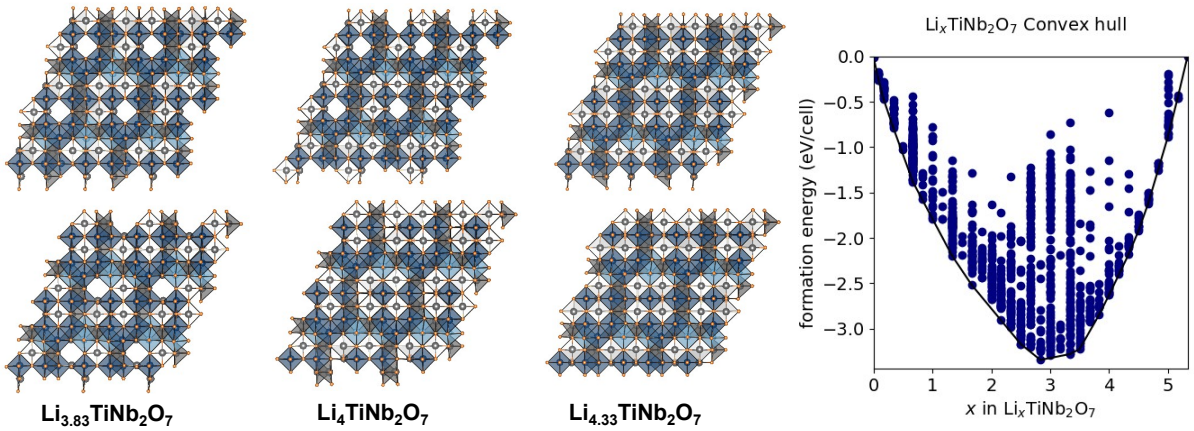

Figure 5.9: Ground state lithium-vacancy orderings at x=3.83, x=4, and x=4.33.

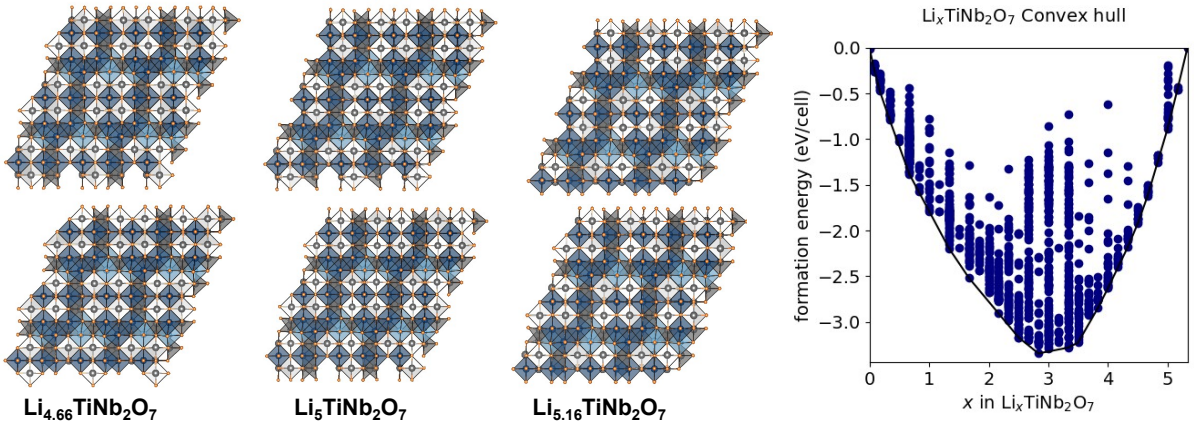

Figure 5.10: Ground state lithium-vacancy orderings at x=4.66, x=5, and x=5.16.

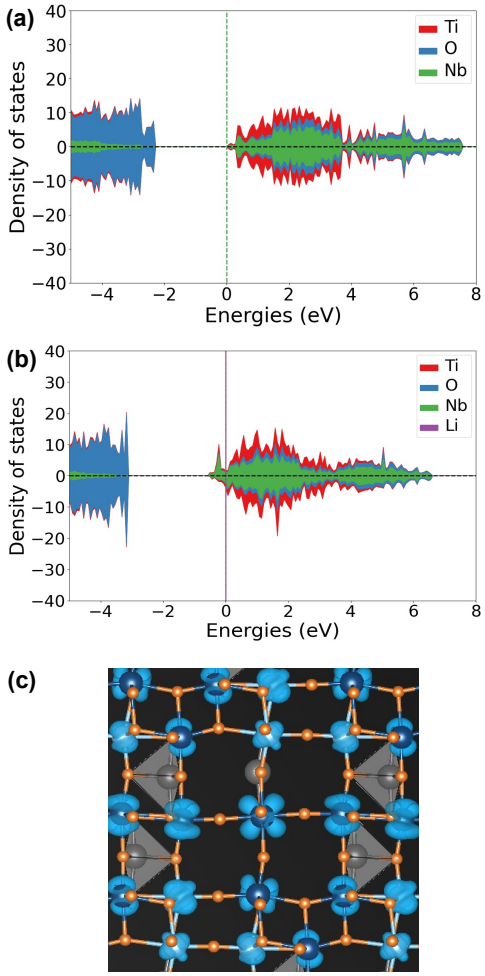

Figure 5.11: The electronic density of states (DOS) of (a) $TiNb_2O_7$ and (b) $LiTiNb_2O_7$ as calculated with DFT-PBE. The positive (negative) DOS corresponds to spin up (down) states. (c) The electronic charge density corresponding to the filled state in the conduction band of $LiTiNb_2O_7$.

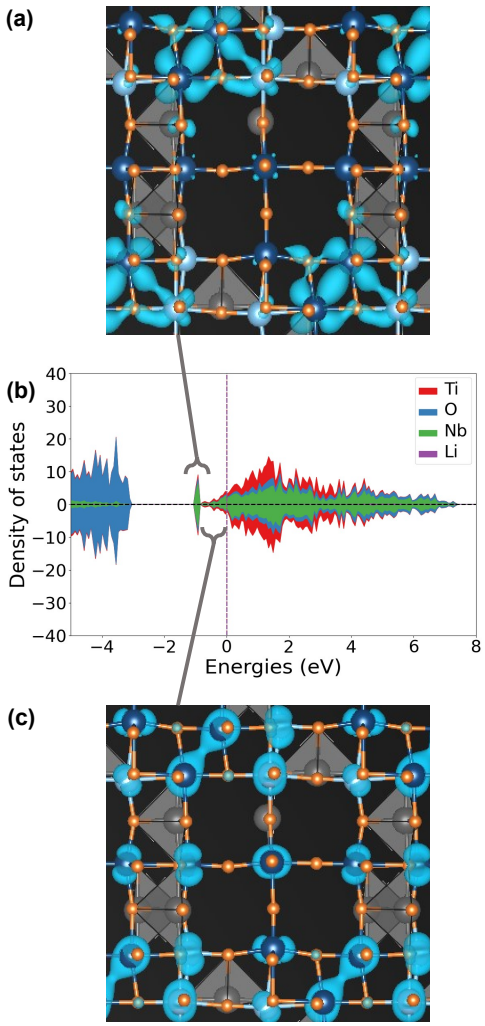

Figure 5.12: (a) The electronic charge density corresponding to the peaks labeled d in the DOS of $Li_{1.66}TiNb_2O_7$ shown in (b). (c) The electronic density of states for the remaining filled states below the Fermi level.

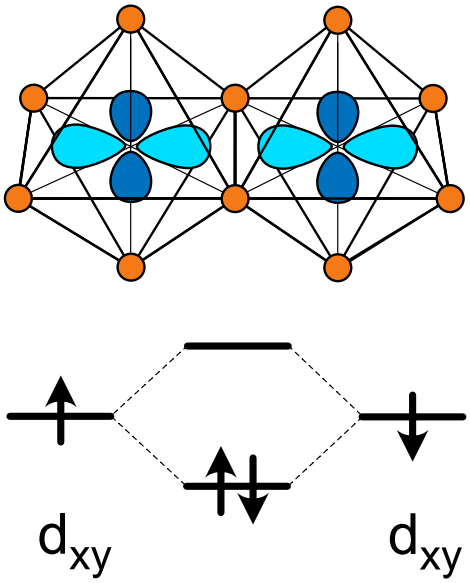

Figure 5.13: The d_{xy} orbitals of edge-sharing transition metal cations can hybridize to form bonding and anti-bonding states. The bonding states have a lower energy than the unhybridized d_{xy} states and can host two electrons of opposite spin.

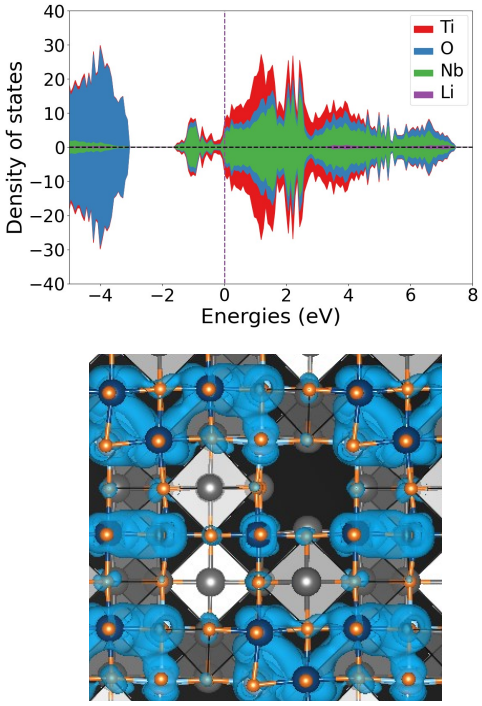

Figure 5.14: Electronic DOS of $Li_{2.5}TiNb_2O_7$ and electronic charge density of states of the states extending from the bottom of the conduction band up to the Fermi level.

$TiNb_2O_7$. The gap separates the filled valence bands, which primarily have oxygen p character, and the bottom of the empty conduction bands, which are derived from the t_{2g} orbitals of the octahedrally coordinated transition metals (i.e. the d_{xy}, d_{xz} and d_{yz} orbitals in an octahedral environment). This is consistent with past calculations by Catti et al [198] and Griffith et al [137].

The addition of Li to $TiNb_2O_7$ leads to a reduction of the formal oxidation states of the Ti and Nb cations. At low Li concentrations, DFT-PBE predicts that the electrons donated to the host by Li tend to delocalize over the different transition metals, with a slight enhancement in the occupancy of the d_{xy} orbital on the central Nb site.[227, 137] This is shown in Figure 5.11(b) for $LiTiNb_2O_7$. There is some degree of spin polarization, with the spin up DOS (positive) having more states below the Fermi level than the spin down DOS (negative). Figure 5.11(b) shows that the donated electrons fill the bottom of the conduction band without substantially altering the DOS of the conduction bands of pristine $TiNb_2O_7$. Figure 5.11(c) plots the electronic charge density for the states between the bottom of the conduction band and the Fermi level of $LiTiNb_2O_7$. The electronic charge density concentrates around the transition metal cations and adopt the characteristic charge density distribution of t_{2g} orbitals (i.e. d_{xy}, d_{xz} and d_{yz}).

The redox mechanism changes qualitatively upon increasing the Li concentration beyond $x = 1$. This is evident in Figure 5.12 for $Li_{1.66}TiNb_2O_7$. New states emerge below the Fermi level (labeled d in Figure 5.12(b)) that are disconnected from the more itinerant bands derived from t_{2g} states. Figure 5.12(a) plots the electronic charge density due to the break away peaks in the DOS of $Li_{1.66}TiNb_2O_7$ (Figure 5.12(b)), clearly showing that the charge density associated with these states is concentrated between a pair of edge-sharing Nb cations. An analysis of the local projected density of states of each of the two Nb atoms of the pair shows that their d_{xy} orbitals have energies that coincide with the peaks below the Fermi level in Figure 5.12(b). The electronic charge

density due to the remaining DOS that extends from the top of the break-away peaks up to the Fermi level is shown in the bottom of Figure 5.12(c). These states have a combined electronic charge density that is more uniformly distributed throughout the crystal and more centered around individual transition metal cations than between metal cations.

The enhanced electron charge density between the pair of edge-sharing Nb in Figure 5.12(a) is consistent with a filled bonding state that arises when the d_{xy} orbitals of a pair of edge-sharing transition metal cations hybridize as schematically illustrated in Figure 5.13.[228, 229, 79] The hybridization between edge-sharing d_{xy} orbitals leads to metal-metal dimer formation and generates bonding states that have a lower energy than the unhybridized d_{xy} orbitals.[228] The bonding states are therefore favorable redox centers to accommodate the electrons donated by Li to the host. It is clear in the DOS of Figure 5.12(b) that a pair of electrons with opposite spin fill the bonding state. The filling of the bonding state of a hybridized metal-metal bond will lead to a shortening of the distance between the neighboring transition metal cations.[79] This is indeed predicted to occur, with the distance between the pair of Nb cations contracting from a value of 3.09 Å at $x = 1$ to 2.69 Å at $x = 1.66$.

Additional metal-metal bonds form between edge-sharing octahedra as electrons are added to $Li_xTiNb_2O_7$ upon further insertion of Li. At $x = 2.5$, for example, a complex of metal-metal bonds become evident in the charge density plot of Figure 5.14. Each edge-sharing pair of transition metal cations with an enhanced charge density along the bond axis also has a shortened metal-metal distance, consistent with the filling of the bonding states that arise from metal-metal dimer formation. Several transition metal cations even participate in two metal-metal dimers. A transition metal with two edge-sharing cation neighbors can form a separate dimer with each neighbor with orthogonal onsite t_{2g} orbitals.[79] Density of states and charge density plots for multiple ground states and low energy states from x=0.33 to x=3.5 is described in Appendix A.

While the DOS plot of Figure 5.11 shows that there is some degree of spin polarization at $x = 1$, the DOS plots of Figures 5.12 and 5.14, show that the filled bonding states of the metal-metal dimers are non-spin polarized. Figure 5.15 collects the calculated magnetic moments of all 937 $Li_xTiNb_2O_7$ structures normalized by the number of Li (i.e. number of electrons donated to the host) as a function of Li concentration. The magnetic moments are expressed in units of a Bohr magneton μ_B and the numerical values plotted in Figure 5.15 are calculated as the difference in number of up spin and down spin electrons per Li multiplied by $g\sqrt{s(s+1)}$, where $g = 2$ and $s = 1/2$. The light blue line connects the magnetic moment per Li of the ground states of $Li_xTiNb_2O_7$. Figure 5.15 shows that at dilute concentrations, the electrons donated to the host adopt a spin-polarized configuration, resulting in a net magnetic moment of the crystal. However, above $x = 1$, the magnetic moment per Li ion decreases to negligible values. It is above this concentration that the bonding states of the metal-metal dimers are predicted to accommodate the electrons donated by Li to the host. Figure 5.15 also shows the magnetic moment per Li (in units of μ_B) as measured experimentally by Griffith et al. [137] The qualitative agreement between the calculated and measured magnetic moment per Li ion is very good. For comparison, Figure 5.15 also shows the calculated magnetic moment per Li in the ground state configurations as calculated with DFT-SCAN. The same trend is predicted, and the values are similar to those predicted with DFT-PBE.

5.3.4 Effect of redox mechanism on structure

The pristine $TiNb_2O_7$ crystal structure has highly distorted MO_6 octahedra (M = Ti or Nb) due to the oxidation states of Ti and Nb and the large number of edge-sharing MO_6 octahedra. The d^0 Ti^{4+} and Nb^{5+} cations are susceptible to second-order Jahn-Teller distortions when octahedrally coordinated by oxygen.[230, 77] This causes a

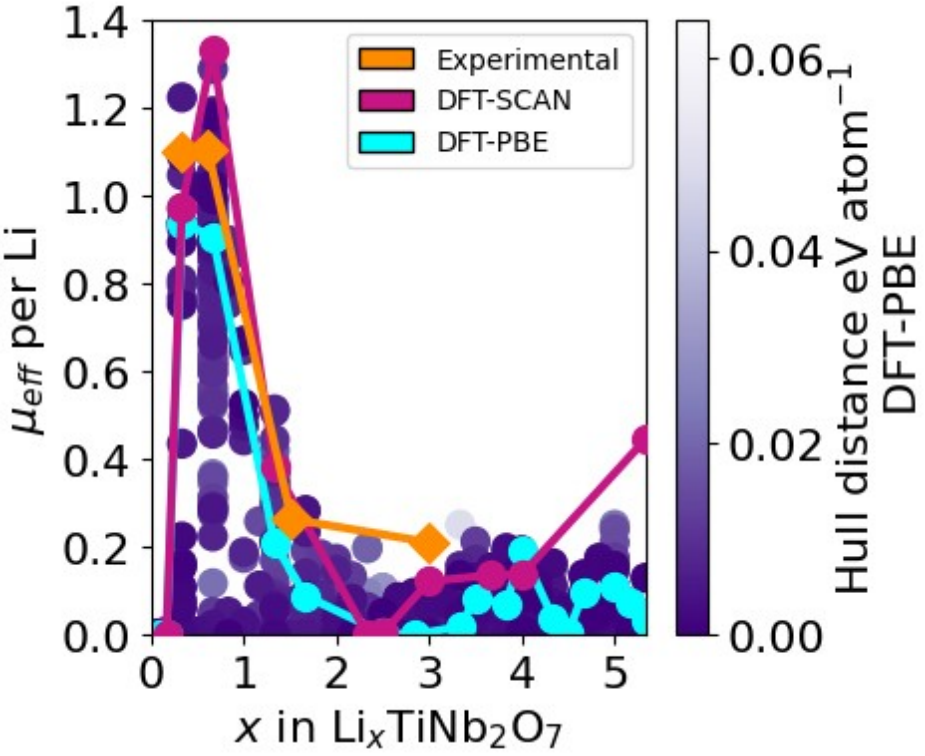

Figure 5.15: Magnetic moments normalized by the number of Li ions of 937 $Li_xTiNb_2O_7$ structures as calculated with DFT-PBE. The magnetic moments per Li of the ground state structures are connected by the blue line. The red points are the magnetic moments per Li of the ground state structures as calculated with DFT-SCAN. Orange points are magnetic moments per Li as measured by Griffith et al.[137]

displacement of the cations away from the center of their coordinating octahedra. The edge-sharing MO_6 octahedra of $TiNb_2O_7$ also undergo significant distortions due to the strong electrostatic repulsion between neighboring Ti^{4+} and Nb^{5+}.[231] This repulsion increases the distance between edge-sharing cations, causing a further off-centering of each cation that simultaneously induces collateral distortions of their surrounding oxygen octahedron.

The donation of electrons to the host upon Li insertion undoes many of the octahedral distortions that are initially present in $TiNb_2O_7$. The reduction of the Ti^{4+} and Nb^{5+} cations eliminates their susceptibility to second-order Jahn-Teller distortions. Furthermore, the redox mechanism described in the previous section, which leads to metal-metal dimer formation, has structural consequences that affect the lattice parameters of the host. Each edge-sharing pair of transition metal cations that hybridize to form metal-metal dimers undergo a contraction that pulls the cations back towards the centers of their octahedra.

Figure 5.16 plots the edge-sharing metal-metal bond lengths as a function of the Li concentration collected from the 937 fully relaxed $Li_xTiNb_2O_7$ structures. It is insightful to inspect the edge-sharing Nb-Nb, Nb-Ti, and Ti-Ti pair distances separately, shown in Figures 5.16(a), (b), and (c), respectively. The nearest neighbor distances of edge-sharing metal-metal pairs in the ground state configurations are shown in gold. The figures show a clear trend towards an overall contraction of the edge-sharing metal-metal bonds with increasing Li concentration. Especially notable is the abrupt contraction in a subset of the bond lengths that occurs between $x = 1$ and $x = 2$. In the lowest energy ground state structures (gold points), this occurs first between Nb-Nb pairs as is evident in Figure 5.16(a) with the two gold points at $x = 1.33$ and $x = 1.66$, having values of approximately 2.7 Å. Edge-sharing Nb-Ti pairs (Figure 5.16(c)) also exhibit dimer formation, with a subset contracting to values close to 2.8 Å, but the contractions only

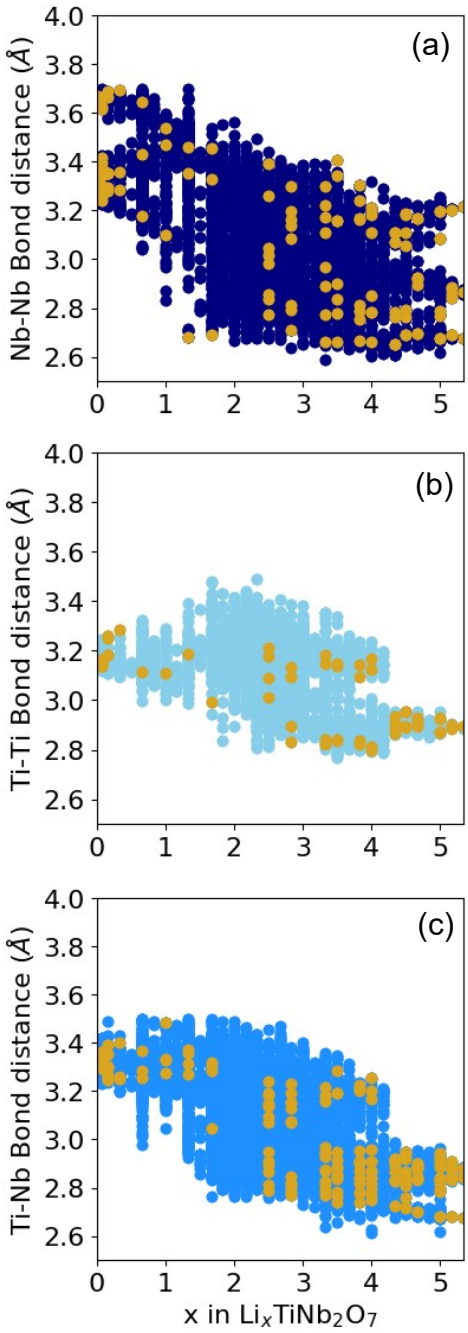

Figure 5.16: Bond lengths in $Li_xTiNb_2O_7$ structures with formation energies within 50meV/atom of the convex hull for edge-sharing (a) Nb-Nb pairs, (b) Ti-Ti pairs, and (c) Ti-Nb pairs. Gold points refer to the pair distances in ground state structures.

set in appreciably after Nb-Nb pairs have started to contract. The contraction between edge-sharing Ti-Ti pairs (Figure 5.16(b)) is less pronounced and only begins to occur at higher Li concentrations.

The onset of metal-metal dimer formation leads to sizable dimensional changes of the host. Figure 5.17(a) collects the change in volumes of the relaxed ground state structures of $Li_xTiNb_2O_7$ relative to that of $TiNb_2O_7$ and compares them to the experimentally measured [169] changes in volume. The agreement between the volume change as calculated with DFT-PBE and the measured volume change is very good. Figure 5.17(b) compares the change in the calculated lattice parameter parallel to the 3×3 blocks of the $Li_xTiNb_2O_7$ host for the ground state structures to the corresponding experimental values.[169] Here as well, the agreement is very good. The b-lattice parameter is predicted to increase abruptly between $x = 1$ and $x = 2.5$ and then levels off at higher Li concentrations. The same trend is observed experimentally.[169]

A useful metric of the dimensional changes of the host is the strain order parameter $e_3 = (2E_{zz} - E_{xx} - E_{yy})/\sqrt{6}$,[86, 27] which measures tetragonal distortions along the 3×3 block axis of $Li_xTiNb_2O_7$. The Cartesian strains, E_{xx}, etc, appearing in the expression of the strain order parameter, e_3, are defined with respect to a Cartesian coordinate system whose $\hat{z}$ axis is parallel to the block length of the $TiNb_2O_7$ host structure. The Cartesian strains are calculated as Hencky strains [86] relative to the dimensions of the fully relaxed $TiNb_2O_7$ host structure without any Li. Figure 5.17(c) collects the e_3 strain for all the 937 fully relaxed structures of $Li_xTiNb_2O_7$. The e_3 strains of the ground state structures are connected with a light blue line. Similar to the variation in the b-lattice parameter in Figure 5.16(b), the e_3 strain order parameter shows a rapid increase in a narrow Li composition interval between $x = 1$ and $x = 2.5$. A positive value of e_3 signifies an expansion along the block length and a contraction along the block waist. The abrupt increase in e_3 and in the b lattice parameter between $x = 1$ and $x = 2.5$ can be attributed

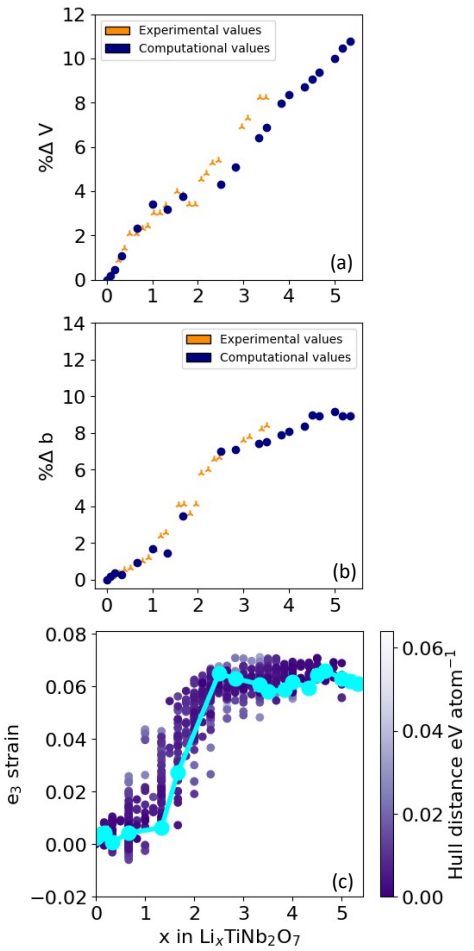

Figure 5.17: (a) Comparison of measured and calculated percent changes in volume of the $Li_xTiNb_2O_7$ unit cell. Points labeled as triangles were measured experimentally by Guo et al [169]. Circles are for the ground state structures of $Li_xTiNb_2O_7$ as calculated with DFT-PBE. (b) Comparison of the percent change in the measured (triangles) and calculated (circles) b lattice parameter. (c) The calculated e_3 strain relative to $TiNb_2O_7$ for 937 $Li_xTiNb_2O_7$ structures.

to the onset of metal-metal dimer formation, which results in a reduction of the distance between edge-sharing transition metal cations and a straightening of the highly distorted octahedra of the pristine $TiNb_2O_7$ crystal structure.

Large volumetric changes of the host accompanying Li insertion are generally undesirable as they can cause mechanical degradation of the electrode composite [232, 233, 234, 235]. Many intercalation compounds expand as Li fills their empty interstitial sites. Furthermore, transition metals change their oxidation state upon Li insertion, which can lead to a change in the metal-oxygen bond lengths and thereby the volume of MO_6 octahedra [236, 237, 145, 153, 238, 4, 27]. In some instances, the change in oxidation state will produce a shape change of the MO_6 octahedron [239, 240]. Both Ti and Nb are susceptible to second order Jahn-Teller distortions when they are in their maximum oxidation state (i.e. Ti^{4+} and Nb^{5+}) [143]. As with first order Jahn-Teller distortions, second order Jahn-Teller distortions produce noncentrosymmetric displacements of the ions of a molecule or a cluster that lead to distinctive shape changes.

The degree with which the MO_6 octahedra of $TiNb_2O_7$ distort upon Li insertion can be analyzed by projecting the ionic displacements of each octahedron on symmetry adapted collective displacements as described in Section 2.5.1. Figures 5.18(a) and (b), for example, show the average amplitude of the symmetry preserving breathing mode of the TiO_6 and NbO_6 octahedra as a function of Li concentration. Also shown is the one standard deviation spread around the average. The averages were collected from the 937 Li-vacancy orderings in $Li_xTiNb_2O_7$ as relaxed with DFT-PBE. Figure 5.18 shows that the average volumes of the NbO_6 and TiO_6 octahedra increase steadily with the concentration of Li. Of particular interest in Figure 5.18(b) is the abrupt increase between $x = 1$ and $x = 2$ in the volume of the NbO_6 octahedra that share four edges with neighboring octahedra (purple curve). This concentration interval coincides with the start of the metal-metal dimer redox mechanism, with the first pairs that form dimers involving

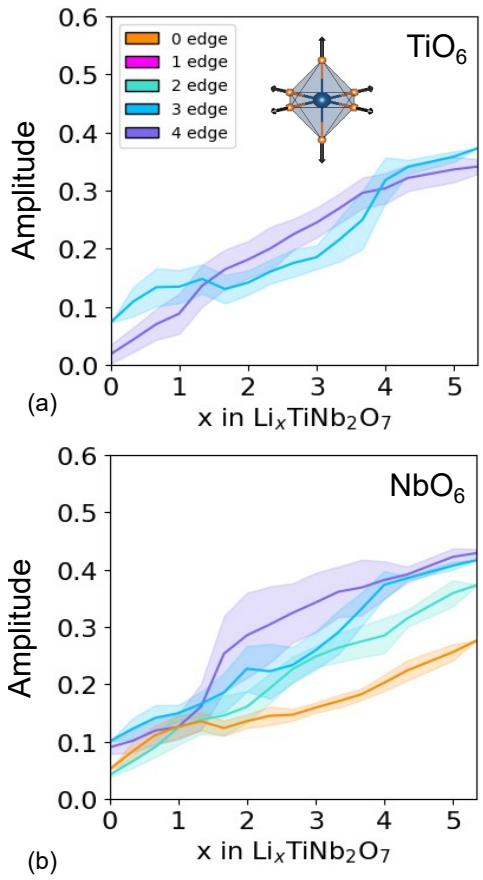

Figure 5.18: The amplitude of the octahedral breathing mode for (a) the TiO_6 octahedra and (b) the NbO_6 octahedra as a function of lithium composition.

Nb cations in octahedra that share four edges with neighboring octahedra. Figure 5.18(b) also shows that the Nb in the corner-sharing octahedron at the center of the 3×3 block (orange curve) expands between $x = 0$ and $x \approx 1$ but then remains more or less constant until $x \approx 3$. This is consistent with the analysis of Morris and Griffith,[143, 137, 144] who showed that the transition metal cations of the corner-sharing octahedra at the center of the blocks of Wadsley-Roth phases play an important role in the redox processes at dilute Li concentrations.

There are a total of 15 symmetry adapted collective displacement modes for a perfect MO_6 reference octahedron. These naturally divide into six irreducible subspaces as described in Section 2.5.1. The breathing mode shown in the inset of Figure 5.18 forms a one-dimensional subspace. Another one is of dimension two and is spanned by the well-known first-order Jahn-Teller collective displacement modes. There are four additional irreducible subspaces, each of dimension three (see Section 2.5.1 for more details). Two of these are useful to analyze the distortion modes of Wadsley-Roth phases such as $Li_xTiNb_2O_7$ as they measure the extent of second-order Jahn-Teller distortions and of the octahedral shape changes that accommodate the changes in the distance between edge-sharing cations.

Figure 5.19(a) shows the three symmetry adapted collective displacement modes that characterize a second-order Jahn-Teller distortion of a d^0 transition metal coordinated by an octahedron of oxygen ions. The three collective displacement modes of Figure 5.19(a) each describe an off-centering of the transition metal along one of the Cartesian axes and form a basis with which to describe an arbitrary off-centering. A measure of the degree of off-centering is the Euclidean length of the three amplitudes of the collective distortion modes of Figure 5.19(a) as described in Section 2.5.1. Figures 5.19(b) and (c) shows the average Euclidean length of the off-centering distortion mode along with a one standard deviation spread for the TiO_6 and NbO_6 octahedra as a function of Li concentration.

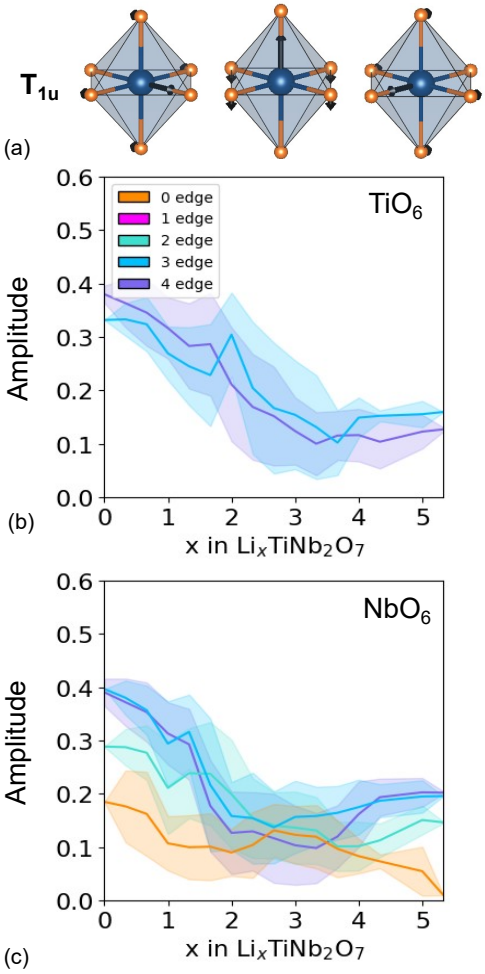

Figure 5.19: (a) Symmetry adapted collective displacement modes that characterize a second-order Jahn-Teller distortion of a d^0 transition metal that is octahedrally coordinated by oxygen. The average amplitude of this type of displacement mode as a function of Li concentration for (b) TiO_6 and (c) NbO_6 octahedra. The amplitudes are calculated as a Euclidean distance within the space spanned by the three collective displacement modes of (a).

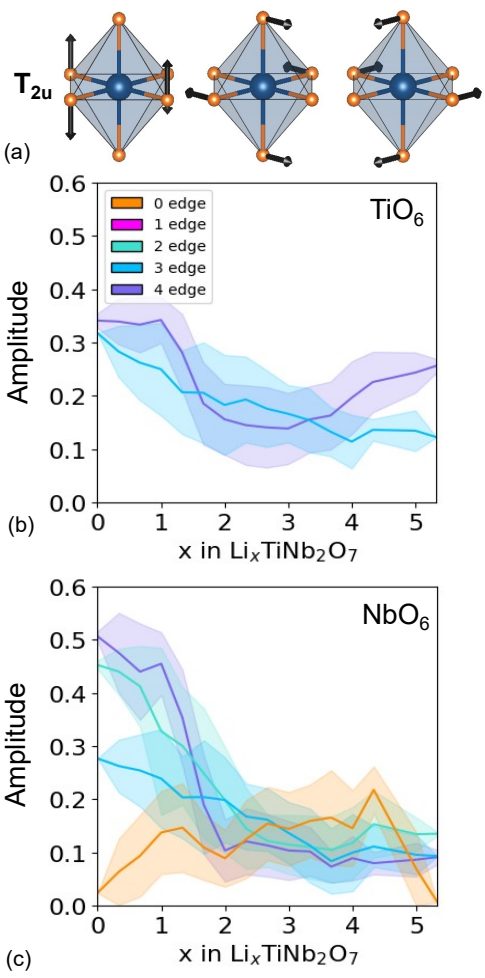

Figure 5.20: (a) Symmetry adapted collective displacement modes of the oxygen octahedra that have large amplitudes in $TiNb_2O_7$. The average amplitude of this type of displacement mode as a function of Li concentration for (b) TiO_6 and (c) NbO_6 octahedra. The amplitudes are calculated as a Euclidean distance within the space spanned by the three collective displacement modes of (a).

The averages were again taken over the 937 fully relaxed $Li_xTiNb_2O_7$ structures. The large values at low Li concentrations indicate that the cations are displaced away from the center of their coordinating octahedra. The off-centering is more pronounced for the cations that share more edges with neighboring octahedra. The Nb of the corner-sharing octahedron at the center of the 3×3 block (orange curve in Figure 5.19(c)) exhibits the smallest degree of off-centering, which decreases abruptly around $x \approx 1$. As the central Nb reduces its oxidation state from its starting value of Nb^{5+}, its susceptibility to a second-order Jahn-Teller distortion is lowered and the degree to which it is off-centered decreases. The other transition metal cations, which are more off-centered at a Li concentration of $x = 0$ than the central Nb due to the electrostatic repulsion with neighboring edge-sharing transition metal cations, also become less off-centered with increasing Li concentration. The decrease in the degree of off-centering occurs at slightly higher Li concentrations than that of the central Nb and coincides with the composition at which metal-metal dimers start to form. The formation of bonding states between neighboring transition metal cations leads to metal-metal dimers, as described above, and an overall centering of the transition metal cations within their octahedra.

Figure 5.20(a) shows a second set of symmetry adapted collective displacement modes of MO_6 octahedra whose amplitudes in $Li_xTiNb_2O_7$ undergo large changes with Li concentration. The three collective displacement modes of Figure 5.20(a) also form a basis to describe octahedral distortions that reside within a T_{2u} irreducible subspace, with each collective displacement involving four equatorial oxygen ions that distort perpendicular to their equatorial plane. These displacement modes measure the collateral distortions of the oxygen octahedra in response to the large relaxations that lead to an off-centering of edge-sharing transition metal cations.[231] Figure 5.20(b) and (c) plots the average Euclidian distance of the amplitudes of the three orthogonal displacement modes for the TiO_6 and NbO_6 octahedra as a function of Li concentration. The octahedral distortions

are large at dilute Li concentrations but decrease substantially over a small concentration interval between $x = 1$ and $x = 2$ upon the formation of metal-metal dimers. Upon forming metal-metal dimers, the transition metal cations move to the center of their octahedra, thereby allowing the oxygen ions to adopt positions that are closer to those of an ideal octahedron.

5.3.5 Finite temperature thermodynamic properties and Li site occupancy

Room temperature electrochemical properties were calculated by combining cluster expansions with Monte Carlo simulations. A cluster expansion is a surrogate model that interpolates the energies of different Li-vacancy orderings as calculated with a computationally expensive first-principles method. The cluster expansion can then be used in Monte Carlo simulations to calculate the energies of microstates sampled in large unit cells according to the probability distribution of statistical mechanics. The cluster expansions used in this study were trained to the formation energies of 937 Li-vacancy orderings in $Li_xTiNb_2O_7$ shown in Figure 5.4(a). A Bayesian approach was followed to enable uncertainty quantification of calculated thermodynamic properties due to numerical noise on the training data and cluster expansion truncation and parameter selection. Ten different cluster expansions were sampled from a Bayesian posterior probability distribution as described in Section 5.2.1 and by Ober et al.[223] Each cluster expansion was used in Monte Carlo simulations to calculate equilibrium voltage curves (related to the Li chemical potential according to the Nernst equation [2]) and equilibrium Li site occupancies as a function of the overall Li concentration.

Figure 5.21(a) shows ten voltage curves as a function of Li concentration, each calculated with a different cluster expansion sampled from a Bayesian posterior distribution.

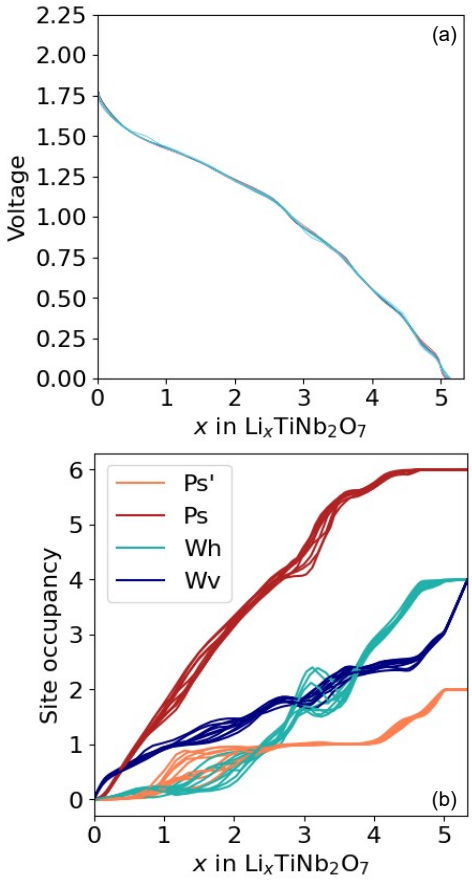

Figure 5.21: (a) Voltage profile at 300K of $Li_xTiNb_2O_7$ as calculated with Monte Carlo simulations applied to cluster expansions of the formation energy. The Ti-Nb ordering of $TiNb_2O_7$ is that of Figure 5.1. (b) Lithium site occupancy as a function of lithium concentration as calculated with Monte Carlo simulations applied to 10 different cluster expansions of the formation energy.

The voltage curves were calculated with grand canonical Monte Carlo simulations, which generates the average Li concentration at each Li chemical potential and temperature. The smooth sloping voltage curves reflect a solid solution. The Monte Carlo simulations predict that the Li ions and vacancies are disordered at room temperature.

Similar to experimentally measured voltage profiles of $Li_xTiNb_2O_7$,[213, 16, 215] the calculated voltage curve exhibits an initial steep decrease between $x = 0$ and $x \approx 0.5$, which is followed by a flatter concentration dependence between $x \approx 0.5$ and $x \approx 2$. Beyond $x \approx 2$, the decrease in voltage with Li concentration is again steeper and exhibits several weak steps. We note that the middle portion, while having a shallow slope, is not as flat as that exhibited by experimental curves.[156]

Figure 5.21(b) shows the Li site occupancy as a function of Li concentration. Each Li site has ten curves, one for each cluster expansion sampled from the posterior distribution. It is clear in Figure 5.21(b) that differences in predicted site occupancies as calculated with the different cluster expansions are small. The predicted trends in Figure 5.21(b) are consistent with those predicted at zero Kelvin. Li primarily fills the pyramidal P_s sites, which steadily become enriched with Li until they saturate around x=4. The vertical window sites, W_v, also accommodate Li ions early on, but do not saturate until approximately x=5. The horizontal window sites, W_h, only start filling around x=2. The pyramidal P_s' sites are overall least favored and only saturate at the highest Li concentration.

It is of interest to analyze the Li site occupancy based on the surrounding Ti concentration. This is shown in Figure 5.22. Each Li site is distinguished by the number of Ti cations that share an edge with the Li site. The darker blue curves and uncertainty bounds track the concentration of Li in sites that are surrounded by more Ti, as indicated in the insets, while the lighter green curves track the Li concentration in sites surrounded by more Nb. Overall, Figure 5.22 shows that Li tends to first fill sites that

are surrounded by more Ti than Nb.

5.4 Discussion

This study examines the importance of Ti-Nb ordering on lithium site filling in $TiNb_2O_7$ and examines structural changes as a function of lithium concentration. For experimentally synthesized $TiNb_2O_7$, disorder is present on the transition metal sublattice. Orderings with Ti on M1 and M2 sites are found to be lower in energy than orderings with Ti in M3, M4, and M5 sites, corroborating earlier neutron diffraction work by Dreele et al [138].

Our first-principles study of the $Li_xTiNb_2O_7$ Wadsley-Roth phase has shed light on the redox mechanisms accompanying the electrochemical lithiation of $TiNb_2O_7$. At least two redox mechanisms are identified based on an analysis of 937 fully relaxed $Li_xTiNb_2O_7$ structures. At dilute Li concentrations DFT-PBE calculations predict that electrons donated by Li reduce Ti and Nb more or less uniformly. The calculations predict some degree of spin polarization for $x < 1$. At higher Li concentrations, DFT-PBE calculations predict that the redox mechanism changes qualitatively, shifting from the filling of cation-centric t_{2g} orbitals to the filling of the bonding states that arise when the t_{2g} orbitals of edge-sharing transition metal cations hybridize to form metal-metal dimers. The redox then occurs on extended molecular orbital-like states with enhanced charge density between pairs of edge-sharing transition metal cations. The first metal-metal dimers to form involve Nb cations that occupy the sites with the highest number of edge-sharing neighbors. The large electrostatic interactions between highly oxidized edge-sharing neighbors increases the driving force to undergo redox at those sites in order to lower their formal oxidation state. Nb-Nb dimer formation is followed by Nb-Ti dimer formation, with less pronounced activity predicted to occur between Ti-Ti pairs.

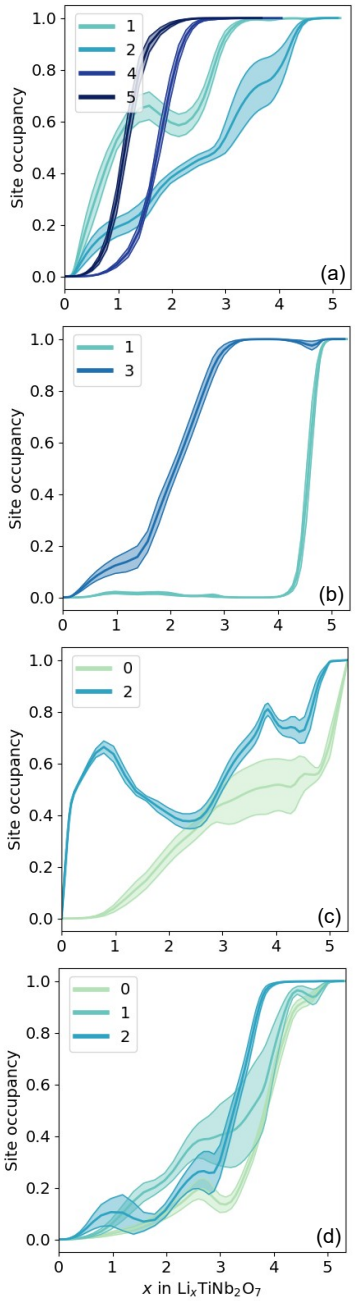

Figure 5.22: The Li concentration of different sites coordinated by varying amounts of edge-sharing Ti for the (a) P_s, (b) P'_s, (c) W_v and (d) W_h sites.

The dimer formation between edge-sharing transition metals has structural consequences. The distance between metal-metal pairs that host the electrons donated by Li in bonding states undergo a contraction, which in turn, induces a straightening of the oxygen octahedra surrounding the affected transition metal cations. This leads to an elongation of the block length of the $TiNb_2O_7$ host that has macroscopic ramifications. The predicted variations in volume and b lattice parameter as a function of Li concentration are in good agreement with experiment,[169] indicating that DFT-PBE is capable of accurately describing the redox mechanisms in this material. The structural distortions of the host induced by metal-metal dimer formation not only affect the macroscopic dimensions of the crystal, but also those of the interstitial Li sites. The window sites, for example, are highly distorted in the pristine $TiNb_2O_7$ structure, and unfavorable for Li occupancy. Above $x \approx 2$, however, when the MO_6 octahedral distortions become less extreme, the window sites become more square planar and more favorable for Li occupancy.

The predicted variation in the magnetic moment of $Li_xTiNb_2O_7$ as a function of Li concentration is also in very good agreement with the measurements of Griffith et al [137]. DFT-PBE predicts some degree of spin polarization that leads to a net magnetic moment at low Li concentrations. The net magnetization is predicted to drop to negligible values, however, once the metal-metal dimer redox mechanism commences. The DFT-PBE calculations predict that the bonding states associated with the metal-metal dimers are filled by an equal number of spin up and spin down electrons and do not contribute to a net magnetic moment. Griffith et al [137] suggested that a Hubbard correction to DFT-PBE is necessary to describe the electronic structure of $Li_xTiNb_2O_7$ at dilute Li concentrations. The analysis of a large number of Li-vacancy orderings at dilute concentrations in the current study, however, has shown that DFT-PBE without a Hubbard U correction is already capable of predicting the observed magnetic behavior

as a function of Li concentration.

We expect that a redox mechanism involving the bonding states of metal-metal dimers is not restricted to $Li_xTiNb_2O_7$, but is common in other Wadsley-Roth phases as well. In fact, similar metal-metal bonding has been predicted to occur in $Li_xPNb_9O_{25}$. However, since $Li_xPNb_9O_{25}$ has only one type of transition metal and has a higher degree of cation ordering than $Li_xTiNb_2O_7$, the metal-metal bonds are more extended and the electronic states that emerge are more delocalized. Due to the presence of Ti and Nb disorder in $Li_xTiNb_2O_7$, in contrast, the metal-metal dimer formation is more localized on individual edge-sharing pairs and therefore more apparent as a mechanism of redox.

The formation of metal-metal dimers to accommodate the charge donated by Li falls into a class of molecular-orbital like redox mechanisms that is increasingly being explored as an alternative to cation-centric redox mechanisms of conventional battery intercalation compounds.[241, 242, 243, 244] Other compounds exhibiting molecular-orbital redox mechanisms include $Na_2Mn_3O_7$ [241] and $Li_xScMo_3O_8$.[243, 244] In $Na_2Mn_3O_7$, redox has been predicted to occur on anti-bonding states distributed over an extended ring of π-bonded Mn and oxygen orbitals surrounding a cation vacancy.[241] In $Li_xScMo_3O_8$, charge donated by Li is accommodated on molecular-orbital-like states derived from Mo metal trimer clusters formed by the hybridization of t_{2g} orbitals.[243, 244]

The redox mechanism described here for $Li_xTiNb_2O_7$ induces a structural changes due to the contraction in the distance between edge-sharing transition cations to form a favorable bonding state. This is similar to anion redox enabled by the formation of sulfur-sulfur S_2^{2-} dimers.[245, 246, 247, 248, 249, 250, 251] More extreme redox mechanisms that require a change in the coordination environment include the $Mn^{4+} \rightarrow Mn^{7+}$ or a $Cr^{3+} \rightarrow Cr^{6+}$ redox couples that are accompanied by a migration from an octahedral site to an adjacent tetrahedral site.[252, 253, 254] While significant structural changes due to redox processes are undesirable as they can lead to mechanical damage of the

electrode material and hysteresis phenomena,[255, 256] the redox mechanism involving metal dimer formation is less extreme than coordination changing redox mechanisms. The crystallographic diversity of Wadsley-Roth phases, with widely varying numbers and distributions of edge-sharing octahedra, opens up opportunities to tailor the sequence of redox processes and their structural consequences.

When compared to PNb_9O_{25}, $TiNb_2O_7$ has marked differences with regards to lithium site stabilities. In PNb_9O_{25}, pyramidal sites exclusively fill at low levels of lithiation and upon crystallographic distortions that come with reliving the second order Jahn-Teller distortions, window sites become favorable. For the ground state $TiNb_2O_7$ ordering this differs. At low levels of lithiation, pyramidal sites are stable, but window sites quickly begin to fill even before the second order Jahn-Teller distortion is relieved. By the lithium concentration that the second order Jahn-Teller distortion is removed, x=2 as determined by examining $\Gamma_{IV}(T_{1u})$, one-fourth of available window sites are already filled with window sites.

Due to the gradual increase in window site filling the ground state $TiNb_2O_7$ ordering, there is no two phase region predicted. Experimentally synthesized $TiNb_2O_7$ indeed contains a small two phase region occurring at x=1. It important to note though that experimentally synthesized is disordered. Furthermore, it is important to note that different $TiNb_2O_7$ orderings display differing lithium site stabilities, that can make it such that this two-phase region is induced by portions of the differing transition metal orderings available in the disordered $TiNb_2O_7$ compound.

The predicted voltage profile and site occupancies are reasonably robust as demonstrated with uncertainty quantification methods. These methods were also useful for predicting likely ground state candidates to provide training data for the overall model.

For structural changes in the material, we find that the distortion amplitudes for the octahedra change as a function of their octahedral edge sharing. For almost every dis-

tortion mode, corner-sharing octahedra had the smallest induced distortions. Octahedra that share more edges also exhibit the largest distortions. For the distortion associated with off-centering of the central-ion, corner-sharing octahedra see a small decrease between compositions of x=0 and x=1. This is likely caused by a relaxation of the second-order Jahn Teller distortion. On the other hand, if one examines octahedra that share four edges (Figures 5.20 and 5.19), the $\Gamma_{IV}(T_{1u})$ distortion decreases most rapidly between x=1 and x=2. This is the composition range where metal-metal bonding occurs for the 4-edge sharing Nb sites, from delocalized electrons at x=1 (Figure 5.11(b)) to the beginning of metal-metal bonding on the four edge-sharing sites 5.12(b) at x=1.66 (This metal-metal bond is also seen at x=1.33). After this compositions metal-metal bonding on the 4 edge-sharing states occur for more lithium vacancy orderings and the Nb-Nb bond distances quickly decrease by x=2 (Figure 5.19). As further evidence the bond distances for the M1 Nb sites that initially undergo metal-metal bonding are examined. For the M1 site the Nb-Nb bond distance is 3.09 Angstrom at x=1, before metal-metal bonding occurs. This bond distance quickly falls to 2.69 Angstrom at x=1.33, when metal bonding starts to occur in the ground state structure. The decrease in the lowest Nb-Nb pair distances for all lithium-vacancy orderings in 5.16(a) suggests that many other lithium-vacancy orderings also undergo this decrease in Nb-Nb bond distances at equal to and greater than x=1.33.

Additionally many of the observed crystallographic distortions are consistent with experiment. Catti. et al. showed through neutron powder diffraction that a volume increase of 8.4% occurs by a composition of x=3.33, in line with the volume expansion determined in 5.17(a). Additionally a volume increase of all octahedra was experimentally observed over this composition regime, in line with 5.18. Moreover, neutron diffraction showed that the 4 edge sharing sites (M1 and M2) had the largest octahedral volumes. In 5.18, we see at intermediate compositions that the highest volume octahedra are

the ones with the largest amounts of edge-sharing [198]. Moreover, with respect to lithium insertion at intermediate compositions, this study showed a nearly 1 to 1 ratio of pyramidal sites to window sites as predicted in 5.21(b).

5.5 Conclusion

Our comprehensive study of the $TiNb_2O_7$ system presents significant insights into the lithiation mechanism, crystallographic distortions, and electronic structure of this material. As we lithiate, the transition metal bond distances quickly decrease at a composition of x=1.33, as metal-metal bonds form in the high edge sharing octahedra. As this occurs the $\Gamma_V(T_{2u})$ and $\Gamma_{IV}(T_{1u})$ distortion modes quickly decrease, with the change occurring to a greater extent for octahedra that share more edges. The relaxation of these distortions cause an increase in the e_3 strain. Comparisons with experiment shows that these calculations are accurate at predicting the structural parameters as a function of lithium concentration.

Inducing these structural and electronic changes through lithiation suggests potential methods for tuning Wadsley-Roth phases for higher lithium-ion electrode performance. Structures with lower amounts of octahedral edges can help reduce e_3 strain in these structures. Metal-metal bonds can be induced in particular sites that share higher amounts of edge sharing. This bonding mechanism can further be turned on or off as you intercalate or extract lithium. With our combined knowledge of which transition metal sites prefer to stay to the edges of the blocks (transition metals with lower electrostatic repulsions), and knowledge of which Wadsley-Roth types are allowed to form, the E_1 shift being the most favorable, we have a general route for predicting the structural properties of disordered Wadsley-Roth materials upon lithiation.

Chapter 6

Conclusion

High power density battery materials require specific and accurate theoretical design to maximize performance. Through this thesis, we perform a high-throughput study of the Wadsley-Roth crystallographic shear phase anode chemistries. By examining lithium intercalation mechanisms in these phases, design metrics were ascertained. Wadsley-Roth phases can be split into five main classes: $E_0[n \times \infty]$, $E_0[n \times m]$, $E_{x,y}[n \times m]$, $T[n \times m]$, and $M[n \times m]$. These phase types differ by the arrangement and connectivity of the blocks used to construct these Wadsley-Roth phases.

We focus on phase stability in both non-disordered, pristine Wadsley-Roth phases and disordered Wadsley-Roth phases. For pristine Wadsley-Roth phase structures, we find that phase stability is dependent on the interplay between polyhedral edge sharing and resulting distortions. For example, in the maximum oxidation structure Nb_2O_5, the $E_1[4 \times 4]$ structure is the most stable. The cause of this is two fold. To a first order approximation, the energy is controlled by electrostatics. The $E_1[4 \times 4]$ shift type has less octahedral edge sharing than $E_0[4 \times 4]$ and $E_3[4 \times 4]$. The Nb_2O_5 structures with these shift types contain octahedra that share five edges, while $E_1[4 \times 4]$ and $E_2[4 \times 4]$ Nb_2O_5 structures have octahedra that share a maximum of 4 edges. In fact the total amount of

edge sharing per unit cell for $E_1[4\times4]$ and $E_2[4\times4]$ Nb_2O_5 structures is equivalent. This begs the question of why $E_1[4\times4]$ is more stable than $E_2[4\times4]$. The answer lies in how these octahedra share these edges. Specifically, the cause is distortions, the secondary factor for phase stability. The octahedra in $E_1[4\times4]$ are more flexible and have a greater ability to induce octahedral distortions favorable to structure as a whole than $E_2[4\times4]$ Nb_2O_5. Crystallographically, the main difference is a set of octahedra that share 2 edges, that are connected along the infinite axis (the vertical axis) in $E_1[4\times4]$ Nb_2O_5 while in $E_2[4\times4]$ Nb_2O_5 these octahedra share 2 edges connected along the a and b lattice vectors in plane with the blocks (the horizontal axis). This difference induces a difference in the off-centering of the central transition metal ions. For $E_1[4\times4]$ the octahedra are more flexible, allowing the central ions in the 2 edge-sharing octahedra to off-center a necessary amount to accommodate distortions in other octahedra in the system. These distortions are favorable for phase stability of $E_1[4\times4]$ Nb_2O_5 over $E_2[4\times4]$ Nb_2O_5. This trend holds throughout the Nb-O Wadsley-Roth phases and even Ti-Nb-O Wadsley-Roth phases. E_1 type Wadsley-Roth phases are consistently predicted to be the lowest in energy with DFT-PBE. For Nb_3O_7, $Nb_{12}O_{29}$, and Nb_2O_5, the E_1 shift type is the most stable. Even for the type M, mixed phases, stable phases are ones that include elements of the E_1 shift type, $Nb_{22}O_{54}$ and $Nb_{25}O_{62}$.

For disordered Wadsley-Roth phases, electrostatics and distortions are also important for determining the most stable ordering on the transition metal sublattice. For the high power density Wadsley-Roth phase material, $TiNb_2O_7$, distortions are what cause the most stable $TiNb_2O_7$ ordering. In $TiNb_2O_7$, the lowest energy ordering is not the one that would be the lowest purely as a result of electrostatics. The Ti-Nb ordering that is the lowest energy, instead, is the one that minimizes energy when both electrostatics and distortions on the central ion are considered. To a first order approximation, the energy of $TiNb_2O_7$ orderings is dependent on electrostatics between the central cations (Nb^{5+}

and Ti^{4+}). The energy of an ordering is linearly dependent on the amount of octahedral edge-sharing of the Nb ions. Niobium ions are larger and more electropositive, therefore the position of the ions in the $TiNb_2O_7$ orderings strongly impact the relative energy. The lowest energy orderings are ones where Nb ions share the fewest edges (and Ti ions share the most). As the amount of octahedral edges shared by NbO_6 octahedra increases, the energy increases.

As we lithiate Wadsley-Roth phase materials, particular structural distortions are consistent among different Wadsley-Roth phases. At low lithium concentrations, for most Wadsley-Roth phases, pyramidal sites are predicted to be the most stable sites. It's only with increasing lithium concentration that window sites and pyramidal sites both become stable. This site stability is consistent with regards to differing shift types in that $E_0[2 \times \text{inf}]$, the ground state $TiNb_2O_7$ ordering, and PNb_9O_{25} all follow this lithiation mechanism. While this lithiation mechanism is stable as a function of shift type, it can be changed as a function of block size and disorder in the transition metal sublattice. The most stable sites in $E_0[4 \times 4]$ Nb_2O_5 at the dilute limit are window sites, and lithium site stability at both the dilute and intermediate composition in $TiNb_2O_7$ is dependent on the ordering in the transition metal sublattice. Particularly, $TiNb_2O_7$ orderings that have Ti ions in the central or two-edge sharing sites show more stability of the window sites at the dilute limit.

With regards to distortions upon lithiation, for maximum oxidation state Wadsley-Roth phases both $\Gamma_V(T_{2u})$ and $\Gamma_{IV}(T_{1u})$ distortions significantly decrease as a function of lithium concentration. Such maximum oxidation state structures include PNb_9O_{25}, the ground state ordering of $TiNb_2O_7$, $E_1[4 \times 4]$ Nb_2O_5, and $E_0[2 \times \infty]$ Nb_2O_5. Particularly this decrease occurs in line with an increase in the e_3 crystallographic strain. This trend shows two predominant crystallographic mechanisms upon lithiation: (1) that the Nb (and Ti) ions return to the center as more lithium enters the system and (2) the

$\Gamma_V(T_{2u})$ distortion is likely intrinsically liked to the $\Gamma_{IV}(T_{1u})$ distortion. The first of these points is hypothesized to be a result of relaxation of the SOJT as more electrons are introduced to the system. The link between this mechanism and the increase in e_3 crystallographic strain is further proof that the e_3 strain is directly caused by the removal of the SOJT upon lithiation. The second finding, the decrease in $\Gamma_V(T_{2u})$ with decreasing $\Gamma_{IV}(T_{1u})$ distortion amplitudes is more complex. The $\Gamma_V(T_{2u})$ distortion is one where two oxygen's move perpendicularly to a separate set of two other oxygens in a transition metal octahedra. This distortion differs from $\Gamma_{IV}(T_{1u})$, the distortion corresponding to off-centering of the central ion, in that the central ion is immobile. This indicates that as the central ion off-centers, nearby oxygens distort to compensate for the movement of the central ion, and that this mechanism disappears as the central ion re-centers in the octahedra.

For many Wadsley-Roth phases, particularly $TiNb_2O_7$ and PNb_9O_{25}, the structure is electronically insulating before lithiation. It is only after lithium insertion that the structure becomes metallic. Electronic conductivity is required for the redox reactions at the cathode and anode to occur as lithium ions intercalate into the anode/cathode with charging/discharging, so metallicity is intrinsically linked to battery electrode performance.

Future study recommendations include the usage of disorder to tune electrochemical performance in Wadsley-Roth phases. In $TiNb_2O_7$, lithium site stabilities are ordering dependent. This means that if disorder can be tuned in this structure, lithium ordering stability and therefore voltage profiles and performance can be tuned. Unfortunately, for this structure the temperature stability window for the structure is narrow, and there is little room for experimentally inducing disorder in $TiNb_2O_7$. For other Wadsley-Roth structures, such as tungsten niobium oxides or chromium niobium oxides, the stability window may differ. Any experimental or theoretical study of lithiation mechanisms as a

function of transition metal disorder should take the stability of the Wadsley-Roth phase as a whole as a factor when performing the study.

Beyond the Wadsley-Roth phases, we recommend using the tools used in this thesis to study other oxide and sulfide materials. Particularly, the distortion amplitude study can be applied to other binary and ternary oxide materials to determine if particular distortion modes change as you change the central cation species or determine the degree to which differing binary oxide materials undergo second order Jahn-Teller distortions. Overall this method can be useful in performing high level examinations in phase stability in other battery electrode chemistries.

We also recommend using the Wadsley-Roth enumeration code to examine Wadsley-Roth phase stability in other ternaries. Due to the expensive and heavy nature of most transition metals currently used in Wadsley-Roth phases, experimentalists can benefit from information of possible phase stability of Wadsley-Roth phase structures that feature lower cost or lighter transition metals. Furthermore, differing transition metals with differing oxidation states can be used as a way to tune the block sizes in the Wadsley-Roth phases as well as a potential route to control metal-metal bonding in these phases.

Appendix A

Charge Density Evolution in Lithiated $TiNb_2O_7$

A.1 NbO_6 octahedra density of states

At low levels of lithiation (up to x=1) charge is delocalized among the Nb sites. As lithium concentration increases to x=1.33 a dimer begins to form on the M1 Nb site and M1' Nb site with the d_{xy} states forming metal-metal bonds and then the d_{xz} state (Figures A.1, A.3, and A.5). M1 and M1' sites are specifically four-edge sharing sites. It is not until higher composition that sites that share more edges begin to bond. Upon higher compositions (x=2.5 and higher) M2 Nb sites begin to form dimers begin to form on the four edge sharing and three edge sharing sites (Figures A.2, A.4, and A.6).

A.2 TiO_6 octahedra density of states

At low levels of lithiation (up to x=1) charge is delocalized among the Ti sites, in the same way as the Nb sites. Unlike for the 4 edge sharing Nb site, electrons on Ti remain

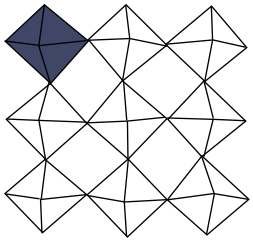

$LiTiNb_2O_7$

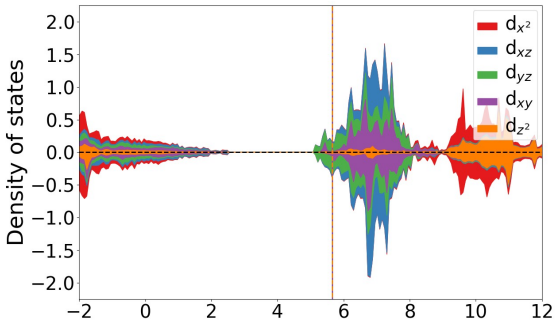

$Li_{1.33}TiNb_2O_7$

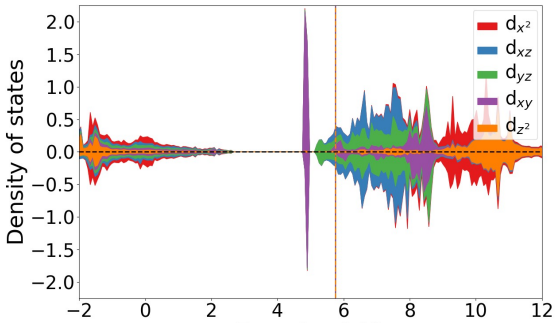

$Li_{2.5}TiNb_2O_7$

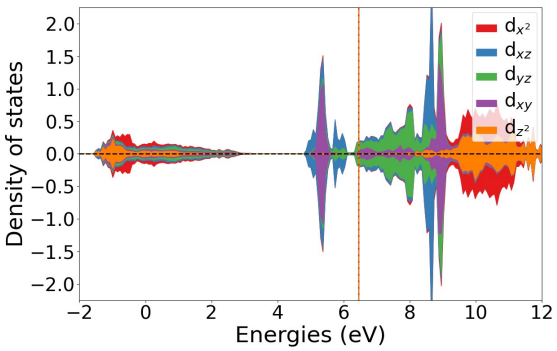

Figure A.1: Projected density of states for the M1 Nb Site for x=1, x=1.33, and x=2.5 in $Li_xTiNb_2O_7$

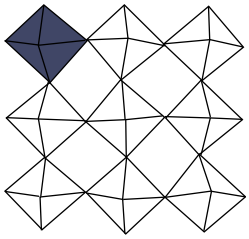

$Li_{2.83}TiNb_2O_7$

$Li_{3.33}TiNb_2O_7$

$Li_{3.5}TiNb_2O_7$

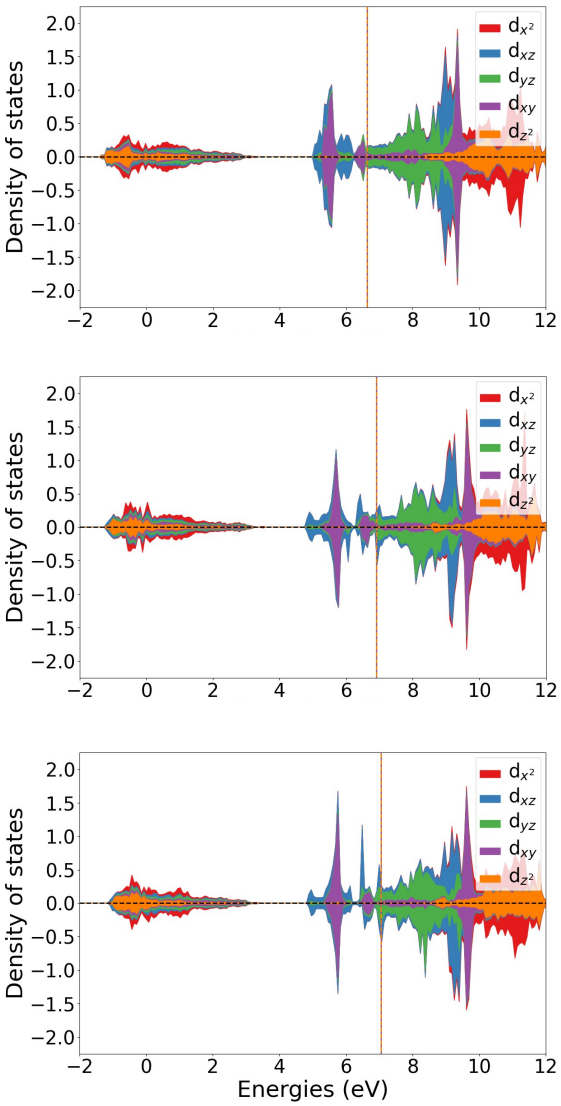

Figure A.2: Projected density of states for the M1 Nb Site for x=2.83, x=3.33, and x=3.5 in $Li_xTiNb_2O_7$

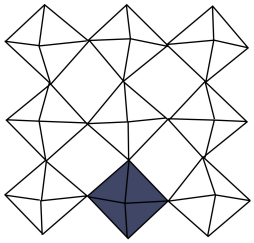

$LiTiNb_2O_7$

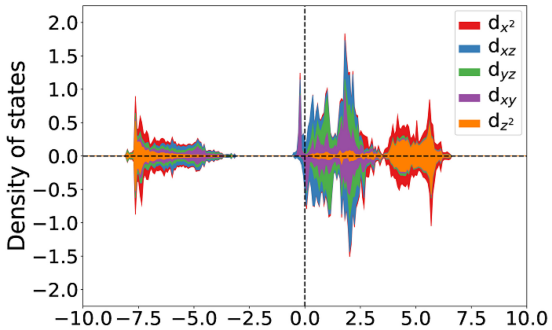

$Li_{1.33}TiNb_2O_7$

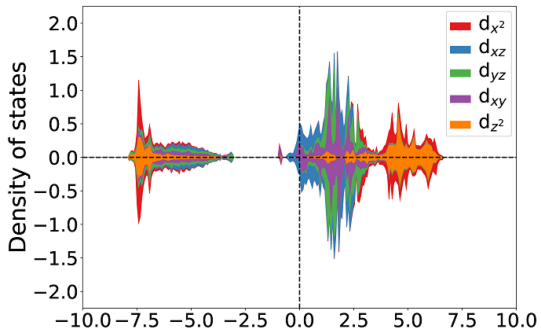

$Li_{2.5}TiNb_2O_7$

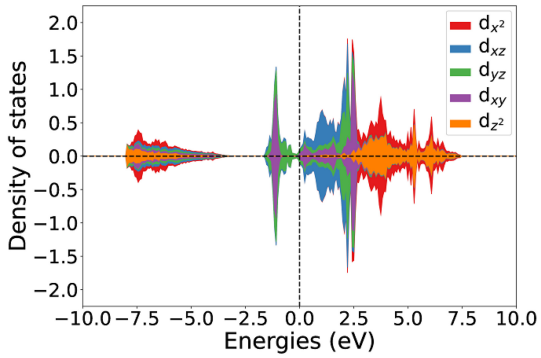

Figure A.3: Projected density of states for the M3 Nb Site for x=1, x=1.33, and x=2.5 in $Li_xTiNb_2O_7$

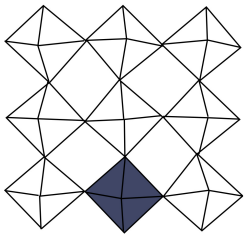

$Li_{2.83}TiNb_2O_7$

$Li_{3.33}TiNb_2O_7$

$Li_{3.5}TiNb_2O_7$

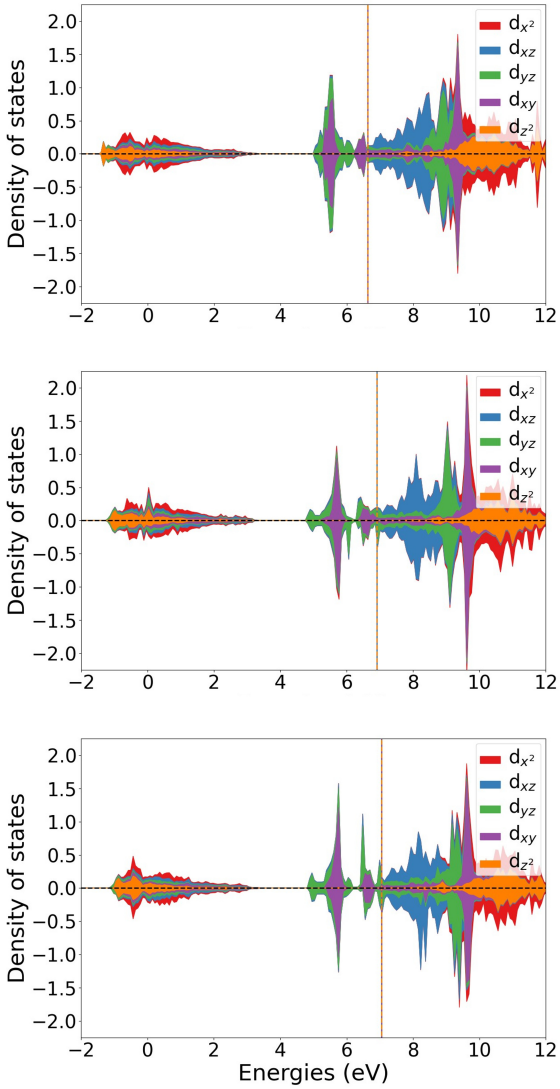

Figure A.4: Projected density of states for the M3 Nb Site for x=2.83, x=3.33, and x=3.5 in $Li_xTiNb_2O_7$

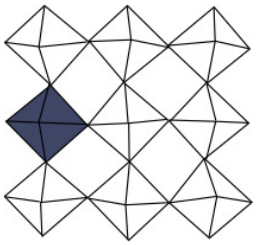

$LiTiNb_2O_7$

$Li_{1.33}TiNb_2O_7$

$Li_{2.5}TiNb_2O_7$

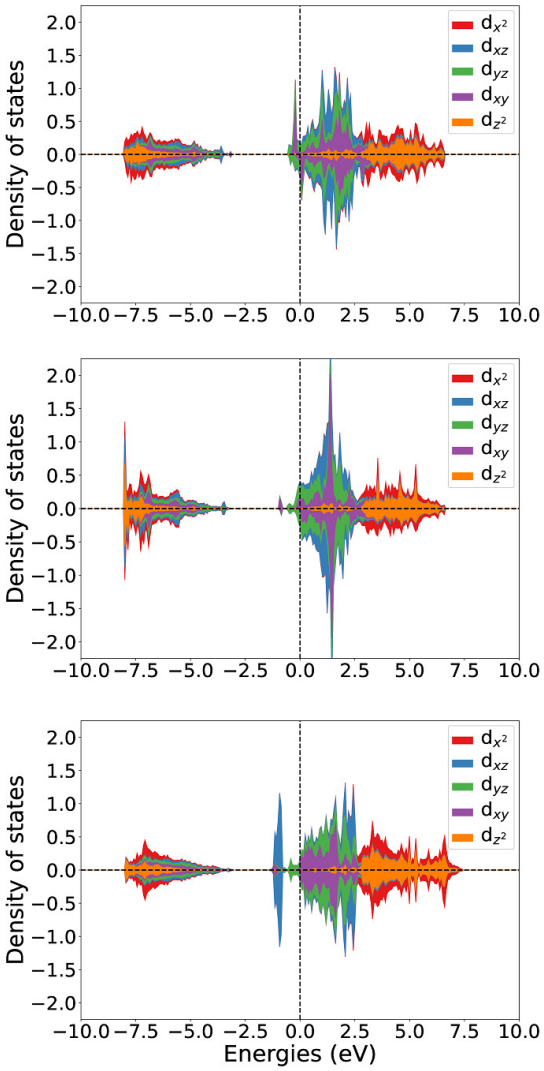

Figure A.5: Projected density of states for the M5 Nb Site for x=1, x=1.33, and x=2.5 in $Li_xTiNb_2O_7$

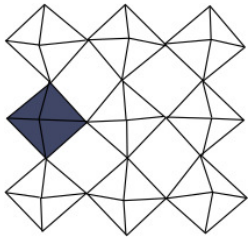

$Li_{2.83}TiNb_2O_7$

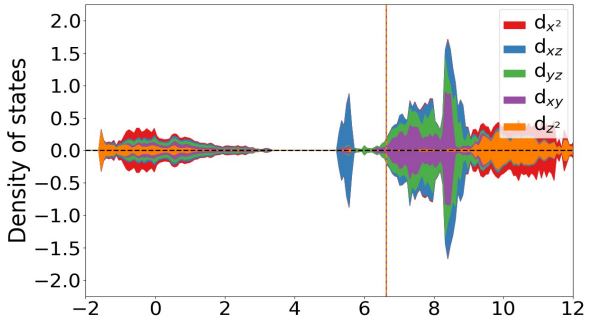

$Li_{3.33}TiNb_2O_7$

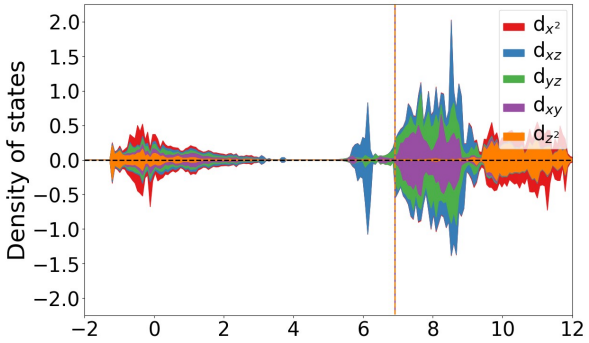

$Li_{3.5}TiNb_2O_7$

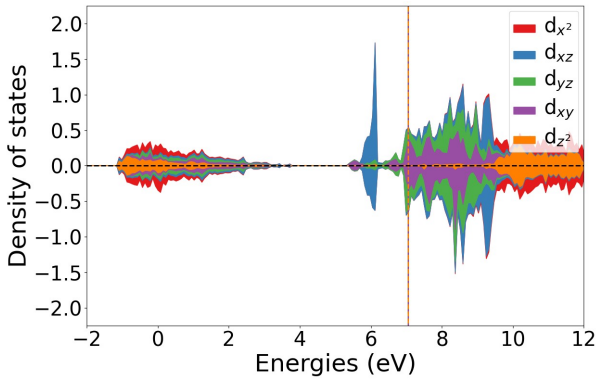

Figure A.6: Projected density of states for the M5 Nb Site for x=2.83, x=3.33, and x=3.5 in $Li_xTiNb_2O_7$

delocalized for the x=1.33 ground states. Delocalization continues until a composition of approximately x=2.5 (Figures A.7, A.9, and A.11). Specifically, the M2 site begins to have bonding states filled at the same energy levels as states on M1 and M1' Nb sites (Figures A.8, A.10, and A.12). Four-edge sharing Ti sites begin bonding before the three-edge sharing Ti site (M3).

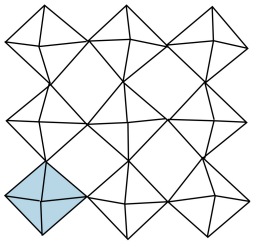

$LiTiNb_2O_7$

$Li_{1.33}TiNb_2O_7$

$Li_{2.5}TiNb_2O_7$

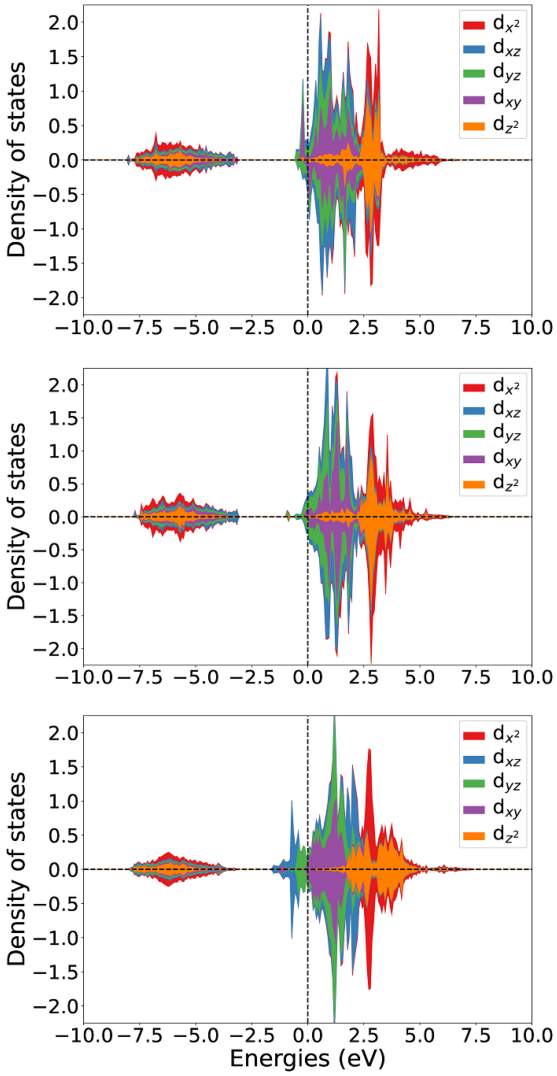

Figure A.7: Projected density of states for the M2 Ti Site for x=1, x=1.33, and x=2.5 in $Li_xTiNb_2O_7$

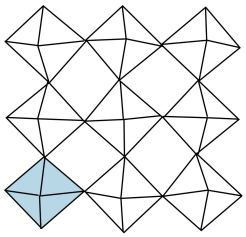

$Li_{2.83}TiNb_2O_7$

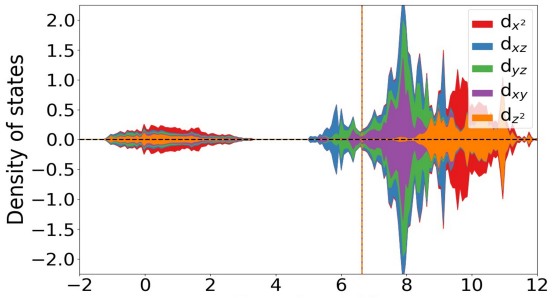

$Li_{3.33}TiNb_2O_7$

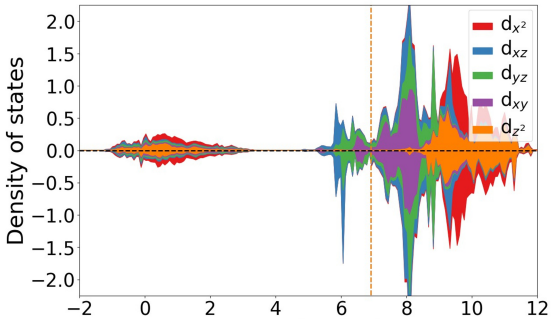

$Li_{3.5}TiNb_2O_7$

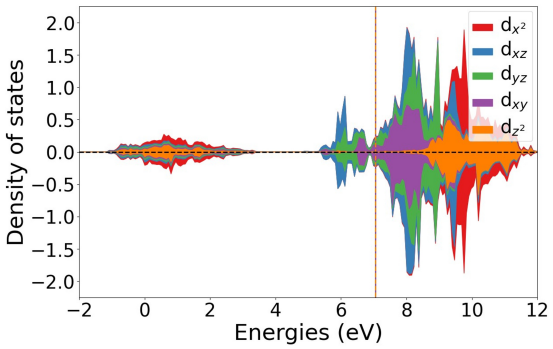

Figure A.8: Projected density of states for the M2 Ti Site for x=2.83, x=3.33, and x=3.5 in $Li_xTiNb_2O_7$

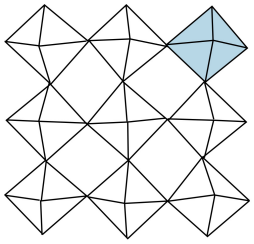

$LiTiNb_2O_7$

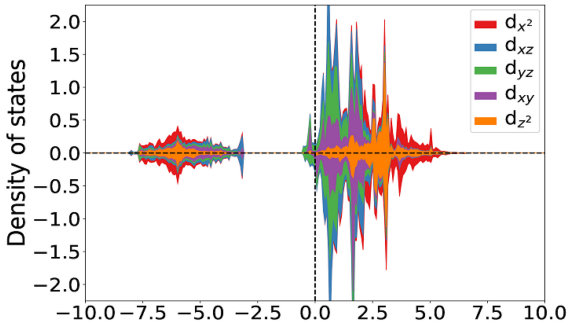

$Li_{1.33}TiNb_2O_7$

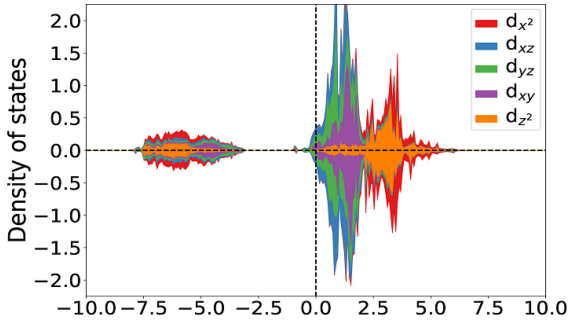

$Li_{2.5}TiNb_2O_7$

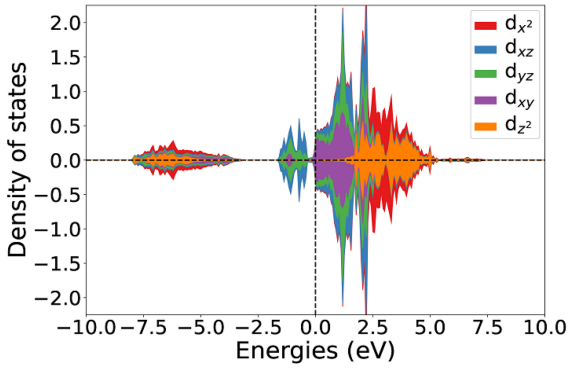

Figure A.9: Projected density of states for the M2' Ti Site for x=1, x=1.33, and x=2.5 in $Li_xTiNb_2O_7$

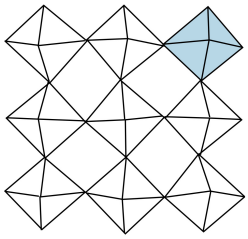

$Li_{2.83}TiNb_2O_7$

$Li_{3.33}TiNb_2O_7$

$Li_{3.5}TiNb_2O_7$

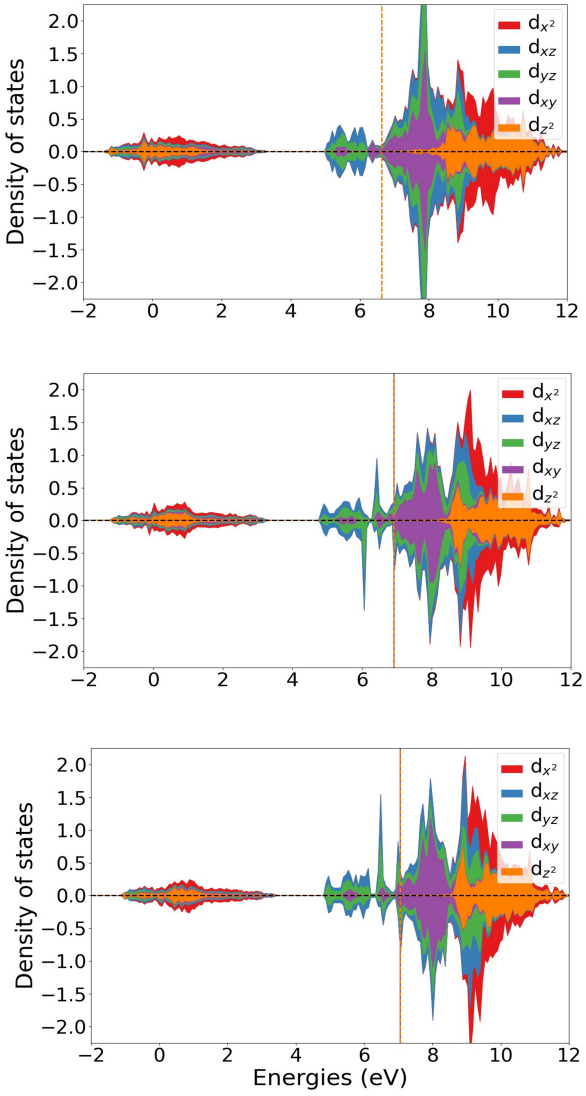

Figure A.10: Projected density of states for the M2' Ti Site for x=2.83, x=3.33, and x=3.5 in $Li_xTiNb_2O_7$

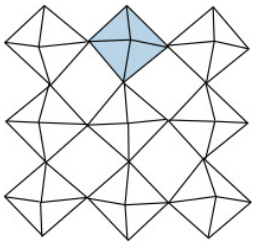

$LiTiNb_2O_7$

$Li_{1.33}TiNb_2O_7$

$Li_{2.5}TiNb_2O_7$

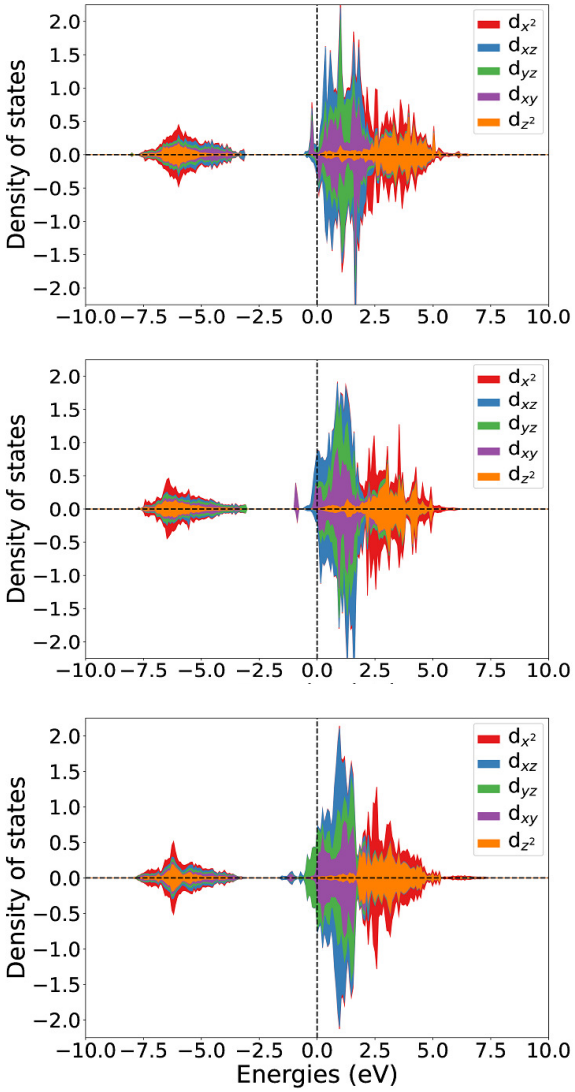

Figure A.11: Projected density of states for the M3 Ti Site for x=1, x=1.33, and x=2.5 in $Li_xTiNb_2O_7$

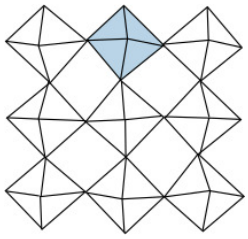

$Li_{2.83}TiNb_2O_7$

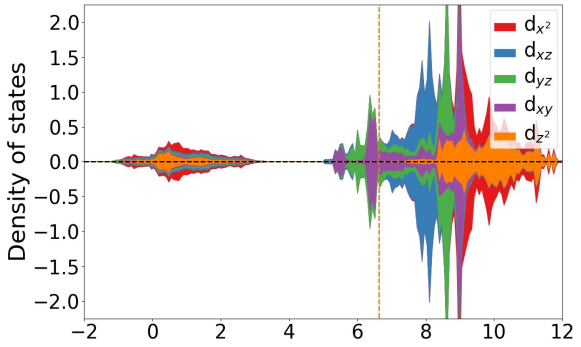

$Li_{3.33}TiNb_2O_7$

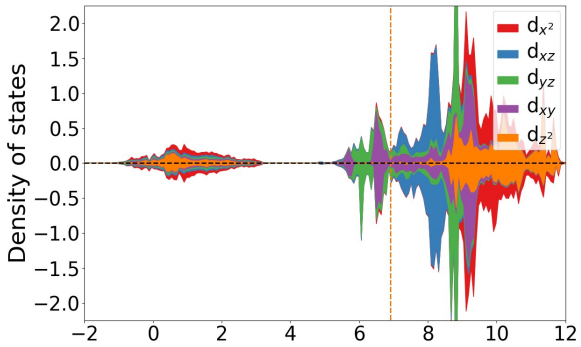

$Li_{3.5}TiNb_2O_7$

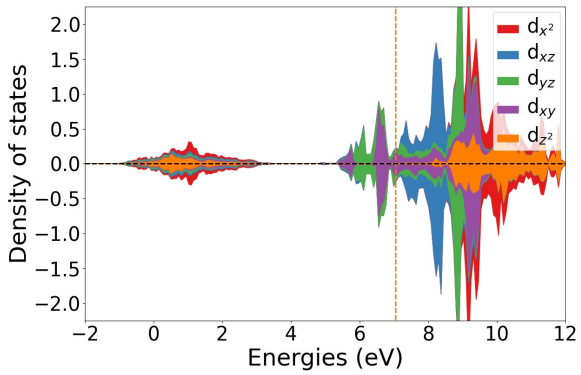

Figure A.12: Projected density of states for the M3 Ti Site for x=2.83, x=3.33, and x=3.5 in $Li_xTiNb_2O_7$

Bibliography

[1] L. K. Mitropoulos, P. D. Prevedouros, and P. Kopelias, *Total cost of ownership and externalities of conventional, hybrid and electric vehicle*, *Transportation research procedia* **24** (2017) 267–274.

[2] A. Van der Ven, Z. Deng, S. Banerjee, and S. P. Ong, *Rechargeable alkali-ion battery materials: theory and computation*, *Chemical reviews* **120** (2020), no. 14 6977–7019.

[3] C. Jiang, H. Li, and C. Wang, *Recent progress in solid-state electrolytes for alkali-ion batteries*, *Science bulletin* **62** (2017), no. 21 1473–1490.

[4] M. Li, J. Lu, Z. Chen, and K. Amine, *30 years of lithium-ion batteries*, *Advanced Materials* **30** (2018), no. 33 1800561.

[5] H. Kim, G. Jeong, Y.-U. Kim, J.-H. Kim, C.-M. Park, and H.-J. Sohn, *Metallic anodes for next generation secondary batteries*, *Chemical Society Reviews* **42** (2013), no. 23 9011–9034.

[6] M. S. Whittingham, *Electrical energy storage and intercalation chemistry*, *Science* **192** (1976), no. 4244 1126–1127.

[7] J. B. Goodenough, *Metallic oxides*, *Progress in solid state chemistry* **5** (1971) 145–399.

[8] K. Mizushima, P. Jones, P. Wiseman, and J. B. Goodenough, *Li_xCoO_2 (0¡ x¡-1): A new cathode material for batteries of high energy density*, *Materials Research Bulletin* **15** (1980), no. 6 783–789.

[9] A. Manthiram, *A reflection on lithium-ion battery cathode chemistry*, *Nature communications* **11** (2020), no. 1 1550.

[10] S. Moharana, G. West, M. Walker, X. S. Yan, and M. Loveridge, *Controlling Li dendritic growth in graphite anodes by potassium electrolyte additives for Li-ion batteries*, *ACS Applied Materials & Interfaces* **14** (2022), no. 37 42078–42092.

[11] L. Kong, Y. Xing, and M. G. Pecht, *In-situ observations of lithium dendrite growth*, *Ieee Access* **6** (2018) 8387–8393.

[12] N. Williard, W. He, C. Hendricks, and M. Pecht, *Lessons learned from the 787 dreamliner issue on lithium-ion battery reliability*, *Energies* **6** (2013), no. 9 4682–4695.

[13] L. Mo and H. Zheng, *Solid coated $Li_4Ti_5O_{12}$ (LTO) using polyaniline (PANI) as anode materials for improving thermal safety for lithium ion battery*, *Energy Reports* **6** (2020) 2913–2918.

[14] H. Zhang, Y. Yang, H. Xu, L. Wang, X. Lu, and X. He, *$Li_4Ti_5O_{12}$ spinel anode: Fundamentals and advances in rechargeable batteries*, *InfoMat* **4** (2022), no. 4 e12228.

[15] R. Cava, D. Murphy, and S. Zahurak, *Lithium insertion in Wadsley-Roth phases based on niobium oxide*, *Journal of the electrochemical society* **130** (1983), no. 12 2345.

[16] J.-T. Han and J. B. Goodenough, *3-v full cell performance of anode framework $TiNb_2O_7$/spinel $LiNi_{0.5}Mn_{1.5}O_4$*, *Chemistry of materials* **23** (2011), no. 15 3404–3407.

[17] G. Liu, L. Zhao, R. Sun, W. Chen, M. Hu, M. Liu, X. Duan, and T. Zhang, *Mesoporous $TiNb_2O_7$ microspheres as high performance anode materials for lithium-ion batteries with high-rate capability and long cycle-life*, *Electrochimica Acta* **259** (2018) 20–27.

[18] G. Zhu, Q. Li, Y. Zhao, and R. Che, *Nanoporous $TiNb_2O_7$/C composite microspheres with three-dimensional conductive network for long-cycle-life and high-rate-capability anode materials for lithium-ion batteries*, *ACS applied materials & interfaces* **9** (2017), no. 47 41258–41264.

[19] K. Ise, S. Morimoto, Y. Harada, and N. Takami, *Large lithium storage in highly crystalline $TiNb_2O_7$ nanoparticles synthesized by a hydrothermal method as anodes for lithium-ion batteries*, *Solid State Ionics* **320** (2018) 7–15.

[20] R. Roth and A. Wadsley, *Multiple phase formation in the binary system Nb_2O_5–WO_3. I. preparation and identification of phases*, *Acta Crystallographica* **19** (1965), no. 1 26–32.

[21] R. Roth and A. Wadsley, *Mixed oxides of titanium and niobium: the crystal structure of $TiNb_{24}O_{62}$ ($TiO_{2.12}Nb_2O_5$)*, *Acta Crystallographica* **18** (1965), no. 4 724–730.

[22] R. Roth, A. Wadsley, and S. Andersson, *The crystal structure of PNb_9O_{25} (P_2O_5. $9Nb_2O_5$)*, *Acta Crystallographica* **18** (1965), no. 4 643–647.

[23] P. Hohenberg and W. Kohn, *Inhomogeneous electron gas*, *Physical review* **136** (1964), no. 3B B864.

[24] A. J. Cohen, P. Mori-Sánchez, and W. Yang, *Challenges for density functional theory*, *Chemical reviews* **112** (2012), no. 1 289–320.

[25] G. R. Schleder, A. C. Padilha, C. M. Acosta, M. Costa, and A. Fazzio, *From DFT to machine learning: recent approaches to materials science–a review*, *Journal of Physics: Materials* **2** (2019), no. 3 032001.

[26] P. Geerlings, F. De Proft, and W. Langenaeker, *Conceptual density functional theory*, *Chemical reviews* **103** (2003), no. 5 1793–1874.

[27] M. Saber, M. B. Preefer, S. K. Kolli, W. Zhang, G. Laurita, B. Dunn, R. Seshadri, and A. Van der Ven, *Role of electronic structure in Li ordering and chemical strain in the fast charging Wadsley-Roth phase PNb_9O_{25}*, *Chemistry of Materials* **33** (2021), no. 19 7755–7766.

[28] M. B. Preefer, M. Saber, Q. Wei, N. H. Bashian, J. D. Bocarsly, W. Zhang, G. Lee, J. Milam-Guerrero, E. S. Howard, R. C. Vincent, *et. al.*, *Multielectron redox and insulator-to-metal transition upon lithium insertion in the fast-charging, Wadsley-Roth phase PNb_9O_{25}*, *Chemistry of Materials* **32** (2020), no. 11 4553–4563.

[29] R. G. Parr, *Density functional theory*, *Annual Review of Physical Chemistry* **34** (1983), no. 1 631–656.

[30] J. Kohanoff and N. Gidopoulos, *Density functional theory: basics, new trends and applications*, *Handbook of molecular physics and quantum chemistry* **2** (2003), no. Part 5 532–568.

[31] M. Born and R. Oppenheimer, *Zur quantentheorie der molekeln*, *Annalen der physik* **389** (1927), no. 20 457–484.

[32] J. C. Tully, *Perspective on "zur quantentheorie der molekeln"*, *Theoretical Chemistry Accounts* **103** (2000), no. 3-4 173–176.

[33] M. Stone, *Born-Oppenheimer approximation and the origin of Wess-Zumino terms: Some quantum-mechanical examples*, *Physical Review D* **33** (1986), no. 4 1191.

[34] E. Kaxiras and J. D. Joannopoulos, *Quantum theory of materials*. Cambridge University Press, 2019.

[35] D. Fredkin and N. Werthamer, *Towards a quantum many-body theory of lattice dynamics. I. time-dependent Hartree approximation*, *Physical Review* **138** (1965), no. 5A A1527.

[36] J. C. Slater, *The theory of complex spectra*, *Physical Review* **34** (1929), no. 10 1293.

[37] J. Zhang and N. J. Mauser, *Optimal Slater-determinant approximation of fermionic wave functions*, *Physical Review A* **94** (2016), no. 3 032513.

[38] P. Echenique and J. L. Alonso, *A mathematical and computational review of Hartree-Fock SCF methods in quantum chemistry*, *Molecular Physics* **105** (2007), no. 23-24 3057–3098.

[39] J. C. Slater, *A simplification of the Hartree-Fock method*, *Physical review* **81** (1951), no. 3 385.

[40] E. J. Baerends, D. Ellis, and P. Ros, *Self-consistent molecular Hartree—Fock—Slater calculations I. the computational procedure*, *Chemical Physics* **2** (1973), no. 1 41–51.

[41] W. Kohn, *Density-functional theory for excited states in a quasi-local-density approximation*, *Phys. Rev. Lett.* **56** (May, 1986) 2219–2220.

[42] W. Kohn, A. D. Becke, and R. G. Parr, *Density functional theory of electronic structure*, *The Journal of Physical Chemistry* **100** (1996), no. 31 12974–12980.

[43] N. D. Mermin, *Thermal properties of the inhomogeneous electron gas*, *Physical Review* **137** (1965), no. 5A A1441.

[44] J. P. Perdew, K. Burke, and Y. Wang, *Generalized gradient approximation for the exchange-correlation hole of a many-electron system*, *Physical Review B* **54** (1996), no. 23 16533.

[45] K. F. Garrity, J. W. Bennett, K. M. Rabe, and D. Vanderbilt, *Pseudopotentials for high-throughput DFT calculations*, *Computational Materials Science* **81** (2014) 446–452.

[46] G. Kresse and D. Joubert, *From ultrasoft pseudopotentials to the projector augmented-wave method*, *Physical review b* **59** (1999), no. 3 1758.

[47] D. Hamann, *Semiconductor charge densities with hard-core and soft-core pseudopotentials*, *Physical Review Letters* **42** (1979), no. 10 662.

[48] H. J. Monkhorst and J. D. Pack, *Special points for Brillouin-zone integrations*, *Physical review B* **13** (1976), no. 12 5188.

[49] D. J. Chadi and M. L. Cohen, *Special points in the Brillouin zone*, *Physical Review B* **8** (1973), no. 12 5747.

[50] U. von Barth, *Basic density-functional theory—an overview*, *Physica Scripta* **2004** (2004), no. T109 9.

[51] P. Ziesche, S. Kurth, and J. P. Perdew, *Density functionals from LDA to GGA*, *Computational materials science* **11** (1998), no. 2 122–127.

[52] N. Mardirossian and M. Head-Gordon, *Thirty years of density functional theory in computational chemistry: an overview and extensive assessment of 200 density functionals*, *Molecular Physics* **115** (2017), no. 19 2315–2372.

[53] J. P. Perdew, A. Ruzsinszky, J. Tao, V. N. Staroverov, G. E. Scuseria, and G. I. Csonka, *Prescription for the design and selection of density functional approximations: More constraint satisfaction with fewer fits*, *The Journal of chemical physics* **123** (2005), no. 6 062201.

[54] F. Furche and J. P. Perdew, *The performance of semilocal and hybrid density functionals in 3d transition-metal chemistry*, *The Journal of chemical physics* **124** (2006), no. 4 044103.

[55] A. J. Archer and R. Evans, *Dynamical density functional theory and its application to spinodal decomposition*, *The Journal of chemical physics* **121** (2004), no. 9 4246–4254.

[56] J. Sun, A. Ruzsinszky, and J. P. Perdew, *Strongly constrained and appropriately normed semilocal density functional*, *Physical review letters* **115** (2015), no. 3 036402.

[57] L.-W. Wang, *Divide-and-conquer quantum mechanical material simulations with exascale supercomputers*, *National Science Review* **1** (2014), no. 4 604–617.

[58] A. D. Becke, *A new mixing of Hartree-Fock and local density-functional theories*, *The Journal of chemical physics* **98** (1993), no. 2 1372–1377.

[59] J. P. Perdew, M. Ernzerhof, and K. Burke, *Rationale for mixing exact exchange with density functional approximations*, *The Journal of chemical physics* **105** (1996), no. 22 9982–9985.

[60] J. Harl and G. Kresse, *Accurate bulk properties from approximate many-body techniques*, *Physical review letters* **103** (2009), no. 5 056401.

[61] L.-W. Wang, *Relationship between the random-phase approximation ground-state total energy and GW quasiparticle energy*, *Physical Review B* **82** (2010), no. 11 115111.

[62] F. Furche, *Developing the random phase approximation into a practical post-kohn–sham correlation model*, *The Journal of Chemical Physics* **129** (2008), no. 11 114105.

[63] M. Fuchs and X. Gonze, *Accurate density functionals: Approaches using the adiabatic-connection fluctuation-dissipation theorem*, *Physical Review B* **65** (2002), no. 23 235109.

[64] J. J. Mortensen, K. Kaasbjerg, S. L. Frederiksen, J. K. Nørskov, J. P. Sethna, and K. W. Jacobsen, *Bayesian error estimation in density-functional theory*, *Physical review letters* **95** (2005), no. 21 216401.

[65] V. Polo, E. Kraka, and D. Cremer, *Electron correlation and the self-interaction error of density functional theory*, *Molecular Physics* **100** (2002), no. 11 1771–1790.

[66] J. M. Sanchez, F. Ducastelle, and D. Gratias, *Generalized cluster description of multicomponent systems*, *Physica A: Statistical Mechanics and its Applications* **128** (1984), no. 1-2 334–350.

[67] J. Sanchez, *Cluster expansion and the configurational theory of alloys*, *Physical Review B* **81** (2010), no. 22 224202.

[68] A. Diaz-Ortiz, H. Dosch, and R. Drautz, *Cluster expansions in multicomponent systems: precise expansions from noisy databases*, *Journal of Physics: Condensed Matter* **19** (2007), no. 40 406206.

[69] A. Van der Ven, J. C. Thomas, B. Puchala, and A. R. Natarajan, *First-principles statistical mechanics of multicomponent crystals*, *Annual Review of Materials Research* **48** (2018) 27–55.

[70] M. D. Radin, S. Hy, M. Sina, C. Fang, H. Liu, J. Vinckeviciute, M. Zhang, M. S. Whittingham, Y. S. Meng, and A. Van der Ven, *Narrowing the gap between theoretical and practical capacities in Li-ion layered oxide cathode materials*, *Advanced Energy Materials* **7** (2017), no. 20 1602888.

[71] J. Gibbs, *A method of geometrical representation of the thermodynamic properties of substances by means of surface. the collected works*, 1873.

[72] M. S. Shell, *Thermodynamics and statistical mechanics: an integrated approach*. Cambridge University Press, 2015.

[73] M. W. Chase and N. I. S. O. (US), *NIST-JANAF thermochemical tables*, vol. 9. American Chemical Society Washington, DC, 1998.

[74] M. Kunz and I. D. Brown, *Out-of-center distortions around octahedrally coordinated d^0 transition metals*, *Journal of Solid State Chemistry* **115** (1995), no. 2 395–406.

[75] K. M. Ok, P. S. Halasyamani, D. Casanova, M. Llunell, P. Alemany, and S. Alvarez, *Distortions in octahedrally coordinated d^0 transition metal oxides: A continuous symmetry measures approach*, *Chemistry of materials* **18** (2006), no. 14 3176–3183.

[76] R. G. Pearson, *Symmetry rule for predicting molecular structures*, *Journal of the American Chemical Society* **91** (1969), no. 18 4947–4955.

[77] P. S. Halasyamani, *Asymmetric cation coordination in oxide materials: Influence of lone-pair cations on the intra-octahedral distortion in d^0 transition metals*, *Chemistry of materials* **16** (2004), no. 19 3586–3592.

[78] M. A. Halcrow, *Jahn-Teller distortions in transition metal compounds, and their importance in functional molecular and inorganic materials*, *Chemical Society Reviews* **42** (2013), no. 4 1784–1795.

[79] D. I. Khomskii and S. V. Streltsov, *Orbital effects in solids: basics, recent progress, and opportunities*, *Chemical Reviews* **121** (2020), no. 5 2992–3030.

[80] J. S. Bechtel, J. C. Thomas, and A. Van der Ven, *Finite-temperature simulation of anharmonicity and octahedral tilting transitions in halide perovskites*, *Physical Review Materials* **3** (2019), no. 11 113605.

[81] H. W. Kuhn, *The Hungarian method for the assignment problem*, *Naval research logistics quarterly* **2** (1955), no. 1-2 83–97.

[82] L. E. Kavraki, *Geometric Methods in Structural Computational Biology*. Rice University, 2009.

[83] W. Kabsch, *A discussion of the solution for the best rotation to relate two sets of vectors*, *Acta Crystallographica Section A: Crystal Physics, Diffraction, Theoretical and General Crystallography* **34** (1978), no. 5 827–828.

[84] W. Kabsch, *A solution for the best rotation to relate two sets of vectors*, *Acta Crystallographica Section A: Crystal Physics, Diffraction, Theoretical and General Crystallography* **32** (1976), no. 5 922–923.

[85] M. S. Dresselhaus, G. Dresselhaus, and A. Jorio, *Group Theory: Application to the Physics of Condensed Matter*.

[86] J. C. Thomas and A. Van der Ven, *The exploration of nonlinear elasticity and its efficient parameterization for crystalline materials*, *Journal of the Mechanics and Physics of Solids* **107** (2017) 76–95.

[87] S. Liang, X. Wang, R. Qi, Y.-J. Cheng, Y. Xia, P. Müller-Buschbaum, and X. Hu, *Bronze-phase TiO_2 as anode materials in lithium and sodium-ion batteries*, *Advanced Functional Materials* **32** (2022), no. 25 2201675.

[88] M. Fehse and E. Ventosa, *Is TiO_2(B) the future of titanium-based battery materials?*, *ChemPlusChem* **80** (2015), no. 5 785–795.

[89] Y. Liu and Y. Yang, *Recent progress of TiO_2-based anodes for Li ion batteries*, *Journal of Nanomaterials* **2016** (Feb, 2016) 8123652.

[90] J. Jin, S.-Z. Huang, J. Liu, Y. Li, D.-S. Chen, H.-E. Wang, Y. Yu, L.-H. Chen, and B.-L. Su, *Design of new anode materials based on hierarchical, three dimensional ordered macro-mesoporous TiO_2 for high performance lithium ion batteries*, *Journal of Materials Chemistry A* **2** (2014), no. 25 9699–9708.

[91] D. Opra, S. Gnedenkov, S. Sinebryukhov, A. Podgorbunsky, A. Sokolov, A. Ustinov, V. Kuryavyi, V. Mayorov, and V. Zheleznov, *Doping of titania with manganese for improving cycling and rate performances in lithium-ion batteries*, *Chemical Physics* **538** (2020) 110864.

[92] J. Qu, J. E. Cloud, Y. Yang, J. Ding, and N. Yuan, *Synthesis of nanoparticles-deposited double-walled TiO_2-B nanotubes with enhanced performance for lithium-ion batteries*, *ACS Applied Materials & Interfaces* **6** (2014), no. 24 22199–22208.

[93] K. J. Griffith, Y. Harada, S. Egusa, R. M. Ribas, R. S. Monteiro, R. B. Von Dreele, A. K. Cheetham, R. J. Cava, C. P. Grey, and J. B. Goodenough, *Titanium niobium oxide: from discovery to application in fast-charging lithium-ion batteries*, *Chemistry of Materials* **33** (2020), no. 1 4–18.

[94] D. Murphy, R. Cava, S. Zahurak, and A. Santoro, *Ternary $Li_x TiO_2$ phases from insertion reactions*, *Solid State Ionics* **9** (1983) 413–417.

[95] C.-T. Hsieh, B.-S. Chang, J.-Y. Lin, and R.-S. Juang, *Improvement of rate capability of spinel lithium titanate anodes using microwave-assisted zinc nanocoating*, *Journal of alloys and compounds* **513** (2012) 393–398.

[96] J. Bhattacharya and A. Van der Ven, *Phase stability and nondilute Li diffusion in spinel $Ti_{(1+x)} Ti_2 O_4$*, *Physical Review B* **81** (2010), no. 10.

[97] K. J. Griffith, K. M. Wiaderek, G. Cibin, L. E. Marbella, and C. P. Grey, *Niobium tungsten oxides for high-rate lithium-ion energy storage*, *Nature* **559** (2018), no. 7715 556–563.

[98] C. P. Koçer, K. J. Griffith, C. P. Grey, and A. J. Morris, *First-principles study of localized and delocalized electronic states in crystallographic shear phases of niobium oxide*, *Physical Review B* **99** (2019), no. 7 075151.

[99] L. Frevel and H. Rinn, *Powder diffraction standards for niobium pentoxide and tantalum pentoxide*, *Analytical Chemistry* **27** (1955), no. 8 1329–1330.

[100] J. Weissman, E. I. Ko, P. Wynblatt, and J. Howe, *High-resolution electron microscopy and image simulation of TT-, T-, and H-niobia and model silica-supported niobium surface oxides*, *Chemistry of Materials* **1** (1989), no. 2 187–193.

[101] D. Chen, J.-H. Wang, T.-F. Chou, B. Zhao, M. A. El-Sayed, and M. Liu, *Unraveling the nature of anomalously fast energy storage in T-Nb_2O_5*, *Journal of the American Chemical Society* **139** (2017), no. 20 7071–7081.

[102] K. Kato, *Structure refinement of H-Nb_2O_5*, *Acta Crystallographica Section B: Structural Crystallography and Crystal Chemistry* **32** (1976), no. 3 764–767.

[103] A. L. Viet, M. Reddy, R. Jose, B. Chowdari, and S. Ramakrishna, *Nanostructured Nb_2O_5 polymorphs by electrospinning for rechargeable lithium batteries*, *The Journal of Physical Chemistry C* **114** (2010), no. 1 664–671.

[104] K. J. Griffith, A. C. Forse, J. M. Griffin, and C. P. Grey, *High-rate intercalation without nanostructuring in metastable Nb_2O_5 bronze phases*, *Journal of the American Chemical Society* **138** (2016), no. 28 8888–8899.

[105] R. Li, Y. Qin, X. Liu, L. Yang, C. Lin, R. Xia, S. Lin, Y. Chen, and J. Li, *Conductive $Nb_{25}O_{62}$ and $Nb_{12}O_{29}$ anode materials for use in high-performance lithium-ion storage*, *Electrochimica Acta* **266** (2018) 202–211.

[106] Y. Li, C. Sun, and J. B. Goodenough, *Electrochemical lithium intercalation in monoclinic $Nb_{12}O_{29}$*, *Chemistry of Materials* **23** (2011), no. 9 2292–2294.

[107] R. Cava, D. Murphy, E. Rietman, S. Zahurak, and H. Barz, *Lithium insertion, electrical conductivity, and chemical substitution in various crystallographic shear structures*, *Solid State Ionics* **9** (1983) 407–411.

[108] R. Cava, D. Murphy, and S. Zahurak, *Secondary lithium cells employing vanadium tungsten oxide positive electrodes*, *Journal of The Electrochemical Society* **130** (1983), no. 1 243.

[109] R. Cava, D. Kleinman, and S. Zahurak, *$V_{3.2}W_{1.8}O_{13}$ and studies of the V_2O_5-WO_3- VO_2 ternary system*, *Materials research bulletin* **18** (1983), no. 7 869–873.

[110] E. Wang, N. Kimura, and M. Greenblatt, *Lithium Insertion in $V_3Nb_9O_{29}$. A Wadsley-Roth Type Phase*, *Journal of the Electrochemical Society* **132** (1985), no. 6 1505.

[111] A. F. Fuentes, E. B. Garza, A. M. de la Cruz, and L. M. Torres-Martínez, *Lithium and sodium insertion in $W_3Nb_{14}O_{44}$, a block structure type phase*, *Solid State Ionics* **93** (1997) 245–253.

[112] A. F. Fuentes, A. M. De La Cruz, and L. M. Torres-Martínez, *A study of lithium insertion in $W_4Nb_{26}O_{77}$: Synthesis and characterization of new phases*, *Solid State Ionics* **92** (1996), no. 1-2 103–111.

[113] A. Wadsley, *Mixed oxides of titanium and niobium. II. the crystal structures of the dimorphic forms $Ti_2Nb_{10}O_{29}$*, *Acta Crystallographica* **14** (1961), no. 6 664–670.

[114] R. Roth and A. Wadsley, *Multiple phase formation in the binary system Nb_2O_5–WO_3. II. The structure of the monoclinic phases $WNb_{12}O_{33}$ and $W_5Nb_{16}O_{55}$*, *Acta Crystallographica* **19** (1965), no. 1 32–38.

[115] R. Roth and A. Wadsley, *Multiple phase formation in the binary system Nb_2O_5–WO_3. III. The structures of the tetragonal phases $W_3Nb_{14}O_{44}$ and $W_8Nb_{18}O_{69}$*, *Acta Crystallographica* **19** (1965), no. 1 38–42.

[116] R. Roth and A. Wadsley, *Multiple phase formation in the binary system Nb_2O_5–WO_4. IV. The block principle*, *Acta Crystallographica* **19** (1965), no. 1 42–47.

[117] V. Plies and R. Gruehn, *Zum thermischen verhalten von R-Nb_2O_5 und strukturverwandtem V_3MoO_{10} und $V_5W_3O_{20}$*, *Journal of the Less Common Metals* **42** (1975), no. 1 77–88.

[118] K. E. Wyckoff, D. D. Robertson, M. B. Preefer, S. M. Teicher, J. Bienz, L. Kautzsch, T. E. Mates, J. A. Cooley, S. H. Tolbert, and R. Seshadri, *High-capacity Li^+ storage through multielectron redox in the fast-charging Wadsley-Roth phase $(W_{0.2}V_{0.8})_3O_7$*, *Chemistry of Materials* **32** (2020), no. 21 9415–9424.

[119] J. t. Allpress and R. Roth, *The effect of annealing on the concentration of Wadsley defects in the Nb_2O_5- WO_3 system*, *Journal of Solid State Chemistry* **3** (1971), no. 2 209–216.

[120] J. Allpress and A. Wadsley, *Multiple phase formation in the binary system Nb_2O_5- WO_3: VII. Intergrowth of H- Nb_2O_5 and $WNb_{12}O_{33}$*, *Journal of Solid State Chemistry* **1** (1969), no. 1 28–38.

[121] B. Gatehouse and A. Wadsley, *The crystal structure of the high temperature form of niobium pentoxide*, *Acta Crystallographica* **17** (1964), no. 12 1545–1554.

[122] K. J. Griffith, A. Senyshyn, and C. P. Grey, *Structural stability from crystallographic shear in TiO_2-Nb_2O_5 phases: Cation ordering and lithiation behavior of $TiNb_{24}O_{62}$*, *Inorganic chemistry* **56** (2017), no. 7 4002–4010.

[123] X. Wu, J. Miao, W. Han, Y.-S. Hu, D. Chen, J.-S. Lee, J. Kim, and L. Chen, *Investigation on $Ti_2Nb_{10}O_{29}$ anode material for lithium-ion batteries*, *Electrochemistry communications* **25** (2012) 39–42.

[124] G. Kresse and J. Hafner, *Ab initio molecular dynamics for liquid metals*, *Physical Review B* **47** (1993), no. 1 558.

[125] G. Kresse and J. Hafner, *Ab initio molecular-dynamics simulation of the liquid-metal–amorphous-semiconductor transition in germanium*, *Physical Review B* **49** (1994), no. 20 14251.

[126] G. Kresse and J. Furthmüller, *Efficient iterative schemes for ab initio total-energy calculations using a plane-wave basis set*, *Physical review B* **54** (1996), no. 16 11169.

[127] G. Kresse and J. Furthmüller, *Efficiency of ab-initio total energy calculations for metals and semiconductors using a plane-wave basis set*, *Computational materials science* **6** (1996), no. 1 15–50.

[128] P. E. Blöchl, *Projector augmented-wave method*, *Physical review B* **50** (1994), no. 24 17953.

[129] C. Developers, *CASM*, 2023.

[130] J. C. Thomas and A. Van der Ven, *Finite-temperature properties of strongly anharmonic and mechanically unstable crystal phases from first principles*, *Physical Review B* **88** (2013), no. 21 214111.

[131] B. Puchala and A. Van der Ven, *Thermodynamics of the Zr-O system from first-principles calculations*, *Physical review B* **88** (2013), no. 9 094108.

[132] B. Puchala, J. C. Thomas, A. R. Natarajan, J. G. Goiri, S. S. Behara, J. L. Kaufman, and A. Van der Ven, *CASM—a software package for first-principles based study of multicomponent crystalline solids*, *Computational Materials Science* **217** (2023) 111897.

[133] N. H. Bashian, M. B. Preefer, J. Milam-Guerrero, J. J. Zak, C. Sendi, S. A. Ahsan, R. C. Vincent, R. Haiges, K. A. See, R. Seshadri, *et. al.*, *Understanding the role of crystallographic shear on the electrochemical behavior of niobium oxyfluorides*, *Journal of Materials Chemistry A* **8** (2020), no. 25 12623–12632.

[134] M. Israelsson and L. Kihlborg, *The crystal structure of monoclinic wolfram vanadium oxide, $W_3V_5O_{20}$, an oD structure related to R-Nb_2O_5*, *Journal of Solid State Chemistry* **1** (1970), no. 3-4 469–477.

[135] W. Mertin, S. Andersson, and R. Gruehn, *Über die kristallstruktur von M-Nb_2O_5*, *Journal of Solid State Chemistry* **1** (1970), no. 3-4 419–424.

[136] X. Huang, W. Zhou, X. Chen, C. Jiang, and Z. Zou, *High performance Li-ion hybrid capacitors with micro-sized $Nb_{14}W_3O_{44}$ as anode*, *Electrochimica Acta* **368** (2021) 137613.

[137] K. J. Griffith, I. D. Seymour, M. A. Hope, M. M. Butala, L. K. Lamontagne, M. B. Preefer, C. P. Kocer, G. Henkelman, A. J. Morris, M. J. Cliffe, *et. al.*, *Ionic and electronic conduction in $TiNb_2O_7$*, *Journal of the American Chemical Society* **141** (2019), no. 42 16706–16725.

[138] R. V. Dreele and A. K. Cheetham, *The structures of some titanium-niobium oxides by powder neutron diffraction*, *Proceedings of the Royal Society of London. A. Mathematical and Physical Sciences* **338** (1974), no. 1614 311–326.

[139] N. H. Gunda, B. Puchala, and A. Van der Ven, *Resolving phase stability in the Ti-O binary with first-principles statistical mechanics methods*, *Physical Review Materials* **2** (2018), no. 3 033604.

[140] N. S. H. Gunda, B. Puchala, and A. Van der Ven, *Resolving phase stability in the Ti-O binary with first-principles statistical mechanics methods*, *Phys. Rev. Materials* **2** (2018) 033604–033616.

[141] C. Nico, T. Monteiro, and M. P. Graça, *Niobium oxides and niobates physical properties: Review and prospects*, *Progress in Materials Science* **80** (2016) 1–37.

[142] A. A. Voskanyan, M. Abramchuk, and A. Navrotsky, *Entropy stabilization of TiO_2–Nb_2O_5 Wadsley–Roth shear phases and their prospects for lithium-ion battery anode materials*, *Chemistry of Materials* **32** (2020), no. 12 5301–5308.

[143] C. P. Koçer, K. J. Griffith, C. P. Grey, and A. J. Morris, *Cation disorder and lithium insertion mechanism of Wadsley-Roth crystallographic shear phases from first principles*, *Journal of the American Chemical Society* **141** (2019), no. 38 15121–15134.

[144] C. P. Koçer, K. J. Griffith, C. P. Grey, and A. J. Morris, *Lithium diffusion in niobium tungsten oxide shear structures*, *Chemistry of Materials* **32** (2020), no. 9 3980–3989.

[145] W. Ye, H. Yu, X. Cheng, H. Zhu, R. Zheng, T. Liu, N. Long, M. Shui, and J. Shu, *Highly efficient lithium container based on non-wadsley-roth structure $Nb_{18}W_{16}O_{93}$ nanowires for electrochemical energy storage*, *Electrochimica Acta* **292** (2018) 331–338.

[146] Z. Lv, H. Zhu, W. Meng, L. Wei, Y. Yang, Y. Zhang, M. Ye, and C. C. Li, *Cation mixing in Wadsley-Roth phase anode of lithium-ion battery improves cycling stability and fast Li^+ storage*, *Applied Physics Reviews* **8** (2021), no. 3 031404.

[147] C. Yang, S. Deng, C. Lin, S. Lin, Y. Chen, J. Li, and H. Wu, *Porous $TiNb_{24}O_{62}$ microspheres as high-performance anode materials for lithium-ion batteries of electric vehicles*, *Nanoscale* **8** (2016), no. 44 18792–18799.

[148] S. Patoux, M. Dolle, G. Rousse, and C. Masquelier, *A reversible lithium intercalation process in an ReO_3 type structure PNb_9O_{25}*, *Journal of The Electrochemical Society* **149** (2002), no. 4 A391.

[149] C. Yang, S. Yu, Y. Ma, C. Lin, Z. Xu, H. Zhao, S. Wu, P. Zheng, Z.-Z. Zhu, J. Li, *et. al.*, *Cr^{3+} and Nb^{5+} co-doped $Ti_2Nb_{10}O_{29}$ materials for high-performance lithium-ion storage*, *Journal of Power Sources* **360** (2017) 470–479.

[150] X. Zhu, Q. Fu, L. Tang, C. Lin, J. Xu, G. Liang, R. Li, L. Luo, and Y. Chen, *$Mg_2Nb_{34}O_{87}$ porous microspheres for use in high-energy, safe, fast-charging, and stable lithium-ion batteries*, *ACS applied materials & interfaces* **10** (2018), no. 28 23711–23720.

[151] Q. Fu, X. Liu, J. Hou, Y. Pu, C. Lin, L. Yang, X. Zhu, L. Hu, S. Lin, L. Luo, *et. al.*, *Highly conductive $CrNb_{11}O_{29}$ nanorods for use in high-energy, safe, fast-charging and stable lithium-ion batteries*, *Journal of Power Sources* **397** (2018) 231–239.

[152] C. Lin, S. Yu, S. Wu, S. Lin, Z.-Z. Zhu, J. Li, and L. Lu, *$Ru_{0.01}Ti_{0.99}Nb_2O_7$ as an intercalation-type anode material with a large capacity and high rate performance for lithium-ion batteries*, *Journal of Materials Chemistry A* **3** (2015), no. 16 8627–8635.

[153] Y. Yang and J. Zhao, *Wadsley–Roth crystallographic shear structure niobium-based oxides: Promising anode materials for high-safety lithium-ion batteries*, *Advanced Science* **8** (2021), no. 12 2004855.

[154] C. Lin, G. Wang, S. Lin, J. Li, and L. Lu, *$TiNb_6O_{17}$: a new electrode material for lithium-ion batteries*, *Chemical Communications* **51** (2015), no. 43 8970–8973.

[155] R. Tao, T. Zhang, S. Tan, C. J. Jafta, C. Li, J. Liang, X.-G. Sun, T. Wang, J. Fan, Z. Lu, *et. al.*, *Insight into the Fast-Rechargeability of a Novel $Mo_{1.5}W_{1.5}Nb_{14}O_{44}$ Anode Material for High-Performance Lithium-Ion Batteries*, *Advanced Energy Materials* **12** (2022), no. 36 2200519.

[156] J.-T. Han, Y.-H. Huang, and J. B. Goodenough, *New anode framework for rechargeable lithium batteries*, *Chemistry of Materials* **23** (2011), no. 8 2027–2029.

[157] J. Anderson, J. Browne, and J. Hutchison, *Electron microscopy of the niobium oxides. I. twinning and defects in H- Nb_2O_5*, *Journal of Solid State Chemistry* **5** (1972), no. 3 419–431.

[158] R. Katal, S. Masudy-Panah, M. Tanhaei, M. H. D. A. Farahani, and H. Jiangyong, *A review on the synthesis of the various types of anatase TiO_2 facets and their applications for photocatalysis*, *Chemical Engineering Journal* **384** (2020) 123384.

[159] W. Hu, L. Li, G. Li, C. Tang, and L. Sun, *High-quality brookite TiO_2 flowers: synthesis, characterization, and dielectric performance*, *Crystal Growth and Design* **9** (2009), no. 8 3676–3682.

[160] K. Mukai and I. Yamada, *Columbite-type TiO_2 as a negative electrode material for lithium-ion batteries*, *Journal of the Electrochemical Society* **164** (2017), no. 14 A3590.

[161] M. N. Tahir, P. Theato, P. Oberle, G. Melnyk, S. Faiss, U. Kolb, A. Janshoff, M. Stepputat, and W. Tremel, *Facile synthesis and characterization of functionalized, monocrystalline rutile TiO_2 nanorods*, *Langmuir* **22** (2006), no. 12 5209–5212.

[162] F. D. Angelis, C. D. Valentin, S. Fantacci, A. Vittadini, and A. Selloni, *Theoretical studies on Anatase and less common TiO_2 phases: Bulk, surfaces, and nanomaterials*, *Chemical Reviews* **114** (2014), no. 19 9708–9753.

[163] G. Zubi, R. Dufo-López, M. Carvalho, and G. Pasaoglu, *The lithium-ion battery: State of the art and future perspectives*, *Renewable Sustainable Energy Rev.* **89** (2018) 292 – 308.

[164] J. Vetter, P. Novák, M. R. Wagner, C. Veit, K.-C. Möller, J. Besenhard, M. Winter, M. Wohlfahrt-Mehrens, C. Vogler, and A. Hammouche, *Ageing mechanisms in lithium-ion batteries*, *J. Power Sources* **147** (2005) 269–281.

[165] L. E. Downie, L. J. Krause, J. C. Burns, L. D. Jensen, V. L. Chevrier, and J. R. Dahn, *In situ detection of lithium plating on graphite electrodes by electrochemical calorimetry*, *J. Electrochem. Soc.* **160** (2013) A588.

[166] S. Rajendran, A. Pilli, O. Omolere, J. Kelber, and L. M. R. Arava, *An All-Solid-State Battery with a Tailored Electrode–Electrolyte Interface Using Surface Chemistry and Interlayer-Based Approaches*, *Chem. Mater.* **33(9)** (2021) 3401–3412.

[167] R. Fantin, E. Trevisanello, R. Ruess, A. Pokle, G. Conforto, F. H. Richter, K. Volz, and J. Janek, *Synthesis and Postprocessing of Single-Crystalline $LiNi_{0.8}Co_{0.15}Al_{0.05}O_2$ for Solid-State Lithium-Ion Batteries with High Capacity and Long Cycling Stability*, *Chem. Mater.* **33(7)** (2021) 2624–2634.

[168] X. Lu, Z. Jian, Z. Fang, L. Gu, Y.-S. Hu, W. Chen, Z. Wang, and L. Chen, *Atomic-scale investigation on lithium storage mechanism in $TiNb_2O_7$*, *Energy Environ. Sci.* **4** (2011) 2638–2644.

[169] B. Guo, X. Yu, X.-G. Sun, M. Chi, Z.-A. Qiao, J. Liu, Y.-S. Hu, X.-Q. Yang, J. B. Goodenough, and S. Dai, *A long-life lithium-ion battery with a highly porous*

$TiNb_2O_7$ anode for large-scale electrical energy storage, *Energy Environ. Sci.* **7** (2014) 2220–2226.

[170] Q. Cheng, J. Liang, Y. Zhu, L. Si, C. Guo, and Y. Qian, *Bulk $Ti_2Nb_{10}O_{29}$ as long-life and high-power Li-ion battery anodes*, *J. Mater. Chem. A* **2** (2014) 17258–17262.

[171] D. Saritha, V. Pralong, U. Varadaraju, and B. Raveau, *Electrochemical Li insertion studies on $WNb_{12}O_{33}$—a shear ReO_3 type structure*, *Journal of Solid State Chemistry* **183** (2010), no. 5 988–993.

[172] L. Yan, H. Lan, H. Yu, S. Qian, X. Cheng, N. Long, R. Zhang, M. Shui, and J. Shu, *Electrospun $WN_{12}O_{33}$ nanowires: superior lithium storage capability and their working mechanism*, *J. Mater. Chem. A* **5** (2017) 8972–8980.

[173] L. Yan, J. Shu, C. Li, X. Cheng, H. Zhu, H. Yu, C. Zhang, Y. Zheng, Y. Xie, and Z. Guo, *$W_3Nb_{14}O_{44}$ nanowires: Ultrastable lithium storage anode materials for advanced rechargeable batteries*, *Energy Storage Materials* **16** (2019) 535–544.

[174] D. Cao, Z. Yao, J. Liu, J. Zhang, and C. Li, *H-Nb_2O_5 wired by tetragonal tungsten bronze related domains as high-rate anode for Li-ion batteries*, *Energy Storage Materials* **11** (2018) 152–160.

[175] R. Kodama, Y. Terada, I. Nakai, S. Komaba, and N. Kumagai, *Electrochemical and in situ XAFS-XRD investigation of Nb_2O_5 for rechargeable lithium batteries*, *J. Electrochem. Soc.* **153** (2006) A583.

[176] V. Augustyn, J. Come, M. A. Lowe, J. W. Kim, P.-L. Taberna, S. H. Tolbert, H. D. Abruña, P. Simon, and B. Dunn, *High-rate electrochemical energy storage through Li^+ intercalation pseudocapacitance*, *Nat. Mater.* **12** (2013) 518–522.

[177] J. W. Kim, V. Augustyn, and B. Dunn, *The effect of crystallinity on the rapid pseudocapacitive response of Nb_2O_5*, *Adv. Energy Mater.* **2** (2012) 141–148.

[178] J. Jiang and J. R. Dahn, *Dependence of the heat of reaction of $Li_{0.81}C_6$ (0.1 V), $Li_7Ti_5O_{12}$ (1.55 V), and $Li_{0.5}VO_2$ (2.45 V) reacting with nonaqueous solvents or electrolytes on the average potential of the electrode material*, *J. Electrochem. Soc.* **153** (2005) A310.

[179] J. Sun, R. C. Remsing, Y. Zhang, Z. Sun, A. Ruzsinszky, H. Peng, Z. Yang, A. Paul, U. Waghmare, X. Wu, *et. al.*, *Accurate first-principles structures and energies of diversely bonded systems from an efficient density functional*, *Nature chemistry* **8** (2016), no. 9 831.

[180] K. Momma and F. Izumi, *VESTA 3 for three-dimensional visualization of crystal, volumetric and morphology data*, *J. Appl. Crystallogr.* **44** (2011) 1272–1276.

[181] A. Van der Ven, J. C. Thomas, Q. Xu, B. Swoboda, and D. Morgan, *Nondilute diffusion from first principles: Li diffusion in Li_xTiS_2*, *Phys. Rev. B* **78** (2008) 104306.

[182] J. Bhattacharya and A. Van der Ven, *First-principles study of competing mechanisms of nondilute Li diffusion in spinel Li_xTiS_2*, *Phys. Rev. B* **83** (2011) 144302.

[183] D. Chang, H. Huo, K. E. Johnston, M. Ménétrier, L. Monconduit, C. P. Grey, and A. Van der Ven, *Elucidating the origins of phase transformation hysteresis during electrochemical cycling of Li–Sb electrodes*, *J. Mater. Chem. A* **3** (2015) 18928–18943.

[184] D. Chang, M.-H. Chen, and A. Van der Ven, *Factors contributing to path hysteresis of displacement and conversion reactions in Li ion batteries*, *Chem. Mater.* **27** (2015) 7593–7600.

[185] A. Emly and A. Van der Ven, *Mg intercalation in layered and spinel host crystal structures for Mg batteries*, *Inorg. Chem.* **54** (2015) 4394–4402.

[186] J. Vinckeviciute, M. D. Radin, and A. Van der Ven, *Stacking-sequence changes and Na ordering in layered intercalation materials*, *Chem. Mater.* **28** (2016) 8640–8650.

[187] S. K. Kolli and A. Van der Ven, *Controlling the electrochemical properties of spinel intercalation compounds*, *ACS Appl. Energy Mater.* **1** (2018) 6833–6839.

[188] S. K. Kolli and A. Van der Ven, *First-principles study of spinel $MgTiS_2$ as a cathode material*, *Chem. Mater.* **30** (2018) 2436–2442.

[189] J. L. Kaufman and A. Van der Ven, *Na_xCoO_2 phase stability and hierarchical orderings in the O3/P3 structure family*, *Phys. Rev. Mater.* **3** (2019) 015402.

[190] J. L. Kaufman and A. Van der Ven, *Ordering and Structural Transformations in Layered K_xCrO_2 for K-Ion Batteries*, *Chem. Mater.* **32** (2020) 6392–6400.

[191] B. H. Toby and R. B. Von Dreele, *GSAS-II: the genesis of a modern open-source all purpose crystallography software package*, *J. Appl. Crystallogr.* **46** (2013) 544–549.

[192] A. Benabbas, M. M. Borel, A. Grandin, A. Leclaire, and B. Raveau, *Redetermination of the structure of PNb_9O_{25}*, *Acta Crystallogr., Sect. C: Cryst. Struct. Commun.* **47** (1991) 849–850.

[193] C. L. Farrow, P. Juhas, J. W. Liu, D. Bryndin, E. S. Božin, J. Bloch, T. Proffen, and S. J. L. Billinge, *PDFfit2 and PDFgui: computer programs for studying nanostructure in crystals*, *J. Phys.: Condens. Matter* **19** (2007) 335219.

[194] R. J. Cava, A. Santoro, D. Murphy, S. Zahurak, and R. Roth, *The structures of the lithium inserted metal oxides $Li_{0.2}ReO_3$ and $Li_{0.36}WO_3$*, *J. Solid State Chem.* **50** (1983) 121–128.

[195] N. H. Bashian, S. Zhou, M. Zuba, A. M. Ganose, J. W. Stiles, A. Ee, D. S. Ashby, D. O. Scanlon, L. F. Piper, B. Dunn, *et. al.*, *Correlated polyhedral rotations in the absence of polarons during electrochemical insertion of lithium in ReO_3*, *ACS Energy Lett.* **3** (2018) 2513–2519.

[196] M. Catti and M. R. Ghaani, *On the lithiation reaction of niobium oxide: structural and electronic properties of $Li_{1.714}Nb_2O_5$*, *Physical Chemistry Chemical Physics* **16** (2014), no. 4 1385–1392.

[197] I. Pinus, M. Catti, R. Ruffo, M. M. Salamone, and C. M. Mari, *Neutron diffraction and electrochemical study of $FeNb_{11}O_{29}/Li_{11}FeNb_{11}O_{29}$ for lithium battery anode applications*, *Chemistry of Materials* **26** (2014), no. 6 2203–2209.

[198] M. Catti, I. Pinus, and K. Knight, *Lithium insertion properties of $Li_xTiNb_2O_7$ investigated by neutron diffraction and first-principles modelling*, *J. Solid State Chem.* **229** (2015) 19–25.

[199] A. Van der Ven, J. C. Thomas, Q. Xu, and J. Bhattacharya, *Linking the electronic structure of solids to their thermodynamic and kinetic properties*, *Mathematics and computers in simulation* **80** (2010) 1393–1410.

[200] H. Yu, J. Zhang, R. Zheng, T. Liu, N. Peng, Y. Yuan, Y. Liu, J. Shu, and Z.-B. Wang, *The journey of lithium ions in the lattice of PNb_9O_{25}*, *Mater. Chem. Front.* **4** (2020) 631–637.

[201] A. O. Kondrakov, A. Schmidt, J. Xu, H. Geßwein, R. Monig, P. Hartmann, H. Sommer, T. Brezesinski, and J. Janek, *Anisotropic lattice strain and mechanical degradation of high-and low-nickel NCM cathode materials for Li-ion batteries*, *J. Phys. Chem. C* **121** (2017) 3286–3294.

[202] M. M. Thackeray, Y. Shao-Horn, A. J. Kahaian, K. D. Kepler, E. Skinner, J. T. Vaughey, and S. A. Hackney, *Structural Fatigue in Spinel Electrodes in High Voltage (4 V) $Li/Li_xMn_2O_4$ Cells*, *Electrochem. Solid-State Lett.* **1** (1998) 7.

[203] J. G. Goiri and A. Van der Ven, *Phase and structural stability in Ni-Al systems from first principles*, *Phys. Rev. B* **94** (2016) 094111.

[204] M. D. Radin and A. Van der Ven, *Stability of prismatic and octahedral coordination in layered oxides and sulfides intercalated with alkali and alkaline-earth metals*, *Chem. Mater.* **28** (2016) 7898–7904.

[205] A. A. Belak, Y. Wang, and A. Van der Ven, *Kinetics of anatase electrodes: the role of ordering, anisotropy, and shape memory effects*, *Chem. Mater.* **24** (2012) 2894–2898.

[206] E. B. Isaacs, S. Patel, and C. Wolverton, *Prediction of Li intercalation voltages in rechargeable battery cathode materials: Effects of exchange-correlation functional, van der Waals interactions, and Hubbard U*, *Phys. Rev. Mater.* **4** (2020) 065405.

[207] A. Van der Ven, M. K. Aydinol, G. Ceder, G. Kresse, and J. Hafner, *First-principles investigation of phase stability in Li_xCoO_2*, *Phys. Rev. B* **58** (1998) 2975.

[208] C. M. Hayner, X. Zhao, and H. H. Kung, *Materials for rechargeable lithium-ion batteries*, *Annual review of chemical and biomolecular engineering* **3** (2012) 445–471.

[209] A. S. Mussa, A. Liivat, F. Marzano, M. Klett, B. Philippe, C. Tengstedt, G. Lindbergh, K. Edström, R. W. Lindström, and P. Svens, *Fast-charging effects on ageing for energy-optimized automotive $LiNi_{1/3}Mn_{1/3}Co_{1/3}O_2$/graphite prismatic lithium-ion cells*, *Journal of Power Sources* **422** (2019) 175–184.

[210] X. Zhang, Z. Li, L. Luo, Y. Fan, and Z. Du, *A review on thermal management of lithium-ion batteries for electric vehicles*, *Energy* **238** (2022) 121652.

[211] R. Qian, C. Yang, D. Ma, K. Li, T. Feng, J. Feng, and J. H. Pan, *Robust lithium storage of block copolymer-templated mesoporous $TiNb_2O_7$ and $TiNb_2O_7$@ C anodes evaluated in half-cell and full-battery configurations*, *Electrochimica Acta* **379** (2021) 138179.

[212] S. Lou, X. Cheng, Y. Zhao, A. Lushington, J. Gao, Q. Li, P. Zuo, B. Wang, Y. Gao, Y. Ma, *et. al.*, *Superior performance of ordered macroporous $TiNb_2O_7$ anodes for lithium ion batteries: understanding from the structural and pseudocapacitive insights on achieving high rate capability*, *Nano Energy* **34** (2017) 15–25.

[213] S. W. Baek, K. E. Wyckoff, D. M. Butts, J. Bienz, A. Likitchatchawankun, M. B. Preefer, M. Frajnkovič, B. S. Dunn, R. Seshadri, and L. Pilon, *Operando calorimetry informs the origin of rapid rate performance in microwave-prepared $TiNb_2O_7$ electrodes*, *Journal of Power Sources* **490** (2021) 229537.

[214] Q. Cheng, J. Liang, N. Lin, C. Guo, Y. Zhu, and Y. Qian, *Porous $TiNb_2O_7$ nanospheres as ultra long-life and high-power anodes for lithium-ion batteries*, *Electrochimica Acta* **176** (2015) 456–462.

[215] V. Aravindan, J. Sundaramurthy, A. Jain, P. S. Kumar, W. C. Ling, S. Ramakrishna, M. P. Srinivasan, and S. Madhavi, *Unveiling $TiNb_2O_7$ as an insertion anode for lithium ion capacitors with high energy and power density*, *ChemSusChem* **7** (2014), no. 7 1858–1863.

[216] Y. Yang, Y. Yue, L. Wang, X. Cheng, Y. Hu, Z.-z. Yang, R. Zhang, B. Jin, and R. Sun, *Facile synthesis of mesoporous $TiNb_2O_7$/C microspheres as long-life and high-power anodes for lithium-ion batteries*, *International Journal of Hydrogen Energy* **45** (2020), no. 22 12583–12592.

[217] A. Ashish, P. Arunkumar, B. Babu, P. Manikandan, S. Sarang, and M. Shaijumon, *$TiNb_2O_7$/Graphene hybrid material as high performance anode for lithium-ion batteries*, *Electrochimica Acta* **176** (2015) 285–292.

[218] L. Hu, C. Lin, C. Wang, C. Yang, J. Li, Y. Chen, and S. Lin, *$TiNb_2O_7$ nanorods as a novel anode material for secondary lithium-ion batteries*, *Functional Materials Letters* **9** (2016), no. 06 1642004.

[219] Y. Zhang, C. Kang, W. Zhao, B. Sun, X. Xiao, H. Huo, Y. Ma, P. Zuo, S. Lou, and G. Yin, *Crystallographic engineering to reduce diffusion barrier for enhanced intercalation pseudocapacitance of $TiNb_2O_7$ in fast-charging batteries*, *Energy Storage Materials* **47** (2022) 178–186.

[220] K. Tang, X. Mu, P. A. van Aken, Y. Yu, and J. Maier, *"Nano-pearl-string" $TiNb_2O_7$ as anodes for rechargeable lithium batteries*, *Advanced Energy Materials* **3** (2013), no. 1 49–53.

[221] J. Meng, Q. He, L. Xu, X. Zhang, F. Liu, X. Wang, Q. Li, X. Xu, G. Zhang, C. Niu, *et. al.*, *Identification of phase control of carbon-confined Nb_2O_5 nanoparticles toward high-performance lithium storage*, *Advanced Energy Materials* **9** (2019), no. 18 1802695.

[222] *CASM Developers, CASM, v0.2.1. Available from https://github.com/prisms-center/CASMcode, 2018.*, .

[223] D. Ober and A. Van der Ven, *Thermodynamically informed priors for uncertainty propagation in first-principles statistical mechanics*, *In preparation* (2023).

[224] A. Van der Ven, J. Bhattacharya, and A. A. Belak, *Understanding li diffusion in li-intercalation compounds*, *Accounts of chemical research* **46** (2013), no. 5 1216–1225.

[225] S. K. Kolli and A. Van der Ven, *Elucidating the factors that cause cation diffusion shutdown in spinel-based electrodes*, *Chemistry of Materials* **33** (2021), no. 16 6421–6432.

[226] J. Bhattacharya and A. Van der Ven, *Phase stability and nondilute li diffusion in spinel $li_{1+x}ti_2o_4$*, *Physical Review B* **81** (2010), no. 10 104304.

[227] T. Chatterji, T. C. Hansen, M. Brunelli, and P. F. Henry, *Negative thermal expansion of ReO_3 in the extended temperature range*, *Applied physics letters* **94** (2009), no. 24 241902.

[228] S. V. Streltsov and D. I. Khomskii, *Covalent bonds against magnetism in transition metal compounds*, *Proceedings of the National Academy of Sciences* **113** (2016), no. 38 10491–10496.

[229] S. V. Streltsov and D. I. Khomskii, *Orbital physics in transition metal compounds: new trends*, *Physics-Uspekhi* **60** (2017), no. 11 1121.

[230] R. G. Pearson, *The second-order Jahn-Teller effect*, *Journal of Molecular Structure: THEOCHEM* **103** (1983) 25–34.

[231] M. Saber, C. Reynolds, J. Li, T. M. Pollock, and A. Van der Ven, *Chemical and structural factors affecting the stability of wadsley-roth block phases*, *Inorganic Chemistry, submitted* (2023).

[232] J. Xu, R. D. Deshpande, J. Pan, Y.-T. Cheng, and V. S. Battaglia, *Electrode side reactions, capacity loss and mechanical degradation in lithium-ion batteries*, *Journal of The Electrochemical Society* **162** (2015), no. 10 A2026.

[233] S.-c. Yang, Y. Hua, D. Qiao, Y.-b. Lian, Y.-w. Pan, and Y.-l. He, *A coupled electrochemical-thermal-mechanical degradation modelling approach for lifetime assessment of lithium-ion batteries*, *Electrochimica Acta* **326** (2019) 134928.

[234] M. Ebner, F. Marone, M. Stampanoni, and V. Wood, *Visualization and quantification of electrochemical and mechanical degradation in Li ion batteries*, *Science* **342** (2013), no. 6159 716–720.

[235] S. Müller, P. Pietsch, B.-E. Brandt, P. Baade, V. De Andrade, F. De Carlo, and V. Wood, *Quantification and modeling of mechanical degradation in lithium-ion batteries based on nanoscale imaging*, *Nature communications* **9** (2018), no. 1 2340.

[236] M. Ko, S. Chae, and J. Cho, *Challenges in accommodating volume change of Si anodes for Li-ion batteries*, *ChemElectroChem* **2** (2015), no. 11 1645–1651.

[237] L. Zhang, M. Al-Mamun, L. Wang, Y. Dou, L. Qu, S. X. Dou, H. K. Liu, and H. Zhao, *The typical structural evolution of silicon anode*, *Cell Reports Physical Science* (2022) 100811.

[238] S. Liu, B. Shen, Y. Niu, and M. Xu, *Fabrication of WS_2-nanoflowers@ rGO composite as an anode material for enhanced electrode performance in lithium-ion batteries*, *Journal of colloid and interface science* **488** (2017) 20–25.

[239] C. Marianetti, D. Morgan, and G. Ceder, *First-principles investigation of the cooperative Jahn-Teller effect for octahedrally coordinated transition-metal ions*, *Physical Review B* **63** (2001), no. 22 224304.

[240] D. Spada, B. Albini, P. Galinetto, D. Versaci, C. Francia, S. Bodoardo, G. Bais, and M. Bini, *$FeNb_{11}O_{29}$, anode material for high-power lithium-ion batteries: Pseudocapacitance and symmetrisation unravelled with advanced electrochemical and in situ/operando techniques*, *Electrochimica Acta* **393** (2021) 139077.

[241] D. A. Kitchaev, J. Vinckeviciute, and A. Van der Ven, *Delocalized metal–oxygen π-redox is the origin of anomalous nonhysteretic capacity in li-ion and na-ion cathode materials*, *Journal of the American Chemical Society* **143** (2021), no. 4 1908–1916.

[242] M. Zhang, D. A. Kitchaev, Z. Lebens-Higgins, J. Vinckeviciute, M. Zuba, P. J. Reeves, C. P. Grey, M. S. Whittingham, L. F. Piper, A. Van der Ven, *et. al.*, *Pushing the limit of 3d transition metal-based layered oxides that use both cation and anion redox for energy storage*, *Nature Reviews Materials* **7** (2022), no. 7 522–540.

[243] K. E. Wyckoff, J. L. Kaufman, S. W. Baek, C. Dolle, J. J. Zak, J. Bienz, L. Kautzsch, R. C. Vincent, A. Zohar, K. A. See, *et. al.*, *Metal–metal bonding as an electrode design principle in the low-strain cluster compound $liscmo_3o_8$*, *Journal of the American Chemical Society* **144** (2022), no. 13 5841–5854.

[244] K. E. Wyckoff, L. Kautzsch, J. L. Kaufman, B. R. Ortiz, A. Kallistova, G. Pokharel, J. Liu, K. M. Taddei, K. M. Wiaderek, S. H. Lapidus, *et. al.*, *Electrochemical control of magnetism on the breathing kagome network of $li_xscmo_3o_8$*, *Chemistry of Materials* (2023).

[245] D. W. Murphy and F. A. Trumbore, *The chemistry of tis_3 and $nbse_3$ cathodes*, *Journal of The Electrochemical Society* **123** (1976), no. 7 960.

[246] P. Gard, C. Sourisseau, G. Ouvrard, and R. Brec, *Infrared study of lithium intercalated phases in the li_xfes_2 system (0 x 2). characterization of a new iron disulfide*, *Solid State Ionics* **20** (1986), no. 3 231–238.

[247] L. Blandeau, G. Ouvrard, Y. Calage, R. Brec, and J. Rouxel, *Transition-metal dichalcogenides from disintercalation processes. crystal structure determination and mossbauer study of li_2fes_2 and its disintercalates li_xfes_2 (0.2 x 2)*, *Journal of Physics C: Solid State Physics* **20** (1987), no. 27 4271.

[248] J. Rouxel, *Anion–cation redox competition and the formation of new compounds in highly covalent systems*, *Chemistry–A European Journal* **2** (1996), no. 9 1053–1059.

[249] S. Britto, M. Leskes, X. Hua, C.-A. Hébert, H. S. Shin, S. Clarke, O. Borkiewicz, K. W. Chapman, R. Seshadri, J. Cho, *et. al.*, *Multiple redox modes in the reversible lithiation of high-capacity, peierls-distorted vanadium sulfide*, *Journal of the American Chemical Society* **137** (2015), no. 26 8499–8508.

[250] S. Saha, G. Assat, M. T. Sougrati, D. Foix, H. Li, J. Vergnet, S. Turi, Y. Ha, W. Yang, J. Cabana, *et. al.*, *Exploring the bottlenecks of anionic redox in li-rich layered sulfides*, *Nature Energy* **4** (2019), no. 11 977–987.

[251] C. J. Hansen, J. J. Zak, A. J. Martinolich, J. S. Ko, N. H. Bashian, F. Kaboudvand, A. Van der Ven, B. C. Melot, J. Nelson Weker, and K. A. See, *Multielectron, cation and anion redox in lithium-rich iron sulfide cathodes*, *Journal of the American Chemical Society* **142** (2020), no. 14 6737–6749.

[252] M. D. Radin, J. Vinckeviciute, R. Seshadri, and A. Van der Ven, *Manganese oxidation as the origin of the anomalous capacity of mn-containing li-excess cathode materials*, *Nature Energy* **4** (2019), no. 8 639–646.

[253] J. Vinckeviciute, D. A. Kitchaev, and A. Van der Ven, *A two-step oxidation mechanism controlled by mn migration explains the first-cycle activation behavior of li_2mno_3-based li-excess materials*, *Chemistry of Materials* **33** (2021), no. 5 1625–1636.

[254] Z. Lu and J. Dahn, *In situ and ex situ xrd investigation of li $[cr_xli_{1/3-x/3}mn_{2/3-2x/3}]o_2$ (x= 1/3) cathode material*, *Journal of the Electrochemical Society* **150** (2003), no. 8 A1044.

[255] A. Van der Ven, K. A. See, and L. Pilon, *Hysteresis in electrochemical systems*, *Battery Energy* **1** (2022), no. 2 20210017.

[256] H.-C. Yu, C. Ling, J. Bhattacharya, J. C. Thomas, K. Thornton, and A. Van der Ven, *Designing the next generation high capacity battery electrodes*, *Energy & Environmental Science* **7** (2014), no. 5 1760–1768.